Image Based Mechanical Characterization Methods For Stretchable Electronic Interconnects

Sandra van de Looij - Kleinendorst

NWO | Netherlands Organisation
for Scientific Research

Cover design by Sandra van de Looij - Kleinendorst

Image Based Mechanical Characterization Methods For Stretchable Electronic Interconnects

PROEFSCHRIFT

ter verkrijging van de graad van doctor aan de Technische Universiteit Eindhoven, op gezag van de rector magnificus prof.dr.ir. F.P.T. Baaijens, voor een commissie aangewezen door het College voor Promoties, in het openbaar te verdedigen op dinsdag 26 november 2019 om 13:30 uur

door

Sandra Marjolein van de Looij - Kleinendorst

geboren te Dordrecht

Dit proefschrift is goedgekeurd door de promotoren en de samenstelling van de promotiecommissie is als volgt:

voorzitter:	prof.dr.ir. A.A. van Steenhoven
1e promotor:	dr.ir. J.P.M. Hoefnagels
2e promotor:	prof.dr.ir. M.G.D. Geers
leden:	dr. J. Réthoré (L'école Centrale de Nantes)
	prof.dr. I. De Wolf (KU Leuven/IMEC)
	prof.dr.ir. C.W.J. Oomens
	dr.ir. M. Langelaar (Technische Universiteit Delft)
	dr. B. Blaysat (Université Clermont Auverne)

Het onderzoek of ontwerp dat in dit proefschrift wordt beschreven is uitgevoerd in overeenstemming met de TU/e Gedragscode Wetenschapsbeoefening.

Abstract

Stretchable electronics is an increasingly studied field of research, with mainly biomedical applications, such as skin-adhered patches for monitoring e.g., blood flow, or an inflatable ultrasound sensor at a catheter tip for minimal invasive surgery. Key in designing reliable electronic interconnects is understanding the mechanical behavior of the structures upon stretching. Mechanical properties are influenced by the small size (in the order of several hundreds of nanometers to tens of microns) and microfabrication processing conditions. Hence, it is important to experimentally investigate the stretchable interconnects as processed, as opposed to for example a standardized tensile test on the bulk material. In this thesis, various specialized Digital Image Correlation (DIC) based techniques are developed for the analysis of experiments with stretchable electronic interconnect structures, based on digital images captured with in-situ microscopy during the experiment.

In the first part of the thesis, a novel global digital image correlation method is developed using adaptive refinement of isogeometric shape functions. Here, the shape functions are automatically adjusted to be able to describe the kinematics of the sought displacement field with an optimized number of degrees of freedom. The method is also extended to a quasi-3D digital *height* correlation technique, in which height profiles are analyzed, yielding three-dimensional surface displacement fields. The method is applied to experiments on aluminum stretchable electronic interconnects adhered to a polyimide substrate, which entail localized buckles upon deformation with complex kinematics and hence analysis of the experiment benefits from the developed adaptive iso-GDIC method. The resulting displacement fields are compared to numerical cohesive zone simulations, in order to characterize the interface between the metal interconnect and the polymeric substrate. It is found that a mixed-mode cohesive zone model with different interface behavior in the shear and normal direction is required to describe realistic in-plane and out-of-plane deformations.

In the second part, a novel *freestanding* stretchable electronic interconnect design is analyzed using an Integrated DIC (IDIC) based technique, in which full-field experimental data is correlated with a Finite Element model of the specimen, in order to identify the parameters in this numerical model. To this end, this method is enhanced to Integrated Digital Height Correlation (IDHC) to be able to correlate the complex 3D interconnect behavior to determine the elastoplastic properties, which are largely influenced by the microscopic dimensions of the structure.

Furthermore, the novel Mechanical Shape Correlation (MSC) technique, used for parameter identification, is introduced. In contrast to regular IDIC techniques, where the images consist of a grayscale speckle pattern applied to the sample, in MSC the images are projections based on the contour lines of the test specimen only. This makes the technique suited for the freestanding stretchable electronic interconnects, where large deformations and rotations cause parts of the sample to rotate in and out-of-view. The large specimen outline changes significantly upon deformation, which is exploited in the MSC algorithm. Attention is paid to the influence of algorithmic choices and experimental issues. To identify the elastoplastic properties of a freestanding stretchable structure in a real experiment, alignment, pre-processing and boundary conditions in the simulation are analyzed to obtain a good agreement between the experimental and simulated images.

Samenvatting

Rekbare elektronica is een in toenemende mate bestudeerd onderzoeksveld, met voornamelijk biomedische toepassingen. Voorbeelden daarvan zijn op de huid gekleefde pleisters om bloedstroom te monitoren en een opblaasbare echosensor voor op het uiteinde van een katheter die bij kijkoperaties wordt gebruikt. De sleutel om tot betrouwbare ontwerpen voor elektrische verbindingen, zogenaamde 'interconnects', te komen is het begrijpen van het mechanische gedrag van deze structuren bij uitrekking. De mechanische eigenschappen worden beïnvloed door de kleine dimensies (in de ordegrootte van enkele honderden nanometers tot tientallen microns) en door de verwerkingscondities tijdens het micro-fabricageproces. Daarom is het belangrijk om *geproduceerde* rekbare interconnects experimenteel te onderzoeken, in tegenstelling tot het uitvoeren van gestandaardiseerde trekproeven op proefstukken van bulkmateriaal. In dit proefschrift worden verschillende gespecialiseerde 'Digital Image Correlation' (DIC)-technieken beschreven voor de analyse van rekbare elektronische interconnects, op basis van digitale beelden die tijdens het experiment gemaakt zijn met in-situ microscopie.

In het eerste deel van het proefschrift wordt een nieuwe 'global digital image correlation' (GDIC)-methode beschreven die gebruik maakt van adaptieve verfijning van isogeometrische vormfuncties. De vormfuncties worden automatisch aangepast om de kinematica van het gezochte verplaatsingsveld te kunnen beschrijven met een geoptimaliseerd aantal vrijheidsgraden. Deze methode wordt ook uitgebreid naar een quasi-3D 'digital *height* correlation' (DHC)-techniek, waarbij hoogteprofielen worden geanalyseerd om drie-dimensionale verplaatsingsvelden van het oppervlak te verkrijgen. De methode wordt toegepast bij experimenten op rekbare elektronische interconnects van aluminium die op een polyimide substraat zijn gelijmd. Bij deformatie ontstaan lokaal kreukels met een complex verplaatsingsveld en dus heeft de analyse voordeel bij gebruik van de ontwikkelde 'adaptive iso-GDIC'-methode. De resulterende verplaatsingsvelden worden vergeleken met numerieke 'cohesive zone'-simulaties om het grensvlak tussen de metalen structuur en het polymeren substraat te kunnen karakteriseren. Hieruit wordt geconcludeerd dat voor het beschrijven van realistische in- en uit-het-vlak-vervormingen, het noodzakelijk is om een '*mixed-mode* cohesive zone'-model te gebruiken, waarbij het gedrag verschillend is tussen de afschuifrichting en de normaalrichting.

In het tweede deel wordt een vernieuwende *vrijstaande* rekbare interconnect geanaly-

seerd met behulp van een op 'Integrated DIC'(IDIC) gebaseerde techniek. 'Full-field' experimentele data wordt gecorreleerd met een eindige-elementen-model van het proefstuk, met als doel het identificeren van parameters in dit numerieke model. Daarom wordt de methode uitgebreid naar 'Integrated Digital Height Correlation' (IDHC) om het complexe drie-dimensionale gedrag van de structuren te kunnen analyseren. Dit wordt gebruikt om elastoplastische eigenschappen te bepalen, die sterk beïnvloed worden door de microscopische dimensies van de structuur.

Daarnaast wordt de nieuwe 'Mechanical Shape Correlation' (MSC)-techniek geïntroduceerd, die ook wordt gebruikt voor parameter-identificatie. In tegenstelling tot reguliere IDIC-technieken, waar de beelden bestaan uit een spikkelpatroon van grijswaarden op het proefstuk, zijn de beelden in MSC projecties die gebaseerd zijn op alleen de contour van de structuur. Dit maakt deze techniek geschikt voor de vrijstaande rekbare elektronische interconnects, omdat grote deformaties en rotaties ervoor zorgen dat delen van de structuur in en uit beeld verschijnen en verdwijnen. De grote omtrek van de structuur verandert significant tijdens deformatie, hetgeen wordt benut in het MSC-algoritme. Er wordt aandacht besteed aan de invloed van keuzes die in het algoritme gemaakt moeten worden en aan experimentele uitdagingen. Om de elastoplastische eigenschappen van een vrijstaande rekbare interconnect te identificeren uit een echt experiment, moet de overeenkomst tussen de experimentele en de gesimuleerde beelden geoptimaliseerd worden: daartoe worden de uitlijning van het experiment met de simulatie, voorbewerking van de beelden en de randvoorwaarden in de simulatie geanalyseerd.

Contents

Glossary

Acronyms

2D	-	Two-dimensional
3D	-	Three-dimensional
CAD	-	Computer Aided Design
CCD	-	Charge-Coupled Device (camera chip)
CTE	-	Coefficient of Thermal Expansion
DHC	-	Digital Height Correlation
DIC	-	Digital Image Correlation
DOF(s) / DoF(s)	-	Degree(s) of Freedom
DVC	-	Digital Volume Correlation
EBSD	-	Electron Backscatter Diffraction
FE / FEM	-	Finite Element(s) / Finite Element Model(ing)
FEMU	-	Finite Element Model Updating
FOV	-	Field of View
GDIC	-	Global Digital Image Correlation
IC	-	Integrated Circuit
IDHC	-	Integrated Digital Height Correlation
IDIC	-	Integrated Digital Image Correlation
IGA	-	Isogeometric Analysis
iso-GDIC / iso-DHC	-	Isogeometric GDIC / DHC
LED	-	Light Emitting Diode
MEMS	-	Micro-Electronical Mechanical Systems
MSC	-	Mechanical Shape Correlation
NaN	-	Not a Number
NURBS	-	Non-Uniform Rational B-Spline(s)
OIM	-	Orientation Imaging Microscopy
PDMS	-	Poly(dimethylsiloxane)
PI	-	Polyimide
PIV	-	Particle Image Velocimetry
PMMA	-	Poly(methyl methacrylate)
RMS	-	Root Mean Squared
ROI	-	Region of Interest

ROPE	-	Rotation and Out-of-Plane Elongation, name of free-standing stretchable electronic interconnect
SDM	-	Signed Distance Map
SEI	-	Stretchable Electronic Interconnects
SEM	-	Scanning Electron Microscopy
SSD	-	Sum of Squared Differences (correlation coefficient in local DIC)
TPU	-	Thermoplastic polyurethane
TSL	-	Traction Separation Law
VIC	-	Virtual Image Correlation
ZOI	-	Zone of Interest

Symbols[1]

Notation	Meaning
$\mathbf{a}$, $\boldsymbol{\alpha}$	Vector or array (Chapter 2)
$\mathbf{A}$	Matrix (Chapter 2)
$\underline{a}$, $\underline{\alpha}$	Vector (rest of thesis)
$\underline{\underline{A}}$	Tensor (rest of thesis)
$\mathbb{a}$	Array (rest of thesis)
$\mathbb{A}$	Matrix (rest of thesis)

$\mathbb{a}$, $\boldsymbol{\lambda}$	Column with degrees of freedom λ_j (Chapter 2), or a_j (rest of thesis)	
A	Hardening coefficient in (rate) power law model for hardening (Chapters 5, 6 and 7)	[MPa] or [N/μm^2]
A_i	Area inside curve, used in Chan-Vese segmentation algorithm (Chapter 7)	
A_{in}	Rectilinear arm length, dimension of horseshoe patterned interconnect design (Chapter 4)	
$\mathbf{b}$, $\mathbb{b}$	Right hand side member of the correlation algorithms, with components b_j ($\mathbf{b}$ in Chapter 2, $\mathbb{b}$ in rest of thesis)	
B_j	Bernstein polynomials (Chapter 3)	
c_1, c_2	Average intensities of (grayscale) image, used in Chan-Vese segmentation algorithm (Chapter 7)	
C_j	Refinement indicator (Chapters 2 and 3)	
C	Evolving curve describing contour in Chan-Vese segmentation algorithm (Chapter 7)	

---

[1]Note that sometimes different symbols for the same variable are used in different chapters, because a different notation was used in the various (published) papers that make up this thesis.

C_{ij}^e	Extraction operators (for Bézier extraction of B-splines) (Chapter 3)	
D	Diagonal matrix containing eigenvalues (spectral decomposition of M) (Chapter 5)	
$\underline{e}_x$, $\underline{e}_y$, $\underline{e}_z$	Vectors used to map scalar NURBS functions on each of the three components of shape functions describing the displacement field (Chapter 2)	
$\underline{e}_x$, $\underline{e}_y$	Orientation vectors used for projection of simulation data on image plane (Chapter 6)	
E	Young's Modulus (whole thesis)	[GPa]
f	Undeformed, reference image (whole thesis)	
$\underline{\underline{F}}$	Deformation gradient tensor (Chapter 3)	
F	Energy functional in Chan-Vese algorithm (Chapter 7)	
g	Deformed image(s) (whole thesis)	
$\tilde{g}$	Back-transformed image (whole thesis)	
$\underline{G}$	True image gradient (Chapter 3)	
G_c	Work of separation (also known as fracture energy, interfacial toughness or critical energy release rate), also comes with superscripts ^{n} for normal direction and ^{s} for shear direction (Chapter 4)	[J/m^2]
h	Signed distance maps from numerical simulation in MSC algorithm (Chapter 6)	
ℓ_c	Correlation length (Chapter 2)	
L	Length of curve, used in Chan-Vese segmentation algorithm (Chapter 7)	
m	Hardening exponent in (rate) power law model for hardening (Chapters 5, 6 and 7)	[-]
$\mathbf{M}$, $\mathbb{M}$, M	Correlation matrix (Hessian in the minimization algorithms), with components M_{ij} ($\mathbf{M}$ in Chapter 2, $\mathbb{M}$ in Chapters 3 and 6, M in Chapters 5 and 7)	
$\underline{N}$	Normal vector used for projection of simulation data on image plane (Chapter 6)	
N_i	(One-dimensional) B-spline shape function (Chapters 2 and 3)	
O_x, O_y	Subpixel location of origin, alignment DoF for MSC (Chapter 7)	
p	Polynomial order (Chapters 2 and 3)	

$\mathbf{p}_A$, $\underline{p}_i$	Control point for geometry parametrization ($\mathbf{p}_A$ in Chapter 2, $\underline{p}_i$ in Chapter 3)	
P	Perturbation factor in MSC algorithm (Chapters 6 and 7)	
pxs	Pixel size, alignment DoF for MSC (Chapter 7)	[mm]
Q	Matrix with its columns containing eigenvectors (spectral decomposition of M) (Chapter 5)	
r, Ψ	Residual image (Ψ in Chapter 2, r in the rest of the thesis)	
t	Time, increments (Chapter 6)	[-]
T	Threshold on refinement indicator (Chapter 3)	
T	Temperature (Chapter 4)	[K]
u_0	Intensity value of (grayscale) image, used in Chan-Vese segmentation algorithm (Chapter 7)	
$\mathbf{u}$, $\underline{U}$	(In-plane) displacement field between reference and deformed image ($\mathbf{u}$ in Chapter 2, $\underline{U}$ in Chapter 3)	[px] or [μm]
U_x, U_y	In-plane displacements of right clamping pad, boundary condition DoF for MSC (Chapter 7)	[mm]
u	Displacement in x-direction (whole thesis)	[px] or [μm]
v	Displacement in y-direction (whole thesis)	[px] or [μm]
w	Displacement in (out-of-plane) z-direction (whole thesis)	[μm]
$\mathbf{x}_0$, $\underline{x}$	Vector with 2D coordinates of the undeformed image configuration ($\mathbf{x}_0$ in Chapter 2, $\underline{x}$ in rest of thesis)	[px] or [μm]
x, y	Image coordinates (whole thesis)	[px] or [μm]
X, Y, Z	Physical or simulation coordinates (Chapter 6)	[μm]
δ_c	Critical opening displacement, also comes with superscripts ^{n} for normal direction and ^{s} for shear direction (Chapter 4)	[μm]
δ_f	Mean Intensity Gradient of an image (region) (Chapters 2 and 3)	
ϵ, ε	Error (whole thesis)	[px], [μm], unit of objective parameter or [-]
$\bar{\varepsilon}_p$	Equivalent plastic strain (Chapters 5, 6 and 7)	[-]
θ_L, θ_R	Rotation of left and right clamping pad, boundary condition DoF for MSC (Chapter 7)	[°]
κ	Curvature (Chapter 4)	[μm^{-1}]

$\boldsymbol{\lambda}$, $\mathbb{a}$	Column with degrees of freedom λ_j (Chapter 2), or a_j (rest of thesis)	
μ	Penalty parameter on curve length, used in Chan-Vese segmentation algorithm (Chapter 7)	
ν	Penalty parameter on area inside curve, used in Chan-Vese segmentation algorithm (Chapter 7)	
ν	Poisson ratio (Chapter 4)	[-]
$\boldsymbol{\xi}$, $\underline{\xi}$	Vector with 2D coordinates of parametric domain on which B-spline/NURBS shape functions are defined ($\boldsymbol{\xi}$ in Chapter 2, $\underline{\xi}$ in Chapter 3)	
Ξ	Knot vector (for B-splines) (Chapters 2 and 3)	
σ_y	Evolving yield stress (Chapters 5, 6 and 7)	[MPa] or [N/μm^2]
σ_{y0}	Initial yield strength (whole thesis)	[MPa] or [N/μm^2]
τ_{max}	Maximum traction, also comes with superscripts ^{n} for normal direction and ^{s} for shear direction (Chapter 4)	[MPa]
$\boldsymbol{\phi}$, $\underline{\varphi}$	(Two-dimensional) shape functions ($\boldsymbol{\phi}$ in Chapter 2, $\underline{\varphi}$ in rest of the thesis)	
$\underline{\phi}$	Approximated mapping function (Chapters 3 and 6)	
ϕ	Rotation of rectilinear arm part of horseshoe shaped interconnect (Chapter 4)	[°]
$\underline{\Phi}$	Mapping function for mapping reference coordinates to deformed coordinates (Chapters 3 and 6)	
Ψ, r	Residual image (Ψ in Chapter 2, r in the rest of the thesis)	
Ψ	Cost function, based on residual, defined for minimization in correlation algorithm (Chapters 3 and 6)	

Chapter 1
Introduction

The development of stretchable electronics enables applications that seemed like science-fiction not that long ago. The close integration of conductive materials with a soft matrix material facilitates a wide range of applications, mainly in the biomedical field, as the gap between traditionally rigid electronics and soft biological tissue is bridged by the flexible and stretchable characteristics of stretchable electronics. For example, health monitoring patches that adhere to the skin [73, 81, 160], smart contact lenses [109], flexible devices for cardiac diagnostics [51, 144] and stretchable surgical tools, such as a balloon catheter with sensors for blood flow monitoring [72, 80] are being developed, see Figure 1.1. Also outside the biomedical field stretchable electronics have found ground: applications include smart textiles [145], flexible displays [118], solar cells [88], and LED arrays [153]. The reader is referred to Ref. [158] for an overview of applications.

There are basically two approaches for the design of stretchable electronics [96, 166]. The first is to use conductive materials that are stretchable [162]. Examples include elastomeric substrates with thin metal films with cracks [84] or buckles [21] to accommodate stretching, composites of an elastomer infiltrated with carbon-nanotubes [63, 131], metal particles [120], or networks of nanowires [62], conductive polymers [54] and liquid metal inside microchannels in an elastomeric matrix [165]. The second strategy is to design stretchable structures from a conductive material with low intrinsic stretchability [1], e.g. wavy silicon ribbons or arches [70, 71], serpentine or horseshoe shaped interconnects [47, 48, 67], fractal designs [92, 146] and origami [135, 136] and kirigami [33, 151] inspired designs.

This thesis builds upon the second approach, i.e., structural designs for stretchable interconnects. The first part of the thesis considers an aluminum horseshoe patterned interconnect adhered to a polyimide substrate [25, 26, 89], see Figure 1.2a. Designs of meandering interconnect structures are commonly used in the field of stretchable electronics, as deformations of these structures accommodate relatively large global strains, while the local strains in the interconnect material remain limited due to the underlying compliant substrate that distributes the stress over the interconnect mate-

(a) Artificial skin [74]

(b) Monitoring patch [160]

(c) Flexible skin display [141]
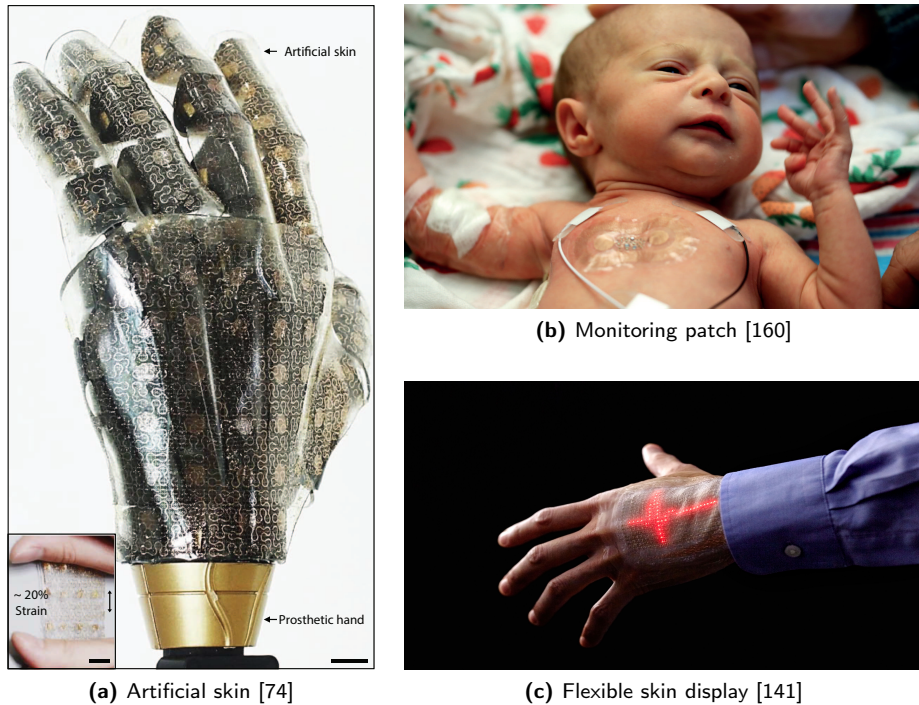
Figure 1.1: Examples of applications of stretchable electronics. In (a) an artificial skin with strain, temperature and pressure sensor arrays, covering a prosthetic hand is shown. In (b) a monitoring patch for vital signs that is soft enough for premature baby's skin is shown. In (c) an ultrathin flexible skin display that can withstand ∼45% stretching without loss of electrical and mechanical function is shown with a moving electrocardiogram waveform measured by a sensor mounted on the skin.

rial [30, 60, 61]. However, functional reliability is endangered when the interconnect delaminates from the substrate, see Figure 1.2b, causing localized strains that may lead to failure of the metal interconnect and finally to loss of function of the device [137]. It is, therefore, important to understand and predict the interface delamination behavior. The challenge herein lies in the microscopic scale at which delamination occurs, which calls for highly accurate techniques for identification of these small-scale localized deformations.

For horseshoe interconnects and most of the other discussed designs a stretch percentage of up to 100% is reached, which is sufficient for many of the mentioned applications, as shown in Figure 1.2. However, to expand the range of applications it is desirable to maximize the stretchability even further. To this end, a novel strategy for ultra-stretchable electronics was recently introduced that overcomes the fundamen-

(a) Horseshoe design [27]

(b) Deformed horseshoe interconnect

(c) Freestanding ROPE design
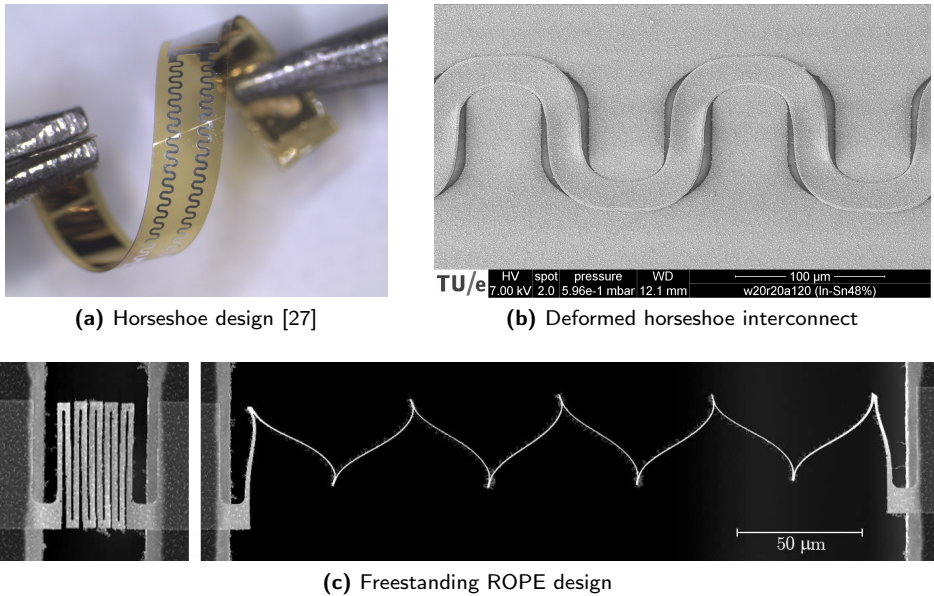
Figure 1.2: The two interconnect designs considered in this thesis. (a) An aluminum horseshoe patterned interconnect attached to a polyimide substrate; (b) The same interconnect after stretching, unveiling the main deformation mode, delamination (c) A freestanding stretchable electronic interconnect design, also denoted ROPE interconnect, in undeformed state (left) and stretched by approximately 650% (right). Upon stretching the interconnect deforms three-dimensionally: the beams rotate and bend to align with the stretch direction.

tal limitations on stretchability, by demonstrating a stretchability well beyond 100%, see Figure 1.2c, even reaching a 2000% elastic stretchability for certain designs [132]. A paradigm shift in the design strategy was proposed, by making the interconnects freestanding and designing such that the full three-dimensional deformation is exploited to reach maximum stretchability, see Figure 1.2c. This freestanding interconnect is also called the ROPE (Rotation and Out-of-Plane Elongation) interconnect. An important part of this design is the integration with standard IC (Integrated Circuit) micro-fabrication methods, to ensure manufacturability of these miniature freestanding interconnects and to enable future high density integration of these interconnects in IC systems to make the intrinsically rigid IC's (highly) stretchable. A potential future application is an advanced inflatable ultrasound detector at a catheter tip for minimal invasive surgery, with variable zoom capability, see Figure 1.3.

The second part of this thesis elaborates on this freestanding interconnect design as shown in Figure 1.2c, because it is important to identify and predict the mechanical behavior and failure mechanisms of these interconnects and the complete stretchable

IC device.

(a) Smart ablation catheter[1]   (b) Inflation of catheter tip
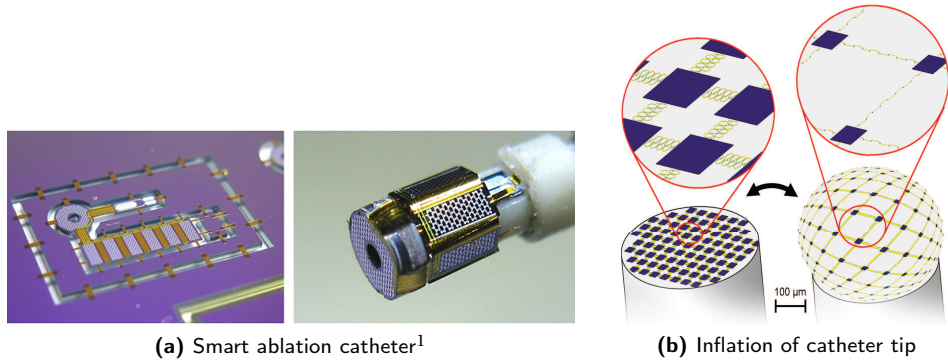
Figure 1.3: A potential novel application of ultra-stretchable electronics, for which the SLIC project aims to solve the fundamental challenges. Left: a smart ablation catheter for treatment of cardiac arrhythmia, developed by Philips Research, with ultrasound ablation depth monitoring to accurately monitor the depth of ablation. Right: a schematic of the potential future possibility of inflating the flat tip of the catheter for variable zoom capability, if ultra-stretchable interconnects are used to connect the CMUT (Capacitive Micromachined Ultrasonic Transducers) array.

For both designs the material behavior depends on size effects due to miniaturization and the processing history of the stretchable structures and hence, bulk material properties cannot be applied [49, 82, 152]. Also different deformation modes, induced by different loading conditions, can affect the measured material properties [45]. Therefore, in order to characterize the mechanics and establish realistic models for the prediction of the deformation and failure behavior, it is important to test original (as-processed) structures in realistic loading conditions, as opposed to performing for example a uniaxial tensile test on a standardized (macroscopic) test specimen produced from the bulk interconnect material. However, the deformations of the stretchable interconnects are large, three-dimensional and complex: Buckling occurs, surfaces rotate out-of-view and other surfaces appear in-view. Therefore, existing methods are difficult to apply, making it is necessary to develop more advanced characterization methods.

Research objective

The research goal of this work is the development of state-of-the-art image based algorithms for the mechanical characterization of stretchable electronic interconnect

---

[1]Image taken from `http://informed-project.eu/index.php/demonstrators`

structures and the identification of material parameters in representative mechanical models.

Methods

The algorithms that are presented in this thesis can be divided in two groups: Global Digital Image Correlation (GDIC) based techniques and Integrated Digital Image Correlation (IDIC) based techniques. The former are developed in view of the characterization of delamination of (horseshoe-patterned) interconnects from a (rubber) substrate, as shown in Figures 1.2a and b. The latter are developed for material identification of the freestanding stretchable electronic interconnect design, see Figure 1.2c. The key difference between GDIC and IDIC is the integration of a mechanical model to guide the correlation of the images or height profiles.

Part I: Advancement of Global Digital Image Correlation Techniques

Digital Image Correlation (DIC) is a full-field measurement method to compute kinematic quantities, i.e., displacement and strain information, from digital images taken of a specimen during a mechanical deformation process. The method does not require a special set-up and can be applied to any type of image, e.g., photographs, micrographs (captured for instance with an optical microscope or a scanning electron microscope), computer tomographic images, profilometric images, etc. Therefore, DIC is a very versatile method that is widely used.

DIC originates from the field of fluid mechanics, where it is better known as Particle Image Velocimetry (PIV) [3]. In the 1980's the method was adopted to the field of solid mechanics [31, 105, 108, 149]. The DIC method consists of an algorithm searching for the displacement field(s) that best matches the difference between two (or more) images of a specimen during deformation. This displacement field is found by minimizing the difference between the images and solving the resulting system of equations. The problem is ill-posed by nature since the number of unknowns equals twice (in 2D) or three times (in quasi-3D) the number of pixels, because the vector displacement per pixel is sought, while only one gray value per pixel is known.

To be able to solve the system, the amount of degrees of freedom (DOFs) is reduced by regularizing the displacement field. Various approaches exist for this purpose, mainly categorized as *local* and *global* approaches [57]. In the local method the image is subdivided in smaller subsets, each of which is given a certain amount of kinematic freedom, e.g., rigid body motion, shear and warping, to obtain the best correlation between the images [31, 85, 156]. The displacement field is then obtained by combining

the displacement vectors of each subset. The more subsets are used, the more complex the displacement fields that may be correlated. However, with more degrees of freedom the sensitivity to image noise increases as well [20, 128]. In contrast, in the global approach the displacement field of the entire image is regularized and optimized in a single optimization step [11, 29, 147]. Naturally, the shape functions describing the displacement field must be more complex than the simple subsets ones in the local approach and these global shape functions can be tailored to the considered experiment. Like for local DIC, also in the global method there is a trade-off between the number of degrees of freedom (i.e., the complexity of the displacement field that might be described by the shape functions) and noise-robustness.

Adaptive isogeometric Digital Image Correlation

In order to analyze localized displacements in the horseshoe shaped stretchable electronic interconnects, which buckle upon stretching, an image correlation algorithm with adaptive refinement is developed. First a DIC algorithm, which calculated the two-dimensional in-plane displacement field is presented. A set of tailored NURBS shape functions (used because of their versatility) is autonomously optimized, such that enough freedom is allowed for the kinematic description of the displacement field. Yet, the amount of DOFs remains limited in order to promote noise robustness and decrease the sensitivity of convergence towards local minima. Moreover, the shape functions are only refined at the locations where this is necessary, i.e., the areas of localized displacements, which means that these locations, which are not known a priori, do not need to be supplied to the algorithm. Hence, the method is less dependent on user input. In Chapter 2 the adaptive isogeometric digital image correlation algorithm is presented, where it is applied to both virtual and real experiments revealing a displacement field with strong localizations, see Figure 1.4a.

Adaptive isogeometric Digital Height Correlation

The method is extended to quasi-3D, or digital height correlation (DHC), in Chapter 3, in order to compute not only the in-plane displacement components, but also the out-of-plane displacement of the considered surface, with the objective to characterize the buckling deformation of the aluminum-polyimide horseshoe interconnects from Figure 1.2a. Adaptive refinement is again used because of the localizations in the displacement field, i.e., the buckles, of which the location is not known a priori. For DHC the input images are not grayscale images with a speckle pattern as in Figure 1.4a, but height maps captured with an optical profilometer, containing three-dimensional data of the sample surface. The speckle pattern, required for DIC methods, is now a three-dimensional pattern consisting of nano-particles. The method is applied to the

horseshoe patterned stretchable interconnects, see Figure 1.4b, and in Chapter 4 the calculated displacements are compared to numerical simulations with a cohesive zone model in order to assess the main deformation mechanism; i.e., delamination of the interconnect from the substrate.

2D 3D

(a) Grayscale image for
Adaptive isogeometric digital image correlation

(b) Height map of horseshoe interconnect for
Adaptive isogeometric digital height correlation

Part I:
Global DIC
methods

(c) Signed Distance Map of ROPE interconnect
for Mechanical Shape Correlation (MSC)

(d) Height Map of ROPE interconnect for
Integrated Digital Height Correlation (IDHC)

Part II:
Integrated
methods
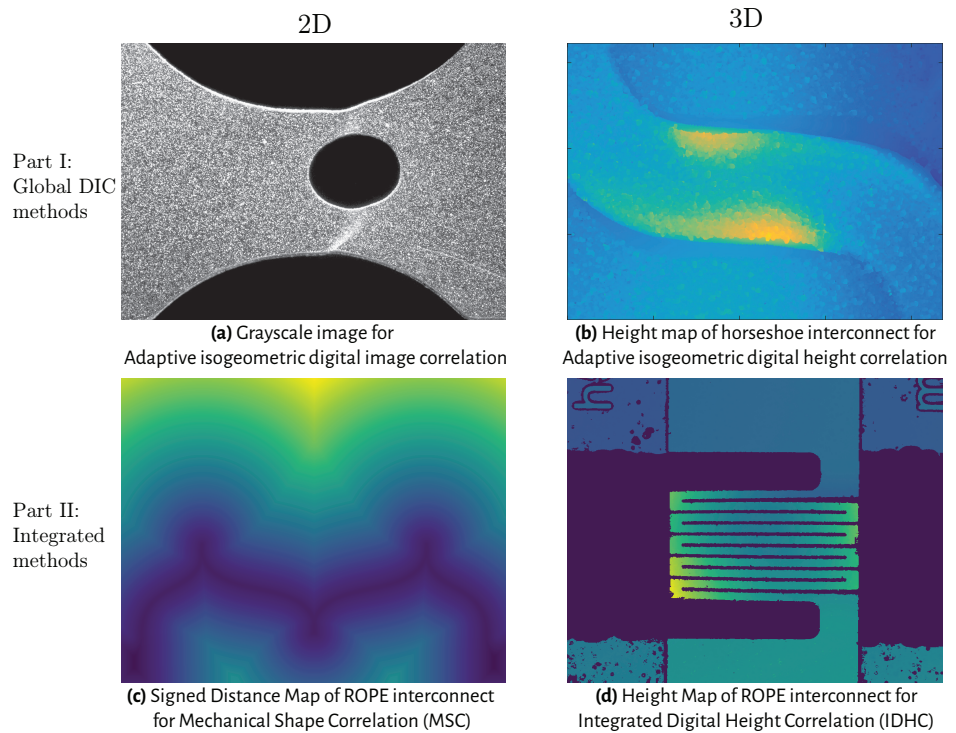
Figure 1.4: Overview of the image types used for the characterization methods in this thesis. In Part I, Global Digital Image Correlation (GDIC) based techniques are extended, with (a) self-adaptive isogeometric GDIC for correlating grayscale images yielding 2D (in-plane) displacement fields and (b) self-adaptive isogeometric Digital Height Correlation (DHC) to obtain full three-dimensional displacement fields by correlating height maps. In Part II, Integrated DIC (IDIC) approaches are introduced for the analysis of the complex 3D displacement field of the ROPE interconnects and identification of material parameters, with (c) the newly introduced Mechanical Shape Correlation method for material parameter identification from the deformation of the outline of a 3D shape by correlating signed distance maps and (d) Integrated DHC (IDHC) for material parameter identification through direct correlation of surface topographies.

Part II: Advancement of Integrated Digital Image Correlation

Another way of regularizing the displacement field is by conjugating the global shape functions with a (mechanical) model, ensuring that the displacements calculated by the mechanical model are kinematically admissible; this is referred to as *Integrated* Digital Image Correlation [100, 115, 121]. The techniques considered in the second part of this thesis are part of this category.

Integrated Digital Height Correlation

For identification of material parameters in the numerical model of the freestanding interconnects an integrated digital height correlation (IDHC) algorithm is developed in Chapter 5. The method is designed to analyze the height maps taken with an optical profilometer during an out-of-plane loading experiment of the interconnects, see Figure 1.4d, in which one of the main deformation modes is triggered, i.e., bending of the beam in an S-shape. The correlation is coupled to a finite element model of the same specimen geometry, loaded at the interconnect's ends by application of an out-of-plane displacement that is measured a-priori from the experimental height maps using global DHC, in which the material parameters concerning the plastic behavior are unknown and the objective for identification using the IDHC algorithm.

Mechanical Shape Correlation

When the freestanding interconnects are loaded in the stretch direction, the beams of which the structure is composed rotate out-of-view, see Figure 1.2c. This makes it impossible to apply existing DIC techniques, as current techniques require that the surfaces of interest remain in-view. Therefore, a new algorithm is proposed that correlates the *shape* of the specimen in the image series, see Figure 1.4c, rather than the surface of the sample: Mechanical Shape Correlation (MSC). The technique is an integrated approach, where the same finite element model as used for IDHC is coupled to the correlation. The specimen contour is extracted from both the experimental images and the numerical simulation and correlated to each other in order to identify material parameters in the model.

The MSC method is introduced in Chapter 6, where it is tested by means of virtual experiments, but also a number of experimental issues are identified and tackled. In Chapter 7 the algorithm is applied to a real experiment with the freestanding stretchable interconnect geometry, in order to identify the material parameters that describe the plastic regime.

Part I

Advancement of Global Digital Image Correlation Techniques

Chapter 2
On the use of adaptive refinement in isogeometric digital image correlation

Abstract

A novel global digital image correlation method was developed using adaptive refinement of isogeometric shape functions. Non-Uniform Rational B-Spline (NURBS) shape functions are used because of their flexibility and versatility, which enables them to capture a wide range of kinematics. The goal of this work was to explore the full potential of isogeometric shape functions for digital image correlation (DIC). This is reached by combining a global DIC method with an adaptive refinement algorithm: adaptive iso-GDIC. The shape functions are automatically adjusted to be able to describe the kinematics of the sought displacement field with an optimized number of degrees of freedom. This results in an accurate method without the need of making problem-specific choices regarding the structure of the shape functions, which makes the method less user input dependent than regular global DIC methods, while keeping the number of degrees of freedom limited to realize optimum regularization of the ill-posed DIC problem. The method's accuracy is demonstrated by a virtual experiment with a predefined, highly localized displacement field. Real experiments with a complex sample geometry demonstrate the effectiveness in practice.

2.1   Introduction

Digital Image Correlation (DIC) is a computational technique used for determining displacement fields. DIC was first developed in the 1980s and introduced in the field of solid mechanics by Peters [108], Sutton [149] and Chu [31]. See Pan et al. [105] for an extensive review on the development of the digital image correlation method. DIC has become a standard technique for material scientists to couple experiments and numerical simulations by analyzing displacement fields from mechanical tests, from which strain fields can be determined.

In the digital image correlation algorithm a system of equations needs to be solved in order to obtain the two-dimensional displacement field. In this system the unknowns are the vector displacements per pixel. The known variable is the brightness field, which is a scalar value per pixel. Since the number of unknowns exceeds the number of equations, the problem is ill-posed by nature. To overcome this problem the displacement field is regularized with so called shape functions. The coefficients associated with the basis functions in this discretization are referred to as degrees of freedom (DOFs).

There are several possibilities for this regularization. A distinction is made between a *local* and a *global* approach. In the local method the region of interest (ROI) is divided in small subsets, zones of interest (ZOIs), which are correlated in both images in order to find their displacement. The total displacement field then is interpolated to obtain full-field information. In the global digital image correlation (GDIC) method the correlation of the two images is executed over the entire domain at once, hence the term 'global' [11, 29, 147]. Typically, continuity of the displacement field is imposed (except when discontinuities are deliberately introduced [110, 111]), making GDIC less sensitive to image noise, see e.g. Hild et al. [57].

In contrast to the local method, where displacements are calculated at every subset center, the global approach provides a displacement at every pixel. Therefore, the information density is generally higher. However, because of the higher amount of regularization the global method is more reliant on the choice of certain important variables the user makes. In particular, the choice of the shape functions is critical, since these must be able to capture the kinematics of the sought displacement field. This choice can be difficult, as the displacement field is generally unknown in advance. Therefore, GDIC is able to provide more accurate results, but only if the user supplies the algorithm with the correct problem-specific kinematic description.

An interesting type of shape functions is Non-Uniform Rational B-Splines (NURBS). NURBS originate from computer aided design (CAD) modeling, where they are the industry standard. NURBS are able to represent many geometric shapes -in particular conic sections- exactly, whereas standard finite element shape functions approximate them. Hughes et al. proposed to use the geometrical representation of CAD-models

directly for finite element analysis: Isogeometric Analysis (IGA) [34, 64].The use of B-Splines in a digital image correlation setting was pioneered by Cheng [29]. Recently Beaubier et al. directly utilized the CAD-representation of their subject for the DIC correlation algorithm [6]. Advantages of NURBS were investigated by Elguedj et al. [41], who concluded that, compared to high order Lagrange shape functions, NURBS need fewer functions to adequately describe the displacement field, which improves the conditioning of the problem and thereby the noise robustness of the correlation algorithm.

To explore the full potential of NURBS shape functions for DIC, this paper presents a global DIC method that adaptively adjusts the shape functions to capture the kinematics required to compute the displacement field. To this end, GDIC is combined with an adaptive refinement algorithm for the NURBS shape functions: adaptive iso-GDIC. As will be shown, the flexibility of the shape functions and its ability to perform automatic adaptive refinements makes the novel approach suitable for various types of DIC problems. Most importantly, it provides an accurate method without the need of supplying the algorithm with specific prior information about the problem. An optimum number of degrees of freedom is pursued, such that enough freedom is allowed to capture the kinematics of the problem, but not too much freedom, so noise robustness is assured. This is an advantage over the existing digital image correlation methods, since it combines high strain field accuracy with user-friendliness and a low level of expertise.

This paper is organized as follows. In section 2.2 the isogeometric GDIC methodology is discussed. Here, the two-dimensional global digital image correlation algorithm is introduced and NURBS shape functions are elaborated, as well as the isogeometric parametrization of the geometry. In Section 2.3, a virtual experiment is executed to test the performance of NURBS shape functions for a GDIC problem, in comparison to other, more commonly used types of shape functions. The adaptive refinement algorithm and the choices made in its design are detailed in section 2.4. In section 2.5 a virtual experiment is executed in order to give a proof of concept of the isogeometric GDIC algorithm with adaptive refinement. Furthermore, the results of this test-case are compared to conventional, non-adaptive DIC algorithms. In section 2.6 real experiments with a complex specimen geometry are carried out to explore the method's performance in practice, after which general conclusions are drawn in section 2.7.

2.2   Methodology for iso-GDIC

In this section the characteristics of isogeometric global digital image correlation, or iso-GDIC, are discussed. First, the two-dimensional GDIC algorithm is explained. Next, the isogeometric shape functions, NURBS, are introduced. Besides using NURBS shape functions for the discretization of the displacement field, they are also used for the

parametrization of the geometry, which is clarified in the last part of this section.

2.2.1 Two-dimensional global digital image correlation algorithm

The goal of Global Digital Image Correlation (GDIC) is to quantify the displacement field of a deformed specimen by correlating digital images of the specimen. The starting point for a GDIC problem is the reference image and the deformed image. The images are characterized by the intensity of the individual pixels, which is represented by the scalar field $f(\mathbf{x}_0)$ for the reference image and $g(\mathbf{x})$ for the image corresponding to the deformed specimen. Material points are assumed to retain the same intensity upon deformation and since every material point needs to be preserved, *brightness conservation* holds:

$$f(\mathbf{x}_0) - g(\mathbf{x}_0 + \mathbf{u}(\mathbf{x}_0)) = \Psi(\mathbf{x}_0) \approx 0. \tag{2.1}$$

Herein $\Psi(\mathbf{x}_0)$ is the residual image, which is zero for all positions for the case that the displacement field $\mathbf{u}(\mathbf{x}_0)$ is calculated perfectly and no noise is present in the images. In GDIC the optimal correlation is obtained when minimizing $\Psi(\mathbf{x}_0)$ using the least squared approach:

$$\mathbf{u}(\mathbf{x}_0) = \arg\min \int_{\Omega_0} \left[f(\mathbf{x}_0) - g(\mathbf{x}_0 + \mathbf{u}(\mathbf{x}_0)) \right]^2 \, d\mathbf{x}_0. \tag{2.2}$$

Since this is an ill-posed problem, by virtue of the fact that a vector-valued displacement field is sought, while only scalar brightness values are known and in general the number of pixels exceeds the number of unique brightness values, the displacement field is regularized as follows:

$$\mathbf{u}(\mathbf{x}_0) \approx \mathbf{u}^*(\mathbf{x}_0, \boldsymbol{\lambda}) = \sum_{j=1}^{m} \lambda_j \boldsymbol{\phi}_j(\mathbf{x}_0), \tag{2.3}$$

where λ_j are the degrees of freedom (DOFs) and $\boldsymbol{\phi}_j(\mathbf{x}_0)$ are their associated shape functions. As explained above, many different choices are possible for the shape functions, which is a challenging decision. The shape functions must be able to capture the (often highly inhomogeneous) kinematics of the sought displacement field, which is generally unknown in advance.

Combining equations 2.2 and 2.3 the discretized problem is obtained:

$$\begin{cases} \Psi(\mathbf{x}_0, \boldsymbol{\lambda}) & = & f(\mathbf{x}_0) - g(\mathbf{x}_0 + \mathbf{u}^*(\mathbf{x}_0, \boldsymbol{\lambda})) \\ \boldsymbol{\lambda} & = & \arg\min \int_{\Omega_0} \Psi(\mathbf{x}_0, \boldsymbol{\lambda})^2 \, d\mathbf{x}_0. \end{cases} \tag{2.4}$$

This problem is iteratively solved by optimizing the unknowns $\boldsymbol{\lambda}$ by a Gauss-Newton scheme, yielding the following system of equations:

$$\mathbf{M}\delta\boldsymbol{\lambda} = \mathbf{b} \tag{2.5}$$

where $\delta\boldsymbol{\lambda}$ is the DOFs update and

$$M_{ij} = \int_{\Omega_0} \left[(\nabla_0 f \cdot \boldsymbol{\phi}_i)(\nabla_0 f \cdot \boldsymbol{\phi}_j) \right] d\mathbf{x}_0 \tag{2.6a}$$

$$b_j = \int_{\Omega_0} \left[(\nabla_0 f \cdot \boldsymbol{\phi}_j(\mathbf{x}_0)) \left[f(\mathbf{x}_0) - g(\mathbf{x}(\mathbf{x}_0, \boldsymbol{\lambda})) \right] \right] d\mathbf{x}_0. \tag{2.6b}$$

The calculation of the domain integral for M_{ij} and b_j is executed by summation over all pixels, as Gauss quadrature schemes, traditionally used in finite element calculations, cannot be used for DIC, due to the highly irregular pattern of the images [11]. Because the image gradient $\nabla_0 f$ and the gray level values f and g are naturally already known at each pixel location, the shape functions $\boldsymbol{\phi}$ are also evaluated there. To this end a nearest neighbour inverse mapping algorithm is employed, which was found to provide a good combination of sufficient accuracy, robustness and computational speed. This algorithm locates for each pixel the closest local, parameterized coordinate pair and assigns the values of the shape functions at this location to the pixel.

2.2.2 NURBS shape functions

In this work, the potential of Non-Uniform Rational B-Splines (NURBS) as shape functions for DIC (see equation 2.3) is explored. B-Splines are piecewise polynomial shape

functions which are defined recursively by the Cox-de Boor relation [18, 35]:

$$
N_{i,0}(\xi) \;=\; \begin{cases} 1 & \text{if } \xi_i \leq \xi < \xi_{i+1} \\ 0 & \text{otherwise} \end{cases} \tag{2.7a}
$$

$$
N_{i,p}(\xi) \;=\; \frac{\xi - \xi_i}{\xi_{i+p} - \xi_i} N_{i,p-1}(\xi) + \frac{\xi_{i+p+1} - \xi}{\xi_{i+p+1} - \xi_{i+1}} N_{i+1,p-1}(\xi), \tag{2.7b}
$$

where ξ is the coordinate in the parametric domain. A graphical interpretation is shown in Figure 2.1a. The basis functions are defined over a knot vector $\Xi = \{\xi_1, \xi_2, ..., \xi_{n+p+1}\}$, where n is the number of shape functions and p denotes the polynomial order of the shape functions. The knots divide the parametric domain in intervals, or elements. At the element boundaries the continuity of the shape functions is reduced.

NURBS are rationalized B-splines, which are defined as:

$$
R_i(\xi) = \frac{N_i(\xi) W_i}{w(\xi)}, \tag{2.8}
$$

where W_i are scalar control point weights and $w(\xi) = \sum_{i=1}^{n} N_i(\xi) W_i$ is the weighting function. NURBS are able to represent many shapes exactly, in particular conic sections. However, in this work all weights W_i are set to 1, as it was found that B-Splines are sufficiently versatile to parameterize the sample geometries. However, the method can easily be extended to applications where non-unity weight factors are required. Furthermore, in this work so called *open* B-splines are used, where the first and last knot are repeated $p+1$ times. However, we do use *non-uniform* B-splines, such that the knots are not restricted to a uniform distribution.

When taking the tensor product of the shape functions in two directions, with local parametric coordinates ξ and ζ, two-dimensional NURBS shape functions are obtained:

$$
\phi_A(\boldsymbol{\xi}) = R_i(\xi) R_j(\zeta), \tag{2.9}
$$

with $A = A(i, j)$ and $\boldsymbol{\xi} = (\xi, \zeta)$. An example of a two-dimensional NURBS shape function is shown in Figure 2.1b.
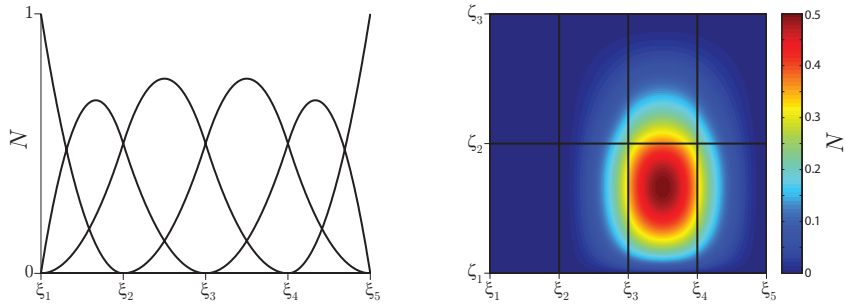
(a) B-splines in the one-dimensional domain. The knots on the parametric domain are given by ξ_i.

(b) A B-spline shape function on the two-dimensional domain. Only one shape function is shown in this representation.

Figure 2.1: Second-order B-spline shape functions in 1D-space and extended to 2D-space. In this case the knots are evenly distributed and the knot vectors are given by $\Xi = \{\xi_1, \xi_1, \xi_1, \xi_2, \xi_3, \xi_4, \xi_5, \xi_5, \xi_5\}$ in and $Z = \{\zeta_1, \zeta_1, \zeta_1, \zeta_2, \zeta_3, \zeta_3, \zeta_3\}$

2.2.3 Geometry parametrization

In isogeometric analysis, NURBS are used both for discretization of the sought displacement field and for parametrization of the geometry of the sample [34, 64]. The mapping of the parametric coordinate $\boldsymbol{\xi}$ to the coordinate $\mathbf{x}$ in the physical domain is done by defining control points $\mathbf{p}_A$, such that

$$\mathbf{x}(\boldsymbol{\xi}) = \sum_A \phi_A(\boldsymbol{\xi})\mathbf{p}_A = \mathbf{P}^T\boldsymbol{\phi}(\boldsymbol{\xi}). \tag{2.10}$$

In Figure 2.2a an example is shown of a B-spline curve $\mathbf{x}(\boldsymbol{\xi})$, using the shape functions of Figure 2.1a and the control points $\mathbf{P}$, as indicated by the red dots in Figure 2.2a. In Figure 2.2b a B-spline surface mesh is shown, constructed in the same manner, using shape functions in 2D-space, as represented in Figure 2.1b, and the control net as indicated by the red dots in Figure 2.2b.

Isogeometric analysis is a powerful tool in representing a large range of displacement fields. The advantage of isogeometric DIC is twofold. First, complex sample geometries can be described accurately and the possibility exists to directly use a CAD-model for the analysis, as Beaubier suggests [6]. This is particularly useful for complex geometries. Secondly, continuity of the shape functions over element boundaries can be controlled by means of knot insertion, which allows for a great flexibility. The multiplicity m of a certain knot determines the continuity of the shape functions at that location, i.e.,

(a) NURBS curve   **(b)** NURBS surface mesh
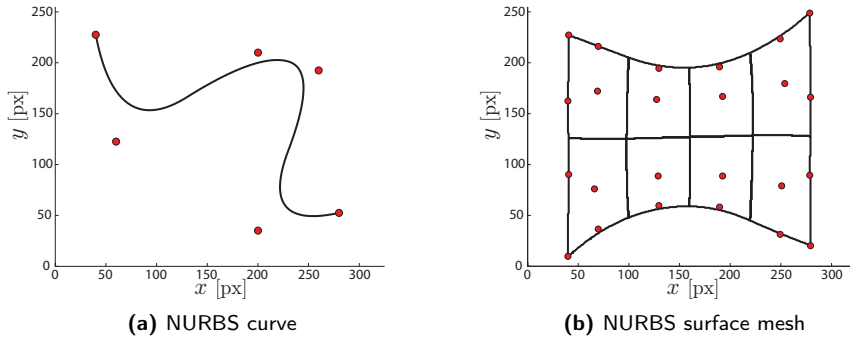
Figure 2.2: A NURBS curve (a) and NURBS surface (b) $\mathbf{x}(\xi)$, constructed from the control net **P** and the shape functions. The control points are indicated by red dots.

the continuity equals $\mathscr{C}^{p-m}$. This is convenient to represent displacement fields that incorporate lowered continuity, e.g., as resulting from highly localized deformation in a material. If every knot is repeated p times, the element boundaries are $\mathscr{C}^0$ continuous, which resembles the situation where traditional finite element shape functions are used, making the approach equivalent to that of Besnard et al. [11]. Furthermore it can easily be shown that if only one element is used, B-splines are equivalent to regular monomials and other globally defined polynomial shape functions up to order p that are expected to work best for smooth, regular displacement fields. Thus NURBS shape functions provide a generic manner of describing many different forms of displacement fields and form a superset of other types of shape functions, including FEM (Lagrange) shape functions and globally defined polynomials.

2.2.4   Blurring step

In (global) DIC approaches it might occur that the method converges to a local minimum, as opposed to the global minimum (see equation 2.2), leading to an erroneous solution. In order to prevent this, for each increment the DIC problem is first solved for a blurred version of the images f and g, using a Gaussian kernel (size 10×10 pixels, standard deviation 1.5 pixels). The result is used as an initial guess for the non-blurred images. This method has proven to reduce the bias error of the digital image correlation method [107]. In literature also other methods to solve this problem are known. Multi-grid algorithms have been used where the DIC problem is, in n steps, first solved for 'coarse-grained' versions of the images [11, 110], i.e., the images are decomposed into super-pixels of $2^n \times 2^n$ pixels by averaging the gray level values of these pixels.

2.3   Iso-GDIC results and analysis

The performance of NURBS shape functions for GDIC is first explored by a virtual experiment, where a comparison with Lagrange (traditional FEM) shape functions [65] and globally defined Chebyshev polynomials [22] is made. Comparison is based on the root mean square (RMS) value of the exact error:

$$\varepsilon_{RMS} = \sqrt{\frac{1}{n} \sum_{i=1}^{n} (u_i - u_{i,ref})^2},$$ (2.11)

with n the total number of pixels. In this experiment an image f with a random grayscale speckle pattern is subjected to a predefined displacement field u_{ref} to obtain the deformed image g. The displacement field, which mimics a localization of the strain field, is expressed by:

$$u_{ref}(x, y) = a \arctan(x - b),$$ (2.12)

where $a = u_{max} / \arctan(\frac{1}{2}(x_{max} + x_{min}))$, such that the displacement field range is $[-u_{max}, u_{max}]$, and $b = \frac{1}{2}(x_{max} - x_{min})$, such that the localization occurs in the center of the domain. The applied displacement field is plotted in Figure 2.3.
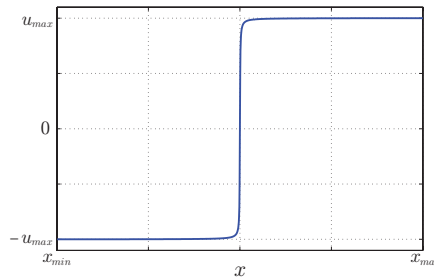
Figure 2.3: The applied displacement field u_{ref}.

In order to make an objective comparison between the three types of shape functions, they should be compared for the same number of degrees of freedom. Therefore, the RMS value of the error in the displacement field is plotted as a function of the number of DOFs in x-direction in Figure 2.4a. The number of DOF's in y-direction is 3 (one element with three shape functions) for all situations, since the localization in the displacement

field only occurs in x-direction. As expected, the error is smaller for a larger number of DOFs. This is due the complexity of the displacement field: a higher number of shape functions is needed to describe the kinematics, resulting in a lower discretization error. As can be seen, a distinction is made for Chebyshev shape functions between *even* and *odd* polynomial orders. For polynomials of even order an extremum occurs at the center of the domain ($x = 0$), while for polynomials of odd order an inflection point occurs at this location. Therefore, Chebyshev functions of an odd polynomial order are better able to capture the steep slope of the arctangent displacement field, which also shows an inflection point at $x = 0$. The error for the odd Chebyshev polynomials is therefore smaller than for the even Chebyshev shape functions, especially for a lower number of DOFs, while for a higher number of DOFs the influence of the even polynomials is cancelled out by the odd polynomial contribution to the solution. For Lagrange shape functions and NURBS a similar distinction is made between *element-centered* and *vertex-centered* meshes. In an element-centered mesh the number of elements is odd, which causes the center of an element to occur at the center of the domain. For a vertex-centered mesh the number of elements is even, which leads to a vertex, i.e., a node for Lagrange shape functions or a knot for NURBS, located at $x = 0$. A vertex induces a line of lowered continuity ($\mathscr{C}^0$ for Lagrange and $\mathscr{C}^{p-m}$ for NURBS), which enables the shape functions to better capture the discontinuity in this particular displacement field. Therefore the RMS-error is lower for the vertex-centered shape functions, as can be seen in Figure 2.4a.

Also the influence of noise on the performance of the different methods is investigated. To this end the virtual experiments are repeated for different levels of artificially imposed noise on the deformed image: a noise level of 100% means that the noise amplitude is of the same order as the gray level values. Three different sets of a constant number of DOFs are used for the three types of shape functions. The RMS-value of the error in the displacement field and its standard deviation (error bars) are shown in Figure 2.4b as a functions of the noise level. It can be seen that for a higher number of DOFs the method is more sensitive to noise: at a certain noise percentage the method does not converge anymore. This is a well known property of GDIC [41, 112]. Furthermore, Chebyshev shape functions are observed to be more sensitive to noise than the other two types, as for higher polynomials orders they don't converge for noise percentages over 20%, while NURBS and Lagrange shape functions go up to 40-50%. The difference in noise-sensitivity between Lagrange and NURBS shape functions is observed to be small. The uncertainty in the RMS-error (error bars in the graph) is slightly smaller for the NURBS and also the increase in error is slightly smaller. However, from this experiment we conclude that there is no significant difference in performance between the two types of shape functions which are more locally defined, i.e. NURBS and Lagrange shape functions. The shape of the mesh is more important than the type of the shape functions.

In order to illustrate the influence of the *continuity* of the shape functions rather than
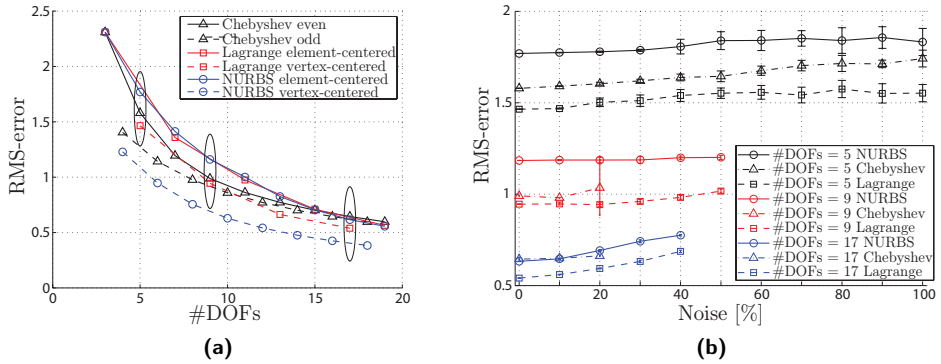
Figure 2.4: RMS value of the error in the displacement field as a functions of the number of degrees of freedom (DOFs) (a) and as a function of noise level (b), plotted for different types of shape functions. The noise level is relative to the amplitude of the gray values of the deformed image g. The combinations of shape functions with an equal number of DOFs that are used in the noise analysis are indicated by ellipses in figure (a). Note that for a clear graphical representation of graph (b) combinations have been chosen, for which the RMS-error of the three types of shape functions does not overlap (as is the case for e.g., 15 DOFs). To do so, the combination always consists of even Chebyshev polynomials, element-centered NURBS and vertex-centered Lagrange shape functions, resulting in the lowest RMS-error for the Lagrange type. However, for the noise sensitivity the absolute error value is not as important as the trend and the variance in the error, thereby justifying this choice.

the *type*, the experiment is repeated, using only NURBS shape functions, however, for a given number of degrees of freedom the knots along the x-axis are redistributed in order to increase the multiplicity of the knot in the center of the domain, where the high gradient in the displacement field occurs, as shown in the inset of Figure 2.5. The virtual experiment is executed for four sets of constant number of DOFs in x-direction: 7, 9, 13 and 17. In each set the knot vector is rearranged as described above. The four sets are again compared by means of the RMS value of the error in the displacement field.

The error is plotted against the multiplicity of the knot in the center of the domain in Figure 2.5. From this graph it is again observed that the error decreases if the amount of degrees of freedom increases, because the complex kinematics of this type of displacement field are difficult to capture with polynomial shape functions and require more degrees of freedom. This time, however, it is noted that a significant improvement is achieved if the multiplicity of the center knot increases. This can be explained by the fact that the continuity decreases when knots are repeated. The applied displacement field approaches a step function with $\mathscr{C}^{-1}$ continuity in the center of the domain. If the continuity of the shape functions is decreased as well, they are better able to approximate the displacement field.
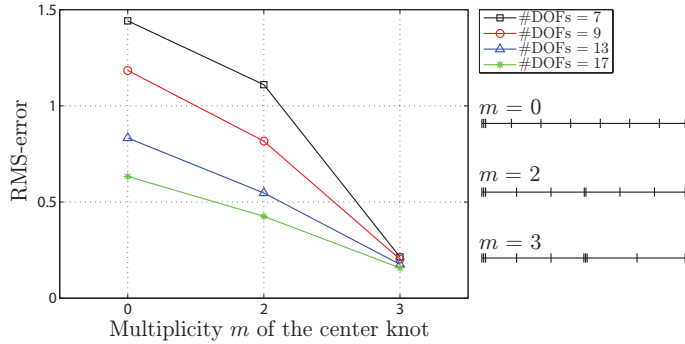
Figure 2.5: RMS value of the error in the displacement field plotted against the multiplicity m of the knot in the center of the x-domain. An example of the rearrangement of the knot vector in order to reach this multiplicities is shown in the inset on the right side of the graph. In this case we see a knot vector in x-direction with 12 knots, for shape functions of order 2 (the multiplicity of the knots at the edges is $p+1=3$). The knots are redistributed such that the total number of knots, and hence degrees of freedom, remains the same. In the center of the domain the multiplicity of the knot is increased.

These virtual experiments illustrate that adding degrees of freedom is particularly useful if they are added at the right location. Moreover, the actual placement of the knots is more important than the amount of DOFs and even more important than the type of shape functions used. An advantageous situation occurs when the number of DOFs remains limited, since this enhances noise robustness, and still complex kinematics can be described. Naturally the displacement field is unknown in advance and the user is generally unable to provide the GDIC algorithm with the most suitable mesh. Therefore, in order to optimally benefit from the flexibility of the shape functions used in isogeometric analysis, we propose to combine the isogeometric digital image correlation algorithm with adaptive mesh refinement. Note that adaptive refinement could also be combined with a GDIC algorithm using other types of shape functions, however, NURBS are a more general approach, since they form a superset of the other types and furthermore have the advantage of being able to describe complex geometries exactly.

2.4   Adaptive refinement

We have seen that on one hand NURBS shape functions provide a flexible tool in describing both simple and complex kinematics of displacement fields, and on the other hand optimized placement of DOFs in a digital image correlation problem is

computationally favorable. Therefore, it is expected that isogeometric digital image correlation combined with an adaptive refinement algorithm yields a powerful method for solving a large variety of DIC problems. In this section a two-dimensional adaptive refinement algorithm of NURBS shape functions is explained, as well as some important choices on criteria used in the algorithm.

2.4.1 Hierarchical mesh refinement

A *hierarchical* approach for refining the mesh is employed, see [155] for details. The key idea to hierarchical refinement is to replace some of the shape functions in the initial basis by shape functions of the refined basis. The bases are constructed hierarchically, which implies that multiple levels of basis functions exist, representing subsequent levels of refinement of the underlying geometry. This is illustrated in one dimension in Figure 2.6. In figure (a) the initial basis is shown and in figure (b) the refined basis.

Now we could mark *elements* for refinement, however, in hierarchical mesh refinement this strategy is not always suitable [83]. It can occur that selecting an element for refinement does not result in any refinement. For example, if the second element in Figure 2.6a is selected, there are no shape functions in the initial basis nor the refined basis that completely lie within this domain. Hence, no shape functions are replaced and no refinement occurs. Therefore, it is more suitable to mark *shape functions* for refinement rather than elements.

Suppose, for example, that shape functions 1 and 7 are selected for refinement, as indicated by the dashed lines in Figure 2.6a. They are replaced by the shape functions of the refined basis that completely lie within the same domain, as indicated by the solid lines in Figure 2.6b. The resulting set of shape functions is shown in Figure 2.6c. It should be noted that in the one-dimensional case the same effect could be obtained by knot insertion. In the two-dimensional case the refinement remains local, this in contrast to tensor product B-splines.

2.4.2 Refinement criteria

In order to determine in which area a finer mesh is required, i.e., which shape functions must be refined, an error estimator is needed. In digital image correlation the accuracy of the method is based on the residual $\Psi(\mathbf{x}_0) = f(\mathbf{x}_0) - g(\mathbf{x}_0 + \mathbf{u}(\mathbf{x}_0))$. Therefore, we propose to let the selection of shape functions be based on the following refinement

(a)

(b)

(c)
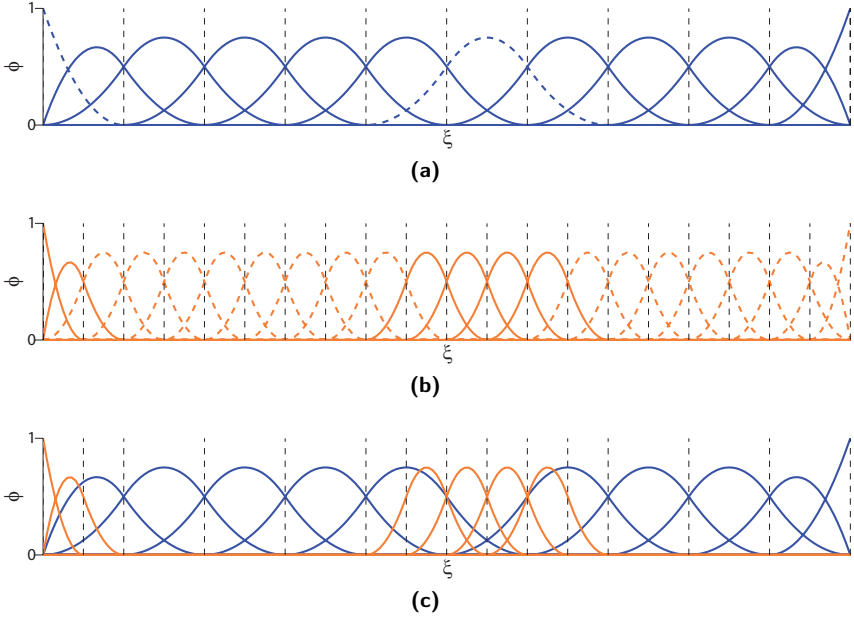
Figure 2.6: The concept of hierarchical refinement. In the top figure an initial basis is shown and in the middle figure a uniformly refined basis. The dashed basis functions in the initial basis are replaced by the solid shape functions of the refined basis. In the lower figure the result of this refinement step is shown. Element boundaries (knot locations) are indicated by vertical black dashed lines.

indicator:

$$C_j = \frac{1}{(f_{max} - f_{min})} \frac{\delta_{f,global}}{\delta_{f,j}} \frac{\int_{\Omega_j} |\Psi(\mathbf{x}_0)| \phi_j(\mathbf{x}_0) \, \mathrm{d}\mathbf{x}_0}{\int_{\Omega_j} \phi_j(\mathbf{x}_0) \, \mathrm{d}\mathbf{x}_0}. \tag{2.13}$$

In this expression j is the index of a shape function ϕ_j and Ω_j indicates its area of support. The refinement indicator is based on the residual $\Psi(\mathbf{x})$ and is scaled with the shape function itself, in order to prevent shape functions with a larger support always being favored for refinement and to scale the influence of the residual with the value of the shape function. Furthermore, the indicator is scaled with the mean intensity gradient $\delta_f = \frac{1}{mn} \sum_{i=1}^{m} \sum_{k=1}^{n} \sqrt{|\nabla f(\mathbf{x}_{i,k})|}$ of the entire image ($\delta_{f,global}$) divided by the mean intensity gradient of the area underneath the shape function ($\delta_{f,j}$). This diminishes the influence of contrast differences in different areas in the pattern. The indicator is also normalized with the range of gray values ($f_{max} - f_{min}$). This makes the indicator independent on the absolute gray values, which allows for a general criterion

based on, for example, the noise level.

It is important that refinement does not take place if the residual due to correlation mismatch is lower than the noise amplitude. The noise level heavily depends on the measurement system used to capture the images, i.e., the camera, lighting conditions, microscope lenses, etc. Therefore the value of the threshold should be determined for every experimental data set separately. The noise level can be evaluated by correlating two or more images with no deformation and determining the average residual with respect to the gray value amplitude. Moreover, a safety factor should be included in the threshold. This safety factor cannot be too low, in order to make sure the residual is above noise level, but must not be too high, since aberrant features must not be neglected. Based on extensive experimentation, a safety factor of 4 is recommended. In this work, a noise level of about 1.5% was found for the images taken with the measurement system used, and thus a normalized residual below 6% is assumed to be acceptable, i.e. shape functions with $C_j > 0.06$ are marked for refinement.

In order to optimize the selection procedure, a second criterion is taken into account. Only shape functions with a refinement indicator C_j larger than $\bar{C} + 1.5\sigma$ are refined, with $\bar{C}$ the mean of the indicators of all shape functions and σ the standard deviation. This criterion makes the algorithm suitable for problems where no refinement is required. Moreover, this is useful in an experimental setting, where typically a sequence of images is correlated. The first couple of images may embody merely homogeneous deformation where no refinement is desirable. Refinement only takes place if both criteria are met.

Finally, it might occur that the level of refinement causes elements to become smaller than a few pixels. This has a negative influence on the conditioning of the problem and increases the noise-sensitivity (see Section 2.3). In order to prevent this, the pattern of image f is evaluated to determine the correlation length ℓ_c. The correlation length is an in-plane length scale of the pattern and is defined as the length where the autocorrelation peak of image f equals a certain threshold, here taken as $\frac{1}{e}$, where e is Euler's number. Elements should contain at least several pattern features, therefore, a threshold is placed at $10\ell_c \times 10\ell_c$ pixels. If an element is smaller than this size, all shape functions associated to this element are marked to have reached the highest level of refinement and no further refinement is allowed.

2.5 Analysis of adaptive iso-GDIC

A virtual experiment is executed to give a proof of concept of the adaptive isogeometric GDIC method. Moreover, the virtual experiment allows for comparison of the new method to an isogeometric GDIC algorithm that does not utilize adaptive refinement,

and a local DIC implementation. In this test-case an image of a speckle pattern on a tensile bar from a real experiment is artificially deformed in order to obtain image g.

The displacement field u in x-direction again represents a tensile experiment with strong localization of the displacement, approaching a step function with $\mathscr{C}^{-1}$ continuity, and is given by equation 2.12. The final displacement is applied in four increments, which are illustrated in Figure 2.7. The corresponding reference image f, intermediate image g_3 and final image g_4 are shown in Figure 2.8.
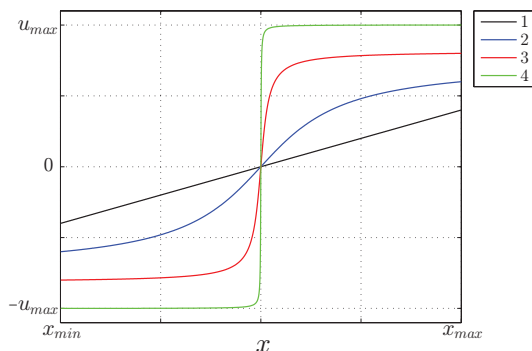
Figure 2.7: Evolution of the applied displacement as a function of the x-coordinate. The displacement is applied in four increments, starting from a linear displacement, towards the final arc-tangent field.

It is recognized that this type of displacement generally is challenging for global DIC methods (except when shape functions are used that are able capture discontinuities [110, 111]), while local DIC methods are better equipped for handling discontinuities, since continuity of the solution is not imposed. The displacement is applied in four increments, ranging from a linear displacement field to the final arc-tangent displacement. All four reference displacement fields in x-direction, u_{ref}, are plotted on the reference image f in Figure 2.9a. The displacement v in y-direction is zero everywhere in the image domain and disregarded in the analysis.

In order to let the virtual experiment optimally resemble a real experiment, a specific procedure for generating the synthetic images is followed, see Neggers [98]. Here the virtual sample space, on which the artificial displacement field is defined, is larger than the field of view, i.e. the final image size. Starting from an initial image, i.e. virtual sample space, of 1300 × 1018 pixels, the size of the final image is chosen 650 × 509 pixels.

The isogeometric GDIC algorithm with adaptive refinement, as described in the previous section, is applied to this problem. NURBS shape functions of the second-order are used.

(a) f, # DOFs = 35   **(b)** g_3, # DOFs = 62   **(c)** g_4, # DOFs = 130
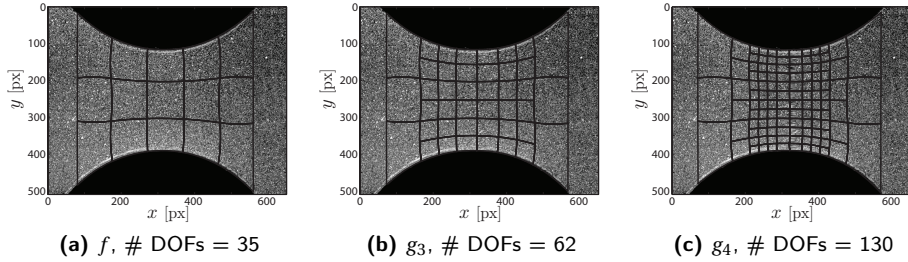
Figure 2.8: Evolution of the image and the mesh after applying the displacement. The reference image f is shown along with intermediate image g_3 and the final deformed image g_4. The evolved meshes are shown on top of the images.

In Figure 2.8 the evolution of the mesh is depicted. It can be seen that refinement indeed takes place in the central area, where the large gradient in the applied displacement field occurs. It is noted that the region of refinement is wide initially. This is due to the fact that shape functions are refined rather than elements: the entire support of the shape function, which consist of multiple elements, is refined. The calculated displacement fields for all four increments are shown in Figure 2.9b.

In order to investigate the influence of adaptive refinement, the virtual experiment is repeated without adaptive refinement. To be able to perform comparison as fair as possible, the amount of degrees of freedom should be the same for both cases. For the non-adaptive iso-GDIC method an uniform mesh of 10 by 9 elements is chosen and second-order NURBS shape functions are used, which yields approximately the same amount of DOFs as the adaptive iso-GDIC experiment after refinement (130 DOFs for the refined problem vs. 132 DOFs for the non-adaptive DIC method). In Figure 2.9c the resulting displacement field is shown.

The displacement field is also calculated using a local digital image correlation method (using MatchID software [95]), choosing optimized settings: subset size 21 pixels, step size 7 pixels, SSD correlation coefficient, bicubic spline interpolation and affine shape functions. The correlated displacement field is depicted in Figure 2.9d. It can be observed that for the last two increments the displacement is not correlated in the center region of the domain. This is because in local DIC only the displacement of the subset centers is calculated and only small deformations of the subsets can be captured. The variation in displacement is large in the center area of the domain and therefore local DIC is not able to correlate the subsets located in this area. Note that the loss of subsets in the central area has already been minimized by using an optimum subset size and step size. Another problem that occurs in local DIC is loss of information at the top and bottom edges of the domain, since subsets of which the center falls outside the domain cannot be correlated.

It should be stressed that finding optimal setting for local DIC to perform best is laborious and requires experience. In the adaptive isogeometric GDIC algorithm important choices are already made in the development of the method, which ensures accurate results, without much expertise of the user needed.
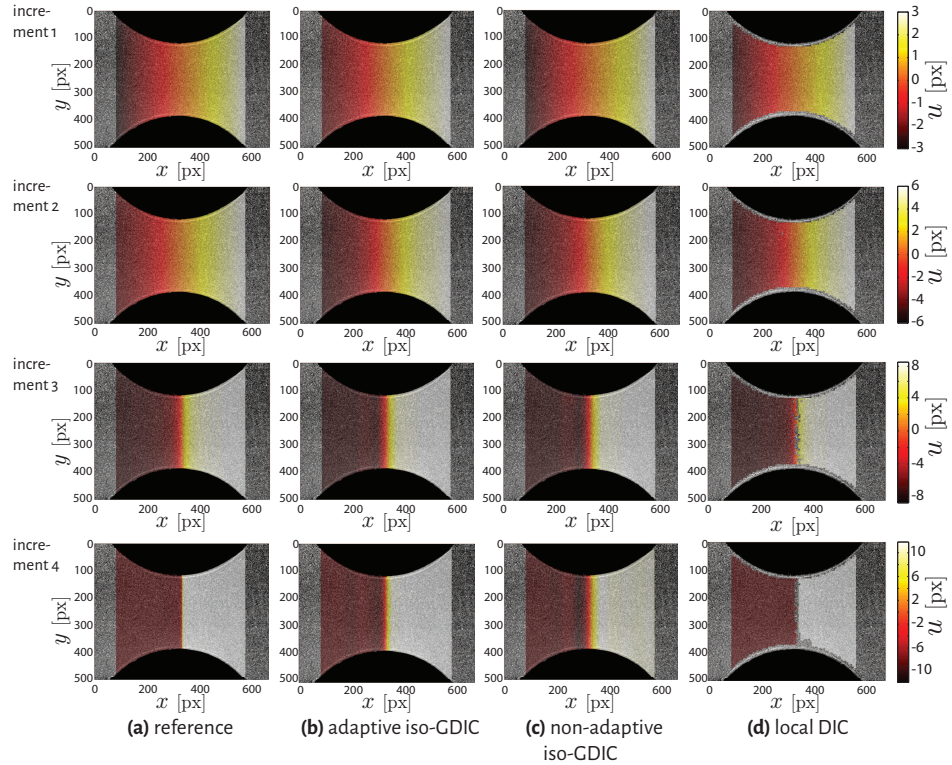
Figure 2.9: Displacement field applied in four increments, as seen in Figure 2.7, ranging from a linear displacement field (first row) toward an arc-tangent displacement field (last row). The reference displacement field is shown in the first column (a). The problem is solved using the adaptive isogeometric GDIC method (b), a non-adaptive iso-GDIC algorithm (c) and a local DIC method (d).

From Figure 2.9 it can be observed that in the first two increments all methods yield approximately the same solution. In order to objectively compare the three methods, the exact error in the displacement field is determined: $\varepsilon = u - u_{ref}$. In Figure 2.10 the error fields are shown. In the first two increments the displacement field is quite homogeneous and it is observed that no large difference in the error field exists between the three methods. In the third increment the local method starts to fail: the concentration

of displacement is too large and subsets in the center region are not able to correlate. This becomes even more apparent in the final increment, where the steep arc-tangent displacement field is applied.
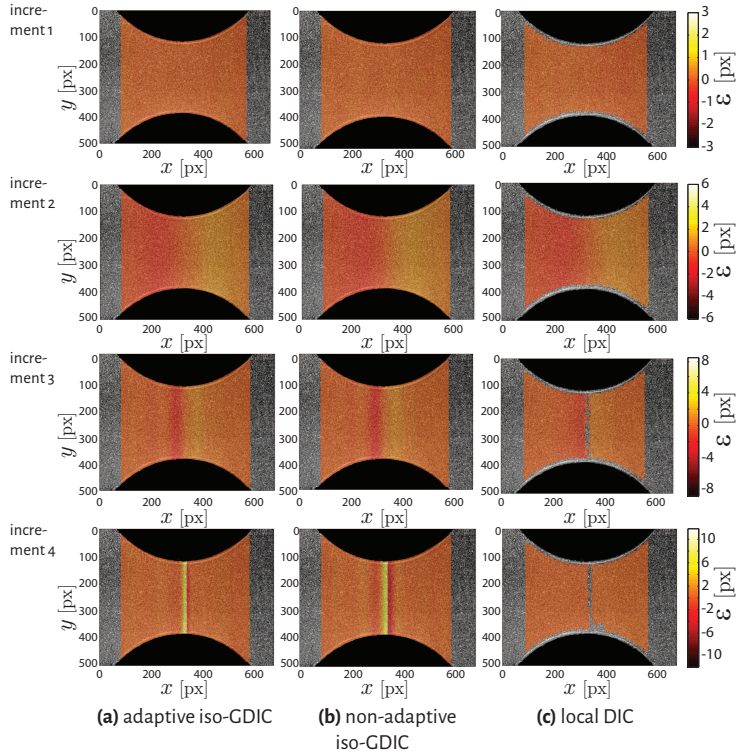
Figure 2.10: Error fields for the four increments and different DIC methods. The error is defined as the difference between the reference displacement field and the calculated displacement field $\varepsilon = u - u_{ref}$ and expressed in terms of pixels. The four rows correspond to the four increments in applied displacement, ranging from a linear, homogeneous, displacement field (top) to the final arc-tangent field (bottom). The first column (a) corresponds to the adaptive iso-GDIC method, (b) to the non-adaptive isogeometric GDIC implementation and the last column (c) to the local DIC method.

Furthermore in this increment a difference between the adaptive method and the non-adaptive method is observed. The refined shape functions are better able to capture the high gradient in displacement in the center of the domain than the non-adaptive isogeometric shape functions, resulting in a smaller region where the error is high. This indicates that the novel, adaptive method offers a more accurate solution than

the non-adaptive method for this problem, while the number of DOFs and hence the computational effort is similar for both methods. Moreover, the adaptive iso-GDIC method performs well for the entire range of displacement fields. However, the real strength of the novel method is that this solution was obtained without supplying problem-specific information to the program beforehand: the area where a finer mesh is required is determined autonomously.

2.6   Application in experimental setting

Real experiments are performed in order to investigate the performance of the adaptive isogeometric GDIC method to practical problems. Uniaxial tensile tests are performed in a microscopic setup.

2.6.1   Test setup and sample

The setup for the experiment consists of a tensile stage, a microscope, a camera and a computer. The microscope used is a Carl Zeiss Discovery.V20 stereo microscope with a Zeiss PlanApo S 1.5x FWD 30mm lens. The Zeiss AxioCam CCD camera is connected to a computer. Images are recorded using AxioVision 4.7 software. The tensile stage (Kammrath & Weiss tensile/compression module with a 500N load cell) is driven by a controller to make sure a tensile speed of 5μm/s is maintained.

Two different test specimen are used. The first sample is a polycarbonate double notched 1mm thick tensile specimen. The second sample has the same material and geometry, however a hole is present. With this material and these geometries, strong localizations of strain and displacement are expected, which makes them a good test-case for demonstrating the adaptive refinement process. A random speckle pattern is applied using spraypaint to make the samples suitable for the DIC analysis.

2.6.2   Results

Double notched tensile sample

The reference image f and the final image g, corresponding to the deformed specimen, are shown in Figure 2.11. More images are recorded during the experiment and the correlation procedure is done in several increments, using these intermediate images. The adaptive isogeometric GDIC algorithm is executed, using second-order B-spline shape functions. The resulting mesh refinement can also be seen in Figure 2.11.
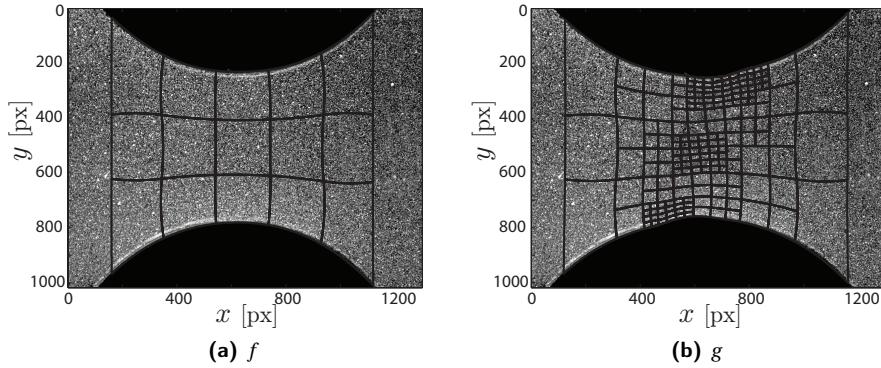
Figure 2.11: Images of the sample before and after deformation in a real experiment, as used in the correlation process. The mesh before and after refinement is also shown.

The displacement u in x-direction and the displacement v in y-direction are shown in Figure 2.12a on the initial image f. It can be seen that indeed localization takes place in the center of the domain, as was expected from the geometry of the sample. In the bottom image of Figure 2.12a it can be seen that the y-displacement is largest in the cental area, at the bottom and top of the domain, indicating that necking occurs here. This is also the region where refinement takes place.

The algorithm is also executed with a conventional GDIC implementation, using a mesh of 14 by 9 evenly spaced elements and second-order B-spline shape functions, resulting in the same number of DOFs as the final refined mesh as shown in Figure 2.11b. The resulting displacement field components u and v are depicted in Figure 2.12b. Due to the homogenous nature of the displacement field, the adaptive algorithm in this case only provides marginally better results than the non-adaptive method, provided the number of DOFs is equilibrated. When compared to the results using the initial mesh of 5 by 3 elements, a substantial improvement in accuracy if observed. This can be seen in Figure 2.13, where the residual image $\Psi(\mathbf{x}_0)$ is compared for the adaptive method before and after refinement, using the meshes of figures 2.11a and 2.11b respectively. The residual is indeed highest in the central area of the sample, where localization takes place. After refinement this area is smaller than before refinement and also the residual level is lower, indicating an improvement of the accuracy. In the next section we further study the accuracy improvement of adaptive iso-GDIC compared to the initial mesh.

Correlation is repeated using a local DIC method (using MatchID software, subset size 35 pixels, step size 10 pixels, SSD correlation coefficient, bicubic spline interpolation and irregular shape functions). Note, however, that settings for e.g. subset size and interpolation scheme have again been optimized to yield the lowest loss of subsets

as possible. The results are shown in Figure 2.12c. It can be seen that in the area where localization takes place the local DIC method is not able to correlate all subsets. This is because the variation in displacement within these subsets is too large and the displacement of the subset center cannot be found.

This indicates that adaptive refinement is a useful tool in solving this type of problems. But above all the solution was found automatically: the algorithm was not supplied with specific foreknowledge about the problem, as usually is needed for a global digital image correlation method to perform well in this type of problem.
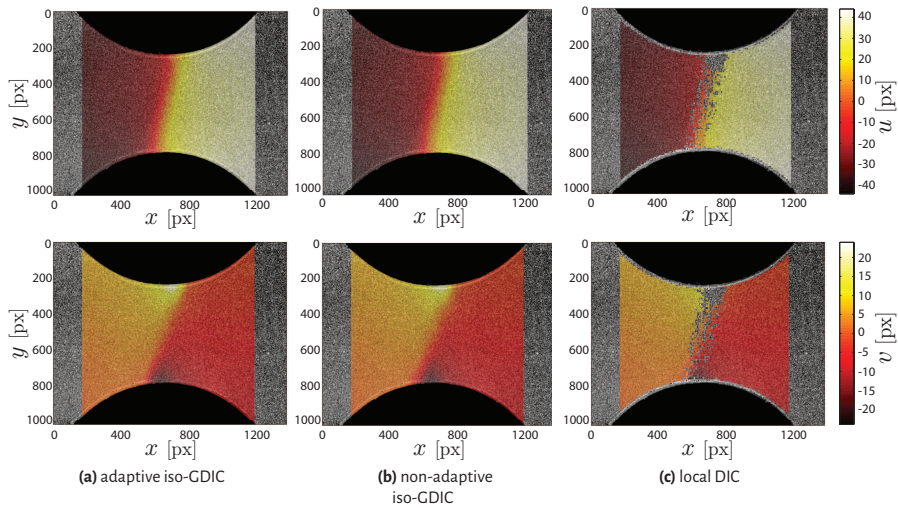
Figure 2.12: Calculated displacement fields u in x-direction (top row) and v in y-direction (bottom row). The displacement is expressed in terms of pixels. The calculated fields are shown for the adaptive method (a), the non-adaptive isogeometric GDIC method (b) and the local DIC algorithm (c). Note that the y-coordinate and its associated v-displacement point in the downward direction.

Double notched tensile sample with hole

The tensile sample before and after deformation can be seen in Figure 2.14. These images, along with a number of intermediate images taken during the experiment, are used in the correlation proces as reference image f and deformed image g. The meshing procedure is similar to that described in Section 2.2.3, however, some additional steps are taken in order to make the mesh conforming the hole. Four elements and their corresponding shape functions that are originally located in or near the hole, are

(a) Before refinement
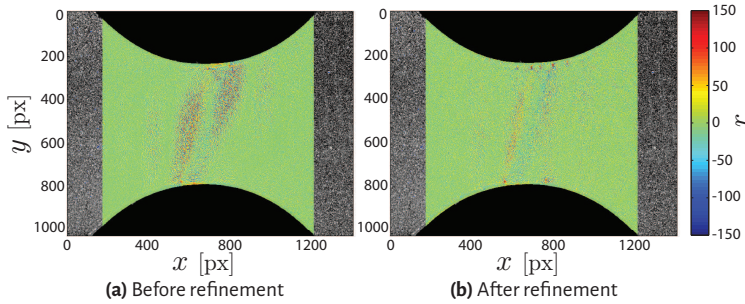
(b) After refinement

Figure 2.13: Residual image $\Psi(\mathbf{x}_0) = f(\mathbf{x}_0) - g(\mathbf{x}_0 + \mathbf{u}(\mathbf{x}_0))$ for the adaptive iso-GDIC method at the onset of localization before (a) and after refinement (b). The residual is expressed in terms of gray values.

removed. Next the control points of the elements surrounding the hole are translated to the edge of the hole, such that the mesh forms a fit around the hole. In order to describe the hole accurately at least 20 elements around the hole are required, resulting in a quite fine initial mesh, see Figure 2.14a. This is a simple meshing procedure, resulting in a parametrization that is $\mathscr{C}^1$ continuous everywhere. Other, more complex, parametrization techniques, including coupled NURBS patches, may also be used. As was investigated in Section 2.3, the accuracy in a localized displacement field, which is to be expected from this sample geometry, can be improved by using lower continuity lines at the localization positions, which could be achieved by a multipatch approach with $\mathscr{C}^0$ coupling. However, in this study we want the algorithm to obtain the optimal solution autonomously, without assuming localized behaviour in advance.

The correlation procedure is executed using adaptive refinement of second-order NURBS shape functions. The adaptively refined mesh is shown in Figure 2.14b. It can be seen that refinement takes place in the area where the largest deformation, i.e., localization, is expected; the least wide material regions.

The final calculated displacement fields u in x-direction and v in y-direction can be seen in Figure 2.15a. From the deformed image it is observed that necking occurs in the small regions around the hole. Indeed in the bottom image of Figure 2.15a, displacement field v, this localization is visible: the displacement in y-direction is largest in this area. Furthermore, a localization in x-displacement in the same area is recognized in the top figure of 2.15a. Displacement in both directions combined indicates shearing.

The displacement fields u and v are also calculated using a non-adaptive iso-GDIC algorithm. Second-order NURBS shape functions are used along with the initial mesh from the adaptive refinement method, as shown in Figure 2.14a. The resulting displacement

(a) f **(b)** g
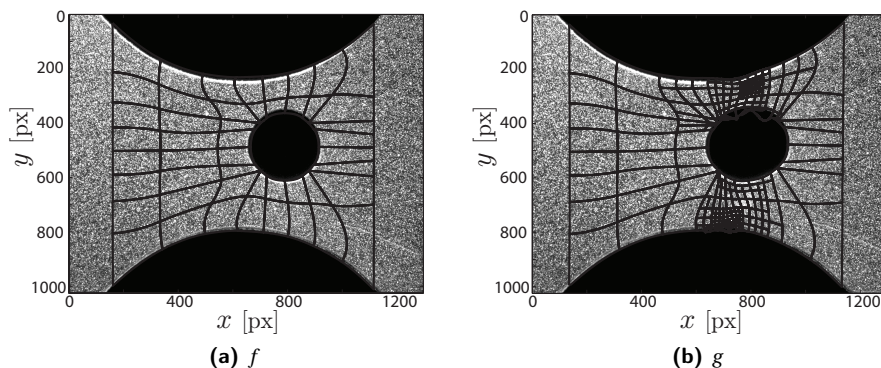
Figure 2.14: Images of the sample before and after deformation, as used in the correlation process. The mesh before and after refinement is also shown.

is shown in Figure 2.15b. It is observed that the displacement field is shows the same global characteristics as the displacement field calculated with the DIC algorithm with adaptive refinement. However, the refined shape functions are better able to capture the localization in the necking area; comparing figures 2.15a and 2.15b the sudden change in displacement is better visible in case adaptive refinement is used. This is also observed when comparing the residual images $\Psi(\mathbf{x}_0)$ for the method before refinement and after refinement, using the meshes of figures 2.14a and 2.14b respectively, see Figure 2.16. It can be seen that the residual again is highest in the area where the sample shows localization of the displacement field, i.e., the area above the hole. After refinement, the residual is significantly lower in this area, indicating that the accuracy of the calculation has increased.

Correlation of the images taken during the experiment is again repeated using an optimized local DIC algorithm (MatchID, subset size 53 pixels, step size 10 pixels, SSD correlation coefficient, bicubic spline interpolation and irregular shape functions). The resulting displacement fields are shown in Figure 2.15c. It is observed that in the area where localization takes place correlation fails. The variation in displacement is rather large in this area and subsets located here fail to correlate.

This again shows the advantages of the adaptive iso-GDIC method: accurate results are obtained, without the need of supplying problem specific information.
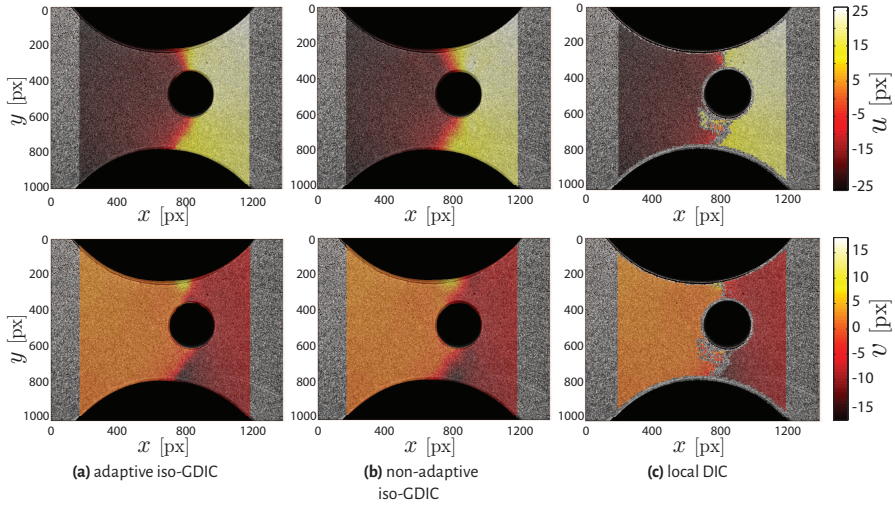
Figure 2.15: Calculated displacement fields u in x-direction (top row) and v in y-direction (bottom row). The displacement is expressed in terms of pixels. The calculated fields are shown for the adaptive method (a), the non-adaptive isogeometric GDIC method (b) and the local DIC algorithm (c).

2.7 Conclusions

A novel method was developed where isogeometric global digital image correlation was combined with an adaptive refinement algorithm: adaptive iso-GDIC. The potential advantage of this method is that it is flexible and can be used for a wide variety of DIC problems. But perhaps even more important is that solutions are found autonomously, which means that the user does not have to make problem specific choices for e.g. the shape functions in global DIC or subset size in local DIC. The NURBS shape functions are able to capture the kinematics of many displacement fields, depending on the structure of the knot vector. In combination with adaptive refinement the shape functions are autonomously adjusted to be able to describe the kinematics of the sought displacement field with an optimized number of degrees of freedom.

A hierarchical mesh refinement algorithm is used in order to prevent inefficient refinement, providing DOFs only where needed, which is beneficial for the conditioning of the ill-posed DIC-problem. Iterating towards the optimum number of DOFs is incorporated in the procedure of marking shape functions for refinement. Shape functions are merely refined if the residual in its region of support is significantly higher than the average.

(a) Before refinement   **(b)** After refinement
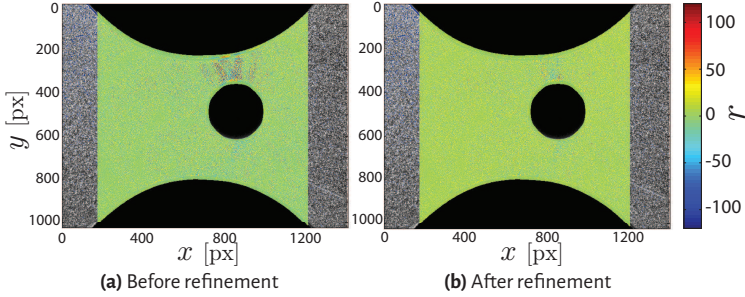
Figure 2.16: Residual image $\Psi(\mathbf{x}_0) = f(\mathbf{x}_0) - g(\mathbf{x}_0 + \mathbf{u}(\mathbf{x}_0))$ for the adaptive iso-GDIC method before (a) and after refinement (b). The residual is expressed in terms of gray values. For illustration an increment is chosen at the onset of localization, where localization still only occurs in the least wide region of the sample, i.e., above the hole, and not yet in the bottom region.

A virtual experiment shows that for a test-case with a strong localization of the displacement, where refinement is desired, the new method yields good results compared to more conventional DIC implementations, in particular a non-adaptive isogeometric GDIC method and local DIC. Most importantly, this result is obtained autonomously. The user does not need to supply the program with specific prior information about the problem, as is required for the more conventional DIC method to obtain accurate results.

Moreover, real experiments with a complex geometry are executed to demonstrate that the novel method also performs well in practice. A notched tensile sample and a specimen with a hole were chosen, which show a localized displacement field under deformation. Mesh refinement also appears in the regions were localization is expected.

In all, it was shown that the isogeometric GDIC adaptive refinement algorithm has some major advantages. The most important advantage is that the number of degrees of freedom is optimized autonomously, which ensures accurate results, without much problem specific input and thus expertise of the user needed. Furthermore, this type of shape function is very flexible, which makes the method rather robust and applicable to a wide range of DIC problems. Last it was shown in specific cases that the method provides better results than more conventional DIC methods, without adaptive refinement. This indicates that adaptive iso-GDIC is a promising technique for accurately solving a wide range of DIC problems.

Chapter 3
Adaptive isogeometric digital height correlation: Application to stretchable electronics

---

Abstract

A novel adaptive isogeometric digital height correlation (DHC) technique has been developed in which the set of shape functions, needed for discretization of the ill-posed DHC problem, is autonomously optimized for each specific set of profilometric height images, without a priori knowledge of the kinematics of the experiment. To this end an adaptive refinement scheme is implemented, which refines the shape functions in a hierarchical manner. This technique ensures local refinement, only in the areas where needed, which is beneficial for the noise robustness of the DHC problem. The main advantage of the method is that it can be applied in experiments where the deformation mechanisms are unknown in advance, thereby complicating the choice of suitable shape functions. The method is applied to a virtual experiment in order to provide a proof of concept. A second virtual experiment is executed with stretchable electronics interconnects, which entail localized buckles upon deformation with complex kinematics. In both cases accurate results were obtained, demonstrating the beneficial aspects of the proposed method. Moreover, the techniques performance on profilometric images of a real experiment with stretchable interconnects was demonstrated.

3.1 Introduction

Digital Image Correlation (DIC) is nowadays an almost indispensable technique in experimental mechanics [106, 150]. Subsequent images of a test specimen taken during an experiment are correlated to determine displacement fields. Initially, DIC was developed to analyse in-plane, two-dimensional, displacements. Meanwhile, several extensions of the method have been developed. The method has been extended to 3D by correlating images from two cameras in stereo to obtain the displacement of a surface in three dimensions: Stereo-DIC [12, 91, 150]. Furthermore, the method has been advanced to a fully 3D method: Digital Volume Correlation (DVC), where also the internal kinematics of the sample is tracked, rather than solely the surface deformation [4, 140]. This is achieved by using for example X-ray tomography scans instead of planar photographic images.

Another recent development concerns the correlation of profilometric images in order to identify both in-plane and out-of-plane deformation fields: Digital Height Correlation (DHC). In figure 3.1a-c, examples from literature are shown where this technique is applied. In all three cases accurate results were obtained on the microscale. Han et al. included mode-I crack displacement fields in the algorithm to describe the kinematics of a propagating crack in a glass specimen [52]. Bergers et al. included the function describing the shape of a single-clamped beam in the algorithm, which was required to calculate the curvature of a bending microbeam with a resolution of $\sim 1.5 \cdot 10^{-6} \mu \text{m}^{-1}$ [9]. Neggers et al. used globally defined, continuously differentiable polynomial functions to accurately capture the local strain and curvature fields of a bulging membrane under pressure [99], which enables the measurement of the local plane strain and biaxial elastic moduli within $\sim 2\%$ accuracy. The results in these cases were convincing, however, in all cases the discretization of the DHC problem (necessary because of the intrinsic ill-posed nature of a DHC formulation) was adapted to the specific mechanics of the considered experiment. However, in most mechanics problems it is not possible to assess the kinematics of the unknown displacement field a priori, for instance in the case of figure 3.1d, where a copper stretchable electronic interconnect delaminates from the rubber substrate and buckles in specific local areas, which is an active field of research [61, 137]. Therefore, a more generic DHC framework is called for, which preferably autonomously adjusts to the kinematics, without using prior knowledge.

For the case of in-plane, two-dimensional DIC, a novel adaptive isogeometric global digital image correlation (iso-GDIC) scheme was recently developed [75]. Isogeometric shape functions for the discretization, both of the sample domain and the unknown displacement field, were used, i.e., Non-Uniform Rational B-Splines (NURBS). It was shown that this type of shape function is versatile and able to capture a wide range of kinematics. This type of shape functions is used increasingly in a DIC setting, both in 2D [29, 41, 75] and 3D (stereo-vision) [6, 39, 40]. NURBS have proven to be less

sensitive to noise than Finite Elements (FE) [114]. Moreover, NURBS originate from CAD-modelling and are able to describe many shapes exactly. In the case of stretchable electronics this is of particular interest.
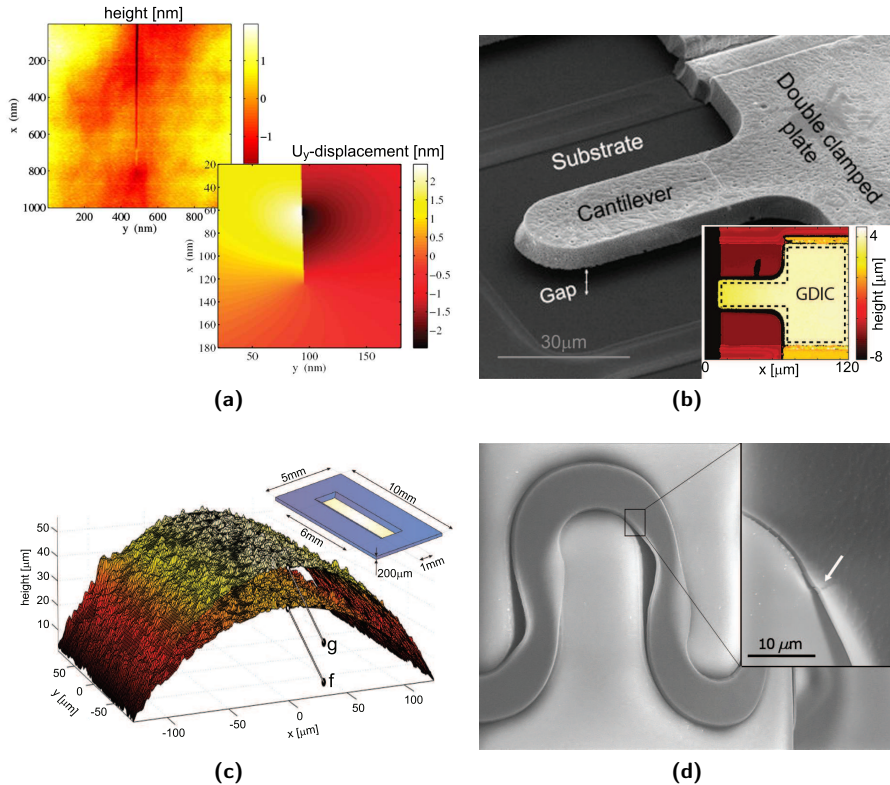
Figure 3.1: Examples of DHC on microscopic height profiles. Top left (a): a topographic image, made with AFM, of a glass sample with a crack, where DHC is used to calculate the three-dimensional displacement field. One component is shown here, from which the stress intensity factors are determined. (Reproduced from [52]). Top right (b): the curvature of a bending cantilever microbeam. (Courtesy of Bergers et al. [9]). Bottom left (c): a bulge test, where DHC is used to calculate local strain and curvature fields of a bulged membrane. (Courtesy of Neggers et al. [99]). Bottom right (d): a stretchable electronics interconnect, which buckles as a results of deformation of the structure. (Reproduced from [89]).

In the three examples shown in figure 3.1a-c a rectangular mesh for the discretization of the DIC problem sufficed for the purpose of the correlation procedure. Yet, to be able to describe both the complex shape of the interconnects and the buckle pattern, which occurs mainly at the edges of the interconnect, to accommodate the sample's edges a

more advanced mesh must be used. Furthermore, the continuity of NURBS functions across the element edge is adjustable by inter alia choosing the polynomial order of the shape functions. This is beneficial in the case where one, for example, is interested in the calculation of the curvature field, which requires at least $\mathscr{C}^1$ continuity. In [75], the DIC algorithm was combined with an adaptive refinement procedure, in order to autonomously optimize the shape functions. The number of degrees of freedom (DoFs) thereby remains limited, which is beneficial for the noise robustness. Refinement is executed locally, such that a finer discretization is only used in areas where this is necessary for accurately capturing the kinematics of the unknown displacement field, thereby compromising noise robustness [148], while retaining a coarser mesh in areas where the kinematics allow for this, preserving noise robustness. Furthermore, problem-specific choices on the discretization are not required in advance. In this paper, a generic nearly autonomous DHC framework is developed, which requires adaptation of the 2D adaptive iso-GDIC formulation toward quasi-3D: DHC. An advanced meshing framework is thereby required, which is generic for a myriad of shape function types, polynomial orders and mesh generating interfaces. In comparison to most global DIC formulations, the proposed method is less user dependent, since the most important choice, for the set of shape functions, is automated. The potential of the novel method is demonstrated on both virtual and real experiments with interface delamination of stretchable interconnects.

In the Methodology section, the methodology used is explained: first NURBS shape functions are introduced, the discretization of the specimen shape is shown and also the refinement procedure of the discretization is clarified. Furthermore, the DHC algorithm is defined. In Section 3.3, the novel adaptive isogeometric global digital height correlation (iso-DHC) technique is applied to two virtual experiments in order to provide a proof of concept. Also noise is included in the analysis. The method is applied to a real experiment with stretchable electronics in Section 3.4. Finally, conclusions are drawn in Section 3.5.

3.2   Methodology

In this section, the methodology for Digital Height Correlation is detailed. First the parametrization procedure for the sample geometry is clarified in Section 3.2.1. The required shape functions are thereby introduced. These are also used for the DHC algorithm, which is addressed in Section 3.2.2. Finally, the adaptive refinement procedure is described in Section 3.2.3.

3.2.1   Isogeometric shape functions and parametrizatiom

The shape functions that are used to parametrize and regularize both the sample geometry and the unknown displacement field are NURBS; Non-Uniform Rational B-Splines. This type of shape function originates from CAD (Computer Aided Design) modeling, but is used increasingly in the computational analysis of mechanical problems: Isogeometric Analysis (IGA) [64]. Both B-splines and their generalizatiom, NURBS, have been used in digital image correlation methods [29, 75].

In this work, the CAD representation of the sample is used directly in the DIC analysis. The procedure to generate the initial discretization is explained by using the commercial CAD program Autodesk AutoCAD [2]. The geometry parametrization could also have been retrieved from other CAD programs. An image of the undeformed sample, the reference image, is loaded in AutoCAD to act as a reference for the creation of the mesh. Thereafter, a NURBS surface is inserted with the desired order and number of degrees of freedom in both directions. Associated with this surface are control vertices, or control points, that can be translated to make the surface fit the sample geometry, utilizing the inserted background image. The geometry parametrization is described by

$$\underline{x}(\underline{\xi}) = \sum_i N_i(\underline{\xi}) \underline{p}_i, \tag{3.1}$$

where $N_i(\underline{\xi})$ are the two-dimensional NURBS shape functions defined on parametric coordinates $\underline{\xi}$; $\underline{p}_i$ are the control points and $\underline{x}(\underline{\xi})$ represents the mapping of the created surface, or mesh, to the physical domain. Since the DHC algorithm concerns images that are defined on a regular grid of pixels, it is necessary to evaluate the shape functions at the pixel locations, instead of the local element grid resulting from equation 3.1. This can either be done by interpolation, or, faster, by a nearest neighbours search algorithm, which couples the shape function value of the nearest local coordinate to the pixel coordinate. A choice for the second option is made because the loss of accuracy was found to be negligible for a fine local element grid, while still keeping a considerable gain in speed. This mapping procedure is illustrated in Figure 3.2.

The fundamental building block of a NURBS surface is the univariate B-Spline [64], which is a piecewise polynomial function of order p that is defined over a knot vector $\Xi = \{\xi_1, \xi_2, ..., \xi_k\}$, where each knot determines an element boundary in the domain. For NURBS these knots are not necessarily uniformly distributed. Also each knot can occur more than once; the continuity of the shape functions across an element border (knot location) is controlled by the multiplicity m of the knot: $\mathscr{C}^{p-m}$. The number of shape functions (and hence number of degrees of freedom, DoFs) is determined by the number of knots k and the polynomial order.
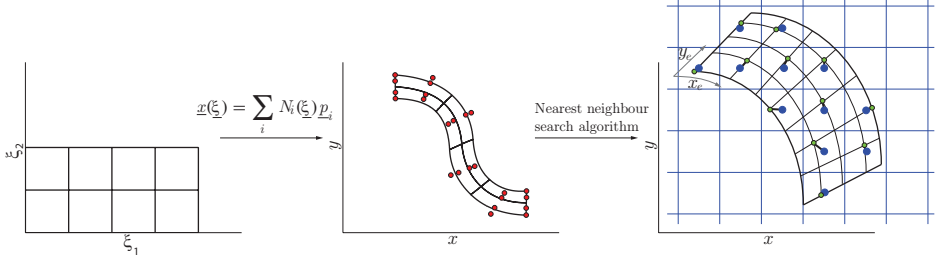
Figure 3.2: Illustration of the mapping procedure of the NURBS mesh from parametric coordinates $\underline{\xi}$ (left) to the global coordinates $\underline{x}$ (center), using equation 3.1. The control points $\underline{p}_i$ are indicated by the red dots. After this mapping the shape functions are known at a local element grid of coordinates $\underline{x}_e(\underline{\xi})$, as indicated in black in the zoom of an element in the right image. For the DHC algorithm it is required that the shape functions are evaluated at the pixel locations, indicated by the blue grid in the same image. Therefore a nearest neighbour search algorithm is employed, which for each pixel center inside an element (blue dots) finds the nearest element grid point (green dots) and assigns the value of the shape function at this point to the pixel. Note that for illustration purpose the pixel grid and element grid are depicted coarse. In reality the element grid is significantly finer than the pixel grid, such that the loss of accuracy of the nearest neighbour mapping method is negligible.

In the isogeometric GDIC approach it is necessary to reconstruct the CAD shape functions and geometry in the DIC code. Here, this information is obtained by extracting the required data from the AutoCAD file (Drawing Exchange Format): i) the chosen polynomial order of the NURBS surface; ii) the unique knot values in both directions and their corresponding multiplicities; iii) the control points and, possibly, their weights. Using the knot information, the Bézier extraction procedure [19] is applied to compute the element extraction operators $\underline{\underline{C}}^e$. With these operators the spline basis functions on an element can be constructed as a linear combination of a canonical set of shape functions, in this case the Bernstein polynomials $\underline{B}$:

$$\underline{N}^e = \underline{\underline{C}}^e \underline{B} \tag{3.2a}$$

$$N_i^e = C_{ij}^e B_j. \tag{3.2b}$$

This proces is illustrated in figure 3.4. The reader is referred to [19] for details on the extraction procedure. The resulting shape function $N_i(\underline{x})$ is composed of the contributions from all elements:

$$N_i(\underline{x}) = \mathop{\text{A}}_{e=1}^{m} N_i^e(\underline{x}). \tag{3.3}$$

Some of the resulting shape functions for second-order NURBS are plotted in figure 3.3.
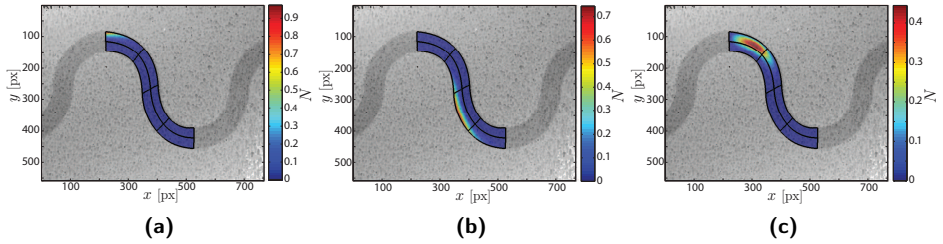
Figure 3.3: Discretization of a stretchable electronics interconnect. The mesh is plotted on top of the profilometric image, where the grayscale intensity levels indicate height values. An example of a corner (a), edge (b) and central (c) shape function are plotted with the mesh, for the case of 2nd order NURBS.

It is emphasized that this extraction is not restricted to B-splines or NURBS, but can also be used to construct e.g., T-Splines [129]. From the perspective of the DIC algorithm, this extraction process provides a unified interface for the implementation of a variety of spline technologies from different CAD interfaces.

The shape functions are not only important for the parametrization of the sample geometry, but are also important for the discretization of the DHC problem, as will be shown in the next section.
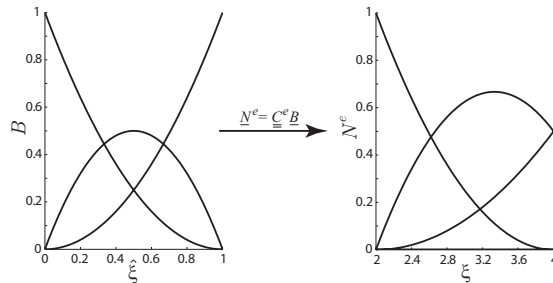
Figure 3.4: Graphic representation of the Bézier extraction process. Left: the second-order Bézier functions $\underline{B}$ of a parent element (with coordinate $\hat{\xi}$) are shown. After multiplication with extraction operators $\underline{\underline{C}}^e$ the shape functions $\underline{N}^e$ on an element e (with parametric coordinate ξ) are obtained (right). Note that the extraction proces also involves a mapping from parent coordinate $\hat{\xi}$ to local, parametric coordinate ξ.

3.2.2   Digital height correlation algorithm

The shape functions are not only used for the parametrization of the specimen geometry, but also for regularizing the displacement field, $\underline{U}(\underline{x})$, in DIC, i.e., in the correlation of the images of a deforming test specimen. The first image, f, is generally a representation of the undeformed, reference state of the specimen, while the subsequent images g represent deformed versions of the test sample.

In regular, two-dimensional DIC the images are characterized by the gray-scale intensities measured at the pixel locations, and the corresponding brightness at the material points is assumed to remain constant upon deformation of the underlying material, i.e. *brightness conservation* holds:

$$f(\underline{x}) - g \circ \underline{\Phi}(\underline{x}) = r(\underline{x}) \approx 0, \tag{3.4}$$

$$\underline{\Phi}(\underline{x}) = \underline{x} + \underline{U}_{xy}(\underline{x}), \tag{3.5}$$

where $r(\underline{x})$ is the residual image, which is zero in the absence of noise and $\underline{\Phi}(\underline{x})$ is a vector function which maps the reference coordinate $\underline{x}$ to the deformed coordinate. Note that throughout this article the same notation is followed as in Ref. [103], i.e. the coordinate $\underline{x}$ refers to the (Lagrangian) reference coordinates, while the deformed coordinates are consistently expressed using the mapping function $\underline{\Phi}(\underline{x})$. The residual is minimized to achieve optimal correlation, thereby obtaining the two-dimensional, in-plane displacement field $\underline{U}_{xy}(\underline{x})$, see e.g. [11, 75].

For those cases where the out-of-plane deformation field $W(\underline{x})$ is also desired, the DIC algorithm can be extended to Digital Height Correlation (DHC) [99]. In that case, the images are not defined by the gray-scale intensities, but each pixel contains a quantitative measurement of the height of the surface, obtained with e.g., optical profilometry, atomic force microscopy, or scanning tunneling microscopy. The conservation relation therefore transforms to *surface height conservation*, i.e.:

$$f(\underline{x}) - (g \circ \underline{\Phi}(\underline{x}) + W(\underline{x})) = r(\underline{x}) \approx 0, \tag{3.6}$$

$$\underline{\Phi}(\underline{x}) = \underline{x} + \underline{U}_{xy}(\underline{x}), \tag{3.7}$$

where $\underline{U}_{xy}(\underline{x})$ is now the in-plane component of the total, three-dimensional displacement field $\underline{U}(\underline{x}) = U(\underline{x})\underline{e}_x + V(\underline{x})\underline{e}_y + W(\underline{x})\underline{e}_z$, which is a function of the two-dimensional position vector $\underline{x} = x\underline{e}_x + y\underline{e}_y$.

Identifying the displacement field that will satisfy equation (3.6) is an *ill-posed* problem, which deteriorates through the inevitably present additional noise field. Therefore, DIC methods approximate the true displacement field with a field represented by a finite

and limited set of unknowns,

$$\underline{U}(\underline{x}) \approx \underline{u}(\underline{x}, \mathbb{a}), \tag{3.8}$$

$$\text{and} \quad \underline{\Phi}(\underline{x}) \approx \underline{\phi}(\underline{x}, \mathbb{a}), \tag{3.9}$$

where $\mathbb{a}$ is a column of degrees of freedom (DoFs), i.e. $\mathbb{a} = [a_1, a_2, \dots, a_{3n}]^T$, with n DoFs for each of the three components of the displacement field $\underline{U}(\underline{x})$. Applying more pixels per DoF allows for attenuation of acquisition noise (e.g. [57]), provided that the discretized displacement field can adequately describe the true displacement field.

As is commonly done in DIC, the displacement field is approximated as a linear summation of DIC basis functions, $\underline{\varphi}_i(\underline{x})$:

$$\underline{u}(\underline{x}, \mathbb{a}) = \sum_{i=1}^{3n} a_i \underline{\varphi}_i(\underline{x}). \tag{3.10}$$

Note, however, that these basis functions are three-dimensional vector-valued fields. For this purpose, the same NURBS shape functions, $N_j(\underline{x})$, that are used for parametrization of the sample geometry, see Section 3.2.1, are implemented. Note that the NURBS functions are two-dimensional, scalar-valued functions and each NURBS function is used three times to describe the three components of the displacement field with independent DoFs:

$$\underline{\varphi}_{i=j} = N_j(\underline{x}) \, \underline{e}_x + 0 \, \underline{e}_y + 0 \, \underline{e}_z \quad \text{for } j = 1, \dots, n, \tag{3.11a}$$

$$\underline{\varphi}_{i=n+j} = 0 \, \underline{e}_x + N_j(\underline{x}) \, \underline{e}_y + 0 \, \underline{e}_z \quad \text{for } j = 1, \dots, n, \tag{3.11b}$$

$$\underline{\varphi}_{i=2n+j} = 0 \, \underline{e}_x + 0 \, \underline{e}_y + N_j(\underline{x}) \, \underline{e}_z \quad \text{for } j = 1, \dots, n. \tag{3.11c}$$

Similar to regular 2D-DIC, a cost function $\Psi(\mathbb{a})$ is defined as the $\mathscr{L}_2(\Omega)$ norm of the residual

$$\Psi(\mathbb{a}) = {}^1\!/_2 \int_\Omega r(\underline{x}, \mathbb{a})^2 \, d\Omega = {}^1\!/_2 \int_\Omega \left[f(\underline{x}) - (g \circ \underline{\phi}(\underline{x}, \mathbb{a}) + w(\underline{x}, \mathbb{a})) \right]^2 d\Omega, \tag{3.12}$$

and a minimization problem is formulated to solve for the DoFs and thus the optimal approximate solution to the displacement field:

$$\underline{u}^{\mathrm{opt}}(\underline{x}) = \underline{u}(\underline{x}, \mathbb{a}^{\mathrm{opt}}) \quad \text{with } \mathbb{a}^{\mathrm{opt}} = \underset{\mathbb{a}}{\mathrm{Argmin}} \, \{\Psi(\mathbb{a})\}. \tag{3.13}$$

The conventional derivation of the DIC solution scheme to determine the *DoFs* $\mathbb{a}$ in Eq. 3.13 involves, first, linearization of the conservation equation, followed by an

iterative optimization algorithm (usually Gauss-Newton), resulting in a two-step linearization with a number of implicit assumptions. This two-step linearized system of equations is then iteratively solved to retrieve the optimal unknowns $\mathbb{a}^{\mathrm{opt}}$. In Ref. [103], however, it was demonstrated that the non-linear conservation equation can be minimized in a consistent mathematical setting, yielding a one-step linearization, thereby highlighting the implicit assumptions made. Here the same one-step linearization is followed, resulting in a system of equations that is iteratively solved for the unknowns $\mathbb{a}$:

$$\mathbb{M} \cdot \delta \mathbb{a} = \mathbb{b} \tag{3.14}$$

where $\delta \mathbb{a}$ is the iterative update of the DoFs. As argued in Ref. [103], the tangent operator $\mathbb{M}$ contains three terms, of which the second term is zero because the adopted basis is here linearly independent, while the third term is neglected as it contains the second gradient of the image making it highly sensitive to measurement noise. In that case, only one tangent operator term remains:

$$\forall (i, j) \in [1, n]^2, M_{ij} = \int_{\Omega} \left[(\underline{\varphi}_i \cdot \underline{G}) (\underline{G} \cdot \underline{\varphi}_j) \right] \mathrm{d}\underline{x}, \tag{3.15a}$$

whereby the right-hand member of Eq. 3.14 is given by

$$\forall i \in [1, n], \ b_i = -\int_{\Omega} \left[(\underline{\varphi}_i \cdot \underline{G}) \, r(\underline{x}, \mathbb{a}) \right] \mathrm{d}\underline{x}. \tag{3.16}$$

Here, $\underline{G}$ is the true image gradient, i.e. the gradient of the image g evaluated at the deformed coordinates:

$$\underline{G} = \underline{\mathrm{grad}}(g) \circ \underline{\phi} - \underline{e}_z = \frac{\partial g}{\partial x}\Big|_{\underline{\phi}(\underline{x})} \underline{e}_x + \frac{\partial g}{\partial y}\Big|_{\underline{\phi}(\underline{x})} \underline{e}_y - \underline{e}_z. \tag{3.17}$$

The term in the z-direction is added for DHC, to correctly deal with the out-of-plane displacements. As detailed in Ref. [103], using the deformation gradient tensor $\underline{\underline{F}}$, the true gradient can be related to the gradient of the back-transformed image, $\tilde{g}(\underline{x}) = g \circ \underline{\phi}(\underline{x}, \mathbb{a}) + w(\underline{x}, \mathbb{a})$:

$$\underline{\mathrm{grad}}(g) \circ \underline{\phi} = \underline{\mathrm{grad}}(\tilde{g}) \cdot \underline{\underline{F}}^{-T}. \tag{3.18}$$

Therefore, to simplify the true gradient to the one typically found in literature, first, small deformations are assumed, i.e. $\underline{\underline{F}}^T \equiv \underline{\underline{I}}$. Second, $\underline{\mathrm{grad}}(\tilde{g})$ is replaced with $\underline{\mathrm{grad}}(f)$, which has been justified in the literature because $\tilde{g}$ is updated at each iteration and converges towards f (see e.g. [113]),

$$\underline{G}(\underline{x}, \mathbb{a}) \approx \underline{\mathrm{grad}}(f) - \underline{e}_z = \frac{\partial f}{\partial x}\Big|_{\underline{x}} \underline{e}_x + \frac{\partial f}{\partial y}\Big|_{\underline{x}} \underline{e}_y - \underline{e}_z. \tag{3.19}$$

For the present case, this simplification to $\mathrm{grad}(f)$ was found to have a negligible effect on the accuracy, in agreement with the guide lines given in Ref. [103]. Therefore, $\mathrm{grad}(f)$ was implemented to reduce computational costs, however, extension to the true gradient is trivial. In order to determine $r(\underline{x}, \mathbb{a})$ in Eq. 3.16, the surface height values in the deformed image $g(\underline{x})$ need to be determined at the deformed planar positions $\underline{\phi}(\underline{x}, \mathbb{a}) = \underline{x} + \underline{u}_{xy}(\underline{x}, \mathbb{a})$, which requires interpolation. Interpolation is a source of error and to minimize its impact a cubic spline interpolation scheme is here implemented, as suggested by Schreier et al. [127].

3.2.3   Adaptive refinement

In order to be able to accurately describe the kinematics of the displacement field, the regularized displacement field $\underline{u}(\underline{x}, \mathbb{a})$ should be sufficiently rich, i.e., should have enough degrees of freedom. However, if too many DoFs are used, the solution becomes highly sensitive to noise [41, 112]. It is therefore important that the number of degrees of freedom is balanced. In certain cases, where the kinematics of the problem is known in advance it is possible to make a good estimation on the number and distribution of DoFs (i.e., the configuration of the mesh) to obtain accurate results, e.g., in the examples shown in Figures 3.1a-c. However, in some cases, including the experiments with stretchable interconnects considered in this work, shown in Figure 3.1d, it is more difficult to asses the kinematics in advance. Furthermore, displacement fields might be rather complex and exhibit localized features, which calls for a more detailed regularization in specific areas.

With an adaptive refinement algorithm the mesh can be optimized autonomously. This can be achieved by either *p-refinement*, where the polynomial order of the shape functions is elevated in designated elements of the mesh [157], or by *h-refinement*, where the elements themselves are refined [75], or isogeometric *k-refinement* [64]. Both h-refinement and p-refinement can be done in an adaptive fashion, where the algorithm autonomously determines in which area refinement is required based on the error or residual $r(\underline{x})$ in that area. In that way the solution is not dependent on user experience. Furthermore, both methods can be implemented efficiently, since only the refined shape functions have to be added in case of p-refinement, or substituted in case of h-refinement, in the column $\underline{\varphi}(\underline{x})$ that contains all shape functions. Hence, there is no need to rebuild the entire set of shape functions. Which type of refinement is used is a matter of taste. Nonetheless, in the case of the three-dimensional deformation of structures, including buckles and delamination, the curvature of the material may be of interest, which requires second-order derivatives of the displacement field. Therefore at least $\mathscr{C}^1$ continuity across element borders is required. Since for NURBS shape functions continuity across element borders is $\mathscr{C}^{p-m}$, with p the polynomial order and m the multiplicity of knots at the element border, $\mathscr{C}^1$ continuity can be achieved by using second-order B-splines with multiplicity 1. With p-refinement-based finite

elements only $\mathscr{C}^0$ continuity can be achieved, which is the reason why in this work it was decided to employ isogeometric analysis. In combination with h-refinement this allows for the refinement of the computational grid, while preserving the necessary continuity properties.

The approach adopted in this paper is a *hierarchical refinement* [83, 155] scheme, identical to the technique used in [75]. In this method multiple bases of shape functions are defined, which represent subsequent levels of uniform refinement. If refinement of a certain shape function is desired, this shape function is replaced by shape functions from the underlying basis that lie in the same support area. The result of this concept is that refinement occurs in a local fashion, in contrast to knot insertion, where the tensor product structure induces refinement of an entire row and an entire column of elements. The idea of hierarchical refinement is depicted in figure 3.5.
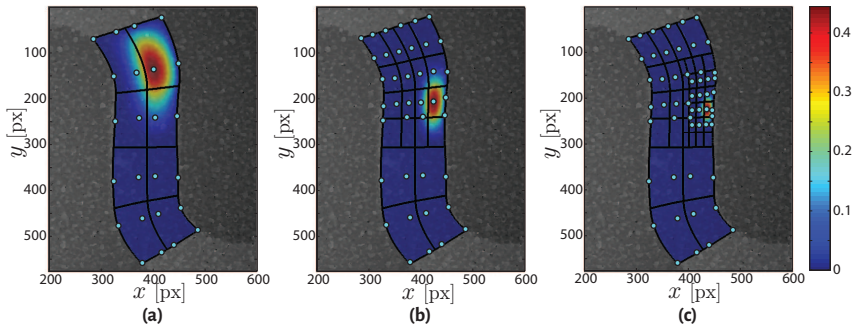
Figure 3.5: A graphical representation of the hierarchical refinement proces: In the left figure the initial mesh is depicted, plotted on top of the undeformed image of the stretchable interconnect. One of the shape functions is shown and the maxima of all shape functions are indicated by blue dots. For this example, only the depicted shape function is selected for refinement and the resulting refined mesh is shown in the middle figure. Note that all elements that form the support of the initial shape function, i.e., the top two by two elements in the left figure, are refined. Again one shape function is shown and the maxima of all shape functions are indicated by blue dots. The refinement proces is repeated for the shape function of the middle figure and the result is shown in the right figure.

Refinement indicator

The selection of shape functions for refinement is based on the residual $r(\underline{x})$, since the residual is also used as an error estimator in the DHC procedure itself. The residual gives full-field information, which makes is possible to distinguish between areas where correlation of the deformed image to the reference image is successful and areas where

it is not possible to approximate the displacement field accurately. For each shape function an averaged value of the residual in the area of its support is calculated and weighted:

$$C_j = \frac{1}{(f_{max} - f_{min})} \frac{\delta_{f,global}}{\delta_{f,j}} \frac{\int_{\Omega_j} |r(\underline{x})| N_j(\underline{x}) \mathrm{d}\underline{x}}{\int_{\Omega_j} N_j(\underline{x}) \mathrm{d}\underline{x}}. \tag{3.20}$$

First, the residual is weighted with the shape function N_j itself, in order to couple the residual in a certain area to the shape function with the largest influence in that area, i.e., a larger value. Furthermore, this scaling assists in preventing larger shape functions always being favored for refinement at the expense of basis functions with a smaller support area. Additionally scaling with the mean intensity gradient $\delta_f = \frac{1}{mn} \sum_{i=1}^{m} \sum_{k=1}^{n} \sqrt{|\nabla f(\underline{x}_{i,k})|}$, which is a measure for contrast, is applied. This is because the residual is not only influenced by non-exact correlation, but also by changes in the contrast in the pattern of the sample. Imagine two neighbouring pixels with a different value (either grey scale intensity or height). Now correlation is slightly inaccurate and the value of one pixel is assigned to the other pixel in the back-transformed image $\tilde{g}$. Since the residual is defined as the difference between the original value of this pixel and the value in the back-transformed image, the residual will be larger if the difference in value between the two neighbouring pixels is larger, i.e., if the contrast in that area is larger. To compensate for this the refinement indicator C_j is scaled with the relative mean intensity gradient $\delta_{f,global}/\delta_{f,j}$, where $\delta_{f,j}$ represents the contrast in the area of support of shape function j and $\delta_{f,global}$ in the entire region of interest. Finally, scaling with the range of pixel values f, here the range of height values, is implemented. This makes it possible to base the refinement criterium on the level of acquisition noise of the images.

A shape function is selected for refinement if the refinement indicator exceeds a certain threshold: $C_j > T$, see Figure 3.6. This threshold is set to $T = \max(\bar{C} + \sigma, T_{nl})$, where $\bar{C}$ is the average of the refinement indicator C_j of all shape functions and σ is the standard deviation. This threshold ensures that only shape functions are refined for which this is necessary, i.e., for which the refinement indicator is significantly large with respect to the other shape functions. If the differences in refinement indicator between the shape functions are too small, e.g., when the displacement field is homogeneous and no refinement is required, this threshold assures that no shape functions are selected for refinement. The value T_{nl} is an absolute threshold which corresponds to the noise level of the images, which has to be determined for each set of experimental images separately, such that refinement is not triggered by artifacts caused by image noise. This choice for the threshold is in correspondence to Ref. [75].

Since the correlation becomes highly sensitive to noise if the number of degrees of
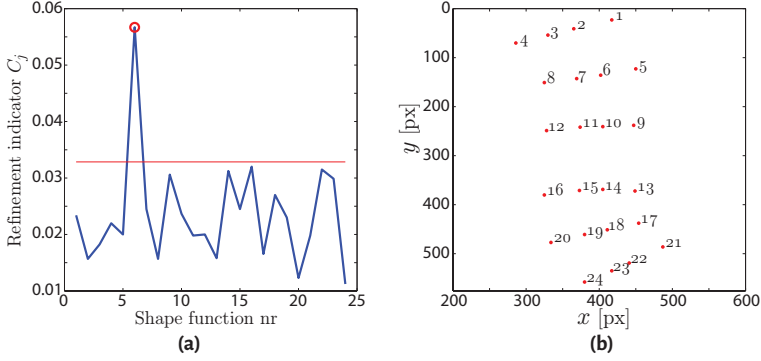
Figure 3.6: The refinement indicator C_j plotted for each shape function j (left). The position (top) of each shape function is shown in the right figure. The red line in the left image represents the threshold $T = \max(\bar{C} + \sigma, T_{nl})$. All shape functions above this threshold are selected for refinement, as indicated by the red circle. In this case, this concerns only one shape function, namely shape function nr. 6, which corresponds to the refinement step between Figure 3.5(a) and 3.5(b).

freedom becomes too large compared to the number of pixels, a minimum is set for the number of pixels within an element. This threshold is based on the correlation length, ℓ_c, which is a measure for the in-plane length scale of the pattern, i.e., the average size of the pattern features. At least several pattern features should be present inside an element, otherwise noise is dominant for correlation. Therefore the minimum element size is set to $10\ell_c \times 10\ell_c$, corresponding to Ref. [75]. The correlation length is determined automatically for each experiment. If an element becomes smaller than this threshold, the shape functions corresponding to this element are excluded from further refinement.

The mathematical formulation allows to use a different set of shape functions for each direction and thus only refine the shape functions for one direction, e.g., only for displacement in the height direction. Especially in this particular example of buckling of a stretchable electronics interconnect a different set of shape functions in the out-of-plane direction and refinement of only this set would make sense, considering the more complex nature of the out-of-plane deformation with respect to the in-plane deformation. However, this buckling case is a specific example and implementation of a scheme that relies on the known kinematics of the particular problem (by either choosing a different set of shape functions for one direction or refining only in this direction or applying both) would imply a loss of generality. Furthermore, the residual field is a result of the correlation of the displacement fields in all directions and hence it is not possible to distinguish between the accuracy of the correlation in the different directions. Therefore, the refinement is carried out in the shape functions in all three

directions and thus the same set of shape functions is used for both x, y and z direction.

3.3 Demonstration: Virtual experiment

The developed adaptive isogeometric digital height correlation algorithm is applied in a virtual setting in order to demonstrate the method. First, a proof of concept is given with a virtual displacement field that represents a localized buckle pattern. Here a rectangular mesh is used. It is demonstrated that the developed adaptive iso-DHC method is easily used for different orders of the NURBS shape functions. Also the influence of noise is investigated. In the subsequent example a more complex geometry is used: a stretchable electronics interconnect, which requires the advanced meshing framework introduced in Section 3.2.1.

3.3.1 Localized buckles

In this experiment a virtual height profile is analytically deformed. The height profile is in this case generated analytically and contains both coarse and fine in-plane features, making it suitable for DHC analysis [100]. The applied out-of-plane displacement field represents a localized buckling pattern, with two sinusoidal peaks of different size, of which one is pointing upwards and the other pointing downwards, see figure 3.9a. The in-plane displacement is zero in both x and y direction in the entire domain and therefore not discussed in the results. In the next example a virtual experiment will be shown where also the in-plane displacement is taken into account. The out-of-plane displacement is applied in four increments in which the amplitude of the sinusoidal peaks increases from 1 to 4 micrometer. The reference image f, the final image g_4 and intermediate images g_1 and g_2 are shown in figure 3.7. The developed DHC method is applied, using second-order ($p = 2$) NURBS shape functions. The nearly autonomous refinement algorithm adaptively refines the mesh in de areas where refinement is required. The resulting meshes are also shown in figure 3.7.

Since refinement is based on the residual field, it is interesting to analyse these fields. In figure 3.8, the residuals are shown for each refinement step, corresponding to the meshes shown in figure 3.7. In the first figure it is observed that the residual is high in the area where the peaks occur, this means that the original set of shape functions, with the mesh of figure 3.7a, is not able to capture the kinematics of these out-of-plane displacement peaks. The shape functions which span the region where the residual is high are refined and the residual decreases, see figure 3.8b. After the last refinement step the residual has decreased to almost zero (figure 3.8d) in the entire region, indicating that the new set of shape functions is successful in describing the displacement field.
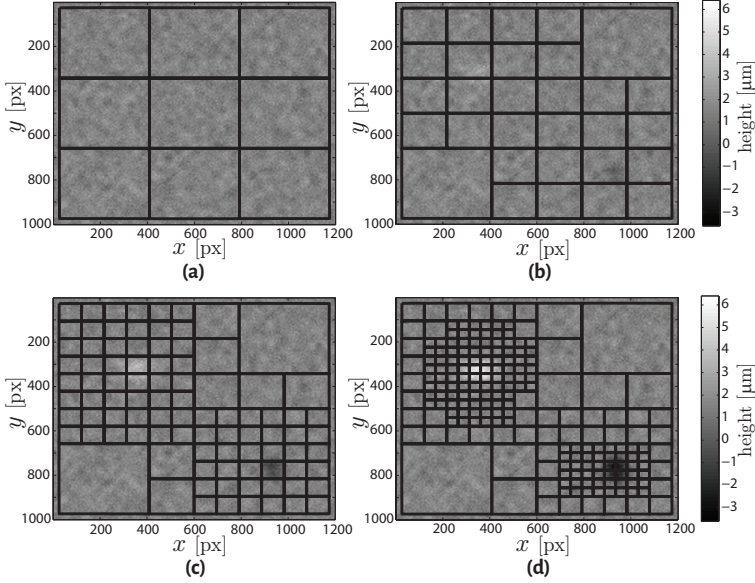
Figure 3.7: Evolution of the profilometric image and the mesh upon deformation. The reference image f (a) is shown with the initial mesh. Intermediate images g_1 and g_2 are shown in (b) and (c) and the final deformed image can be seen in figure (d). The evolved meshes are shown on top of the images. It is observed that the mesh refines in the areas where the sinusoidal peaks occur.

The resulting calculated displacement field is shown next to the analytical displacement field in figure 3.9b. In case of a virtual experiment it is possible to determine the exact error in the calculated displacement field, which is the difference between the exact and calculated displacement fields: $\varepsilon_w = w_{ref}(\underline{x}) - w(\underline{x})$. The error field is displayed in figure 3.11b. In the error field small 'wiggles' appear, that are characteristic for polynomial shape functions. However, looking at the values of the error field, compared to the amplitude of the sinusoidal peaks, the error is reasonably small. The method is therefore able to calculate sufficiently accurate results due to the autonomous refinements.

The adaptive iso-DHC method can readily be used with other polynomials orders of the NURBS shape functions. In the meshing procedure the polynomial order is an input setting in AutoCAD, which can be set to the desired order. In the DHC algorithm, the Bézier functions for different orders need to be implemented in order to use them. In this example we repeat correlation of the above virtual experiment with first and third-order shape functions. The same initial mesh (Figure 3.7a) is used. Note that the number of DoFs is not the same for the three cases, since a set of higher order shape
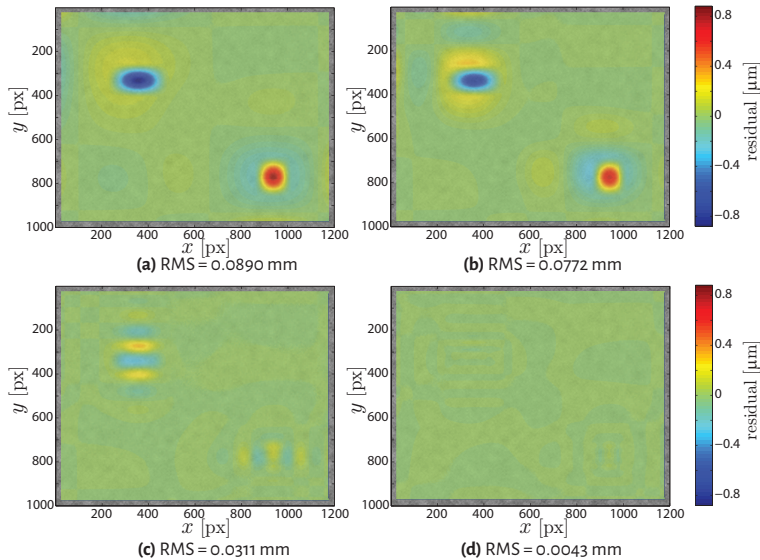
Figure 3.8: Residual fields after each refinement step, using the corresponding meshes in figure 3.7. In this example all refinement steps occur during correlation of image g_1 with image f, where the buckle height equals 1 micrometer. This corresponds to the amplitude of the peaks in the first residual field. It can be seen that the residual decreases significantly and reduces to almost zero after the last mesh refinement. Root Mean Square (RMS) values are also reported beneath the figures.

functions consists of more functions than a lower order basis. The refined meshes for the first and third-order NURBS are shown in figure 3.10. As can be seen, the refinement for the first-order shape functions remains more local than the second-order, while the third-order shape functions refine in a less local fashion. This is because NURBS shape functions overlap multiple elements, depending on their order. A first-order NURBS (not at the edge of the domain) covers two by two elements, while a third-order NURBS occupies four by four elements. As explained in Section 3.2.3 the entire support of the selected shape functions is refined, resulting in less local refinement for higher order shape functions. The resulting decrease in residual corresponding to the refined meshes of figure 3.10 is similar to that of the second-order shape functions, shown in figure 3.8, and therefore not shown.

The error fields resulting from the calculation of the displacement field with the adaptive iso-DHC method with first and third-order NURBS are plotted in Figure 3.11a and 3.11c. Especially for the third-order shape functions the characteristic 'wiggles' are again recovered, however, they now spread out over a larger region, originating from the larger
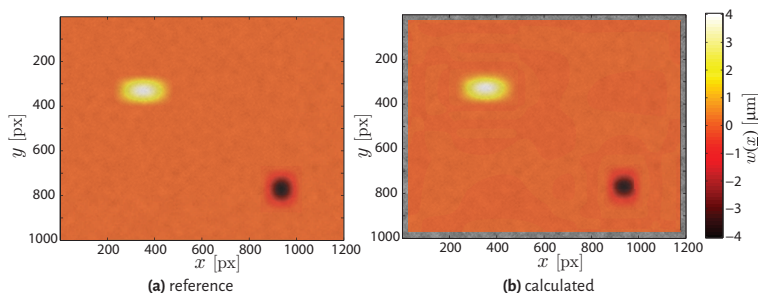
Figure 3.9: Reference (a) and calculated (b) out-of-plane displacement field $w(\underline{x})$ after the final iteration.
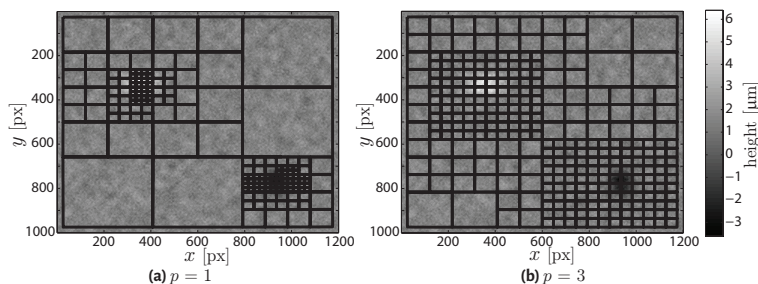
Figure 3.10: Refined meshes for first (left) and third (right) order NURBS, plotted on top of the undeformed image f.

support of the higher order functions. The level of the error is similar to the error of the second-order shape functions. The error field for the first-order shape functions exhibits more local features due to the more local nature of the lower order shape functions, however its features have a significantly higher amplitude, indicating that despite refinement these shape functions are not able to describe the displacement field as accurately as the higher order shape functions.

In this work we demonstrate the method on stretchable interconnects, which have a slender geometry, thereby limiting the number of elements in the width direction. Therefore, the refinement proces should be local. First-order shape functions were found to refine locally, but are not optimally suited for capturing the kinematics of localized buckling, while also providing only $\mathscr{C}^0$ continuity on the element boundaries. Third-order shape functions were found to be less local. Therefore, second-order shape functions form an adequate compromise, with the preferred element boundary
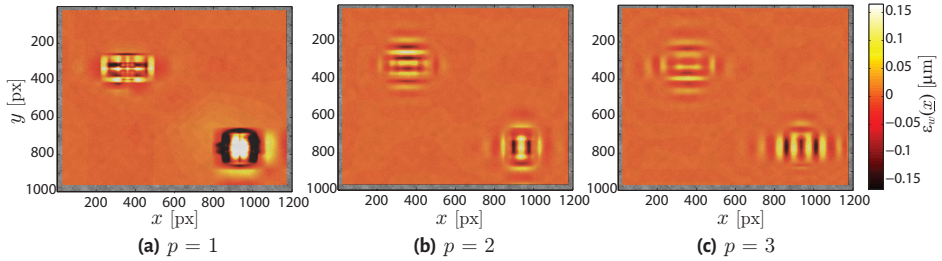
Figure 3.11: Error fields for the correlation of the virtual experiment, using first (a), second (b) and third (c) order NURBS shape functions. Notice that the RMS value of the error for the 1st order NURBS (0.04496 μm) is much larger than for the 2nd (0.01670 μm) and 3rd order (0.01653 μm) NURBS.

continuity of $\mathscr{C}^1$. They will be used for the remainder of the paper.

Noise analysis

The virtual experiment is repeated with shape functions of the second order for a case where noise is present. From real experimental data the noise level is determined by subtracting multiple images taken subsequently, with no deformation, and calculating the RMS value of the residual. The noise level is assessed at about 1.5%. A safety factor of 2 is administered and random noise of 3% of the height level range is artificially applied to the images f and g. The same algorithm is applied, starting from the initial mesh that is shown in Figure 3.7a, and the resulting mesh refinement and residual field after refinement are shown in Figure 3.12. From this image and the corresponding Root Mean Square (RMS) value it is observed that the residual decreases to about the level of the noise (which has an RMS value of 0.0964 μm), indicating that an optimal correlation has been obtained. The refined mesh is essentially the same as the case where no noise is present. The calculated displacement field and corresponding error field, including the RMS value, are similar to Figures 3.9b and 3.11b respectively, and hence are not displayed here. The results illustrate the noise robustness of the proposed method.
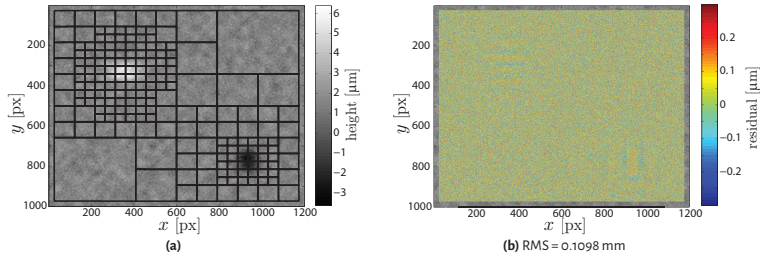
Figure 3.12: The refined mesh (a) and corresponding residual field (b) of the virtual experiment, for the case where a worst-case 3% noise level is present. Note that the color scale of the residual field is much smaller than in Figure 3.8.

3.3.2 Stretchable interconnect

Although the first virtual experiment provides a proof of concept for the adaptive iso-DHC algorithm, a more complex sample geometry and mesh are considered next. The method is applied to a virtual experiment on a stretchable interconnect (SI). To this end, a real height profile (Figure 3.13a) from a stretchable electronics structure, measured using a Sensofar PLμ2300 confocal optical profilometer, is analytically deformed. The applied displacement field again represents localized buckles, as depicted in figure 3.1d. The buckles are represented by two sinusoidal peaks that are cut off at the edge of the SI geometry. In this experiment also in-plane deformation is considered, namely uniaxial stretching in x-direction and rigid body translation in y-direction. Like for the previous case, the final displacement field is applied in four increments, for which the resulting images in step 2 and 4 are shown in Figure 3.13b and 3.13c.

The initial mesh is built with AutoDesk AutoCAD, as described in Section 3.2.1. In this case 6×2 elements is the minimum to accurately describe the sample's contour, see Figure 3.13a. The DHC algorithm is solved and the mesh refines in the regions around the peaks, see Figures 3.13b and 3.13c.

From the residual images, shown in Figure 3.14, it is observed that with the initial mesh it is not possible to accurately capture the kinematics of the buckles, therefore, the residual is high in the area surrounding the buckles. After refining the mesh, the residual decreases. Note that the residual does not decrease to the low level achieved in the virtual experiment of the previous section. This is due to the limited amount of pixels, only 768×558 used here compared to the image with a more common size of 1200×1000 pixels of the previous experiment. To more accurately describe the displacement field with localized buckles the mesh should presumably be refined one more step. However, this is not allowed, since the number of pixels in an element would become too small
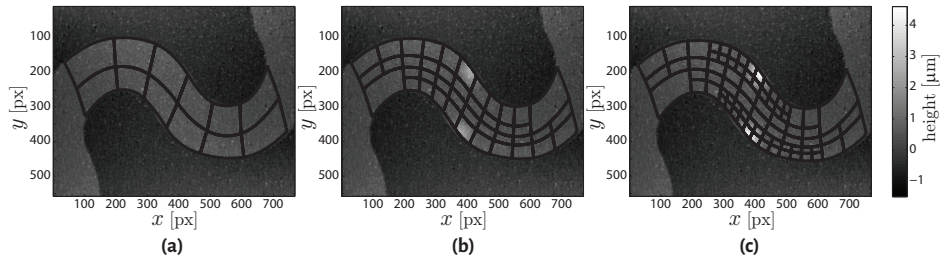
Figure 3.13: The reference image f (left) is shown along with deformed images g_2 (middle) and g_4 (right). The initial mesh and refined meshes are plotted on top.

and the problem becomes more sensitive to noise. Therefore, this result is the best that can be obtained with this image.

(a) RMS = 0.0889 mm   **(b)** RMS = 0.0145 mm   **(c)** RMS = 0.0140 mm
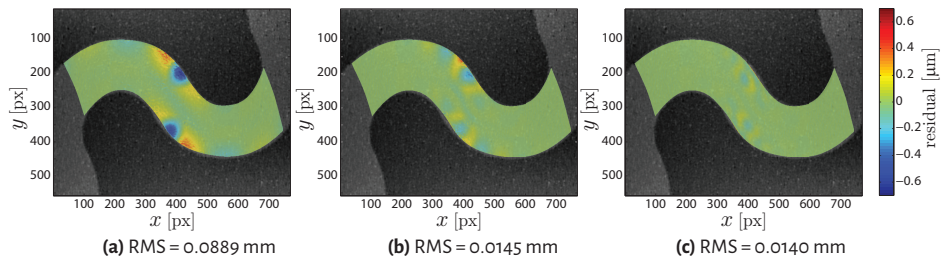
Figure 3.14: The residual images are shown after correlation using the corresponding meshes from figure 3.13. It can be seen that the buckles cannot be described accurately with the initial mesh, resulting in a high residual in this area. After refinement in this region the residual decreases significantly. The RMS values are reported below the figures.

A quantitative measure for the accuracy of the method is shown in figure 3.15. The applied displacement fields $u(\underline{x})$, $v(\underline{x})$ and $w(\underline{x})$, or reference fields, are shown in figure 3.15a and the same fields calculated with the DHC algorithm are depicted in figure 3.15b. Since this is a virtual experiment we are able to calculate the exact error field, which is the difference between the reference and calculated field. This error field is shown for all three directions in figure 3.15c. It is observed that the displacement fields for both the in-plane directions x and y and the out-of-plane direction z are captured well. They are calculated rather accurately, although the error is larger than in the previous test case. However, this is partly due to the lower amount of pixels in the image, which can be optimized by using a profilometer with a high-resolution camera. The novel method, with a complex mesh that was constructed using the proposed mesh-

ing procedure, is adequately able to autonomously determine the degrees of freedom that optimally describe the localized displacement field with a representative buckling profile.

(a) reference   **(b)** calculated   **(c)** error field
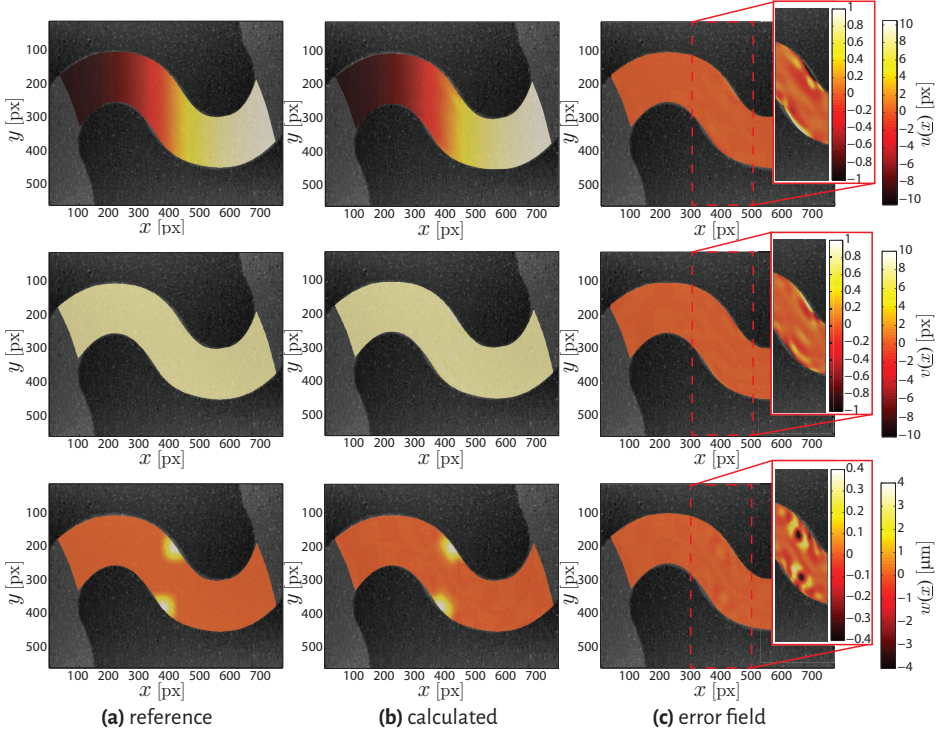
Figure 3.15: Reference (a) and calculated (b) in-plane displacement fields $u(\underline{x})$ (top) and $v(\underline{x})$ (middle) and out-of-plane displacement field $w(\underline{x})$ (bottom) after the final iteration. In figure (c) the error, i.e., the difference between the reference and the calculated displacement field, is depicted. The RMS values of the error in $u(\underline{x})$ and $v(\underline{x})$ are 0.070 pixels (0.0077 μm) and 0.105 pixels (0.0116 μm) respectively and 0.060 μm for the error in the out-of-plane displacement.

3.4   Experiment: Application to stretchable electronics

A real experiment concerning a stretchable electronics interconnect is executed in order to demonstrate the adaptive isogeometric DHC method's performance in a real

situation. If the interconnect is stretched, it buckles in certain regions. The objective of this experiment is to calculate the displacement field describing these buckles as well as the in-plane displacements, with an autonomously optimized set of shape functions.

3.4.1 Specimen and test setup

The specimen used for this experiment is a stretchable electronics interconnect consisting of a 10μm thick polyimide substrate with a 1μm thick aluminum meander. This S-shaped aluminum interconnect structure has width 20μm, inner radius 20μm and a 40μm rectilinear segment between the curvilinear sections, see Figure 3.16. For DHC a certain contrast in height values on the sample, or pattern, is required. For this purpose an Indium-Tin (In-Sn) layer is deposited using a planar magnetron sputtering system. In-situ heating of the sample to 80°C, close to the melting temperature of In-Sn, in combination with a high deposition rate is used to prevent deposition of a homogeneous In-Sn layer, but instead achieve distinct height features. Since the temperature during this pattern deposition procedure is significantly lower than the processing temperature of the sample, it is not degraded using this technique.

The experimental setup consists of a Kammarath&Weiss uniaxial tensile/compression module placed underneath a Sensofar Plμ2300 confocal surface profilometer equiped with a 150X objective. After deposition of the Indium-Tin layer, the Aluminum/Polyimide interconnect is glued onto disposable grippers, that are clamped in the tensile stage, and stretched. After each elongation increment, a topographic image is acquired.

3.4.2 Results

The dimensions of the specimen are very small and therefore application of a pattern with sufficiently distinct features and accurate, reproducible measurement of this height profile with a profilometer is a known challenge, as discussed for instance in [9]. For instance, when comparing the profilometric images of different increments it is observed that the pattern features change between the images, see Figure 3.17. This might be due to a relatively high noise-to-signal ratio caused by steep edges of the tiny pattern features, thereby working at the limits of the profilometer. Measurement of the features from a slightly different position and angle, due to in-plane deformation and especially out-of-plane rotation of the underlying sample, further decreases the measurement reproducibility. These discrepancies between the incremental images make correlation difficult, because the residual will not reduce to (almost) zero for the correct displacement field. The detrimental effects are somewhat reduced by applying some Gaussian blurring (kernel size 10, $\sigma = 2$) to the images before correlation, which is a known technique to reduce bias error [107]. Still it was found that shape functions
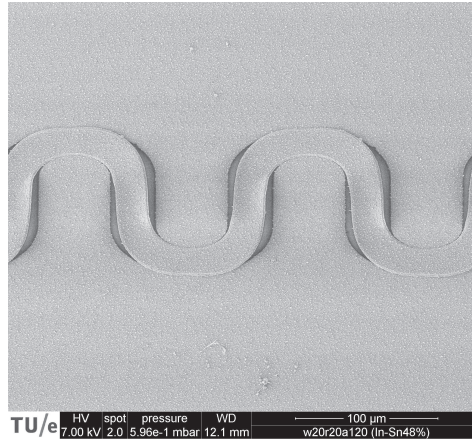
Figure 3.16: Scanning Electron Microscopic image of the aluminum stretchable interconnect on a polyamide substrate, taken after deformation. The interconnect has delaminated from the substrate, which exposes regions of the substrate that are not covered with an Indium-Tin layer. The In-Sn layer is characterized by the granular texture on top of the entire sample. In the rectilinear parts the lighter regions indicate the location of buckles.

with a small support are sensitive to these measurement artifacts, especially the shape functions in the corners of the domain. To complicate the test further, it was observed that the correlation length of the pattern is small. This, in combination with the change in pattern features, makes any DIC algorithm sensitive to a good initial guess. It is a known feature of DIC algorithms that there is a possibility of correlation to a local minimum instead of the global minimum [106]. Starting from a coarse mesh with limited degrees of freedom reduces this risk, while using the correlation result of the coarse mesh as initial guess for correlation for a refined mesh. In the virtual cases this was sufficient and an initial guess of zero displacement everywhere was acceptable, but in this experiment a good initial guess is inevitable. This good initial guess for all images was obtained by a correction for rigid body motion of the specimen center and running the algorithm first over all images with the refinement option turned off, i.e. with the large-area NURBS shape functions shown in Figure 3.18a.

For the correlation we zoom in on one of the rectilinear parts, as this gives the most interesting displacement field, since it buckles upon stretching. The images before and after deformation are shown in Figure 3.18, with the initial and refined mesh (after two refinement steps) plotted on top. The buckles that occur are about 3.5μm high and the mesh refines in the area of the buckles. However, the sensitivity of the corner shape functions to the measurement artifacts is clear in the refined mesh. The mesh is refined in the corner elements, while there is no kinematic reason for it. Refinement
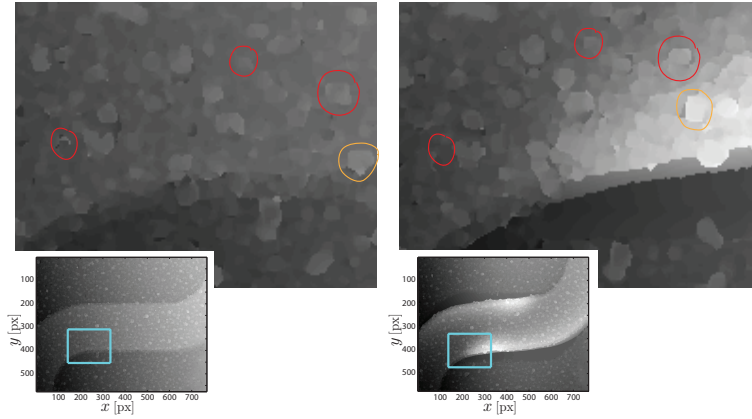
Figure 3.17: Images f and g zoomed in at the same area (blue boxes in insets). It is observed that the pattern features look distinctly different in the two images. For example, the feature in the circles are (almost) unrecognizable. This complicates correlation of the two images.

leads to more freedom in this area, causing a even higher sensitivity to experimental uncertainties and further refinement in the same area. Also note that in the second image it might appear that the refined mesh does not correctly conform the sample anymore, i.e. the mesh appears smaller than the interconnect width, however, this illusion is caused by the delamination and out-of-plane rotation of the interconnect, causing the steep sides of the interconnect to rotate into view, thereby exposing new area that in the first image was not visible. This also becomes clear from the zoomed images in Figure 3.17, where the yellow encircled feature moves away from the 'edge' and another feature appears below it.
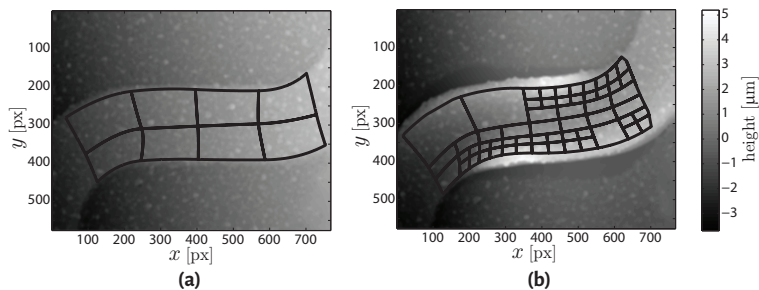
Figure 3.18: The reference image f (left) is shown along with the deformed image g (right). Both images are blurred. The initial mesh and final refined mesh are plotted on top.

Since this is a real experiment, it is not possible to determine the accuracy of the correlation by means of error fields, in contrast to the virtual experiments. The accuracy therefore has to be determined using the residual fields. These fields before and after mesh refinement are shown in Figure 3.19. The buckles clearly show up in the first residual field, as regions with an averaged value that is systematically above (red) or below (blue) zero, which indicates that a finer mesh is desired in these areas to calculate the displacement field accurately. When the mesh refines, in two steps, the final residual field does not have regions with an averaged value systematically different from zero anymore. Note that refinement in the corners does not improve the residual in this area significantly and occasionally even causes the residual to increase, as for example in the right top corner. This is because the increased number of degrees of freedom also increases the sensitivity to the measurement artifacts, which can lead to poorer correlation.
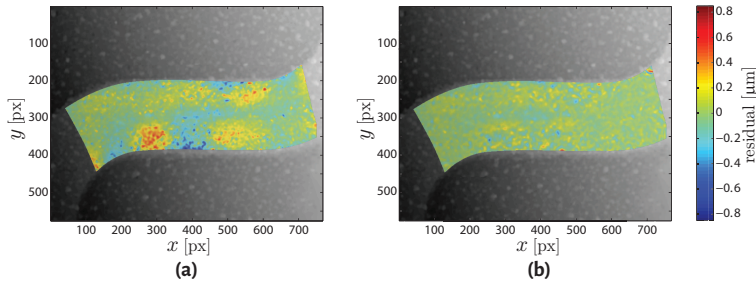
Figure 3.19: The residual images are shown after correlation using the corresponding meshes from figure 3.18. It can be seen that the buckles cannot be described accurately with the initial mesh, resulting in a high residual in this area (RMS value 0.133 μm). After refinement in this region the residual decreases significantly (RMS value 0.062 μm).

The out-of-plane displacement field (Figure 3.20c) clearly shows the buckles observed in Figures 3.16 and 3.18b. The in-plane deformation represents mainly the rigid body rotation of the rectilinear part of the interconnect that occurs upon stretching, as is also observed in these figures. In all, the three-dimensional displacement field in Figure 3.20 seems to have been measured accurately.

To conclude, since the height profiles resulting from this experiment are difficult to process for any digital height correlation algorithm, a good initial guess was necessary to analyze the data with the adaptive isogeometric DHC method. However, then the method was able to provide accurate results, corresponding to the observed in-plane and out-of-plane displacements in the measured height profiles, and correlated to a relatively low residual field. The mesh was optimized autonomously to be able to describe the complex displacement field accurately, but refines in unnecessary areas

due to sensitivity of the small corner shape functions to measurement artifacts. Still, autonomy of the algorithm was partly lost due to the necessity of the preconditioning. As the DHC algorithm seems to work correctly, further improvement should be obtained by application of a height pattern with larger correlation length and more robust measurement of surface height profiles.
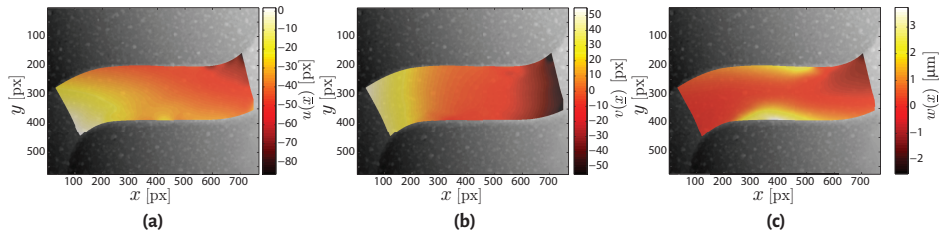
Figure 3.20: The calculated displacement fields $u(\underline{x})$ in x-direction (a), $v(\underline{x})$ in y-direction (b) and $w(\underline{x})$ in z-direction (out-of-plane) (c) are shown on top of undeformed image f. Combining the two in-plane displacement fields yields a rigid body rotation, which can also be seen from the difference between Figures 3.18(a) and (b), as well as a slight elongation of the structure. In the out-of-plane displacement field the observed buckles appear clearly, indicating an accurate calculation of the displacement field.

3.5 Conclusion

A method has been developed which uses an adaptive refinement algorithm to nearly autonomously refine shape functions in a global digital height correlation technique. This method is useful in experiments where the kinematics of the deforming sample are not known in advance. The mesh autonomously adjusts to the displacement field, i.e., optimizing the set of shape functions for capturing the displacement field. An optimized number of shape functions, i.e. number of degrees of freedom, is beneficial in DHC problems. Sufficient DoFs are needed to capture the kinematics of the displacement field, but too many of them make the problem too sensitive to noise. Another advantage of this method is that only little user experience is required to construct a reliable discretization of the problem.

NURBS shape functions are used both for the discretization of the DHC problem and the parametrization of the sample geometry. NURBS were originally developed for CAD modeling and in this work the CAD representation of the sample is directly used for DHC. NURBS shape functions are geometrically rich and can describe many geometrical shapes and displacement fields. With the use of a CAD program for constructing the mesh, nearly any specimen geometry can be meshed. Moreover, one is not restricted to

a particular polynomial order of the shape functions, as the order can simply be selected in the CAD program. In this work, it was chosen to use second-order NURBS, since for buckled samples the curvature of the buckles is of particular interest and to this end second-order derivatives of the calculated displacement field are desired. A hierarchical approach has been implemented for the adaptive refinement of the shape functions. This way refinement is executed in an efficient way and stays local, in contrast to knot insertion where an entire column and row of shape functions are refined due to the tensor product structure. The adaptive refinement is based on the residual field.

A proof of concept of the novel method is given with a virtual experiment with an out-of-plane displacement field with two sinusoidal peaks, representing a localized buckle pattern. The algorithm works adequately and refines in the expected area, yielding an accurate result. The method is also applied to a virtual experiment where a more complex sample shape is used: a stretchable electronics interconnect. It was shown that the method succeeds in capturing both in-plane and out-of-plane deformation fields accurately and refines the mesh in the expected areas.

Finally the adaptive iso-DHC method is tested in an experimental setting, where an in-situ tensile experiment is performed on a stretchable interconnect in a profilometer. This experiment formed a challenge, since the structure is of such small dimensions that reproducible measurement of the miscroscopic height pattern forms a significant challenge. Successfull correlation of the resulting images would be difficult for any DIC algorithm. The problems were overcome by applying blurring of the images and supplying a good initial guess. This is a compromise, since the autonomy of the algorithm is decreased, however, the mesh is still autonomously refined in the necessary regions yielding accurate three-dimensional deformation fields. Further improvement should be sought in more robust measurement of surface height profiles.

Concluding, the novel adaptive isogeometric DHC algorithm is a versatile technique for correlating displacement fields using the height profiles of many different types of experiment, including samples of which the deformation mechanism is unknown in advance (e.g. stretchable electronics interconnects). The shape functions used for discretizing the displacement field adjust autonomously to enrich the kinematics in regions where this is needed, obviating the need for detailed mechanical knowledge in advance. Accurate results have been obtained with the method, making this a promising technique for experimental mechanics of solids.

Acknowledgements

Chapter 4
Experimental-numerical characterization of metal-polymer interface delamination in stretchable electronics interconnects

---

Abstract

Understanding the mechanical behavior and failure mechanisms of stretchable electronics is key in developing reliable and long-lasting devices. In this work a stretchable system consisting of an aluminum serpentine patterned interconnect adhered to a polyimide substrate is studied. In-situ experiments are performed where the stretchable sample is elongated, while the surface topography is measured using a confocal microscope. From the resulting height profiles the three-dimensional deformations are extracted using an adaptive isogeometric digital height correlation algorithm. The displacement information is compared to realistic numerical simulations, in which the interface behavior is described by cohesive zone elements. It is concluded that despite fitting the traction separation law parameters, the model fails to correctly capture the distinct out-of-plane buckling of the interconnect. The model is updated with residual stresses resulting from processing and crystal plasticity induced behavior (decreased yield strength) in the aluminum layer, but both measures are not resulting in the experimentally observed deformations. Finally, mixed-mode cohesive zones are implemented, in which the properties are different in the shear and normal direction. After fitting the

corresponding parameters to the experimental data, the model shows realistic in-plane and out-of-plane deformations. Also a predictive simulation for a different geometry results in the correct experimentally measured behavior. It is concluded that the aluminum-polyimide interface mode-angle dependency explains the observed failure mode of local delamination and buckle formation.

4.1   Introduction

A relatively new and evolving direction for electronic applications is the development of highly deformable systems, i.e., stretchable electronics. Flexible and stretchable electronic devices are mainly used in biomedical applications, in order to bridge the gap between traditionally rigid, flat electronics and soft, curved biological tissue (such as skin and organs). Examples include patches that are adhered to human skin for health monitoring [73, 81], flexible devices for cardiac diagnostics [51, 144], smart contact lenses [109] and stretchable surgical tools, such as a balloon catheter with sensors for blood flow monitoring [72, 80]. Other examples outside the biomedical field are smart textiles [145], flexible displays [118] and solar cells [88], multi-functional flexible patches [161] and LED arrays [153].

Often a stretchable electronics design consists of functional IC (integrated circuit) islands, e.g., sensors, actuators or microprocessors, that are connected by stretchable interconnects (electrical conductive wires), which encompass a thin metal film that is patterned in a meander shape on or encapsulated in a compliant, polymeric, substrate [47, 48]. Elongation of these structures results in bending, twisting and stretching of the initially planar interconnect, inducing large deformations of the substrate, while only small strains are introduced in the metal film [86]. To ensure reliability and sufficient lifetime, it is important to investigate the mechanics of the stretchable devices [55]. One of the main failure mechanisms is delamination between the interconnect and the substrate [61], which is intrinsically coupled to buckling of the metal layer, followed by ductile failure of the interconnect, which in turn leads to complete failure of the electronic device [139].

Most experimental studies of stretchable electronics look at failure from a global perspective, i.e., at which global stretch percentage the interconnects fail, e.g., [48, 61, 86]. However, to understand the failure mechanisms, micron-scale in-situ testing is required, to study failure at the small scale of the damage. In literature multiple studies can be found towards experimental investigation of delamination in metal-polymeric interfaces, i.a., for copper-PDMS systems, where peel tests reveal fibrillation of the PDMS (Poly(dimethylsiloxane)), which induces remarkably high (macroscopically observed) interface toughness[58, 101, 102, 138]. Also buckling-based failure of stretchable electronics has been investigated experimentally, where the influence of meander geometry

on the failure modes is studied [25, 26, 89]. Furthermore, numerical simulations have been performed to model the mechanical behavior of stretchable electronics. Some simulations are dedicated to a realistically modeled full system, but without taking delamination into account [60, 61, 87, 89], others focus purely on the delamination itself using cohesive zone models, where a comparison is made with peel test results [58, 139], however, no realistic stretchable interconnect geometries under real loading conditions are considered. Therefore, there is a gap in the literature with respect to comparison of experimental data to numerical modeling of full stretchable electronics systems, while taking all the main deformation modes, including delamination and buckling, into account. In general, comparison of three-dimensional full-field displacement data with numerical simulations is only done for single materials [9, 10] and not for multi-material samples to the best of our knowledge.

This work aims at the experimental-numerical characterization of interface delamination in stretchable electronics, where the numerical model is a true representation of the real experiment. To this end, in-situ stretching experiments are performed on aluminum-polyimide stretchable electronic interconnects underneath a confocal optical microscope to measure surface topographies at different time increments, see Section 4.2. A recently developed adaptive isogeometric digital height correlation algorithm (DHC) [76] is used to analyze the three-dimensional surface displacement fields from these height profiles. In Section 4.3 the deformation behavior is compared to a numerical simulation, which includes the correct sample geometry and boundary conditions from the experiments and cohesive zones for the interface behavior. The model is improved in several steps until the simulation results reflect the experimentally observed deformation modes. Finally, conclusions are drawn in Section 4.4.

4.2 Experimental characterization: DHC on profilometry data

In this section the tools required for the experimental characterization of the stretchable interconnects are introduced and the results are presented.

4.2.1 Samples

The samples consist of a polyimide (PI) substrate, 10μm thick, with an aluminum (Al) serpentine-shaped, 1μm thin electrical interconnect deposited on top. This PI-Al material configuration can be manufactured through photo-lithography based micro-fabrication, allowing for smaller sizes and thus a higher density of interconnect features compared to, e.g., the copper-PDMS stretchable interconnects studied in [23]. The

samples were micro-fabricated in the same way as presented in [89]. A scanning electron microscopy (SEM) image of the sample, with a height pattern needed for DHC deposited on top, in stretched state is shown in Figure 4.1a. Delamination of the interconnect from the substrate is clearly observed. The grain structure of the aluminum layer is analyzed using Electron Backscatter Diffraction (EBSD), see Figure 4.1b.

Two different S-shaped interconnect geometries are analyzed, namely the w20r20a120 and the w20r40a180 samples. Figure 4.1c displays the geometrical parameters of the samples, i.e., the width (w), radius (r), amplitude (a), and rectilinear arm length(A_{in}) of the stretchable interconnect, clarifying the names of the different samples. Herein, *rectilinear arm* refers to the rectangular part of the interconnect and the bend, or corner, of the S-shaped interconnect is referred as the *curvilinear* segment. Both samples have an identical rectilinear arm to bend ratio of $\frac{A_{in}}{w+r} = 1$. Based on previous research [89], a significant difference regarding initiation of the failure mechanisms is expected for the two sample types as a result of the difference in width compared to the other dimensions.

4.2.2   Experimental setup: in-situ profilometry

Tensile experiments on the stretchable electronics samples were performed in situ, i.e., the samples were stretched using a micro-tensile device placed underneath an optical profilometer, see Figure 4.2. The samples were glued (using Loctite® 401) on disposable PMMA grippers as shown in the inset of Figure 4.2. The grippers and sample were then installed in a Kammrath&Weiss micro-tensile stage equipped with a 50N load cell to impose a uniaxial tensile deformation. A displacement rate of 1μm/s was employed. Surface topographies, to be analyzed later with a digital height correlation (DHC) algorithm in order to obtain the full-field 3D deformation behavior of the stretchable interconnects, were acquired by a confocal optical profilometer (Sensofar Plμ 2300) in intervals of approximately 2% elongation. Tensile deformation was prolonged until 40% applied global strain. For optimal DHC results, the highest spatial resolution is beneficial, therefore a 150X objective with 0.95 aperture was used to collect the surface height profiles, ensuring the largest magnification and numerical aperture. This resulted in a field of view of 85μm in x-direction by 64μm in y-direction (768x576 pixels), which is sufficient to capture the buckling and delamination phenomena of the interconnect in the rectilinear arm area.

For each interconnect geometry three repetitions of the experiment were performed to study the reproducibility of the experimental method and results. As discussed in [8], obtaining stable and reproducible measurements using optical profilometry remains a challenge. To increase stability and reproducibility of the topographic images, the following measures were applied. First, vibrations and drift of the positioning stage of the confocal optical profilometer, onto which the micro-tensile stage is placed, were

(a) Deformed interconnect system

(b) Inverse pole figure map of aluminum surface

Sample name	Width	Radius	Rectilinear arm length	Amplitude
	w	r	A_{in}	a [μm]
	[μm]	[μm]	[μm]	
w20r20a120	20	20	40	120
w20r40a180	20	40	60	180

(c) Interconnect dimensions
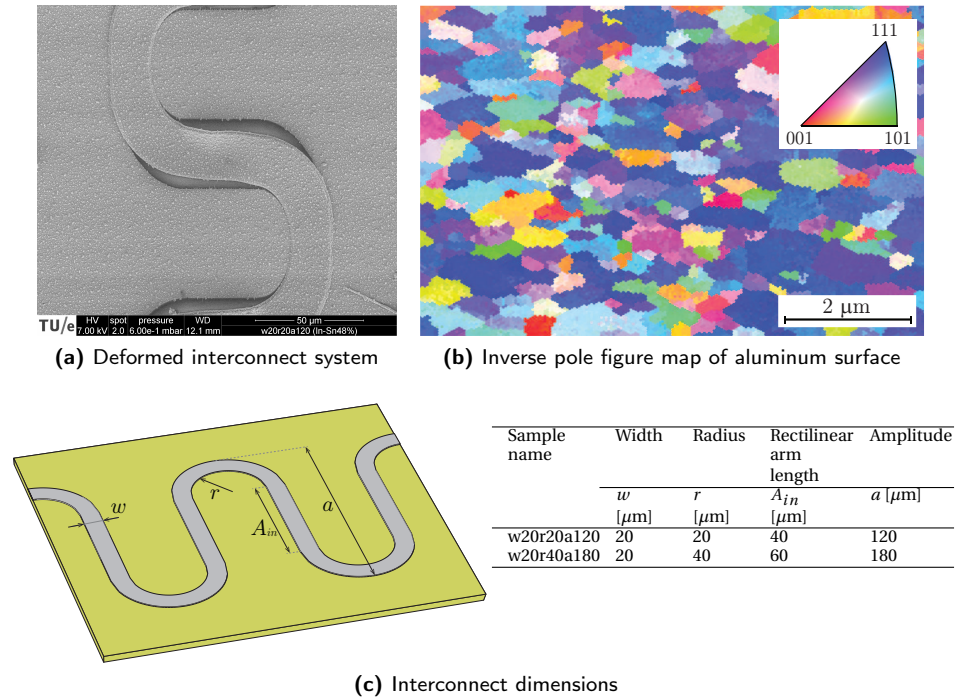
Figure 4.1: (a) SEM image of the deformed specimen (with applied height pattern for DHC on top), in which delamination of the interconnect from the substrate is clearly observed. (b) OIM micrograph of the top surface of the aluminum interconnects, in which grain coloring is conform the inverse pole figure of the specimen's normal. (c) S-shaped interconnect geometry with indicated geometrical parameters: width (w), internal radius (r), amplitude (a), and rectilinear arm length (A_{in}) for the w20r20a120 and w20r40a180 sample.

eliminated by fixating tilt of the positioning stage (using support at the four corner points) to the rigid vibration isolated base of the profilometer, while still allowing translational movements of the micro-tensile stage. Second, a home-developed auto-FOV algorithm was employed to automatically establish the same field of view (FOV) between increments. Thirds, stress relaxation is expected from PI material; preliminary measures showed that equilibrium is achieved within three minutes. On this basis, in order to have reproducible topographic images, acquisitions with confocal laser scanner were taken with a three minutes delay. Fourth, the "confocal smoothing" option in the (proprietary) Sensofar software is used as this was found to slightly increase the reproducibility of the measurements as it seems sensitive to small-scale noise generated by steep features of the pattern. And fifth, before correlation, topographic images were
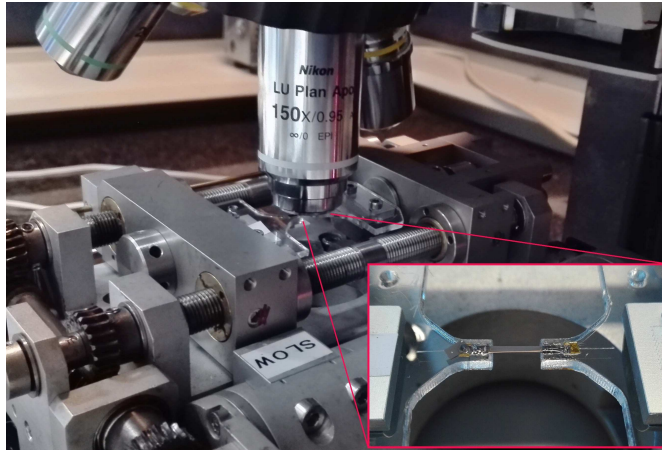
Figure 4.2: In-situ configuration of the tensile stage with sample under the 150X objective of the profilometer. The inset shows a sample glued on disposable PMMA grippers.

blurred using a Gauss filter (kernel size 10 pixels and σ=2), which was shown to improve robustness of the correlation.

4.2.3 Digital Height Correlation

Pattern application

For digital image correlation (or *height* correlation in this case) a distinct speckle pattern is required to distinguish between material points. The stretchable electronics samples considered here exhibit a smooth surface and hence (almost) no natural texture due to surface roughness could be used as a speckle pattern. Therefore, an artificial pattern was applied on the PI-Al samples. In literature a variety of techniques for applying a three-dimensional speckle pattern can be found, such as the application of several types of particles in a solvent, e.g., ink particles, copper or silver nanoparticles [58]. Based on preliminary attempts, neither of these techniques appeared suitable for PI-Al samples, due to agglomeration of the particles at edges of the aluminum interconnect and to the difficulties with obtaining a homogeneous distribution of particles on the interconnect, as well as on the substrate surface. Furthermore, the large difference in reflective properties between the polyimide substrate and the aluminum interconnect are expected to yield complications for the confocal microscopy technique, hence, a pattern that covers the entire surface is desirable. Therefore, we employ a recently developed method, based on DC magnetron sputter deposition of an InSn pattern,

which enables the deposition of a scalable height pattern that can easily be tuned to the particular microscopic technique and to the field of view with pixel size that is employed [59]. For this particular application, a pattern with a relatively large feature size is needed for optimal correlation of surface height profiles measured with optical profilometry. This pattern is achieved with a low chamber pressure of 8 mTorr and substrate temperature of 80°C (note that this is well below the processing temperature of the stretchable interconnect samples to prevent alteration of the interface properties), while the deposition rate was regulated by first using a 20 mA target current for 2 minutes, followed by 60 mA for 7 minutes. Details on this specific pattern and the employed patterning technique in general are provided in [59]. The obtained height pattern shows distinct InSn particles of 0.9 μm, see Figure 4.3. It was also inspected that this pattern does not significantly influence the mechanical behaviour of the stretchable interconnects.

(a) SEM image

(b) Height measurement
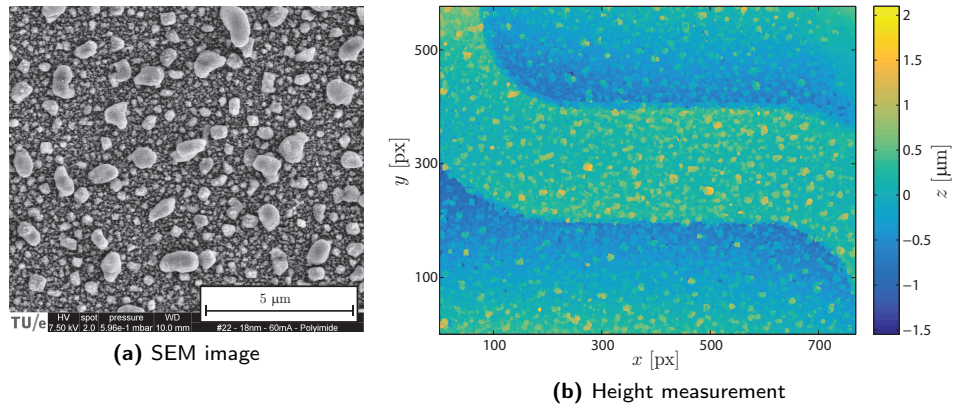
Figure 4.3: The resulting height contrast of the Indium-Tin (InSn) sputter deposition layer: (a) Image taken with scanning electron microscopy (SEM), (b) Surface height profile measured with a confocal optical profilometer (150X objective).

DHC method

To analyze the three-dimensional displacement field of the sample surface during the tensile experiments, digital height correlation is employed. DHC is an extended digital *image* correlation technique, in which height profiles, taken for example using an optical profilometer or an atomic force microscope, are correlated in order to track both the in-plane and out-of-plane displacements of the considered surface [7, 9, 76, 99]. Correlation is based on the minimization of the residual height profile(s) r, which is defined as:

$$r(\underline{x}) = f(\underline{x}) - (g(\underline{x}) \circ \underline{\Phi}(\underline{x}) + U_z(\underline{x})) \approx 0 \qquad (4.1)$$

$$\underline{\Phi}(\underline{x}) = \underline{x} + \underline{U}_{xy}(\underline{x}), \qquad (4.2)$$

with $\underline{x}$ the image coordinates, $f(\underline{x})$ and $g(\underline{x})$ the height profiles in undeformed and deformed configuration respectively, $\underline{U}_{xy}(\underline{x})$ and $U_z(\underline{x})$ the in-plane and out-of-plane displacement components, respectively, and $\underline{\Phi}$ the so-called mapping function that maps the deformed height profile back to the undeformed configuration in order to compare it to the undeformed height profile. The residual approaches zero when the displacements are calculated correctly. However, this is an intrinsically ill-posed problem, since the number of unknowns (i.e., three-dimensional displacements per pixel) exceeds the number of equations (i.e., one scalar residual height value per pixel). Commonly, this is solved by limiting the number of unknowns by means of an approximation of the displacement field with a linear combination of basis functions. It is, however, very important that these basis functions allow for a description which is rich enough to capture the kinematics in the considered problem.

In this case the deformation of the stretchable interconnect entails localized buckling, which calls for a specialized discretization of the displacement field. In this work the DHC approach from [76] is adopted, which makes use of an adaptive refinement scheme to autonomously refine the basis functions locally, thereby attaining an optimal discretization of the displacement field. This is convenient, since the exact location of the buckles is difficult to predict and may differ from experiment to experiment, whereas manual construction of a suitable set of basis functions is challenging and largely requires user expertise on the problem.

4.2.4 Results

The tensile experiment was executed and the topography was measured at several load increments. The resulting height profiles for the load increment of 35% applied global elongation on the edges of the sample are shown in Figure 4.4. Here the localized buckles, i.e., the typical failure mechanism for these geometries, can clearly be seen. In the same Figure also the displacement fields as calculated with the DHC method, both in-plane (u and v) and out-of-plane (w), are depicted. The 3D displacement field is calculated both for the aluminum interconnect and the adjacent polyimide substrate, to account for all deformation modes occurring in the sample, including delamination between the interconnect and substrate.
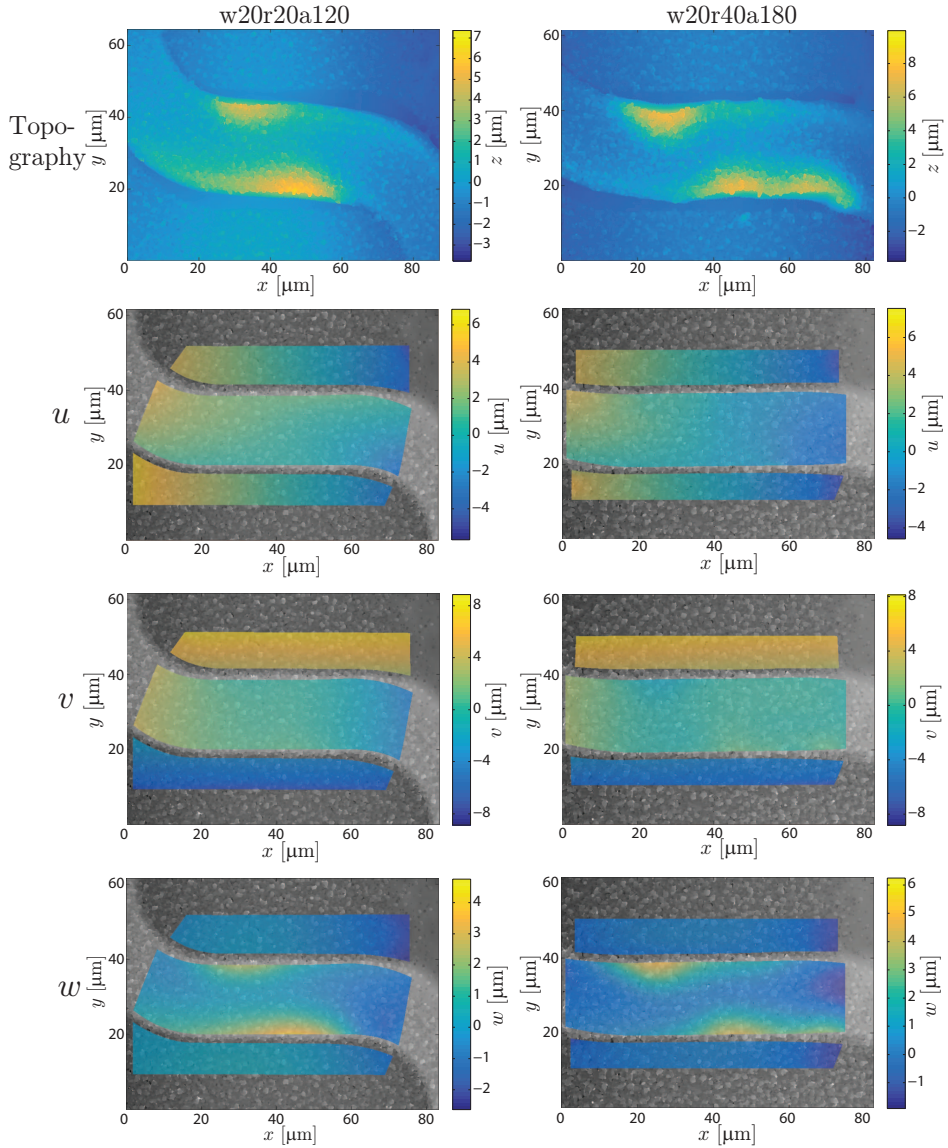
Figure 4.4: Acquired surface height profiles (top) for the w20r20a120 and w20r40a180 geometries, at 35% elongation of the total sample, applied in the y-direction. Furthermore, plotted on top of a grayscale representation of the undeformed topography, the displacements u (in x-direction), v (y-direction) and w (out-of-plane, z-direction), as calculated with the adaptive DHC method, are shown for both geometries. The displacements are calculated for a region of interest both on the aluminum interconnect and on the polyimide substrate.

From the horizontal displacements, i.e., u, it can be derived that both the substrate and the interconnect contract in this direction, due to the Poisson effect upon elongation in the perpendicular y-direction. This Poisson effect is especially strongly present in the substrate, but because the interconnect is adhered to it, contraction is also conveyed, to lesser extent, to the stiffer interconnect.

From the v-displacement mainly rotation of the interconnect towards the direction of elongation can be observed, along with delamination of the interconnect and substrate. The discontinuity in the displacement field between the substrate and the interconnect reveals this delamination. Delamination can also be recognized in the topographic images on top in Figure 4.4, as unpatterned substrate area has been revealed at the edges of the aluminum interconnect, while this area was located underneath the interconnect before deformation (hence, no pattern was deposited here).

The out-of-plane displacement, i.e., w in the bottom of the Figure, clearly shows the buckles in the Al interconnects: the yellow area denotes upward displacement which is discontinuous with respect to the adjacent PI surface. Multiple measurements and displacement field calculations for different samples of the same geometries revealed a significant variation in the exact locations and height of the buckles, caused by stochastic variations in the heterogeneous interface properties [26]. Because the precise interface heterogeneity is unknown for each sample, it is not very meaningful to perform a one-on-one quantitative, absolute comparison between the measured displacement fields and the ones resulting from a numerical simulation. It is more meaningful to analyse several representative scalar indicators for the mechanical behavior of the samples that are extracted from the full-field displacement information. In Figure 4.5 these descriptive parameters are introduced. For the in-plane behavior the contraction δ_U and the rotation ϕ of the rectilinear arm part (line AB in Figure 4.5) are monitored during loading. For the out-of-plane behavior the normal opening δ_n of the interface between the aluminum interconnects and the polyimide substrate is measured.

For both geometries the experiment is performed three times and the results in terms of the scalar parameters are shown in Figures 4.6 and 4.7 for the in-plane (δ_U, ϕ) and out-of-plane (δ_n) behavior respectively. A good repeatability between the individual experiments is observed for the w20r20a120 geometry, while the w20r40a180 sample exhibited a larger scatter in terms of in-plane rotation and normal opening. Especially, the location of the buckles differs significantly from specimen to specimen, as follows from Figures 4.7(d) and (f).

Figures 4.6 and 4.7 show that the delamination between the aluminum interconnects and the polyimide substrate is the most important mechanism occurring during stretching. Delamination occurs when the interface stresses exceed the interface bonding strength. In these particular samples the polyimide substrate is relatively stiff in comparison to other common used substrate materials, e.g., PDMS and TPU. Therefore, the polyimide reacts to the deformation of the stiff metal interconnect with higher stresses
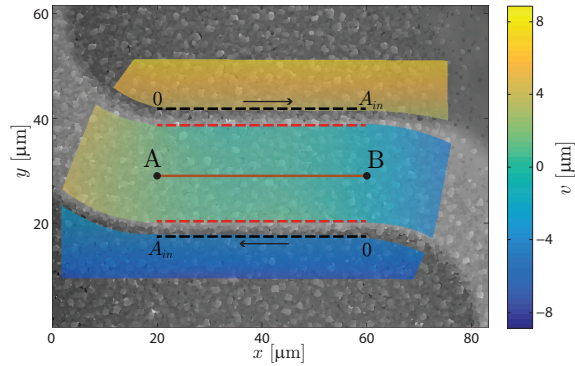
Figure 4.5: Explanatory figure for the descriptive parameters of the mechanical behavior of the electronic interconnect during stretch, that are extracted from the full-field displacement information. The in-plane behavior is characterized by the contraction δ_U and rotation ϕ of the rectilinear arm part AB (orange line). The out-of-plane behavior is described by the normal opening δ_n of the interface, i.e., the buckle height along the path $0 - A_{in}$ (where A_{in} is the rectilinear arm length) at the edge of the aluminum interconnect (red dashed lines), corrected with the substrate curvature, i.e., the height profile of the PI substrate along the same path (black dashed lines).

compared to other, more compliant substrate materials. This induces high stresses on the interface, making this interface more susceptible to delamination.

Comparing Figures 4.6(a) and (b), it is observed that contraction in the rectilinear arm is larger in the w20r40a180 sample, which is to be expected since the rectilinear arm part is longer in this geometry (60 μm vs. 40 μm). According to [89] the rectilinear arm length (A_{in}) has a large influence on the delamination mechanism of the aluminum/polyimide interface. For longer A_{in} ($> 40\mu$m) the lateral contraction of the arm outweighs the axial stretching of the underlying polyimide substrate and the delamination is buckling-based, while for shorter interconnects the axial stretch is relatively large with respect to the lateral compression and the delamination is more shear-based, resulting in a more homogeneous delamination front. Because of this more homogeneous delamination, the interconnect has more freedom to rotate with respect to the substrate, which is indeed observed when comparing Figures 4.6(c) and (d). Also the observation that the buckle locations are less predictable for the longer rectilinear arm lengths (see Figures 4.7(d) and (f)) follows from the fact that the buckling-driven delamination for this geometry is more susceptible to small variations in the heterogeneous interface behavior.

(a) Rectilinear arm contraction δ_U, w20r20a120

(b) Rectilinear arm contraction δ_U, w20r40a180

(c) Rectilinear arm rotation ϕ, w20r20a120

(d) Rectilinear arm rotation ϕ, w20r40a180
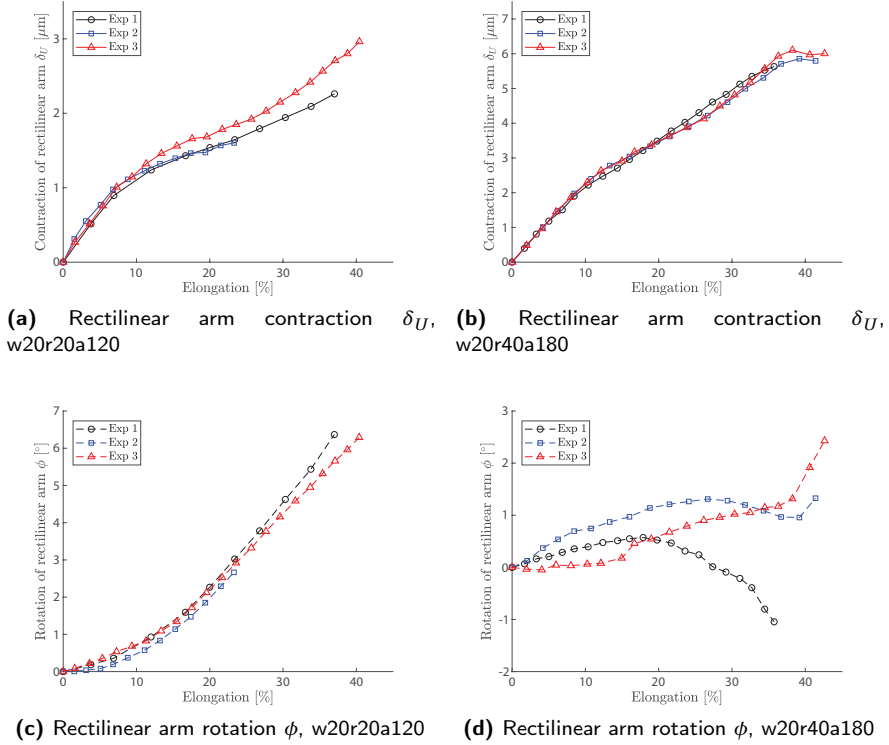
Figure 4.6: The in-plane behavior as characterized by the descriptive parameters δ_U and ϕ (defined in Figure 4.5) for both the w20r20a120 (left) and w20r40a180 (right) geometries. The parameters are plotted for all captured load increments, ranging from 0% to 40% global stretch of the specimen. The data from all three experiments with each sample are shown.

4.3 Numerical simulations

Numerical simulations are a powerful tool to assess the behavior of the stretchable electronics structures for a wide range of interconnect geometries in addition to time-consuming experiments. From numerical results, delamination and buckling phenomena can be studied to predict failure and eventually optimize the design. However, a suitable model for the mechanical response of the materials is required that has to be validated with respect to experimental data of the interconnects.
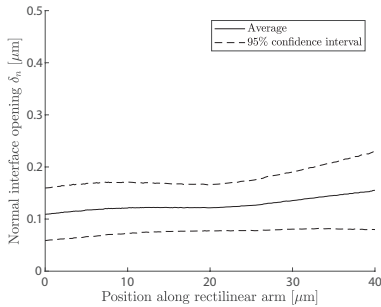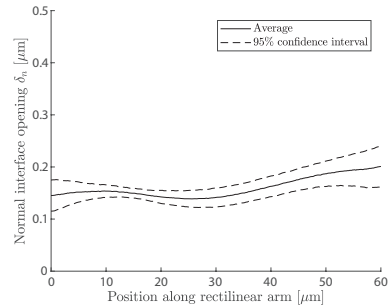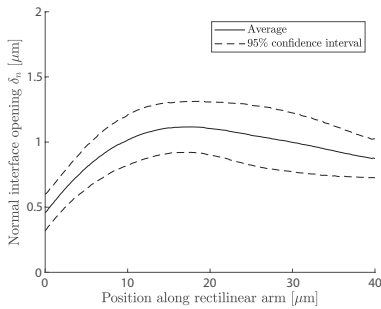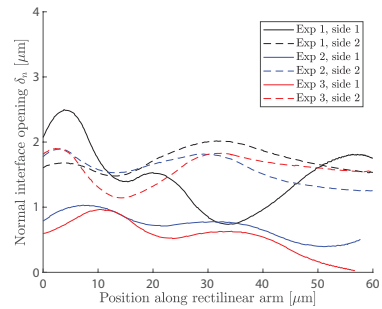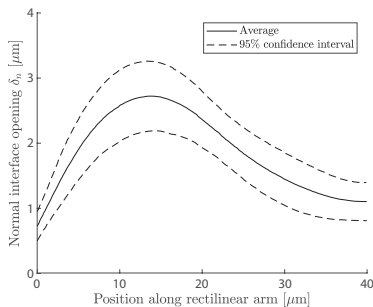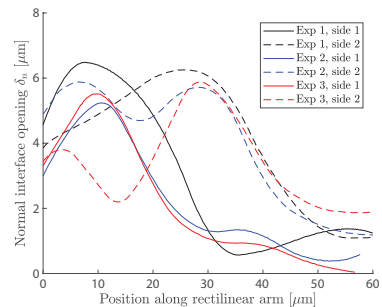
Figure 4.7: The out-of-plane behavior as characterized by the normal opening of the interface (defined in Figure 4.5) for both the w20r20a120 (left) and w20r40a180 (right) geometries. The normal opening δ_n is plotted as profile along the rectilinear arm length for load increments of 7%, 20% and 35% global stretch respectively. In Figures (a), (b), (c) and (e) the profile is shown as an average of the six measurements (two sides for each of the three specimen) with a 95% confidence interval, to illustrate the good agreement between the experiments. For Figures (d) and (f) the profiles from all measurements are shown separately, because the location of the buckles differs too much to make the average value representative.

The three-dimensional finite element model shown in Figure 4.8, developed by [90], is used as a starting point for calibration with the experimental data presented in the previous Section. All finite element models have been developed by using the commercial code ABAQUS[1] model. A submodeling approach is used to increase computational efficiency while maintaining accurate prescription of boundary conditions. In the global part of the model two periods of the interconnect geometry and the underlying substrate, which are assumed to be rigidly bonded, are modeled. Symmetry and periodic boundary conditions are used, see Figure 4.8, and the displacements are prescribed using a reference point.

The material properties are not necessarily the same as for the bulk material because of size effects in the miniaturized microsystem. The yield strength of the aluminum interconnect may be affected, since the relative size of the grains with respect to the specimen dimension increases and, therefore, the number of grain boundaries over the cross-section decreases [68]. Since the grain boundaries act as pinning points for dislocations, a high density of them delays the onset of plasticity, following the well-known Hall-Petch effect. Consequently, the large amount of free surface (and thus the low number of grain boundaries) in these micron-sized structures results in a lower yield strength of the material, with a possible reduction of the yield strength of aluminum to as low as 5 MPa [68]. The material properties of the aluminum interconnect and polyimide substrate were determined previously by means of nano-indentation tests [90], and a good agreement was found with an elasto-plastic material model for both materials, with Young's modulus $E = 72$ GPa, Poisson ratio $\nu = 0.34$ and initial yield strength $\sigma_{y0} = 50$ MPa for the aluminum and $E = 3.2$ GPa, $\nu = 0.3$ and $\sigma_{y0} = 20$ MPa for the polyimide. The grain size distribution was measured using EBSD, see Figure 4.1b, from which it is concluded that the grain size is in the order of 200-600 nm. This implies that a considerable amount of grain boundaries is available, also over the thickness, (i.e., the grains are not columnar), to impede dislocation movement. Hence, the determined initial yield strength of $\sigma_{y0}=50$ MPa, which is slightly lower than the 70 MPa value for bulk material, is not surprising. Moreover, it has been tested (not shown here) that the exact value of aluminum yield strength has only a minor effect on the delamination behavior, i.e., the interface behavior.

The displacement resulting from the FE simulation with this preliminary global model are prescribed at the lateral boundaries of the local model, which is a representation of only half a period of the interconnect featuring a finer mesh. In the local model the behavior of the interface between the substrate and the interconnect is described by a cohesive zone model with a bilinear traction separation law (TSL), in which all dissipative mechanisms of the interface are lumped. The parameters in this model are the maximum traction τ_{max}, the work of separation G_c (also known as fracture energy, interfacial toughness or critical energy release rate) and the critical opening displacement δ_c. The work of separation was determined by [27] using 90° peeltests

---

[1]Dassault Systèmes Simulia©, Providence, RI, US
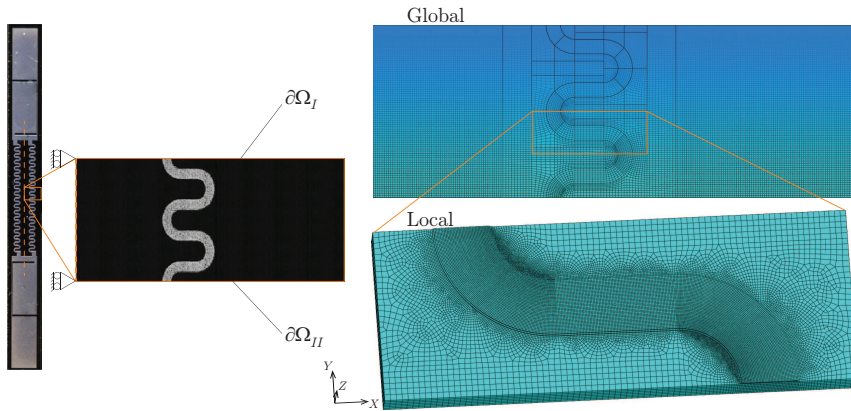
Figure 4.8: Submodeling approach of the finite element model. On the left side a microscopic photograph of an entire specimen is displayed, with a zoom-in on two periods of the aluminum interconnect. On the right side the global model of the same two periods is shown, with the interconnect rigidly bonded to the substrate, which is constructed by using symmetry of the sample (orange dotted line) and periodic boundary conditions on the top and bottom edges $\partial\Omega_I$ and $\partial\Omega_{II}$. The resulting displacements (in x, y and z direction) are prescribed at the lateral boundaries of the local model, which entails half a period of the interconnect, with the interconnect bonded to the substrate with a cohesive zone description.

and was estimated at $G_c = 37$ J/m^2. This value is used in all simulations in this paper.

As previously mentioned, the kinematics of PI is not markedly influenced by the presence of the Al interconnect, owed to the stiffness ratio between Al and PI and the thickness of the metal film compared to the substrate. For this reason, the local boundary conditions applied on the PI boundaries are likely to be reliable even when estimated from a global model with the assumption of perfect bonding between Al and PI.

The optimal values for the other two parameters are studied by performing simulations on the w20r20a120 geometry while varying τ_{max} and δ_c and comparing the results to the corresponding experimental results from the previous Section, see Figure 4.9. It can be seen that the in-plane rotation of the rectilinear arm ϕ can be fitted quite well with a suitable choice of the maximum traction and critical opening displacement ($\tau_{max} = 20$ MPa, $\delta_c = 1$ μm). In contrast, the buckle height is severely underestimated for all investigated combinations. The maximum traction appears to have a larger effect on the behavior, whereas the value for the critical opening displacement is less important. Although the critical opening displacement of 1 μm gives a slightly better fit for the in-plane behavior and the buckle height is not captured well for all combinations, the *location* of the buckle crest seems marginally more accurate for $\delta_c = 0.1$ μm.

The same observations are made for the w20r40a180 geometry (the results are not shown here). Therefore, a key ingredient seems to be missing in the model. In the following Sections potential causes for the underestimation of the normal opening displacement are investigated, i.e., residual stresses in the Al/PI system, crystal plasticity of the aluminum interconnects and mixed-mode interface behavior.

(a) Rotation of rectilinear arm   **(b)** Buckle height
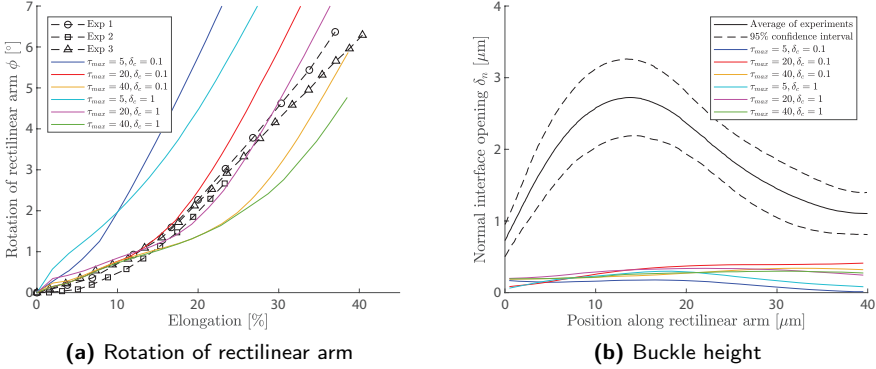
Figure 4.9: Comparison of the (a) in-plane rectilinear arm rotation and (b) the out-of-plane buckling height at 35% globally applied elongation between experiments (data from Figures 4.6c and 4.7e) and numerical simulations using a bilinear TSL. The legend shows the interface properties used for the different simulations, with τ_{max} in MPa and δ_c in μm.

4.3.1 Residual stress

The first effect that is not taken into account in the initial simulations is residual stress. Since the FE model underestimates the opening due to the absence of Al buckling, introducing a compressive residual stress in the Al layer may increase the chance to observe Al buckling in FE analysis, which may testify that residual stresses were the missing ingredient in the numerical analysis. Residual stress in miniaturized systems contributes to the reliability and has been reported as a possible primary source of failure for microelectronic systems [50]. Residual stress in the Al/PI stretchable electronic system can occur due to the curing process of polyimide and the deposition of the aluminum interconnect layer. During the curing cycle of polyimide intrinsic residual stresses are introduced in the substrate. Residual stresses ranging between 4 to 40 MPa were reported for a 10 μm thick PI layer depending on the temperature cycle of the curing process [32]. In addition, thin film deposition of the metal layer causes compressive residual stresses in the aluminum film due to mismatch in the coefficient of thermal expansion (CTE) [143]. When the Al/PI interconnect system is lifted off the silicon wafer in the final processing stage, the residual stress in the PI substrate and Al

film result in a curvature due to the equilibration of the stress state.

The residual stress is added to the local numerical model by lumping the intrinsic and thermal residual stress into a single thermal residual stress introduced in the Al/PI system prior to elongation. This thermal stress is induced in the model by a thermal step while the boundaries of the local model are confined, mimicking that the stretchable interconnect system is still bonded on the silicon wafer. The magnitude of that theoretical thermal step is determined by the measurement of the curvature of a 10 μm thick PI substrate, fully coated with a 1 μm thick deposited Al layer.

The reason for performing this curvature measurement on the fully coated sample is as follows. When fabricated together, fully coated and patterned Al/PI samples will exhibit a difference residual curvature for the same driver of misfit, i.e. the thermal load. Yet, the analytical curvature analysis [42] only holds for flat films on substrates. Therefore, instead of measuring the residual curvature directly from the Al/PI pattern, the residual curvature is measured for a fully coated Al/PI sample and used to estimate an equivalent thermal load as a driver of misfit. Subsequently the same thermal load has been introduced in the Al/PI local model to test its influence on the kinematics of the interconnect.

To estimate the eligible thermal load for simulating residual stresses in the patterned interconnect, the topography of a fully coated Al/PI sample has been measured right after lift off from the carrier Si wafer, yielding a curvature of $\kappa = -5.2 \cdot 10^{-4} \mu\text{m}^{-1}$. The thermal load required to achieve the measured curvature has been estimated following [42], obtaining $\Delta T = -450$ K. The consistency of the analytical estimate has been verified by means of a 2D plane strain FE analysis of a Al/PI bilayer upon thermal load, yielding the same curvature within the uncertainty bound. The same thermal load was used to induce a residual stress field in the local model of the Al/PI interconnect right before stretching.

More precisely, the numerical simulation of the stretchable interconnect is executed as described earlier, with the traction separation law parameters that gave the best fit for the in-plane behavior, i.e., $G_c = 37$ J/m^2, $\tau_{max} = 20$ MPa, $\delta_c = 1$ μm, and with the thermal step of -450 K prior to elongation. Figure 4.10 shows a comparison of FE analysis results with and without residual stresses, using the interface parameters best matching the in-plane experimental descriptors. The stress is concentrated at the transitions between the rectilinear arm and inner radius of the curvilinear segments (see inset in Figure 4.10b) and exceeds the yield strength of the aluminum interconnect, resulting in local plastic deformation in this area. However, upon stretching of the interconnect system the induced plasticity seems to have a negligible effect on the delamination and buckling behavior, and as a result the normal opening remains severely underestimated. Therefore, it is concluded that thermal stress (although its magnitude could not be explicitly estimated for the specific structure) may not play a relevant role in determining the mode I opening of the buckled film owed to the resilience of the aluminum, i.e. its

capability to accommodate the misfit through plastic strain.

(a) Reference simulation, $\Delta T = 0$ K   **(b)** Residual stress included, $\Delta T = -450$ K
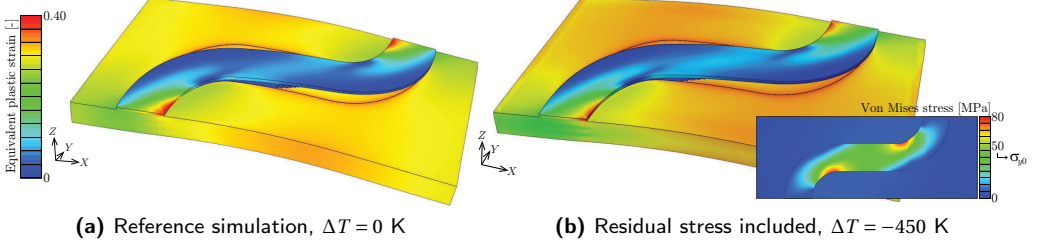
Figure 4.10: FEM results (equivalent plastic strain) for the local model of the w20r20a120 geometry with the reference model (a) and the model where a thermal pre-step of -450 K is included to account residual stress (b). In the inset in (b) the Von Mises stresses resulting from the thermal pre-step are shown.

4.3.2   Mixed mode interface behavior

Finally, the effect of a mixed-mode cohesive zone model on the interconnect deformations is studied. When studying the tractions on the interface just before the onset of delamination in more detail, it becomes apparent that the normal tractions are a factor 4 lower than the tractions in shear mode. This results in pure shear delamination, which induces rotation of the rectilinear arm, accompanied by slight out-of-plane twisting of the curvilinear part, however, no extensive out-of-plane deformation of the rectilinear arm. Therefore, to capture the experimentally observed large buckling behavior of the interconnects, it appears to be necessary to promote mode I delamination over mode II delamination, by imposing different properties of the traction separation law in shear mode and normal mode.

In this mixed-mode interface model the traction separation laws are defined by means of the work of separation G_c, maximum traction τ_{max} and critical opening displacement δ_c, which are defined separately for both modes. Shear behavior is modeled isotropically, the damage criterion is based on maximum stress and damage evolution is based on the energy that is dissipated during the damage process (the fracture energy). The effective critical energy scales linearly between the pure normal and pure shear thresholds, as a function of mode mixity. The latter is measured as the relative contribution of the current pure shear mode (G^s) to the current total energy ($G^T = G^s + G^n$). More details can be found in [36]. In this work, δ_c is assumed to be mode-angle independent and taken 0.05 μm, because some preparatory research with the mixed-mode framework revealed that $\delta_c = 0.05$ μm gives slightly better results in terms of the out-of-plane deformation than $\delta_c = 1$ μm and $\delta_c = 0.1$ μm, which were studied earlier, although it was found again that the value of δ_c only has a minor influence on the delamination

and buckling behavior. As mentioned above, the work of separation in mode I, G_c^n, was determined by 90° peeltests by [27] and established 37 J/m^2, equal to the value used in the previous simulations. For the remaining parameters, G_c^s, τ_{max}^n and τ_{max}^s, no data is available and their effect is studied.

First, the mode I maximum traction of the cohesive zones is lowered with respect to the mode II maximum traction and different ratios and values for τ_{max}^n and τ_{max}^s are tested, see Figures 4.11a and 4.11b. The buckling amplitude is strongly affected positively by a higher ratio of $\tau_{max}^s / \tau_{max}^n$ and the location of the crest shifts more towards the transition from the rectilinear arm to the inner radius of the curvilinear segment, leading to a better agreement with the experimental data. The reason for the shift in crest location is that, with increasing maximum shear traction, delamination is delayed, causing the curvilinear parts of the interconnects to straighten to accommodate stretching of the sample (whereas rotation of the rectilinear arm towards the stretching direction is hindered by interface which is not sufficiently debonded), resulting in compressive stresses in the rectilinear part near the transition region to the inner radius, triggering delamination at this location. For decreasing normal maximum traction, the possibility to delaminate in mode I increases in this region, resulting in the observed behavior of Figure 4.11b.

Not only the ratio, but also the absolute value of the maximum traction is important. For lower absolute values of τ_{max}^s mode II delamination at the outer radius of the curvilinear segments is still energetically more favorable and a lower buckling amplitude is observed, see the difference between $\tau_{max}^s / \tau_{max}^n = 20/4$ and $\tau_{max}^s / \tau_{max}^n = 30/6$, which have the same ratio, but different absolute values. More and earlier mode I delamination in the rectilinear arm also reflected in the decrease of rotation of this part, see Figure 4.11a, which is especially noticeable for an extremely high shear maximum traction versus low normal maximum traction ($\tau_{max}^s / \tau_{max}^n = 40/5$).

Next, the work of separation in shear mode, G_c^s, is studied. The best fit from the previous experiment, i.e., $\tau_{max}^s = 30$ MPa, $\tau_{max}^n = 6$ MPa, is selected for these new simulations. The resulting rectilinear arm rotation and buckle profiles are shown in Figures 4.11c and 4.11d. An increase in G_c^s (for a fixed τ_{max}^s) means a retardation of final failure in shear mode. Consequently, failure in normal mode is promoted, which results again in higher buckling amplitudes and less rotation of the rectilinear arm. For the tested values of G_c^s, $G_c^s = 111$ J/m^2 seems to yield the best quantitative agreement between the simulation and the experiments in terms of both the in-plane and out-of-plane displacements. A value of G_c^s that is three times higher than G_c^n seems well possible, as such a ratio has been observed frequently in the literature, e.g., [66, 124].

(a) Rectilinear arm rotation, $G_c^s = G_c^n = 37$ J/m^2

(b) Buckle height, $G_c^s = G_c^n = 37$ J/m^2

(c) Rectilinear arm rotation, $\tau_{max}^s/\tau_{max}^n = 30/6$

(d) Buckle height, $\tau_{max}^s/\tau_{max}^n = 30/6$
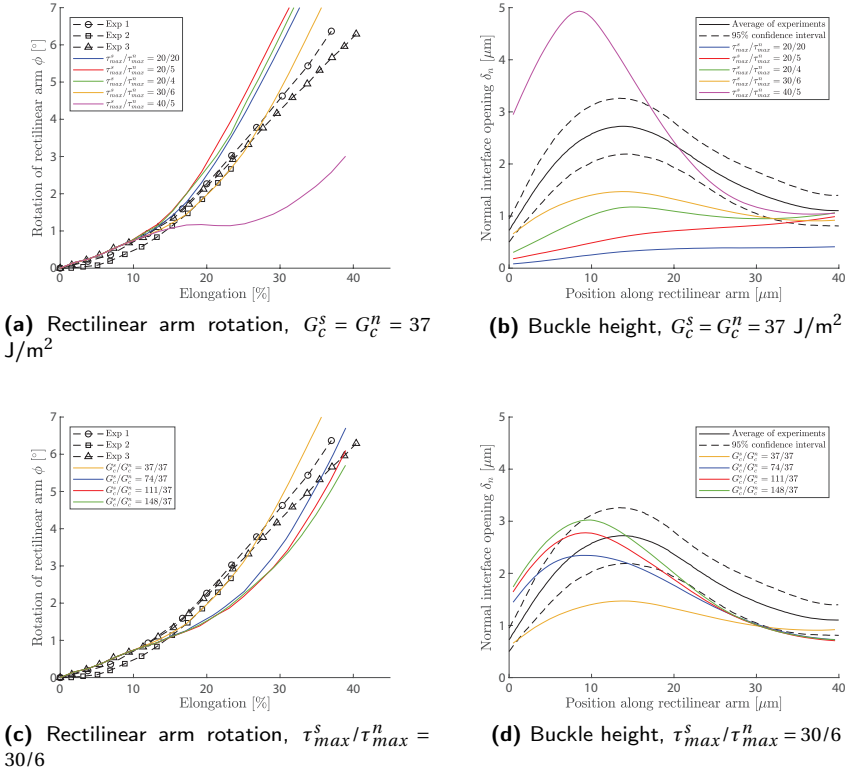
Figure 4.11: Comparison of the (a&c) in-plane rectilinear arm rotation and (b&d) the out-of-plane buckling height at 35% globally applied elongation between experiments (data from Figures 4.6c and 4.7e) and numerical simulations with different ratios of the traction separation law properties. In the first set of simulations (a-b) the work of separations is kept equal for both modes and the maximum traction are varied. In the second set (c-d) the best fit for the tractions ($\tau_{max}^s/\tau_{max}^n = 30/6$) is used, while the mode II work of separation G_c^s is varied.

In summary, a good match with the experiments is found for simulation with a mixed-mode cohesive zone model, with the parameters as listed in Table 4.1. The resulting geometry from the FEM simulation is shown in Figure 4.12a, where is it compared to the experimentally measured height profile. Also, a predictive simulation is performed with the same interface parameters, but for the w20r40a180 geometry, see Figure 4.12b. In both cases a good qualitative agreement between the simulation and experiment is achieved, i.e., the buckle amplitude, location and number of crests are highly comparable.

Table 4.1: List of the mixed-mode traction separation law parameters used in the cohesive zone model that best fits the experimental data.

Parameter		Normal direction (mode I)	Shear direction (mode II)
Work of separation	G_c	37 J/m^2	111 J/m^2
Maximum traction	τ_{max}	6 MPa	30 MPa
Critical opening displacement	δ_c	0.05 μm	0.05 μm

It should be noted that the selected values for the interface properties provide a good, but not perfect fit. Qualitatively, the main cause for the observed deformation behavior was found to be a difference in interface properties between normal and shear direction, i.e., the presence of mixed-mode behavior. Quantitatively, however, the simulations do not exactly equate the observed deformation. Yet, it does not appear to be useful to improve the model further, since the variability in experimental results is relatively high. A perfect fit for one particular experiment would yield a poor prediction for another experiment with the same parameters. Moreover, the goal of this work was not to find a perfect numerical model, but to reveal the underlying cause for the observed buckling behavior in order to gain insight in the failure mechanism of these stretchable interconnects.

(a) w20r20a120   **(b)** w20r40a180
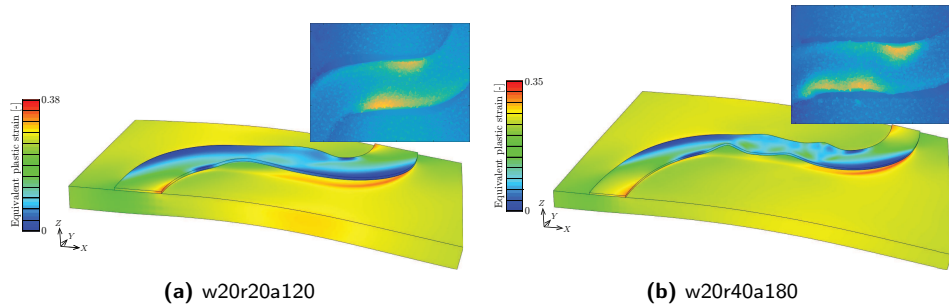
Figure 4.12: FEM results (deformed geometry and equivalent plastic strain) with the mixed-mode cohesive zone model for both geometries. For comparison, the insets show the topographic height profile measurements from the experiments at the same global stretch increment.

The mode sensitivity found in this study may be explained by the absence of fibrillation during interface delamination. In [102] it was found that mode sensitivity is negligible in the considered PDMS-copper interface, because of the complex geometry of the rough copper surface and consequently the alignment of the fibrils with the traction

direction. In case of the here examined polyimide-aluminum system, the aluminum has a relatively smooth surface, as observed by a homogeneous peelfront in mode I peeltests [25]. This may explain the observed much higher mode angle dependency, caused by significant energy dissipation by friction under shear loading, resulting in the experimentally measured deformation profiles.

4.4   Conclusions

Delamination and buckling phenomena, which are known to affect the reliability of stretchable electrical interconnect structures, have been studied by the use of in-plane and out-of-plane descriptors of the deformed geometry of two interconnect geometries upon tensile stretching. This data was obtained by the acquisition of surface height profiles upon stretch using confocal optical profilometry for an in-situ experimental setup. These height profiles were then correlated using adaptive isogeometric digital height correlation to obtain three-dimensional displacement fields of the surface of the aluminum-polyimide interconnect structure.

From the derived three-dimensional displacement fields it was shown that delamination initiates at approximately 7% global elongation for both sample types. A sufficiently large delaminated area under the rectilinear arm is accompanied by a significant rotation of the rectilinear arm which was observed at 18% global elongation for the w20r20a120 geometry and at global strain levels beyond 35% for the w20r40a180 interconnect geometry. In addition, approximately semicircular buckles nucleate along the rectilinear arm at roughly 15%-18% global elongation as a result of lateral compression of the delaminated Al film at the rectilinear arm. This can be attributed to the Poisson compression of the substrate and by a localized region of compression at the transition between rectilinear arm and inner bend of the curvilinear segment. Moreover, the buckling amplitude and pattern were shown to differ between the sample types, which is assigned to the difference of the rectilinear arm length A_{in}.

A numerical model was developed to capture the in-plane and out-of-plane behavior of the stretchable interconnect upon elongation. It was demonstrated that a simple bilinear traction-separation law without mode dependency is insufficient to capture the characteristic buckling behavior of the Al-PI interconnects. Moreover, implementation of residual stress and the effect of a free surface size effect, by lowering the yield strength of aluminum were all shown to be insufficient to capture the experimentally observed behavior of the stretchable interconnects. However, a fair qualitative agreement of the in-plane and out-of-plane behavior of the interconnect has been reached by adopting a mixed-mode cohesive zone model. Characteristic buckling behavior is captured by the numerical model only when the ratio between shear and normal maximum traction is substantially increased. A $\tau_{max}^{s}/\tau_{max}^{n}$ ratio of 30 MPa to 6 MPa and work of separation

of G_c^n=37 J/m^2 and G_c^s=111 J/m^2 seems to yield the best fit of in-plane and out-of-plane deformations of the interconnect of the w20r20a120 geometry to the experiments. Also a predictive simulation with the same parameters for the w20r40a180 geometry yields a good qualitative agreement with the experimental data.

The mode angle dependency may be caused by the low surface roughness of the metal film and the consequential absence of fibrillation. The results of this study could, e.g., be used to improve the processing of the interconnect system, such that the interface toughness in normal direction increases and the mode sensitivity is lowered, which could be realized by manufacturing a fibrillating interface. This would lead to a promotion of shear delamination, causing more rotation of the rectilinear arms with respect to the substrate. Consequently, the high stress concentrations and plastic strains found at the inner bend of the curvilinear parts could be lowered, which improves the durability of the interconnects. That makes this an interesting region for further analysis for a possible optimization of the interconnect design for delayed failure and higher stretchability.

Acknowledgements

Part II

Advancement of Integrated Digital Image Correlation

Chapter 5
Parameter identification of freestanding stretchable electronic interconnects using Integrated Digital Height Correlation

Abstract

For the development of reliable stretchable electronic systems, it is essential to comprehend and predict their mechanical behavior. As stretchable interconnect structures usually have micron- or even nanoscale dimensions, the mechanical behavior is affected by size effects and processing history. It is therefore important to test and analyze original as-processed samples, as opposed to standard tests on bulk material. Dedicated analysis methods are necessary for obtaining the material properties from the tests, as complex three-dimensional deformations complicate the use of existing methods. This paper presents an Integrated Digital Height Correlation (IDHC) method for the mechanical characterization of a recently developed ultra-stretchable freestanding interconnect. Height maps from an out-of-plane loading experiment are correlated to a numerical model, with the aim to identify the material parameters in the plastic regime. The boundary conditions for this model are obtained by applying a global Digital Height Correlation algorithm on the images in order to obtain the three-dimensional displacements of the specimen's clamping pads. The IDHC method is tested on a virtual test case, where it is shown that the algorithm converges to an accurate (error in the order 10^{-3}) solution for the considered set of three plasticity parameters. For the real experiment, simultaneous correlation of all three parameters is not possible due to

an inherently flat residual landscape with many local minima. However, the initial yield strength and hardening exponent were still identified and estimated at 225-300 MPa and 0.15-0.2 respectively. Despite the moderate accuracy of the identification, the potency of the IDHC method for this extremely challenging case of micron-sized delicate freestanding stretchable electronic interconnects is demonstrated.

5.1   Introduction

Stretchable electronics is an emerging field of research, with applications mainly in the biomedical field, used to integrate traditionally rigid electronics with soft biological tissue [80, 142, 159]. In order to develop reliable systems that are safe to use in this biological environment, it is important to characterize the mechanical behavior of the stretchable electronics. Miniaturization of the stretchable electronics leads to size effects, which restricts assessing the material behavior a priori [49, 82, 152]. Moreover, the processing history might affect the material properties, as well as the loading conditions triggering different deformation modes [45]. Therefore, it is essential to perform tests on original as-processed samples of the interconnects in order to characterize their mechanical behavior with all these effects incorporated.

Recently, a freestanding ultra-stretchable interconnect, also called the ROPE (Rotation Out-of-Plane Elongation) interconnect, was developed, see Figure 5.1, which exploits full three-dimensional freedom up to a reversible stretchability of about 2000% [132]. A strong strengthening effect was observed; i.e., by roughly comparing experimental results to numerical simulations, using a standard elasto-plasticity model, a yield strength of roughly ten times higher than the value for bulk aluminum (from which the interconnect is fabricated) was estimated. This observation is important for the stretching behavior of these interconnects and also interesting from a scientific point of view. The objective of this paper is therefore to quantitatively determine the plastic behavior of these interconnects.

The interconnects are designed to be highly compliant, which makes it difficult to employ a (uniaxial) tensile experiment to determine the material properties, as the forces are too low to be measured in a sufficiently accurate manner. Alternatively, a full-field method such as Digital Image Correlation (DIC) may be used to characterize the kinematics of the structure. If an integrated approach is used, i.e., the correlation is complemented by a numerical model, the parameters in this model may be obtained directly [56, 100, 115]. However, these techniques generally require in-plane displacements only, while the considered interconnects deform out-of-plane as well, see Figure 5.1b. In the literature also quasi-3D DIC, or Digital Height Correlation (DHC) methods are described, which require height maps as input images. They are therefore able to track both the in-plane and out-of-plane surface displacements of the considered
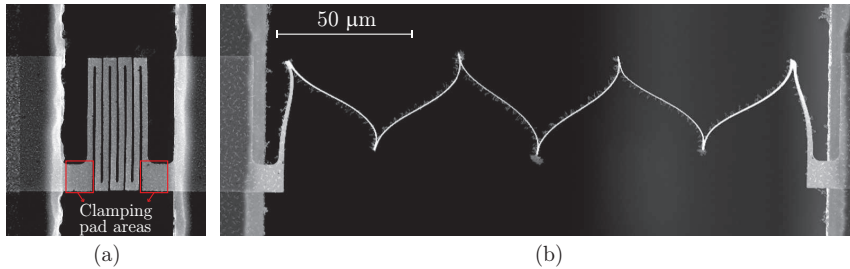
Figure 5.1: ((a) The freestanding ultra-stretchable ROPE interconnect design, consisting of a number of rectangular beams. (b) The interconnect in stretched state; beam members rotate out-of-plane and bend to align with and elongate along the stretch direction.

specimen [9, 10, 52, 76, 99, 133]. In this paper, an Integrated Digital Height Correlation (IDHC) method is proposed to directly identify the plastic material parameters from an experiment on freestanding ultra-stretchable interconnects.

The IDHC method requires that the surface of interest stays in view during the experiment. Hence, it is not possible to load the structure by in-plane stretching as done in [132], because the beam members of the interconnect rotate out-of-view to align with the stretch direction, see Figure 5.1b. Although the outer beam members twist to accommodate rotation of the other beams, the majority of the beams deform in pure bending mode after rotation. This mode can also be triggered by loading the interconnect in the out-of-plane direction, while the beam surfaces stay in view [134].

For integrated methods it is essential that the numerical model mirrors the experiment as close as possible. Especially the boundary conditions are influential [119, 123]. Moreover, in the particular case of miniature freestanding stretchable interconnects, also the initial geometry, which is curved due to residual stresses from manufacturing, requires special attention. The initial geometry will be extracted from the measured height map in the reference configuration. Furthermore, a global DHC method will be used to extract the displacements of the clamping pad areas, see Figure 5.1a, which will then be translated to the model as boundary conditions.

The paper is organized as follows: First the methodology is explained in Section 5.2, which consists of the experimental details, discussion of the integrated digital height correlation algorithm and some aspects of the finite element (FE) model. In Section 5.3, the analysis of the experiment is presented. First a DHC algorithm is employed for preliminary analysis of the boundary conditions for the FE model, after which the IDHC algorithm is tested by means of a virtual experiment. Subsequently, the IDHC algorithm is applied to the experimental data. Finally, conclusions are drawn in Section 5.4.

5.2   Methodology

In this Section the methodology for the analysis of the freestanding stretchable interconnects is explained.

5.2.1   Experiment

In order to identify the mechanical properties of the freestanding stretchable electronic interconnects an experiment is performed in which one of the main deformation modes of these structures is triggered: bending of the interconnect beams. The specimen has a planar design of slender, rectangular beams; the interconnect in this experiment consists of ten beams. The interconnect is embedded in a specially designed chip that allows for meticulous handling of the sensitive samples [132]. To be able to perform a DIC analysis on the samples, a distinct pattern needs to be present. In this case pattern application is complicated, as it is not possible to apply many techniques known from literature [37, 59, 130]. Indeed, pattern application using a fluid or plasma is prohibited, because even small forces resulting from contact with a fluid or charging due to plasma lead to plastic deformation of the highly delicate samples or stiction of the interconnect beams to each other or the substrate. The only possibility for pattern application is a flow of dry particles that individually attach to the interconnect. This was realized by applying silica nano-particles (300 nm) on the interconnect by means of a dried micro-mist application technique. Yet, only a sparse pattern could be accomplished due to the highly delicate nature of the freestanding interconnects [134].

A lab-built dedicated tensile stage for the micron-sized samples is used to load the interconnect structure. The specimen is loaded in the out-of-plane direction, by moving the clamping pads on either side of the interconnect by a prescribed displacement. After loading, the specimen is unloaded again, i.e., the clamping pads are returned to their original position. This proces is repeated, while the displacement-controlled load increases incrementally.

Topographical images are captured during the experiment by means of a confocal optical microscope (Sensofar S Neox, 100× magnification lens with a numerical aperture of 0.9 and working distance 1 mm). In the loaded situation the beams are bend to a steep angle with respect to the microscope, which makes it impossible to capture the height map with the profilometer, see the image marked "topographies extended state" in Figure 5.3. Therefore, the experiment is designed such that images are taken in the unloaded configuration after each loading step, see Figure 5.2. This is a justified approach, since the objective of the experiment is to identify the material properties that represent the plastic regime, and plastic deformation will also be reflected in the unloaded state, as clearly observed in Figures 5.2c and 5.2d. The complete experimental

procedure is described in more detail in [134].

(a) f **(b)** g increment 5 **(c)** g increment 12 **(d)** g increment 13
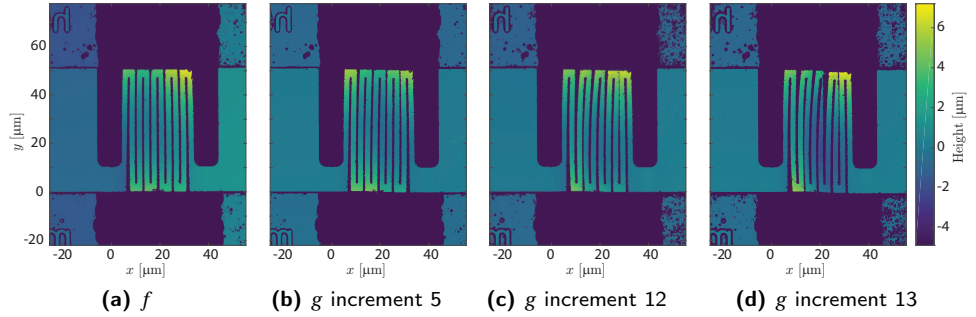
Figure 5.2: Height maps captured during the experiment for a selection of loading increments. The reference image, f, of the undeformed configuration is shown, along with three deformed images g, each obtained after a number of incremental loading-unloading cycles (named here increments).

5.2.2 Integrated Digital Height Correlation

An Integrated Digital Height Correlation (IDHC) algorithm is used to analyse the material properties of the stretchable electronic interconnects. This is an extension of Integrated Digital Image Correlation (IDIC), where the correlation of the images is combined with Finite Element (FE) simulations [56, 100, 115], see Figure 5.3. The calculated displacements following the FE simulation are used to back-deform the images of the deformed sample, in order to get an optimal match with the reference image of the specimen in undeformed configuration. The difference between the images, i.e., the residual, is minimized iteratively. The parameters in the FE model are the degrees of freedom (DoFs) in the correlation, therefore usually this approach is employed if the objective of the experiment is to identify material properties. In the *height* correlation method the images are not grayscale images of the specimen, but topographic height profiles of the sample's surface [10, 76]. Hence, not only the in-plane displacement is tracked, but simultaneously also the out-of-plane deformation is included in the correlation.

In DIC algorithms usually a region of interest (ROI) is selected in the reference image, such that the pattern features in the selected region do not move out of view in the deformed images and to make sure nodal displacements from the FE simulation are available in the entire region of interest. In this case the region of interest is not a rectangular area, but it is based on the shape of the interconnect, as defined in the finite element model. Furthermore, the measured height data contains many not-a-number (NaN) values, especially around the edges of the structure, since the profilometer does
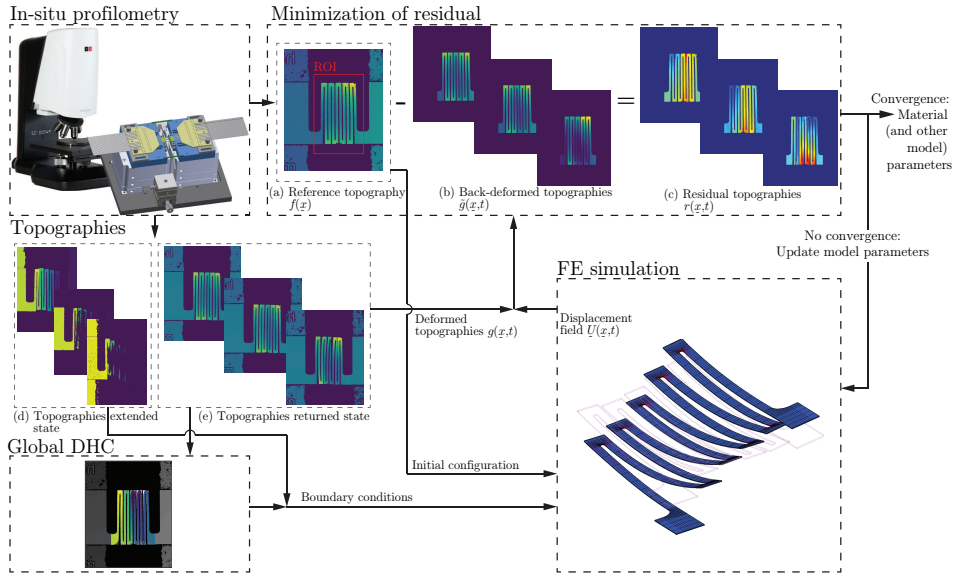
Figure 5.3: Schematic illustration of the Integrated Digital Height Correlation method: The core of the algorithm is the minimization of the residual (c), which is a measure for the optimality of the parameters of the FE model. The topographies captured during the experiment ((a), (d) and (e)) are not only used for the correlation itself, but also to determine boundary conditions required for the FE model. The dynamic range of topographies (a), (b) and (e) is ~-5 to 7 μm. The dynamic range for the first and last topography in (d) is respectively ~[-30 40] and [-100 120]μm.

not measure the heights at steep gradients or edges. These values proliferate during the interpolation step, which is required to determine the back-deformed images [103], and destructively influence the correlation. Therefore, a mask is defined to discard the pixels containing NaN values, both in the reference topography and the back-deformed topographies. This mask is reset and updated adaptively during the iterations to prevent an unnecessary high number of discarded pixels.

5.2.3 Finite Element Model

For IDHC a numerical model is required that represents the experiment. It is therefore important that the model resembles the physical reality as close as possible [123]. To this end, the stretchable interconnect structure with ten beams is modeled conforming the geometry of the design supplied to the manufacturer of the samples. Slight deviations from the design in the real samples, e.g., slightly round finishes of the corners, are

disregarded, but this is justified as they fall outside the region of interest for correlation, since the height measurements at the edges of the sample are not reliable.

One of the main challenges in the model is to obtain the exact reference configuration of the experiment, in which the beams are curved due to residual stresses from processing. To this end, the straight modeled mesh is overlayed on the topographic image of the reference situation and for each node the measured height at its location is translated to this node. However, because of measurement noise (and pattern features), this would result in a non-smooth surface that would unrealistically influence the kinematics in the simulation. To smoothen the curved surface, a regression is made through the measured data, see Figure 5.4, where a second-order polynomial is used along the length of the beams and a first-order polynomial in the width direction. The hinges and clamping areas are smoothed separately, using constraints to connect them appropriately to the beams, ensuring C^1 continuity across the connecting lines.
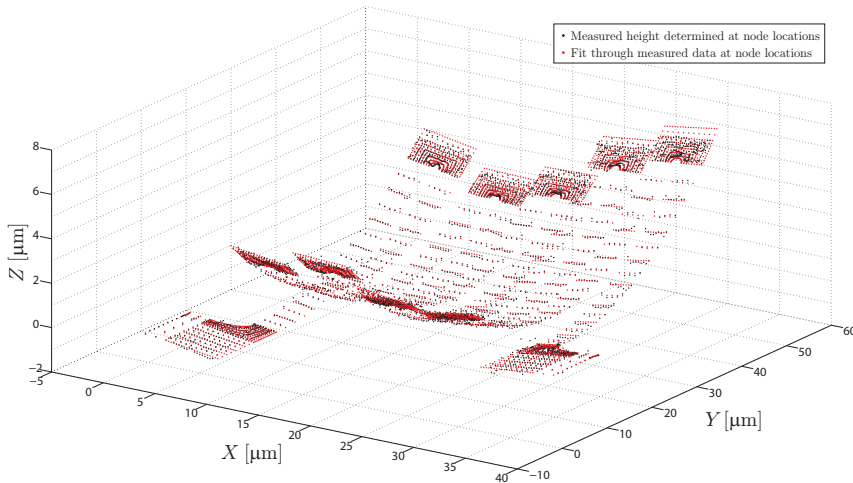
Figure 5.4: Three-dimensional locations of the nodes of the FE model, based on the measured height data (black dots) and a regression through this data (red dots) to smoothen the surface from measurement artifacts. (Note that the axes are not equal for visualization purposes.)

Also the in-plane alignment of the reference configuration, and particularly the lateral bending of the four most right beams, needs to be accounted for in the FE model. This lateral bending is also attributed to the residual stress. As no images of the unwarped interconnect (before chemical etching of the sacrificial layer to release the interconnects) are available, which could be correlated by a DHC method to the topography of the warped interconnect in order to determine the exact in- and out-of-plane deformations due to the residual stresses, the in-plane displacement (from a perfectly straight configuration to the measured situation) can now only be determined manually. This is

done at the corners of the hinges and prescribed in the simulation. The resulting initial configuration, see Figure 5.5, is assumed to be stress-free, because the curved shape is precisely the result of the fact that the freestanding structure can almost completely relax the residual stresses that were acting on it.
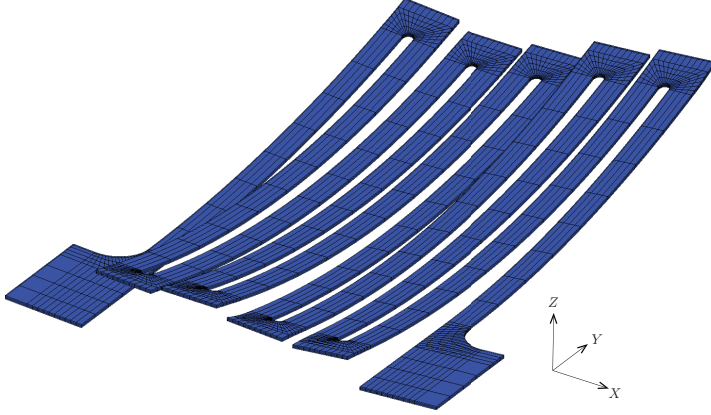
Figure 5.5: FE model of the stretchable interconnect geometry with 10 beams, in the curved initial configuration.

The material model used in the simulation is elasto-plastic, where Hooke's law for elasticity is used and the Von Mises yield criterion [44], with a rate power law model for (isotropic) hardening:

$$\sigma_y = \sigma_{y0} + A\bar{\varepsilon}_p^m, \tag{5.1}$$

where σ_y is the evolving yield stress, $\bar{\varepsilon}_p$ is the equivalent plastic strain, σ_{y0} the initial yield strength, A a hardening coefficient and m the hardening exponent. The latter three are unknown parameters and hence the objective for the identification using the IDHC method. Especially the initial yield strength is interesting to investigate, as it was found by [132] to be influenced drastically by size effects due to the small dimensions and processing conditions (up to ten times its value for the corresponding bulk material).

The boundary conditions in the model are also an important input that need to be in close agreement with the experimental conditions. During the experiment, topographies are measured in both the extended and returned state for all increments. The topographies in the extended state are not useful for correlation, because of the large inaccuracies in the measured height values in the presence of high gradients, see Figure 5.3. The pads, however, are an almost flat area on which the height values are reliable

and therefore used to define the boundary conditions in the extended state. For the boundary conditions in the returned state, the global DHC algorithm from [76] is used to recover the displacement fields from the measured height profiles. The resulting three-dimensional displacements of the pad areas, see Section 5.3.1, are translated to boundary conditions on the nodes of the pads in the model.
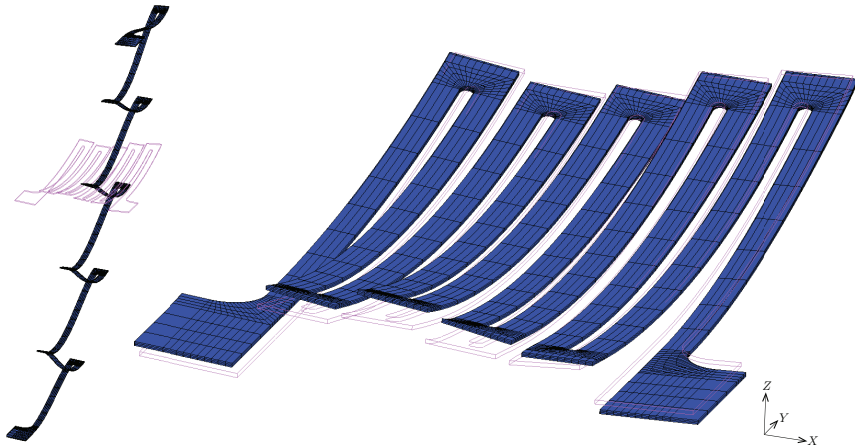
Figure 5.6: FE simulation of increment 8 in the experiment, where the boundary conditions in extended (left) and returned (right) state are derived from the measured topographies.

5.3   Results

In this Section, the results of the analysis of the stretchable interconnect experiment are presented. First the displacements of the beams were determined using an isogeometric global Digital Height Correlation method [76]. Furthermore, the Integrated DHC method is tested by means of a virtual experiment. Finally, the real experiment is analyzed with the IDHC method.

5.3.1   Displacement field analysis with isogeometric Digital Height Correlation

In order to obtain insight in the displacements of the beams, an isogeometric global DHC algorithm is employed. The results can be used to validate the displacements calculated with the FE simulation after the parameter identification with IDHC. Moreover, the

displacements of the clamping pads are essential to define boundary conditions in the FE model for the integrated height correlation. The technique used for this purpose is the isogeometric DHC algorithm introduced in [76], where NURBS shape functions are used for both the parametrization of the geometry and the discretization of the displacement field [75].
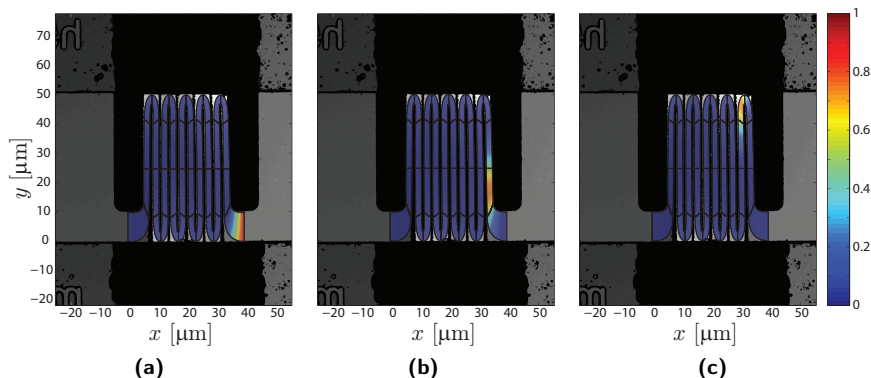
Figure 5.7: Shape functions for the isogeometric DHC analysis of the three-dimensional displacement field of the stretchable interconnect. The shape functions are second-order along the length of the interconnect and zeroth order in the width direction. In total 42 shape functions are defined, of which three are shown here.

The shape function mesh is created using the commercial CAD software Autodesk AutoCAD [1]. Second-order shape functions are used in the length direction of the interconnect, while zeroth order shape functions are used in the width direction, their product resulting in 42 two-dimensional functions for this geometry, see Figure 5.7. For this experiment it is important to limit the number of degrees of freedom (and hence, shape functions), because the correlation sensitivity to local minima is high due to the limited quality of the height pattern (silica particles) and high acquisition noise, especially at the large boundary of the slender structure. Therefore, the number of elements along the length of the interconnect is taken as small as possible while still describing the geometry accurate enough. This choice disregards the outside corners of the hinges, which is acceptable as these corners do not deform anyway. Also the choice for zeroth order shape functions in the width direction of the beams limits the number of degrees of freedom, which is justified because the strain in width direction remains negligible due the long free side edges of the beams. Therefore, the proposed limited set of shape functions is able to fully capture the kinematics of the interconnect structure.

Another measure taken to prevent correlation to a local minimum is to supply an adequate initial guess. Therefore, the rigid body displacements of the clamping pads are

---

[1]Autodesk. *AutoCAD software*. http://www.autodesk.com/products/autocad/overview.
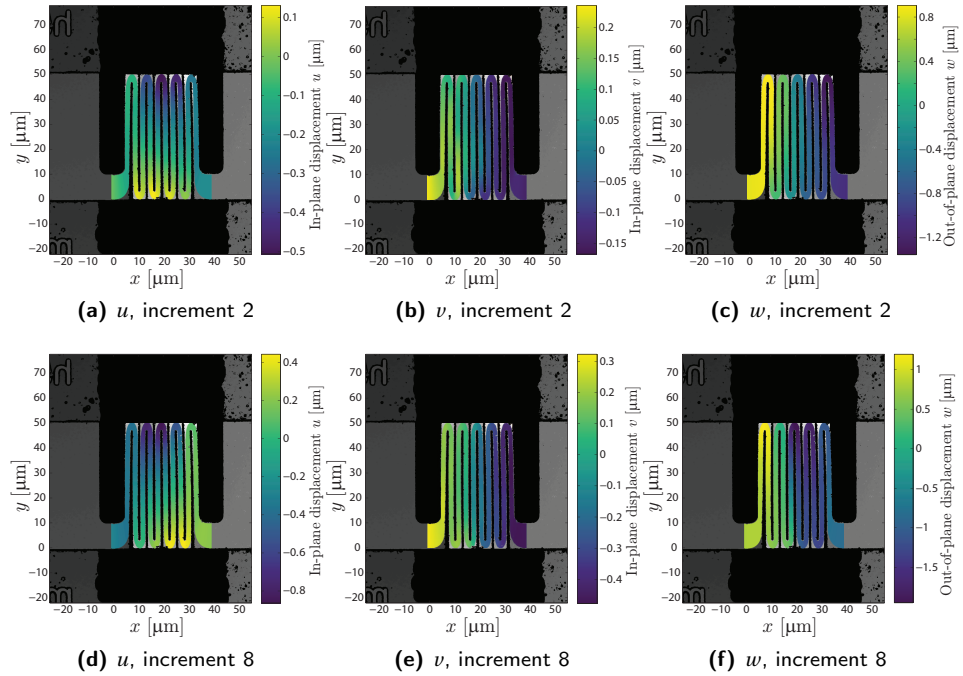
Figure 5.8: Calculated in-plane displacement fields u (in x-direction), v (in y-direction) and out-of-plane displacement field w for two loading increments in the experiment. The displacements are given in micrometers.

estimated manually at pixel level from the topography images and interpolated linearly over the beams.

The resulting displacement fields are shown in Figure 5.8 for one of the first and last increments in the experiment, which provide a good impression of the evolving plastic deformation after unloading at the end of each loading-unloading cycle. The figure shows that the major part of the three-dimensional displacement field for each increment is governed by the actual location of the clamps after unloading, which varies for each increment. Therefore, imposing this measured 3D clamp displacement as a boundary condition on the FE simulation in the IDHC routine is critical for obtaining convergence. Since the error in the displacement fields cannot be determined, as this is a real experiment and the true displacements are unknown, the only available measure for accuracy of the calculated displacements is the residual images, i.e., the difference between the reference image and the incremental (deformed) images back-deformed to the initial configuration using the calculated displacement fields. It can be seen in Figure 5.9 that the residual is close to zero for the entire region of interest. Hence, it is

(a) Increment 2   **(b)** Increment 8
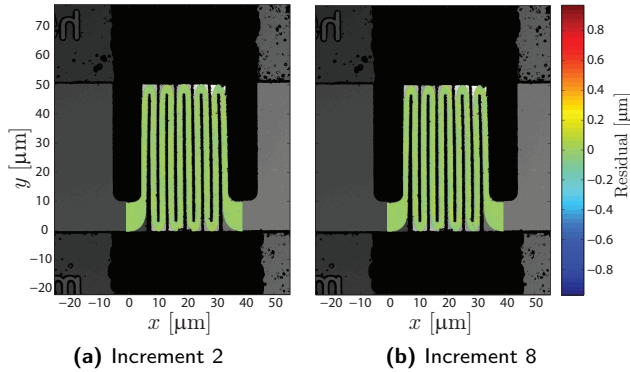
Figure 5.9: Residual images for the corresponding increments shown in Figure 5.8.

concluded that the obtained displacements with DHC are reliable.

5.3.2   IDHC parameter identification on virtual experiments

In order to assess the Integrated Digital Height Correlation framework for an experiment with the complexity of the interconnect structure, a virtual experiment is executed first. In this experiment, the images are created artificially from a finite element simulation and a synthetic reference image. In this virtual test case, a freestanding stretchable interconnect structure of two beams is modeled, which captures the main deformation modes occurring in the considered experiment on a 10-beam structure. Similar to the real experiment, one end of the interconnect is displaced in the out-of-plane direction by a prescribed distance, increasing over a number of cycles, and consecutively returned to its initial height position, see Figure 5.10.

The simulation results, i.e., three-dimensional nodal displacements, are used to deform the synthetic reference topography that contains a computer generated height pattern, see Figure 5.11a, to create the deformed topographies, of which two are shown in Figures 5.11b and c.

In the FE model the same elasto-plastic material model with a rate power law hardening relation (Equation 5.1) is used. The objective of the IDHC correlation of the virtual experiment is to recover the parameters in this model that are used to create the virtual experiment, i.e., $\sigma_{y0} = 200 \cdot 10^{-6} \text{ N}/\mu\text{m}^2$ (= 200 MPa), $A = 6.43 \cdot 10^{-4} \text{ N}/\mu\text{m}^2$ and $m = 0.2$. Therefore, this virtual experiment allows to assess the error sources affecting the IDHC parameter identification.

It is first noted that preliminary virtual experiments immediately demonstrated the im-
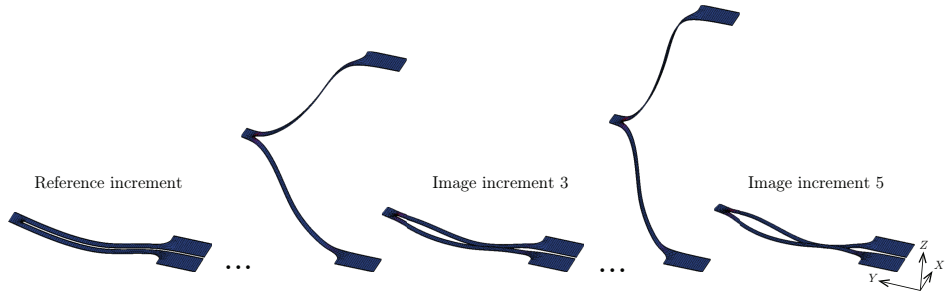
Figure 5.10: FE simulation for the virtual experiment. The interconnect structure consists of two beams, of which one is lifted to a prescribed height and displaced back to the reference position a number of times, with increasing lifting height. The image increments are based on the returned configurations, as indicated in the figure for three increments (the dots indicate loading cycles not shown in this figure).

portance of selecting a proper set of topographies: (i) a sufficient number of increments is required to find a unique solution for the three parameters in the numerical model; (ii) increments should be far enough in the plastic regime to ensure sufficient sensitivity to the parameters. Based on this analysis, it was chosen to include five loading-unloading cycles (or increments) that all fall in the plastic regime, in the IDHC correlation, i.e., five deformed topographies and the reference topography.

To test the performance of the IDHC correlation for identification of the three plasticity parameters on these six topogragies, an initial guess relatively far from the solution is employed, of approximately three times higher values for all three parameters. The convergence behavior is plotted in Figure 5.12. The IDHC algorithm adequately converges towards the expected solution. The initial guess values and the resulting values, with their associated errors, are presented in Table 5.1. This indicates that the algorithm is able to converge even relatively far from the solution, leading to accurate results with errors in the order of 10^{-3}.

Table 5.1: Results for the parameter identification with IDHC for the virtual experiment with a two-beam stretchable interconnect. The initial guess on the parameters is listed, as well as the value resulting from the correlation and the error in the determined parameters.

Parameter			Initial guess	Identified value	Relative error^2
Initial yield strength	σ_{y0}	[N/μm^2]	632$\cdot$10^{-6}	199$\cdot$10^{-6}	3.5$\cdot$10^{-3}
Hardening coefficient	A	[N/μm^2]	2.04$\cdot$10^{-3}	6.43$\cdot$10^{-4}	3.1$\cdot$10^{-4}
Hardening exponent	m	[-]	0.63	0.199	3.1$\cdot$10^{-3}

(a) f **(b)** g, increment 3   **(c)** g, increment 5
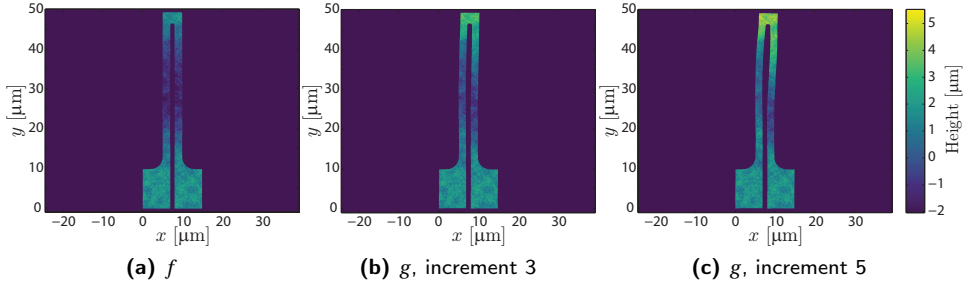
Figure 5.11: Topographies for the virtual experiment to be analyzed with IDHC: Left, the topography of the reference configuration, f; The deformed topographies g of two of the five increments in the middle and on the right.

However, note that the convergence behavior is still oscillatory, even for this virtual experiment where there are no error sources from experimental artifacts and discrepancies between the numerical model and the real world. This indicates that the problem is complex and difficult to correlate, which is also confirmed by the sensitivity analysis of the correlation matrix, see Figure 5.13. In this sensitivity analysis a spectral decomposition is made from the correlation matrix M: $M = QDQ^{-1}$, with the columns of Q being the eigenvectors of M and D a diagonal matrix containing the eigenvalues. From the correlation matrix M itself it becomes clear that the sensitivity towards parameters A and m is much smaller than the sensitivity to σ_{y0}. Furthermore, the eigenvector matrix Q reveals cross-sensitivity between the parameters, especially between A and the other parameters. Although the algorithm works well for this virtual experiment, complications can be expected when additional experimental error sources come into play.

5.3.3   Parameter identification from a real 3D test on a freestanding stretchable interconnect

Finally, the IDHC algorithm is applied to the topographies of the real out-of-plane loading experiment. A set of increments is used, mainly towards the end of the experiment, to incorporate enough topographies where plasticity has a quantifiable effect. The correlation is first executed for all three parameters of the hardening model simultaneously. Despite starting the correlation from various initial guesses and sequential correlation of the parameters no convergence is reached in that case. When looking at the non-convex residual landscape, see Figure 5.14, it is observed that many local minima exist. Furthermore, the landscape is moderately flat in a large area, which is

---

[2]Relative error = |Calculated value - True value|/True value.
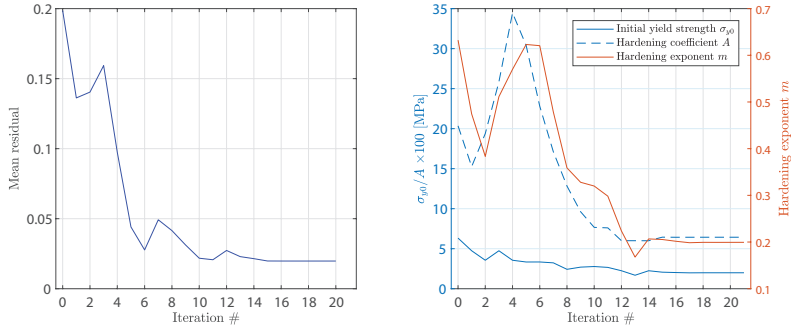
Figure 5.12: IDHC convergence for the virtual experiment. The evolution of the mean value of the residual (averaged both spatially and over time) and of the three resolved parameters, σ_{y0}, A and m is depicted.
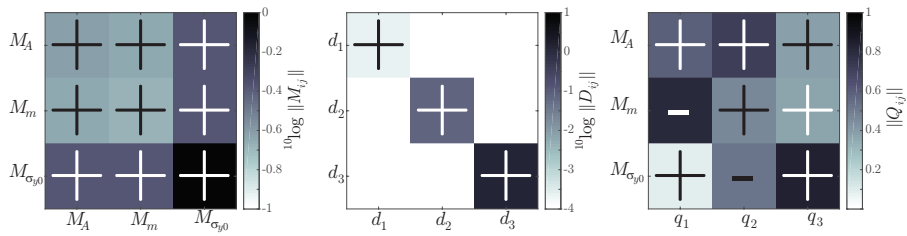
Figure 5.13: Graphical representation of the correlation matrix M and its spectral decomposition; eigenvalue matrix D and eigenvector matrix Q, which represent the sensitivity towards the three degrees of freedom (A, m and σ_{y0}). The symbol in each matrix component displays the sign of the corresponding value.

especially clear from the fitted surface (a third-order polynomial regression through the data) in Figure 5.14b, with an apparent valley around the values [$\sigma_{y0} = 300$ MPa, $m = 0.2$, $A = 644$ MPa] and local fluctuations in the data, see Figure 5.14c. This explains the lack of convergence, which is likely due to experimental error sources, e.g., the limited pattern quality and measurement uncertainties in the topographies, defects in the sample that play an important role in the deformation mechanics, and also model errors, such as discrepancy in the exact geometry, especially the thickness that is not quantified precisely, and the material model itself. An isotropic plasticity model is used, while the small size of the specimen suspects columnar crystals with few grain boundaries inducing size effects that are better modelled with, e.g., a crystal plasticity framework with strain gradient dislocation density effects [43].
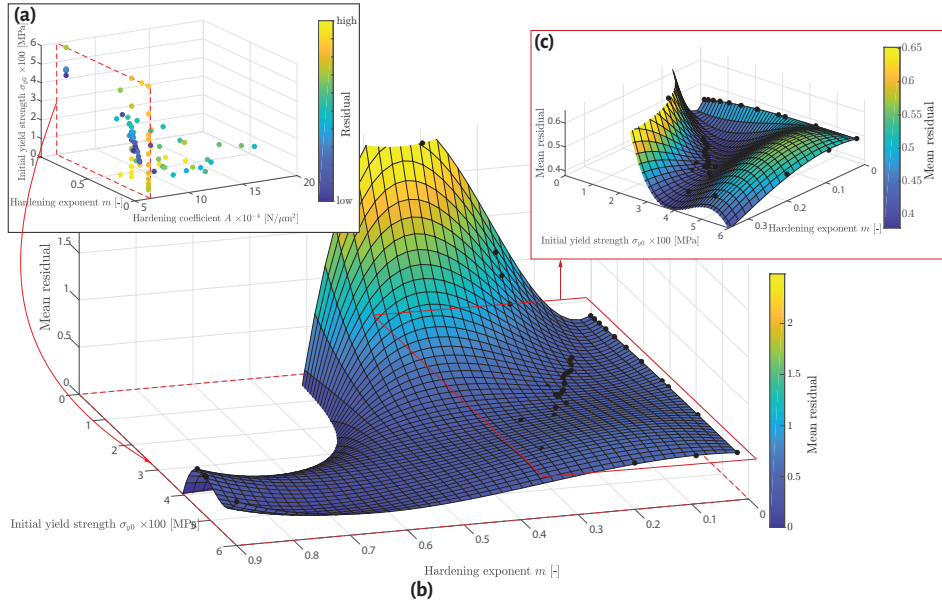
Figure 5.14: (a) Residual landscape as a function of the three parameters A, m and σ_{y0}. For visualisation purposes, the colors indicate the *order* of the mean value of the residual from low to high, instead of their exact value. In (b) the residual landscape for the two-parameter cross section indicated in (a) by a red dotted rectangle is shown. A 3rd order polynomial surface is fit through the data (black markers) for visualization purposes. A zoom of this landscape is depicted in (c).

Next, the correlation is performed only for the initial yield strength σ_{y0}, while the values for A and m are fixed at the values in the apparent minimum, i.e., $m = 0.2$ and $A = 644$ MPa. The correlation is initiated from two different initial guesses: 70 MPa, which is the bulk material property for aluminum, and 600 MPa, which is in the range of what was estimated in [132] for the considered interconnects. The convergence plot is shown in Figure 5.15, where the decrease in the residual becomes apparent, as well as the convergence of the parameter σ_{y0} towards the same value from both initial guesses. The resulting initial yield strength is approximately 300 MPa. This is much smaller than the in [132] estimated 600 MPa, where only a qualitative manual comparison between experiment and an unrefined numerical model was made. However, it is significantly higher than the value for bulk aluminum, and hence, still indicates a strong strengthening effect due to the sub-micron dimension (thickness) of the interconnect. Also, if the result of the numerical simulation is compared to the experimental image for the correlated initial yield strength of 300 MPa and for both the initial guesses, see Figure 5.15, it is observed that the deformed shape is indeed adequately approximated

after IDHC. Yet, in the finite element model a choice was here made for the other two material parameters that describe the plastic regime, hardening coefficient A and exponent m. The choice of these values might induce a model error and affect the resulting value for the initial yield strength.
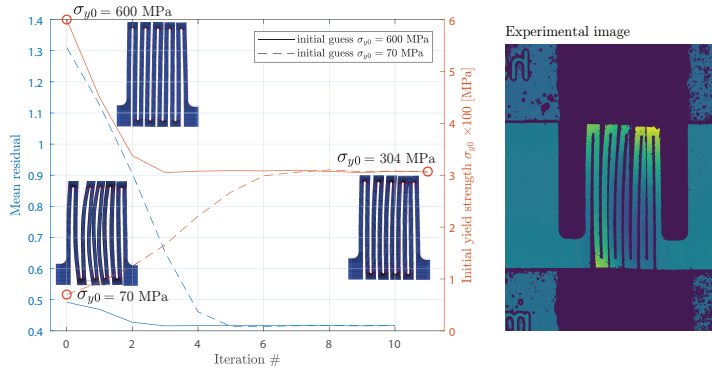
Figure 5.15: Convergence for the correlation of the initial yield strength parameter σ_{y0}. The evolution of the mean value of the residual (averaged both spatially and over time) and of σ_{y0} is depicted. Furthermore, the deformed geometry from the numerical simulations is shown at the final increment, for the two different initial guesses (600 and 70 MPa), and the correlated value (304 MPa). For comparison the experimental geometry from the same increment is depicted as well.

In order to evaluate the accuracy of the determined initial yield strength, the correlation is repeated for different values of m, while A is kept constant at 644 MPa, which appears to be the cross-section with the lowest residual values in Figure 5.14. It is observed in Figure 5.16a that the yield strength converges towards different values for different choices for m and that the residual for all these cases is approximately the same. This is consistent with the valley that appears in the residual landscape of Figure 5.14 and indicates cross-sensitivity between the parameters. Only the case of almost pure plastic behavior, with low hardening ($m = 0.02$) seems to converge worse than the other cases, so it is expected that these values of the yield strength and hardening exponent form a lower bound.

Next, correlation for both the initial yield strength and the hardening exponent is performed simultaneously, see Figure 5.16b, where A is again fixed at 644 MPa. The residual decreases to roughly the same value as for the other correlations, while significant fluctuations are noticed. The lowest residual value indicates that the best fit for the parameters is an initial yield strength of approximately 225-300 MPa, with a hardening exponent of around 0.15-0.2. Although the accuracy of the identification is modest, the adopted procedure still indicates that parameter identification is possible with the IDHC method

and more accurate results are expected upon improvement of the experiment and model.

(a) Convergence for correlation of σ_{y0}, m fixed **(b)** Convergence for correlation of σ_{y0} and m simultaneously
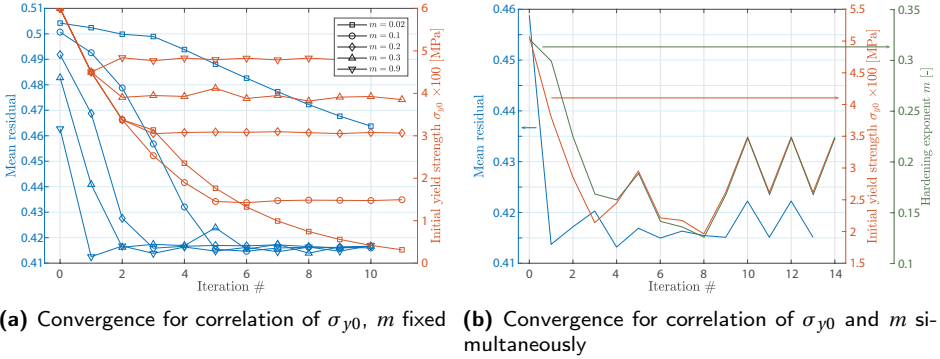
Figure 5.16: (a) Convergence for the correlation of the initial yield strength parameter σ_{y0}, from an initial guess of 600 MPa and different values for the hardening exponent m, ranging from 0.02 (almost pure plasticity) to 0.9 (extreme hardening). (b) Convergence for the simultaneous correlation of σ_{y0} and m. The evolution of the mean value of the residual and the correlation parameters are depicted.

5.4   Conclusions

The mechanical properties of a freestanding aluminum stretchable electrical interconnect have been analyzed by applying an integrated digital height correlation method to topographies measured in-situ during a 3D experiment. The design of the interconnect allows for full three-dimensional deformations, e.g., large rotations and displacements, thereby enabling ultra-stretchability. This complicates the application of commonly used DIC methods for characterization, as the surfaces are required to stay in view during the deformation process and displace in-plane only. Therefore, a digital *height* correlation method was employed, in which the three-dimensional surface displacements can be tracked. An integrated approach was followed, where the correlation of the images is complemented by a finite element model, in which the parameters are unknowns. Moreover, the experiment was designed such that the surfaces remain in view: The specimen is loaded in the out-of-plane direction, thereby triggering the main deformation mode of the stretchable interconnect, i.e., bending of its beam members.

It is of utmost importance that the boundary conditions applied in the finite element model comply with those in the experiment. Therefore, the experimental data was first analyzed using a global DHC method. The displacements of the clamping pads

were identified and used in the numerical model. Also, the initial geometry of the interconnect was established from the reference image and translated to the model, as the as-processed interconnect already has a warped configuration due to relaxed residual stresses from manufacturing, influencing the deformations and inducing model errors when not taken into account.

A virtual experiment was first executed to verify the IDHC algorithm. The stretchable interconnect geometry was implemented, along with a power law hardening model with three parameters, which were the objective for identification. It was shown that even for large mismatches in the initial values, the method converged towards the correct solution with an error in the resulting parameters in the order of 10^{-3}. However, it was also shown that even in this case without experimental uncertainties and model errors, the convergence path was irregular, indicating the complexity of this parameter identification problem. This was also confirmed by a sensitivity analysis of the correlation matrix, which showed large differences in sensitivity towards the individual parameters and also cross-sensitivity between the parameters.

Finally, the real experiment was analyzed. As anticipated, simultaneous correlation of all three plasticity model parameters was not at reach. The non-convex residual landscape is flat in a large area with many local minima. Therefore, the initial yield strength was correlated with the two other parameters fixed. From two different initial guesses the value converged to approximately 300 MPa, which is significantly higher than the value for bulk aluminum and indicates a strong strengthening effect due to miniaturization of the interconnects. The choice made for the other two parameters in the hardening model still influenced the actual value of the correlated parameter. Repeating the correlation for different values of the hardening exponent indeed revealed convergence of the initial yield strength to different values. Subsequently the initial yield strength and hardening exponent were correlated simultaneously. Despite the moderate accuracy of the identification, the initial yield strength was estimated at 225-300 MPa and the hardening exponent at 0.15-0.2. The hardening coefficient was assumed 644 MPa, which appeared to yield the lowest residual in the three-dimensional landscape.

The results show that the IDHC technique is suitable for parameter identification in the challenging case of real three-dimensional experiments on micron-scale freestanding stretchable interconnects. To increase the accuracy of the identification it is recommended to improve the experimental settings and to advance the numerical model in order to diminish as many error sources as possible. E.g., the applied height pattern is object for improvement, the geometry of the interconnect could be modeled more precisely and a material model including dislocation density strain gradient crystal plasticity could be used. This is, however, beyond the scope of the present work, where potency of the IDHC technique was shown and a first estimate of the material parameters for an isotropic hardening plasticity model was determined.

Chapter 6
Mechanical Shape Correlation: a novel integrated digital image correlation approach

Abstract

Mechanical Shape Correlation (MSC) is a novel Integrated Digital Image Correlation (IDIC) based technique used for parameter identification. Digital images taken during an experiment are correlated and coupled to a Finite Element model of the specimen, in order to find the correct parameters in this numerical model. In contrast to regular IDIC techniques, where the images consist of a grayscale speckle pattern applied to the sample, in MSC the images are projections based on the contour lines of the test specimen only. This makes the technique suitable in cases where IDIC cannot be used, e.g., when large deformations and rotations cause parts of the sample to rotate in or out-of-view, or when the speckle pattern degrades due to large or complex deformations, or when application of the pattern is difficult because of small or large specimen dimensions. The method targets problems for which the outline of the specimen is large with respect to the volume of the structure and changes significantly upon deformation. The technique is here applied to virtual experiments with stretchable electronic interconnects, for identification of both elastic and plastic properties. Furthermore, attention is paid to the influence of algorithmic choices. The method reveals fast convergence with high accuracy (with errors down to 10^{-8}) and adequate initial guess robustness. The results

are promising and indicate that the method can be used in cases of either large, complex or three-dimensional displacements and rotations on any scale.

6.1   Introduction

Identification and characterization of the mechanical behavior of structures, components and devices is important for design and reliability engineering, e.g., to determine accurate numerical models, to design novel structures or to monitor structural integrity. A widely used tool for mechanical characterization is digital image correlation (DIC), where deformation of the structure is tracked, usually based on a speckle pattern applied to the object of interest. However, in some cases it is not possible to exploit this technique, for example because pattern application is not feasible. In Figure 6.1 several examples are shown for which in situ mechanical characterization is desired, but for which it is difficult to use digital image correlation. All these cases exhibit a distinct contour, which might be used to track the deformations, rather than a speckle pattern applied to the sample. For example, mechanical characterization of the load-bearing structures of cars is important, which can be done with, e.g., crash tests [53], see Figure 6.1a. The material properties depend on the processing history and hence, testing the parts as processed is important to obtain accurate models. Another example, at much smaller scale, is the ballistic impact on a single wire [5, 38, 117] or plate [104] in order to detect its high-rate dynamic mechanical properties, see Figure 6.1b. Due to the slender nature of this wire it is difficult to apply a speckle pattern for DIC.

A third example is the stretchable electronic interconnect shown in Figure 6.1c. Stretchable electronics is a topic of increasing interest, with mainly biomedical applications where the flexibility and stretchability provides compatibility between rigid electrical components and soft biological tissue, enabling, e.g., health monitoring [73], flexible devices for cardiac diagnostics [51] and stretchable surgical tools [80]. Recently, a novel design was proposed that consists of freestanding interconnects, which are free to deform three-dimensionally, thus enabling an elastic stretchability beyond 2000% [132]. The stretchable interconnects are integrated in for example miniature sensors used for minimally invasive surgery [97] and hence have microscale dimensions. Because of their small dimensions and complex deformation, DIC based on speckle pattern tracking is difficult to employ. Nonetheless, because of the wire-like form of the stretchable interconnects the outline of the structure is large and changes significantly upon stretching. Therefore, a DIC technique is proposed that is based on the evolving contour of the structure.

DIC approaches can be split in roughly three groups [56]. In local DIC approaches, the

---

[1]Still from video taken from `https://www.capetesting.com/resources/videos/`. IMMI and testing division CAPE provided permission to use the image, but were not involved in this research.

(a) Car safety frame crash test[1]and simulation (Reproduced from [53])

(b) Projectile wire test (Reprocuced from [38]).

(c) Deforming stretchable electronic interconnects; horseshoe-shaped and rectangular design
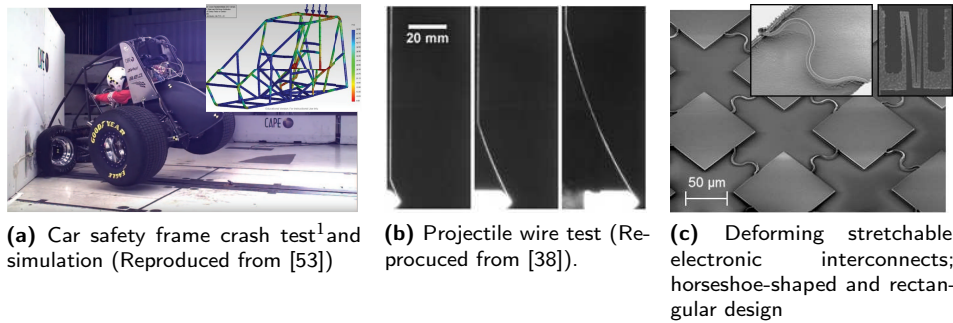
Figure 6.1: Examples of deforming structures, ranging from the scale of meters to micrometers, for which it is difficult to apply digital image correlation for mechanical characterization. In Figure (a) an image taken during a crash test with a car frame is depicted. In Figure (b) an image sequence is shown from a ballistic impact test on a single silk fiber. In Figure (c) two examples of stretchable electronic interconnects between rigid (integrated circuit) islands can be seen; a horseshoe-shaped connect from [126] and a rectangular design introduced in [132].

image is divided in local subsets, each limited in admissible kinematics (e.g., rigid body motion, shear, uniaxial compression and tension). In the global approach the entire image is correlated at once [29, 105]. However, the parametrization of the kinematics should be rich enough to capture the kinematics of the considered experiment, which can be achieved by, e.g., using finite elements (FE) [11] or NURBS shape functions [41, 114]. Furthermore, adaptive refinement algorithms were introduced to achieve an optimal set of shape functions for a wide range of problems [75, 157].

A third approach is the integrated digital image correlation (IDIC) method, where a mechanical, analytical or finite element model, is used for regularization [56, 100, 115]. The degrees of freedom are the model parameters. The goal of such an approach is usually to extract material parameters or other model parameters from the experimental images. The method in this paper also follows an integrated approach, where a FE model is coupled to the correlation process.

The largest difference, however, between IDIC and the proposed Mechanical Shape Correlation (MSC) method is that for MSC contrast in the images is obtained by mapping a signed distance function on the projected contour of the entire specimen, rather than using a grayscale speckle pattern applied to the sample. This projection is based on the outline of the specimen, which changes depending upon the deformation of the sample. This projection can be made for both experimental images and FE simulation results, enabling their correlation. This approach has several advantages. First, the structure is allowed to deform three-dimensionally, since the contour of the sample can still be tracked in projection, while in case of a speckle pattern it is only possible to

track in-plane deformation, except when multiple cameras [91, 150] or an (optical or atomic force) profilometer [52, 76] is used. However, also in these cases the out-of-plane rotation of the sample is still limited, since parts of the structure that rotate out of view (or parts that were not visible in the reference image but rotate into view) cannot be tracked. When correlating images based on the contour of the sample this problem is eliminated. Second, because a speckle pattern is not required, the MSC method can also be applied in cases where pattern application is difficult, such as when the sample dimensions are very small or very large, or when pattern degradation occurs due to large deformations. Therefore, the proposed Mechanical Shape Correlation method provides a solution strategy for integrated DIC problems characterized by large and/or complex, possibly out-of-plane, deformations and cases for which a speckle pattern is not appropriate, as long as the evolving boundary area is significant. The contour is a naturally, always present feature that contains valuable information on the deformations and hence a useful source to base correlation on, especially if other DIC methods or reference point tracking is not easy or possible to employ.

The proposed method shows similarities with Virtual Image Correlation (VIC) [17, 46, 116], where also the contour of a specimen is tracked exploiting digital images of the sample. It differs, however, in its goal to identify model parameters versus determining the position of the contour itself, and in the way the real experimental images are compared to virtual ones. In the MSC method, the created signed distance maps for both the experiment and the simulation, enable full-field correlation for which the difference between the images approaches zero, while in VIC the difference is minimized as well, although only in the vicinity of the contour itself, but can never go to zero, since the virtual image is defined in a different manner than the real experimental image.

The paper is organized as follows. In Section 6.2 the type of images required for MSC is introduced as well as the procedure to obtain them. The images are compared to those used in (Integrated) DIC approaches. In Section 6.3 the algorithm for solving MSC problems is explained and the differences with a regular IDIC algorithm are highlighted. In Section 6.4 virtual experiments are performed to demonstrate the Mechanical Shape Correlation method. The stretchable interconnect structure is split to investigate the two main deformation modes separately, both for elastic and elastoplastic material behavior. The influence of some algorithmic choices for MSC is examined. In Section 6.5 some issues that are to be expected in real experiments are addressed. The paper closes in Section 6.6 with conclusions.

6.2   Images

In Digital Image Correlation (DIC), Finite Element Model Updating (FEMU) or Integrated DIC (IDIC), grayscale images (or brightness fields) with a distinct pattern distin-

guishing individual material points are correlated, see e.g., Figure 6.2a. In contrast, in MSC correlation of the projections of the shape contour of the sample is used instead. This novel technique is based on the assumption that the boundary area is large and the sample shape changes significantly during deformation. In this paper a stretchable electronic interconnect will be investigated, see Figure 6.2b, as a typical example.

(a) Grayscale pattern

(b) Experimental image of a stretchable electronic interconnect

(c) Binary projection

(d) Signed distance map
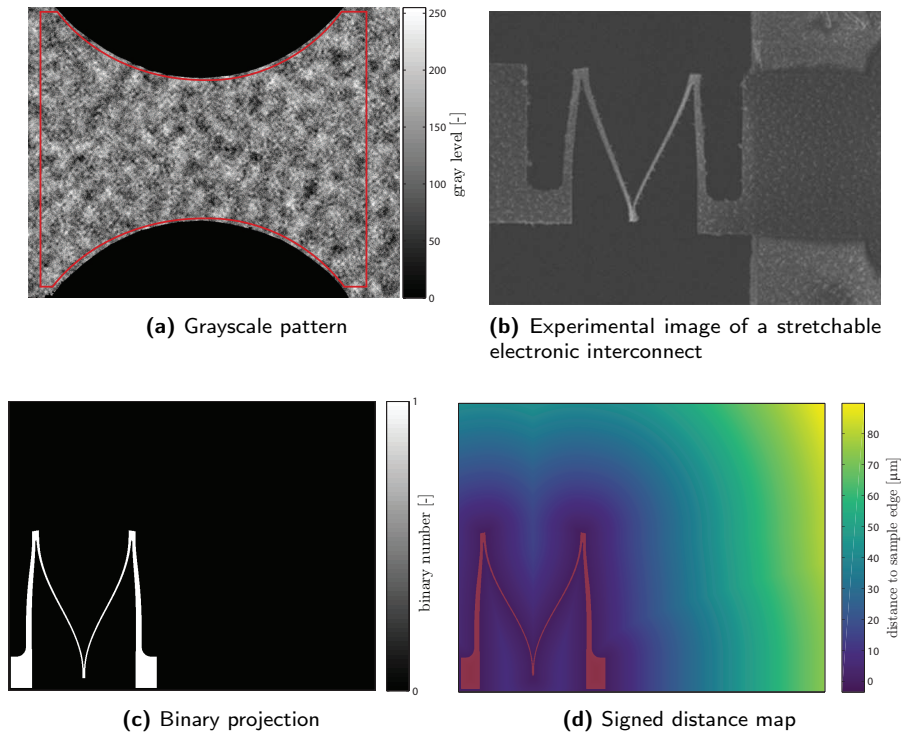
Figure 6.2: Examples of images used for different image correlation techniques. In (a) a dog-bone shaped sample with a grayscale pattern is shown, where the red box indicates the region of interest used for correlation. In Figure (b) a real experimental image of a stretchable electronic interconnect (from [132]) is shown. Figure (c) shows a binary image of the projection of the specimen from (b). In (d) a signed distance map of the same projection is depicted. In orange, the mask used for correlation is shown.

The structure of the interconnects consists of several beams connected to each other and hence the boundary length is relatively large. Because of the small dimensions and the proximity of the boundaries, it is difficult to apply a high quality pattern as used in Figure 6.2a. More importantly, because the structures are freestanding and deform out-of-plane upon stretching the patterned area rotates out of view, prohibiting correlation further. In Mechanical Shape Correlation a planar projection of the structure

is used as the image. In contrast to regular images, where a region of interest is chosen restricting the correlation to where the pattern is present (red box in Figure 6.2a), for MSC the region of interest is generally larger than the sample, since the edges are critical for correlation and need to be in view.

The projection can be rendered in different ways. The simplest method is to convert the physical image to a binary image where the background has a different color (e.g., black) than the structure (e.g., white), see Figure 6.2c. However, since large monochromatic areas occur in the binary images, even relatively large deviations from the solution will not result in a high averaged residual and the method will converge before an accurate solution is obtained. Therefore, instead of using binary images, signed distance maps are extracted, see Figure 6.2d. The location of (the projection of) the sample edge is determined and for each pixel the closest distance to this edge is calculated, see Figure 6.3. Pixels located inside the structure obtain a negative value, while outside the structure a positive value is assigned. This value is designated to the pixel of the resulting MSC image, further called signed distance map. With this approach a displacement of the sample edge is reflected in a significantly large region in the image.
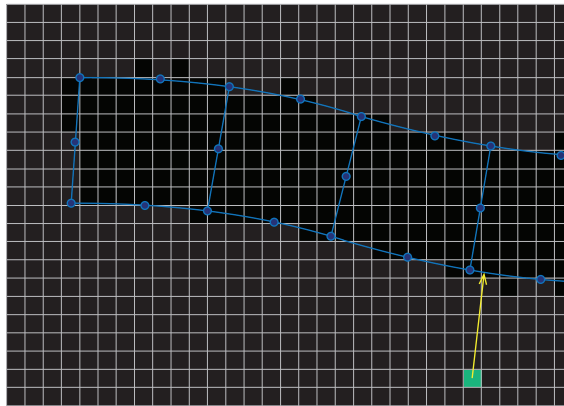
Figure 6.3: Extraction of signed distance maps from FE simulation. The element contours and nodal positions are shown in blue and the pixel grid is depicted. For each pixel in the image the shortest distance to this edge is determined and the value is assigned to the pixels, as represented for the one pixel in green.

Likewise, MSC projections need to be made from simulated results using a FE model. Here, care should be taken that the projections created from the FE simulations adequately resemble the reality. For example, when using shell elements in a simulation, the physical thickness of the sample should be properly incorporated. Shell elements are infinitely thin, henceforth, the thickness of the sample is not visible in the FE deformed geometry. The thickness has to be added to the projection, by defining top and bottom

surfaces of the element based on the translation and rotation data of the element nodes, as illustrated in Figure 6.4.

(a) Quadratic shell element   **(b)** XZ-projection of shell element   **(c)** XZ-projection corrected for thickness
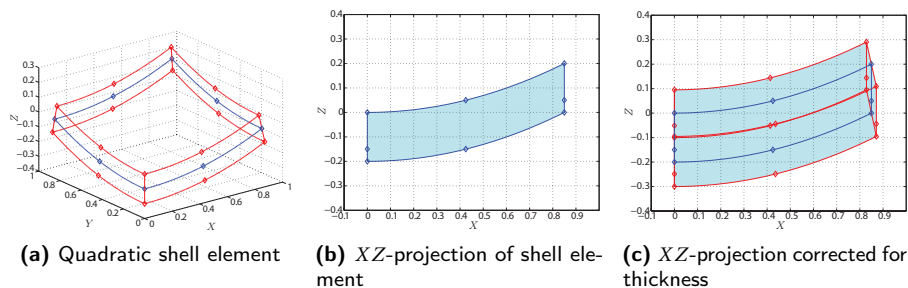
Figure 6.4: An example of a quadratic shell element (with eight nodes) is shown in blue in the left figure. A shell element is infinitely thin and hence the projection (middle figure) will not reveal the thickness of the sample. The thickness is added, see the red element in the left figure, and incorporated in the projection (right figure).

The images shown in Figure 6.2 are all top views from the specimen, i.e., projections on the XY-plane. Evidently, it is possible to make projections from an arbitrary viewpoint, see Figure 6.5. If different viewpoints are accessible, one can choose the view that best reflects the deformation of the sample contour, which is beneficial for the correlation. The same viewpoints are to be used in the experiment and simulation. The view direction is represented by the normal vector $\underline{N}$, which is determined by the azimuth and elevation angle. Special cases include the top projection (on the XY-plane) with [azimuth,elevation]$= [0°, 90°]$, the front projection (on the XZ-plane): $[0°, 0°]$, and the side projection (on the YZ-plane): $[90°, 0°]$. The orientation of the resulting image is determined by the vectors $\underline{e}_x$ and $\underline{e}_y$, forming an orthonormal system together with $\underline{N}$. In order to define a unique coordinate system, in this paper we take $\underline{e}_x$ in the XY-plane, and normal to $\underline{N}$. The projection of the three-dimensional structure on the $\underline{e}_x\underline{e}_y$-plane, i.e., the 2D coordinates of all points in the structure along the $\underline{e}_x$ and $\underline{e}_y$ axes, are then determined by taking the inner product of the 3D point coordinates with the vectors $\underline{e}_x$ and $\underline{e}_y$. In DIC literature the image coordinates are usually denoted by $\underline{x}$, or x and y. Note that the image coordinates x and y do not necessarily coincide with the X- and Y-coordinate from the 3D situation in the FE simulation.

Figure 6.5 displays simple orthographic projection, where perspective is not taken into account. For most examples in this paper this orthographic projection is used, but it is also possible to substitute projection methods including (weak or full) perspective [24]. In that case additional parameters for the construction of the projected image arise, mainly the 3D position of the camera with respect to the imaged object. The influence of misalignments of the camera angles and position, represented by the distance to the sample along the normal vector $\underline{N}$, is investigated in Section 6.5.2.
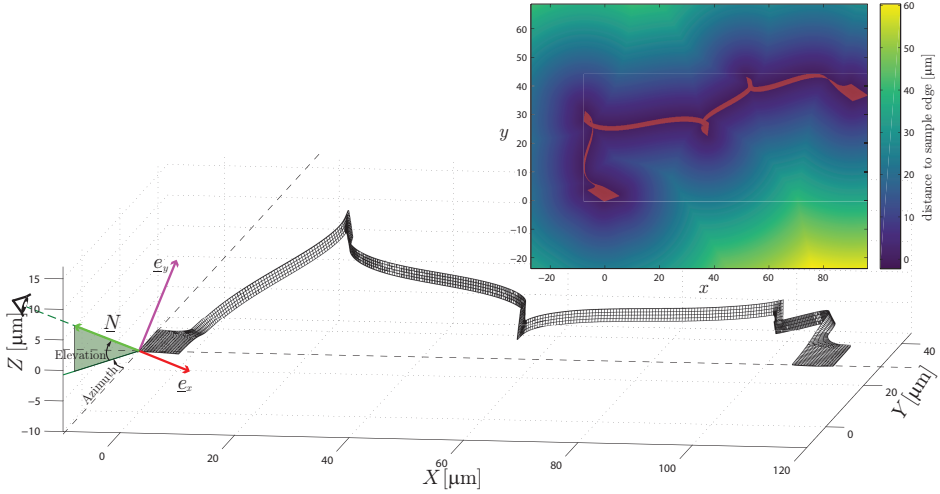
Figure 6.5: Projection from an arbitrary viewpoint: The normal vector $\underline{N}$ determining the view is determined by two angles; the azimuth and the elevation. The azimuth is the angle with the negative Y-axis in counterclockwise direction (hence the particular angle shown here is negative) and the elevation is the angle with the XY-plane in positive Z-direction. The projection plane is then determined by vectors $\underline{e}_x$ and $\underline{e}_y$, of which $\underline{e}_x$ is defined such that it lies in the XY-plane. The resulting signed distance map of a stretchable electronic interconnect, including the mask, is shown in the inset for the considered view.

Finally, the structure itself is masked in the signed distance maps, in the sense that the masked pixels are not incorporated in the correlation process, see the orange region in Figure 6.2d. The mask is created by determining which pixels fall inside the closed polygons formed by the projected sample contours. These pixels are designated as the mask. For the experimental images the contour has to be determined using an image segmentation algorithm (see Section 6.5). Note that when the mask is applied, no negative values exist in the signed distance maps anymore, as only the pixels *inside* the structure, which are now masked, had a negative sign.

The reason for masking is that it is challenging to determine the closest distance for an inner pixel automatically in a robust manner. The inner pixels are close to multiple segments of the contour (e.g., a side and a top edge) and for slight differences in the FE simulation (due to the iterative process and perturbations on the degrees of freedom, see next Section) the closest boundary segment may easily switch, thereby causing jumps in the derivatives of the signed distance maps, which may induce instabilities, affecting correlation. Masking the structure itself is an elegant solution, since correlation is based only on the pixels located outside the structure, for which the closest distance

is always to the outer contour of the structure. The effect of masking was investigated in [78][2], where it was shown that better convergence of the method is achieved when masking the structure.

6.3 The Mechanical Shape Correlation algorithm

The mechanical shape correlation algorithm is based on integrated digital image correlation (IDIC) [100]. Since a different type of images is used, the algorithm needs adaptation. In this section the algorithm is derived in detail, whereby the differences with the conventional IDIC algorithm are clearly indicated.

Conservation equations

In digital image correlation, multiple images of a sample taken during an experiment are correlated in order to identify displacement fields, strain fields or, in integrated DIC, model parameters. In conventional DIC algorithms, the undeformed image is usually labeled f and a sequence of deformed images defined as g. The algorithm is based on *brightness conservation*, which implies that each material point preserves the same brightness upon deformation, resulting in the same gray value in the image. Mathematically this is denoted

$$f(\underline{x}) - g \circ \underline{\Phi}(\underline{x}, t) = r_{\mathrm{DIC}}(\underline{x}, t) \approx 0, \tag{6.1}$$

$$\underline{\Phi}(\underline{x}, t) = \underline{x} + \underline{u}(\underline{x}, t), \tag{6.2}$$

where $r_{\mathrm{DIC}}(\underline{x}, t)$ are the residual images at each time step t and $u(\underline{x}, t)$ the corresponding displacement field. The notation $g \circ \underline{\Phi}(\underline{x}, t)$ signifies that g applies to the mechanical mapping function $\underline{\Phi}$, which in turn depends on the displacement field $\underline{u}$. This means that the image g is back-transformed to the original coordinates $\underline{x}$ using the function $\underline{\Phi}$, such that the brightness values are in the same position as in image f (if $\underline{u}$ is calculated correctly), making the images comparable.

In mechanical shape correlation, however, this is not possible, since three-dimensional displacements and rotations of a three-dimensional sample are considered. Therefore, in the deformed images, the visible specimen faces may differ from those in view in the reference image. Hence, it is impossible to recreate the reference image from the

---

[2]Reference [78] is a conference proceeding from the same authors with additional algorithmic details on the masking procedure and its effect on the MSC correlation results.

deformed images by back-deforming them. Therefore, instead of comparing a single undeformed reference image to back-transformed deformed images, images of all increments of the experiment (indicated by g) are correlated to the corresponding images of the FEM simulation (denoted h). The MSC method is schematically shown in Figure 6.6. Since the images are created in an equivalent manner from the experimental images and the numerical simulation data, 'brightness', or rather 'distance value' conservation still holds, contrary to Virtual Image Correlation algorithms, where the virtual image is not constructed to exactly match the experimental one [46]. The residual, which thus in theory still approaches zero, can be defined:

$$r(\underline{x}, t) = g(\underline{x}, t) - h(\underline{x}, t) \approx 0, \tag{6.3}$$

This is now a *forward* transformation, in contrast to the *back*-deformation of images towards the reference situation in DIC. Accordingly, the residual is not defined in the reference configuration, but in the deformed configurations of each increment. Note that both g and h are time (or increment) dependent and not described by brightness values, but by signed distance values to the edge of the sample. Furthermore, note that in regular (I)DIC this forward transformation could also be done. Image h is then described by $h(\underline{x}, t) = f(\underline{x}) \circ \Phi^{-1}(\underline{x}, t)$, where now the inverse mapping function $\underline{\Phi}^{-1}(\underline{x}, t)$ is used, indicating that the images h are created from the reference configuration f using the calculated displacement field $\underline{u}(\underline{x}, t)$ (from the FEM simulation).

Regularization

The DIC problem is intrinsically ill-posed, since the number of unknowns (multidimensional full-field displacements) exceeds the number of equations (equal to the number of pixels in the image). To reduce the number of degrees of freedom (DoFs), the displacement field is regularized. This regularization is usually done by describing the displacement field as a linear combination of shape functions with corresponding coefficients. These shape functions may span local subsets of the total image, as used in local DIC, or the entire region of interest, i.e., global DIC. In integrated DIC, the regularization is achieved by coupling a finite element model of the sample to the correlation, such that the displacement is confined to what is kinematically admissible by the constitutive model. The unknowns are the model parameters that need to be identified. The real mapping function $\underline{\Phi}(\underline{x}, t)$ is approximated by a mapping function that depends on the constitutive parameters $\mathbb{a}$ used in the FE model:

$$\underline{\Phi}(\underline{x}, t) \approx \underline{\phi}(\underline{x}, t, \mathbb{a}). \tag{6.4}$$
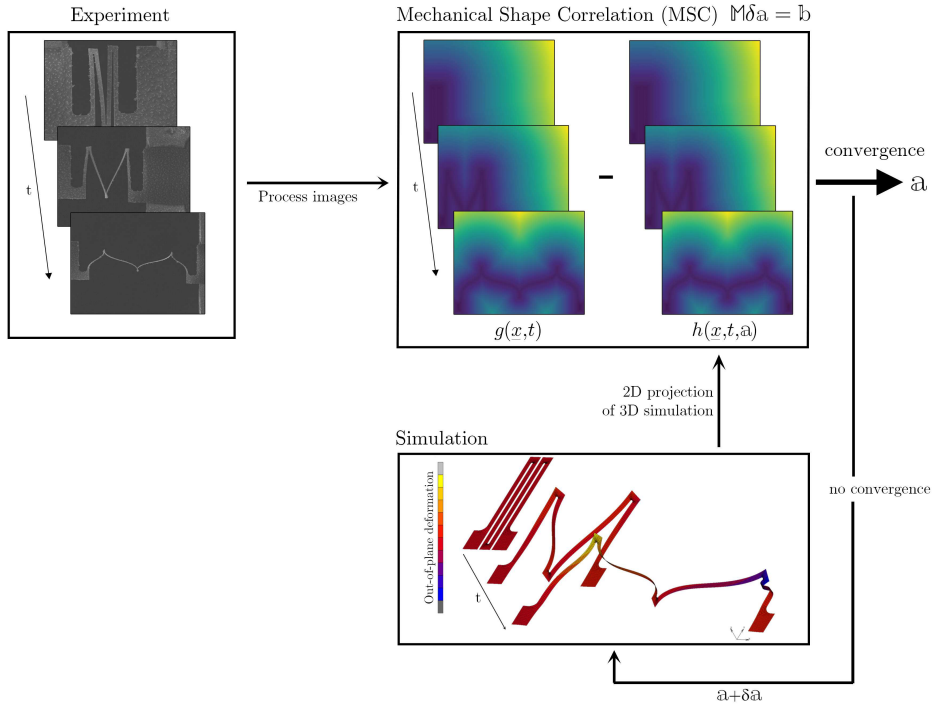
Figure 6.6: Schematic representation of the mechanical shape correlation (MSC) method to identify model parameters $\mathbb{a}$ from an experiment. Simulations supply the images h to which the experiment is compared.

This makes images h also dependent on the model parameters: $h(\underline{x}, t, \mathbb{a})$.

Minimization

In order to find the optimal set of constitutive parameters, similar to other global DIC approaches, the residual is minimized using a least squares approach:

$$\mathbb{a}^{\text{opt}} = \underset{\mathbb{a}}{\text{Argmin}}\, \Psi, \tag{6.5}$$

with Ψ the objective function, defined as

$$\Psi = \frac{1}{2} \int_\tau \int_\Omega r^2(\underline{x}, t, \mathbb{a}) \, \mathrm{d}\underline{x}\mathrm{d}t = \frac{1}{2} \int_\tau \int_\Omega \left[g(\underline{x}, t) - h(\underline{x}, t, \mathbb{a}) \right]^2 \mathrm{d}\underline{x}\mathrm{d}t. \tag{6.6}$$

The solution of 6.5 implies:

$$\forall j \in [1, m], \quad \Gamma_j(\mathbb{a}^{\mathrm{opt}}) = \frac{\partial \Psi}{\partial a_j}(\mathbb{a}^{\mathrm{opt}}) = 0, \tag{6.7}$$

with m the number of degrees of freedom

Linearization and iterative solving

This problem is non-linear and hence a Gauss-Newton scheme is used to linearize and solve the problem:

$$\Gamma_j^{\mathrm{it}+1} \approx \Gamma_j^{\mathrm{it}} + \sum_{i=1}^{m} \frac{\partial \Gamma_j^{\mathrm{it}}}{\partial a_i} \delta a_i = 0, \tag{6.8}$$

with $\Gamma_j^{\mathrm{it}} = \Gamma_j(\mathbb{a}^{\mathrm{it}})$. Rewriting this equation gives:

$$\sum_{i=1}^{m} \frac{\partial \Gamma_j^{\mathrm{it}}}{\partial a_i} \delta a_i = -\Gamma_j^{\mathrm{it}} \tag{6.9}$$

$$\mathbb{M}\delta\mathbb{a} = \mathbb{b}, \tag{6.10}$$

with $M_{ij} = \frac{\partial \Gamma_j^{\mathrm{it}}}{\partial a_i}$ the components of $\mathbb{M}$.

Right hand side

The right hand side b_j is given by

$$b_j = -\Gamma_j^{\text{it}} = -\frac{\partial \Psi}{\partial a_j}(\mathrm{a}^{\text{it}}). \tag{6.11}$$

With Ψ given by equation 6.6, this becomes

$$b_j = -\frac{1}{2}\frac{\partial}{\partial a_j}\int_\tau\int_\Omega r^2(\underline{x}, t, \mathrm{a}^{\text{it}})\,\mathrm{d}\underline{x}\mathrm{d}t = -\int_\tau\int_\Omega r(\underline{x}, t, \mathrm{a}^{\text{it}})\frac{\partial r}{\partial a_j}(\underline{x}, t, \mathrm{a}^{\text{it}})\,\mathrm{d}\underline{x}\mathrm{d}t. \tag{6.12}$$

Usually, in IDIC, the derivative of the residual is written as

$$\frac{\partial r_{\text{DIC}}}{\partial a_j}(\underline{x}, t, \mathrm{a}^{\text{it}}) = -\frac{\partial \phi}{\partial a_j}(\underline{x}, t, \mathrm{a}^{\text{it}}) \cdot \underline{\text{grad}}\,g \circ \underline{\phi}(\underline{x}, t, \mathrm{a}^{\text{it}}). \tag{6.13}$$

The first part, $\frac{\partial \phi}{\partial a_j}$, is referred to as *sensitivity maps* $\underline{H}_j(\underline{x}, t, a_j^{\text{it}})$. The second part, $\underline{\text{grad}}\,g \circ \underline{\phi}(\underline{x}, t, \mathrm{a}^{\text{it}})$, is the *true image gradient* $\underline{G}(\underline{x}, t, \mathrm{a}^{\text{it}})$ [103]. In IDIC, the sensitivity maps are typically calculated using a finite difference scheme:

$$\underline{H}_j(\underline{x}, t, a_j^{\text{it}}) = \frac{\underline{U}^{\text{it}}(\underline{x}, t, a_j^{\text{it}} + \Delta a_j^{\text{it}}) - \underline{U}^{\text{it}}(\underline{x}, t, a_j^{\text{it}})}{\Delta a_j^{\text{it}}}, \tag{6.14}$$

where $\underline{U}^{\text{it}}$ is the displacement field calculated in the FEM simulation and Δa_j is a perturbation of the jth degree of freedom. The displacements are nodal quantities in FEM calculations and the displacement values need to be interpolated at pixel locations, such that the sensitivity map can be multiplied by the image gradient. For IDIC, the region of interest is smaller than the sample itself (see Figure 6.7a), i.e., everywhere in the ROI nodes are present for which the displacements calculated in the FEM step are known. Hence, it is possible to interpolate the displacement field at all pixel locations in the ROI. For MSC, however, the region of interest is larger than the sample, see Figure 6.7b, and there is a large area where the displacement field is not calculated. Hence, it is meaningless to extrapolate the displacement field at the pixels outside the

sample, whereas the gradient is only known outside the mask, i.e., outside the sample. Therefore, $\frac{\partial r}{\partial a_j}(\underline{x}, t, \mathbb{a}^{\text{it}})$ cannot be calculated by means of the usual splitting into G and H made in IDIC.

(a) IDIC   **(b)** MSC
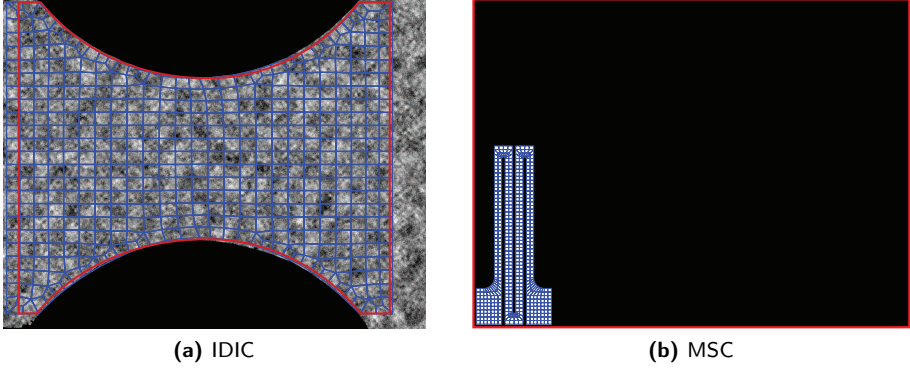
Figure 6.7: Difference in region where the displacement field is known with respect to the region of interest (ROI) for an IDIC procedure (left) and the MSC method (right). The mesh of the FEM simulation is plotted on top of the image. For IDIC, this is the dogbone sample with a grayscale speckle pattern from Figure 6.2a and for MSC this is the binary projection of the stretchable interconnect from Figure 6.2c in the initial configuration. In both images the ROI is displayed by a red outline.

Contrary to the displacement field, the residual field $r(\underline{x}, t, \mathbb{a}^{\text{it}})$ is known at all pixel locations naturally, since it is defined as the difference between two images, i.e., the difference between two signed distance maps. Therefore, instead of splitting the residual derivative in the image gradient and the sensitivity map, the derivative of the residual is calculated directly in MSC:

$$\frac{\partial r}{\partial a_j}(\underline{x}, t, \mathbb{a}^{\text{it}}) = \frac{r^{\text{it}}(\underline{x}, t, a_j^{\text{it}} + \Delta a_j^{\text{it}}) - r^{\text{it}}(\underline{x}, t, a_j^{\text{it}})}{\Delta a_j^{\text{it}}}, \tag{6.15}$$

with

$$r^{\text{it}}(\underline{x}, t, a_j^{\text{it}} + \Delta a_j^{\text{it}}) = g(\underline{x}, t) - h(\underline{x}, t, a_j + \Delta a_j) \tag{6.16a}$$

$$r^{\text{it}}(\underline{x}, t, a_j^{\text{it}}) = g(\underline{x}, t) - h(\underline{x}, t, a_j). \tag{6.16b}$$

The step size Δa_j is an important parameter, which could influence the convergence behavior of the method. This perturbation of the degrees of freedom is determined relative to the DoF itself using a perturbation factor P:

$$\Delta a_j^{\text{it}} = P \cdot a_j^{\text{it}}. \tag{6.17}$$

For the calculation of the derivative of a continuous function using this finite difference scheme, parameter P would ideally be as small as possible, just above numerical accuracy, to ensure an accurate approximation of the derivative. However, in this case the residual is not a continuous function and depends on (non-linear) FE calculations, for which the accuracy is determined by i.a., a set tolerance. If the step size is smaller than appropriate for the given tolerance, the approximated derivative is prone to numerical errors. Therefore, it is important to select a proper value for P, which may be problem specific and it is unfeasible to give a general value for all possible situations. The influence of the step size is investigated in Section 6.4.

Correlation matrix

The correlation matrix is

$$M_{ij} = \frac{\partial \Gamma_j^{\text{it}}}{\partial a_i} = \frac{\partial}{\partial a_i} \int_\tau \int_\Omega r(\underline{x}, t, \mathbb{a}^{\text{it}}) \frac{\partial r}{\partial a_j}(\mathbb{a}^{\text{it}}) \, \mathrm{d}\underline{x}\mathrm{d}t. \tag{6.18}$$

With the product rule this can be split in two parts: $M_{ij} = M_{ij}^a + M_{ij}^b$, with

$$M_{ij}^a = \int_\tau \int_\Omega \frac{\partial r}{\partial a_i}(\mathbb{a}^{\text{it}}) \frac{\partial r}{\partial a_j}(\mathbb{a}^{\text{it}}) \, \mathrm{d}\underline{x}\mathrm{d}t, \tag{6.19a}$$

$$M_{ij}^b = \int_\tau \int_\Omega r(\underline{x}, t, \mathbb{a}^{\text{it}}) \frac{\partial^2 r}{\partial a_i \partial a_j}(\mathbb{a}^{\text{it}}) \, \mathrm{d}\underline{x}\mathrm{d}t. \tag{6.19b}$$

In the first term, the derivative of the residual appears a second time, which is already determined in Equation 6.15. In the second term the second derivative of the residual occurs. In literature second order derivatives in the correlation matrix of a DIC algorithm are usually omitted, since it makes correlation highly sensitive to image acquisition

noise [103]. Analogously, in this case a high sensitivity to the accuracy of the sample edge detection from the experimental images is expected. Furthermore, the second part contains the residual itself, which, according to [103], is high in the beginning of the correlation and may lead to correlation to a local minimum. Therefore, M_{ij}^b is neglected, effectively using a modified Gauss-Newton scheme as in IDIC. This can be justified, since the residual itself decreases during correlation, and hence, term M_{ij}^b approaches zero upon iteration towards the optimal solution.

Note that the problem is not solved incrementally, but all images (or increments) are lumped into a single minimization process including all data, following [13, 100].

Additional residuals

Similar to IDIC, in the MSC framework it is also possible to take into account other experimental data besides the optical part, such as the force history, e.g., [100, 113]. This is achieved by defining a second residual, which is the difference between the experimentally measured values and the values resulting from the FEM simulation, which also depend on the degrees of freedom. This residual is independent from the optical residual and hence the total linearized system of equations can be written as a weighted linear combination of the two separate problems. For the examples in this work, however, correlation is based on the optical residual only and no additional data is used.

Boundary conditions in the FE simulation

It is worth noting that it is not straightforward to apply the exact same boundary conditions of the experiment to the FE simulations. It is very important to prescribe the boundary conditions in the FE simulation as accurately as possible, since deviations in them can significantly decrease the accuracy of the correlation. When a part of the sample remains stationary or a known displacement is applied, then these boundary conditions should of course be used for the FE simulation as well. When the boundary conditions are not known for the experiment, it may be possible to implement a pre-step in the correlation algorithm that uses DIC on subregions of the sample relevant for determining the boundary conditions [119, 123]. It applies regular DIC (global or local) on these subregions to acquire the displacements, which can be translated to kinematic boundary conditions on nodes in the corresponding subregions in the FE simulation. In case of the stretchable electronics samples considered in this paper, the subregions can be the clamping pads, which do not rotate out of view and are hence suitable for DIC.

6.4 Virtual experiments

In order to assess the Mechanical Shape Correlation algorithmic performance, several virtual experiments are performed. For the virtual experiments, the experimental images $g(\underline{x}, t)$ do not originate from real experiments, but from a separate finite element (FE) simulation for which the signed distance projections are stored as images g. In this manner, the undesired side effects of a model error or experimental errors (e.g., residual stresses in the sample and image acquisition noise) are eliminated and an exact investigation of the method itself is achieved.
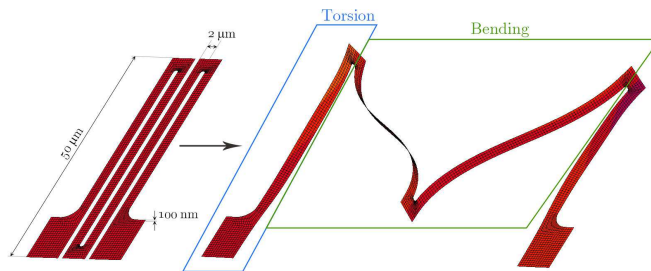
Figure 6.8: The deformation of a stretchable electronic interconnect can be split in two main deformation modes: torsion of the outer beams and bending of the middle beams.

The experiments focus on stretchable electronic interconnects and in particular the structure introduced in [132]. Because of the small dimensions, some mechanical properties are difficult to predict, as they are influenced by size effects. Therefore, it is desired to execute mechanical characterization on the structures as processed. Since these slender wire-like structures exhibit a large evolving boundary area, they form a suitable test case for the MSC method. The deformation of the structures can be described by two main deformation modes: torsion and bending of beams, see Figure 6.8. These two deformation modes are investigated separately. The FE simulations for these simplified experiments are less complex and time-consuming than for the full structure and hence more suitable for an analysis of the influence of different parameters in the MSC algorithm, such as the perturbation factor and the initial guess for the unknown model parameters.

First, finite element simulations based on an elastic material model are executed, using quadratic shell elements. The dimensions of the beams are as follows: the length is $50\,\mu$m, the width $2\,\mu$m and the thickness 100nm. Later, an elastoplastic material model is used, with two unknown parameters.

6.4.1   Bending of beams

The deformation of the middle section of the interconnects is characterized by bending of the beams. The virtual experiment is executed by modeling a simplified version of the stretchable interconnects: two connected beams are modeled, of which one is constrained at the end, while the other is lifted by a prescribed load. The deflection of the beams is therefore sensitive to the Young's modulus E.
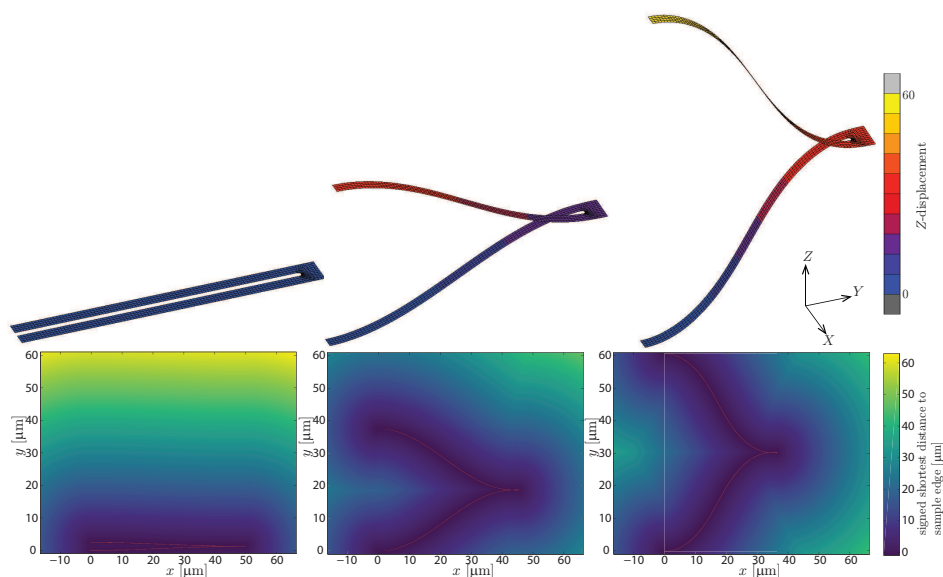
Figure 6.9: Signed distance maps for a selection of increments of the virtual experiment for bending of the middle beams. Side projections, on the YZ-plane are made, with projection angles [azimuth,elevation] = [90°, 0°]. Note that the notation for x and y coordinates in the signed distance maps does not correspond to the coordinate system (XYZ) of the FE simulation. In orange the mask used in the correlation is shown on top of the signed distance maps, however, visibility is limited since this is a side projection of the extremely thin beams (100 nm).

The objective of this virtual experiment is to recover the correct value for this elastic material parameter E. The Young's modulus that was used in creating all the virtual experiments is 69GPa (or $6.9 \cdot 10^{-2} \text{N}/\mu\text{m}^2$, since the structure was modeled in microns). The deformation is most pronounced in a side projection of the specimen and hence, YZ-projections are made for the signed distance map images, see Figure 6.9. The mechanical shape correlation algorithm is executed for this experiment for different values of the perturbation factor P and different initial guess values. For each execution

and each iteration the error in the identified Young's modulus is determined:

$$\epsilon_E = \frac{|E - E_p|}{E_p},$$
(6.20)

with E the value calculated by the algorithm and E_p the solution, i.e., the value used to create the virtual experiment.

The resulting convergence plot is shown in Figure 6.10. For a relatively wide range of initial guesses very accurate results are obtained with errors going down to values of 10^{-8}. For even smaller initial guesses, the Young's modulus is so small, that the extreme compliance of the double bending beam structure leads to nonlinear situations that cannot be captured with the considered FE model. Hence, the MSC method cannot be executed, which is indicated by the black circles in Figure 6.10a. For initial guesses above roughly four times the actual value of E the method loses convergence, illustrated by red circles. Note, however, that the MSC algorithm is based on an unbounded Gauss-Newton minimization scheme, which is relatively simple to implement, but might not yield the best results in terms of initial guess robustness. Other minimization approaches, such as Nelder-Mead or modified Gauss-Newton schemes with an update limit and constraints are expected to increase the initial guess robustness even further [79].

(a) Set of parameters
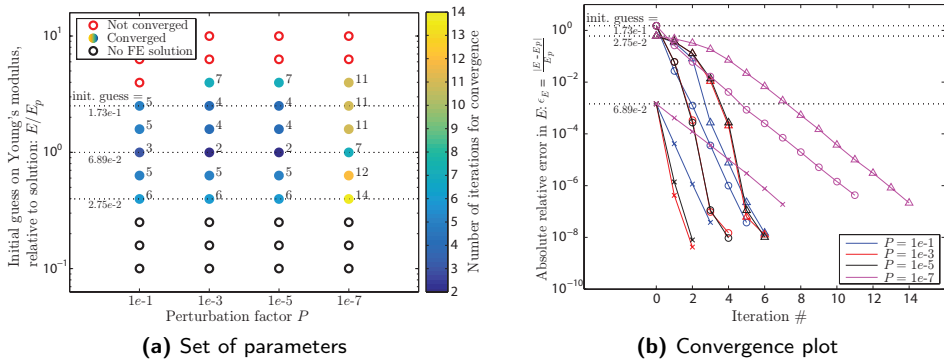
(b) Convergence plot

Figure 6.10: Convergence behavior of the MSC algorithm for the bending beam experiment, for different values of the perturbation factor P and different initial guess values. In figure (a) the initial guess on parameter E (relative to the value used for the virtual experiment E_p) and the perturbation factor P is shown, with for each combination the number of iterations to convergence. For three initial guesses, marked by dotted lines in figure (a), the complete convergence path is shown in figure (b), for all perturbation factors.

The perturbation factor P has a significant effect on the convergence speed, which is

most apparent in Figure 6.10b. Too small values ($P = 10^{-7}$) lead to slow convergence. Indeed, the displacement information is only reflected in the location of the sample edge, which is used for creating the images. A very small perturbation induces only a small difference in location of the sample contour and if this difference is smaller than the pixel size it is not manifested in the residual derivative. Consequently, the search direction is not optimal and correlation is slow. Also for a large value of P ($P = 10^{-1}$) correlation is slow, since the derivative of the residual is not calculated accurate enough. For intermediate values of P there is not a large difference in convergence behavior. As mentioned in Section 6.3, the signed distance maps are smooth and the 'pattern' on the image does not influence the residual and its derivative as much as the small featured speckle patterns used in IDIC. For this experiment, a proper perturbation factor is in the range of 10^{-5} to 10^{-3}. Note, however, that these values might be problem specific and dependent on the pixel size with respect to the sample dimensions, i.e., the resolution of the images.

6.4.2   Torsion of beams

In the second virtual experiment, torsion of the side beams of the stretchable interconnect is investigated. In Figure 6.11 the simulation results are shown. The left side of the beam is clamped and the right side is rotated using a prescribed torque around the X-axis. Therefore, the amount of rotation is dependent on the Young's modulus E. A projection from the side (XZ-projection) is made and the signed distance maps are determined, shown as well in Figure 6.11. The FE model used for creating the virtual images is also imported in the MSC procedure, while the Young's modulus E is the unknown parameter.

The convergence plots for the virtual experiments are shown in Figure 6.12. The convergence behavior is similar to the first virtual experiment in terms of accuracy and dependence on the perturbation factor. A too small or too large value for P leads to slower, but still adequate, convergence. An intermediate value leads to fast convergence and accurate results. Especially the high accuracy is remarkable, since the difference in specimen contour and hence signed distance maps is small for this experiment, even for large steps in the variable E. Given the definition of the signed distance maps, the information on the edge position is spread through the entire image, which results in a strong sensitivity and hence, a high accuracy.

Again, if the initial guess on the Young's modulus is far too low, stability problems in the FE simulation occur, disabling the MSC algorithm, shown with black circles in Figure 6.12a. The range of initial guesses for which convergence takes place, is smaller to some extent than for the previous experiment. This is due to the smaller differences in sample contour upon changes in E and hence, a lower sensitivity to the material parameter.
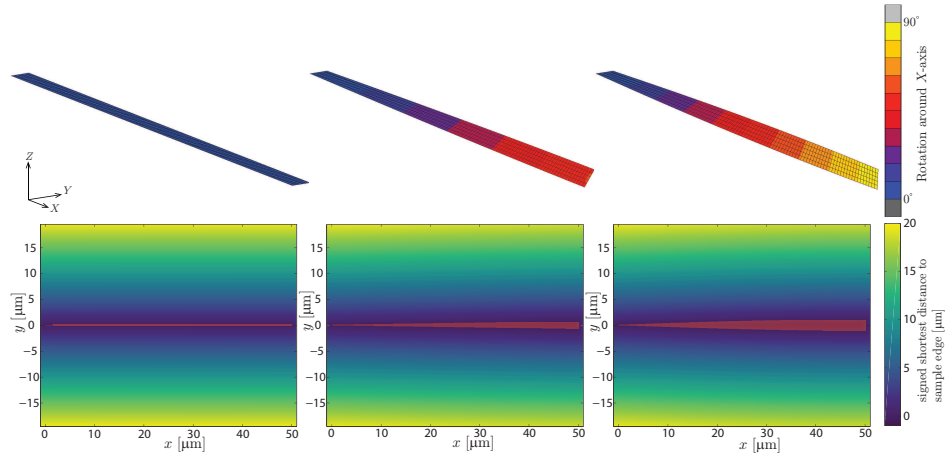
Figure 6.11: Signed distance maps for selected increments of the virtual torsion experiment for the side beams. The projection is an XZ-projection, in which the projection angles are [azimuth,elevation] $= [0°, 0°]$. Note that the notation for x and y coordinates in the signed distance maps does not correspond to the coordinate system (XYZ) of the FE simulation. The mask used in the correlation is shown as well, in orange.

6.4.3 Elastoplastic bending of beams

In the previous experiments only one parameter, namely the Young's modulus, was the unknown parameter. To determine this elastic parameter it was necessary to incorporate the load, which was prescribed as a boundary condition in the FE simulation. In a real experiment, measurement of the load may be complex, especially for very large or small structures. For instance, for the small stretchable electronic interconnects, which are designed to be as compliant as possible, it is challenging to measure the force, since it is difficult to design a load cell that is sensitive enough. Furthermore, the Young's modulus is in general not very sensitive to size effects and therefore in case of these stretchable electronic interconnects not a variable of interest in the Mechanical Shape Correlation procedure. The plastic parameters, such as the yield strength, however, are more important. As was shown in [132], the initial yield strength for these interconnects appears to be much higher in experiments than expected from literature. Hence, the next virtual experiment is focused on identification of plastic parameters. Elastoplastic FEM simulations are performed, where J_2-plasticity is used along with a power law hardening model:

$$\sigma_y = A\left(\varepsilon_0 + \bar{\varepsilon}_p\right)^m, \tag{6.21}$$

(a) Set of parameters
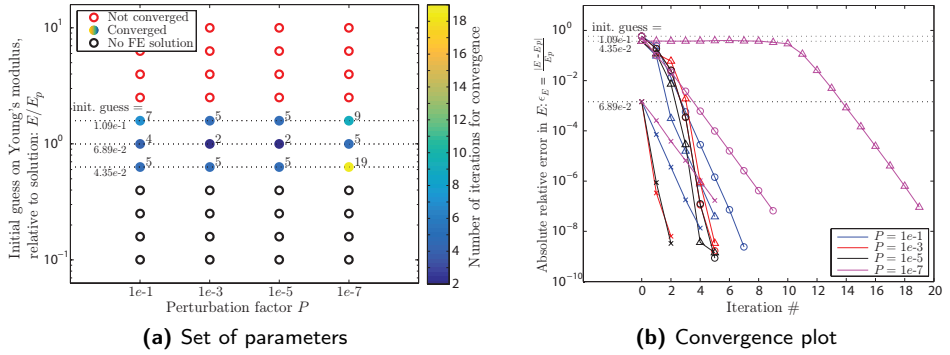
(b) Convergence plot

Figure 6.12: Convergence plot of the MSC algorithm for the torsion beam experiment, for different values of the perturbation factor P and different initial guess values. In figure (a) the set of parameters P and initial guesses on E is shown, with for each combination an indication on the convergence. For three initial guesses the complete convergence path is shown in figure (b), for all perturbations factors.

with σ_y the yield stress, ε_0 the strain at initial yield and $\bar{\varepsilon}_p$ the equivalent plastic strain. Parameter A is a coefficient related to the initial yield strength (σ_{y0}) and m is the hardening exponent.

For the virtual experiment an exponential hardening parameter of 0.2 is used and parameter A is chosen such that it corresponds to an initial yield strength of 200 MPa. Coefficient A can be calculated from the initial yield strength using equation 6.21, taking $\bar{\varepsilon}_p = 0$, since there is no plastic strain yet at initial yield, hence: $A = \sigma_{y0}/\varepsilon_0^m$. Furthermore, the strain at initial yield can be described by the end of the elastic region: $\varepsilon_0 = \sigma_{y0}/E$.

Now the displacements of the beam's ends are prescribed, rather than the force. The signed distance maps look similar to those in Figure 6.9, although the specimen outline changes slightly when plasticity becomes active, i.e., the beams become slightly more straight and less S-shaped due to the evolving plastic hinge. Based on the previous virtual experiments, a perturbation factor P of $1 \cdot 10^{-3}$ is applied. A range of initial guesses for parameters A and m is used, as shown in Figure 6.13a. In this figure it is also depicted which of the parameter combinations converge to the expected solution and which diverge.

Four regimes emerge in the parameter field (Figure 6.13a). Regime 1 is located around the diagonal and the algorithm adequately converges for these initial guess values. For these combinations of A and m the initial yield point σ_{y0}, which can be calculated with Equation 6.21 for $\bar{\varepsilon}_p = 0$, is typically within a factor of 2 from the initial yield strength of the virtual experiment, see the green curves in Figure 6.13b. Therefore, although

(a) Set of parameters

(b) Stress-strain curves
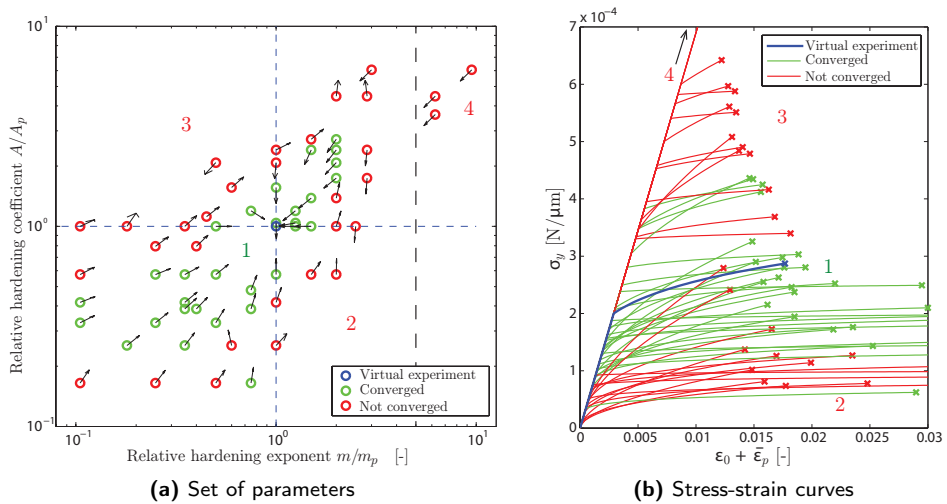
Figure 6.13: Plastic parameters, m and A, used as an initial guess for the MSC procedure (left) and corresponding stress-strain curves (right). The parameters are scaled with the values used for the virtual experiment, $m_p = 0.2$ and A_p corresponding to a yield strength of 200 MPa (or $2 \cdot 10^{-4} \text{N}/\mu\text{m}$). The blue circle indicates the expected solution. The arrows indicate the direction in which the algorithm is converging or diverging. The stress-strain curves according to Equation 6.21 for the parameter combinations are shown on the right. The curves are colored accordingly. The crosses indicate the stress state at the last increment of the FEM simulations. The blue curve corresponds to the virtual experiment with the exact parameter values. Four regimes are indicated by numbers, labeled accordingly in the two figures.

parameters A and m differ significantly from the expected values, the initial guess for the yield strength is not very far from the solution and the method converges. For all these converged solutions the error in A and m is reduced to below 10^{-4}.

In the region located underneath the diagonal, i.e., regime 2 in Figure 6.13, the initial yield strength is strongly underestimated and hence many of the increments are in the plastic regime, while in the virtual experiment they are in the elastic regime, see the blue curve in Figure 6.13b. Note from the convergence path arrows in Figure 6.13a that in this regime both A and m increase. Separately this makes sense, since a higher A corresponds to a higher yield strength (for a fixed m) and a higher value for m brings the material behavior in the plastic (hardening) regime closer to the elastic regime. However, since both parameters influence the initial yield strength, σ_{y0} does not change significantly upon increasing both parameters. Because of this dependence both A and m keep increasing and diverge from the solution.

For the parameter combinations above the diagonal the initial yield strength is overesti-

mated, see the red curves of regime 3 in Figure 6.13. This implies that a large section of the increments, and hence images, is in the elastic regime, thereby strongly reducing the sensitivity to the plastic parameters. This leads to divergence from the solution.

In the fourth regime the initial guess for m is larger than 1, which is not physical and leads to pure elastic behavior. The same complications as in regime 3 hold and divergence results.

This example illustrates that the problem should be well-defined for the MSC algorithm, which is of course also the case for any IDIC approach. For any method it is difficult to obtain parameters describing the plastic material behavior if there are elastic increments influencing the sensitivity. Therefore, one usually first determines when initial yield occurs and exploits this in the correlation of the material parameters by only using the plastic branch in the correlation. Furthermore, in this case, A and m are interdependent via the initial yield strength σ_{y0}, which can lead to a higher initial guess dependence in the correlation. Also the physical implication of variations in the unknown model parameters should be taken into account. Nevertheless, in a relatively large area in the parameter initial guess field fast convergence towards the correct solution is obtained.

6.5 Towards real experiments

In this final Section the influence of some important aspects that play a role in real experiments is investigated. First, in real experiments the contour of the sample needs to be determined from the images taken during the experiment, while up until now the exact contour was directly extracted from the FE simulation. The method used for extracting the contour from grayscale images may influence the accuracy of the localization of the contour and hence the accuracy of the correlation. Second, in a real experiment it can be difficult to exactly determine the camera viewpoint and a misalignment between the experimental images and the projections from the FE simulations may occur. The influence of this misalignment is investigated.

6.5.1 Influence of image segmentation approach

In this virtual experiment the influence of an important factor affecting real experiments is examined, i.e., the extraction of signed distance maps from pixelized experimental images. This is tested virtually, since in a real experiment the reference solution is unknown and performance assessment is not feasible. Until now the signed distance maps were created directly from the sample contour taken from a finite element simulation. However, in a real experiment grayscale images are taken from the sample, in which the exact edge of the sample is undetermined due to the pixel grid of the image. In other

words; a sharp black (for background) and white (for sample) transition is not observed, but around the location of the contour gray pixels occur, since the sample edge crosses these pixels somewhere, see Figure 6.14.
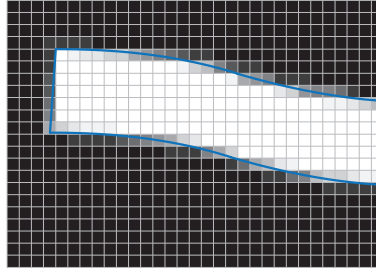
Figure 6.14: Impression of an experimental image, where the black-white transition representing the sample edge is smoothed out to gray levels due to the discrete pixel nature of the image. The actual position of the sample edge is represented by the blue line.

To determine the location of the sample edge in a real image, various image segmentation methods with various degree of complexity have been introduced in the literature, e.g. methods based on a level set framework [28, 154] or even Virtual Image Correlation algorithms [116]. In contrast, as an ultimate test for the MSC framework, here the most rudimentary method is explored, i.e. imposing a threshold on the gray level to determine which pixel centers belong to the sample and which to the background. This way a binary image is created, from which the now sharp black-white transitions can be used to determine the (approximated) location of the sample edge. The shortest distance to this edge can be calculated for each pixel in the image to create the signed distance map. To mimic this proces, in this virtual experiment the signed distance maps are determined as required for an experimental image: create a pixelized binary image first, using the sample contour following from the simulation, and from this image the signed distance map, see Figure 6.15. We call this approach the *pixelized* method, whereas for comparison the original method for creating the signed distance maps from the continuous edge (following from the FE simulation in the virtual experiments and from an advanced image segmentation method in real experiments) is named the *continuous* approach. Note that it is not straightforward to choose a proper threshold for real experimental images, especially if illumination (and hence gray level intensity) is not uniform over the image or changes between the images. One should consider if a single threshold value for all images is sufficient, or if a more sophisticated thresholding strategy, e.g., [16], is required. In contrast, creating a binary image from the numerical contour is fairly simple, as it merely includes checking which pixel centers lie inside the contour and which outside, and there is no need to select a proper threshold.

The influence of using the pixelized method, is investigated here, on the virtual exper-
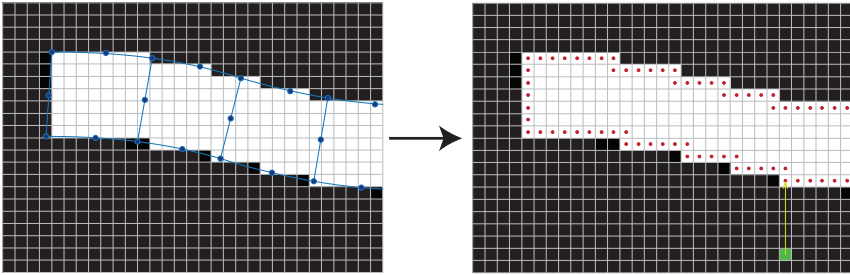
Figure 6.15: Creating signed distance maps via the two stage pixelized approach. The pixel grid of the image is shown and the blue lines represent the element contour as obtained from the simulation. A pixelized binary image is created by determining which pixels are located within this contour, to mimic the effect of the most rudimentary image segmentation method, i.e. imposing a gray level threshold, on a real experimental image; the resulting edge is indicated with red dots. In a second step that is specific for the MSC method, the signed distance map is created based on the pre-allocated edge, as is shown for one pixel.

iment from Figure 6.9, with an elastic material model with the Young's modulus E as material parameter, as in Section 6.4.1. In Figure 6.16a the residual field is shown for one of the increments of the double bending beam experiment, where images g and h are calculated with the pixelized approach. In this residual field lines perpendicular to the structure are observed. Figure 6.17a reveals the origin of these lines. Creating the binary image first induces a shift of the edge in the order of a couple of pixels. Therefore, the difference in signed distance value for pixels positioned in a line perpendicular to the edge around the location of this shift, for a small dislocation of the element contour, is relatively high for the pixelized approach compared to the continuous method (Figure 6.17b). This difference becomes visible when the images are subtracted, i.e., the residual is calculated.

In the derivative of the residual these lines become even more apparent, see Figures 6.16b and 6.16c. Especially for a small perturbation factor the lines dominate the derivative field, which may lead to poor or slow convergence. This is indeed observed in the convergence plots in Figure 6.18, where the MSC algorithm is executed for initial guesses within the converging domain of Section 6.4.1 and the three best perturbation factors. The decrease in convergence performance is larger if the perturbation factor is smaller. The initial guess is not as important. The pixelized approach also impairs the final accuracy of the method, i.e., the error after the final iteration is larger. It is important to note, however, that even when using the most rudimentary image segmentation method, the MSC method still converges within a reasonable amount of iterations (for acceptable values of the perturbation factor) with an accuracy of 10^{-4}, which is a promising result for correlations incorporating this experimental issue. In real

(a) Residual field

(b) Residual derivative, $P = 1e-3$, pixelized

(c) Residual derivative, $P = 1e-5$, pixelized **(d)** Residual derivative, $P = 1e-3$, continuous
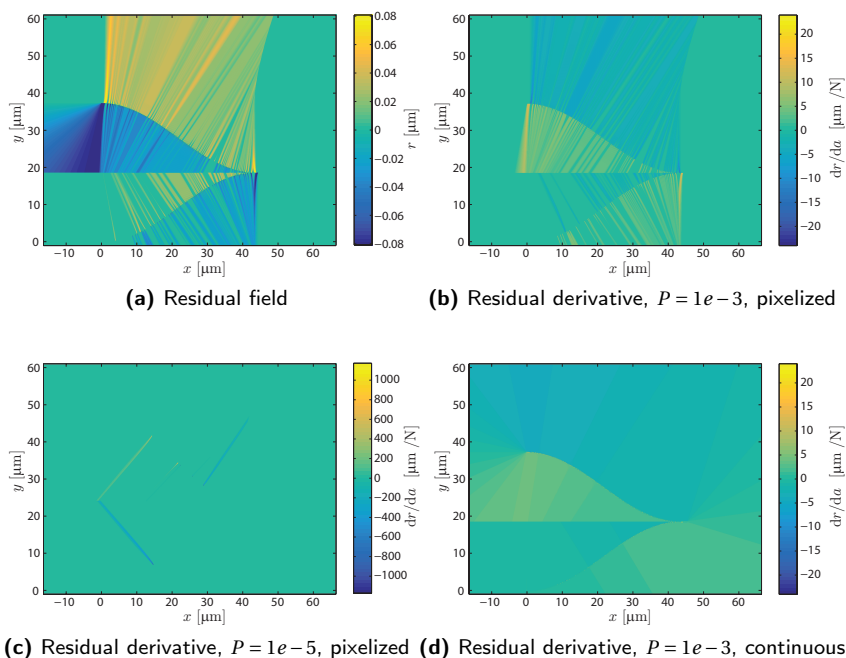
Figure 6.16: Residual field and derivative of the residual, as calculated with Equation 6.15, for one of the increments of the virtual bending beams experiment. The images are created using the pixelized approach for the signed distance maps for Figures (a)-(c). The derivative is calculated for Δa_i with a perturbation factor of $1e-3$ and $1e-5$. The large difference in scale for Figures (b) and (c) occurs due to the difference in order of magnitude in Δa_i, while the derivative is calculated by dividing by this number. In Figure (d) the residual derivative is shown for which the images are created with the continuous approach.

experiments, however, other experimental issues play a role as well and a basic image segmentation method such as binarization may not be adequate to obtain (accurate) correlation and another, more advanced, algorithm might be necessary.

As mentioned before, a possibility for segmenting the image, i.e., differentiating the sample from the background, is a Chan-Vese algorithm [28, 154]. The contour and signed distance map (level sets) following from this algorithm are shown on the left side of Figure 6.19 for a SEM image of a real experiment with the stretchable electronic interconnects from [132]. The Chan-Vese algorithm has two penalty parameters, μ and ν to penalize the length of the curve and the area inside the curve respectively. They can be fine-tuned to make the curve smoother. In Figures 6.19a and b the obtained curve and signed distance map with ($\mu = 0.05, \nu = 0.1$) and without ($\mu = \nu = 0$) penalties on the

(a) Pixelized approach   **(b)** Continuous approach
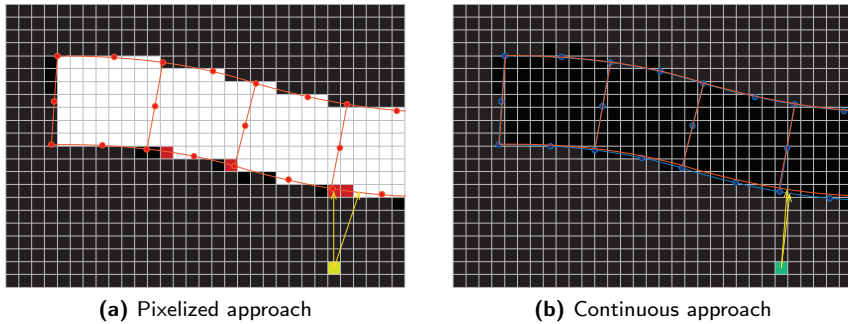
Figure 6.17: Construction of signed distance map for a slightly displaced, due to the update and perturbation of the DoFs, element contour. For the pixelized method (left) the pixels that were located within the edge in the original configuration of Figure 6.3, but not inside the displaced edge are marked red. For comparison, for continuous approach (right) the original element contour (blue) and the displaced edge (orange) are also depicted. In both figures the arrows indicate the closest distance to the binary edge in the original situation and the displaced configuration.

curve length and area are shown. Indeed, the curve where the penalty factors are non-zero is smoother, while the other curve appears wavering because it follows the small "fur-like" features on the surface of the interconnect [69] that are located at the edges. In fact, while these "fur-like" features do not affect the interconnect mechanics, they do significantly alter the signed distance map. Therefore, the micro-fabrication processing should be improved first before a MSC parameter identification on these interconnects can be performed. Nevertheless, a comparison is made with the signed distance maps obtained from numerical simulations. To this end, on the right side of Figure 6.19 the contours and signed distance maps from simulation results are shown. In Figure 6.19c the signed distance map is directly made from the top, bottom and side contours following the FE simulation, consistent with the continuous approach of Figure 6.3 (the binary image behind the contour of Figure c is only shown for visualization purpose, but not used to construct the signed distance map). Note that the resulting signed distance map looks non-smooth at the edges, which is a result of the construction of the signed distance map with a double (top and bottom) contour and a reason to mask out these pixels in the correlation process, as discussed in Section 6.2. The contour (and hence signed distance map) looks significantly different from the ones in Figures 6.19a and b. Besides the simplistic pixelized approach introduced above, another, better, method to make the numerical image correspond to the real one better is to first create a high resolution binary image (e.g., a ten times higher resolution than the experimental image) and then decrease the resolution to the level of the experimental image, whereby the sharp black-white transition is smoothed, thereby mimicking the image capture process of a CCD camera. Then the same Chan-Vese algorithm can be applied to this gray-level

(a) Variation of P

(b) Variation of initial guess, $P = 1e-3$
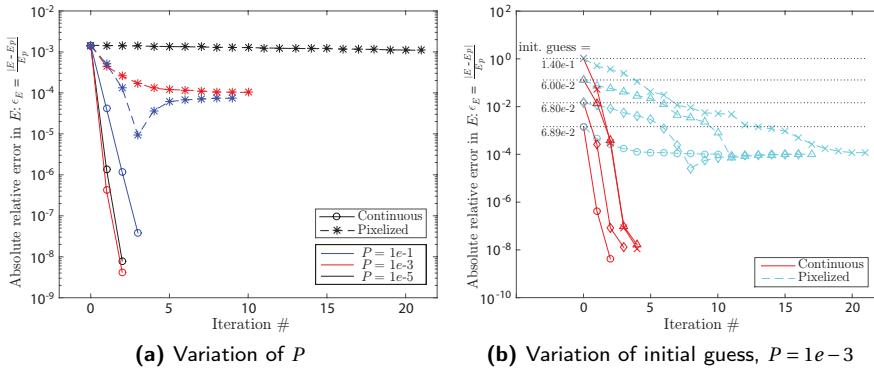
Figure 6.18: Convergence plots of the MSC algorithm for the bending beam experiment. A comparison is made between the continuous approach and the pixelized method for creating signed distance maps. The perturbation factor P is varied, as well as the initial guess.

image to obtain a similar contour and signed distance map as from the real experimental image. The result of this is shown in Figure 6.19d. As the correct plasticity parameters are unknown, the overall shape of the interconnect is different between experiment and simulation, which makes a quantitative comparison impossible. Moreover, the signed distance maps of Figures 6.19b and d are clearly different at the locations of the "fur-like" features. However, from qualitative analysis of a region of a clean edge without these features it is concluded that, for the same Chan-Vese settings, a good resemblance is obtained for the detected edge, in terms of a similar slightly wavy edge and a similar slight short-cut of the edge in the inner corner. Therefore, it is believed that, in absence of "fur-like" features and with further research to select the optimal values of the Chan-Vese penalty parameters, it should be possible to obtain highly similar signed distance maps that are suitable for correlation.

6.5.2 Influence of camera misalignment

Another problem that might arise during real experiments includes inexact agreement between the view of the camera in the experimental setup and the projection angle for the FE simulation. Here the influence of an error in the projection angles and camera position is investigated and a solution is posed. Also, the role of perspective is addressed.

Again, the virtual experiment with the double bending beams with one elastic unknown parameter from Section 6.4.1 is repeated, but now the images are made under an angle instead of the exact YZ-projection. The correlation is performed with an initial guess within the converging regime (Figure 6.10): $E = 10^{-0.2} \cdot E_p$, where E_p is the solution,
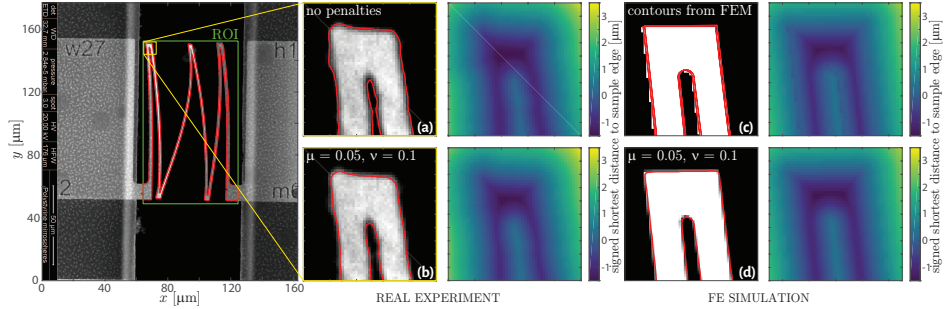
Figure 6.19: Comparison of contours and corresponding signed distance maps obtained from a real experimental (SEM) image and from an FE simulation. For the real experimental image a Chan-Vese algorithm is used to segment the image (figures (a) and (b)), where μ and ν are penalty parameters on the curve length and the area inside the curve respectively, which can be adjusted to obtain a smoother curve. For the numerical images a signed distance map is made directly from the (top and bottom) contours following the simulation (figure (c)) and with the same Chan-Vese algorithm, after mimicking a real experimental image from the simulated contours (figure (d)).

and a perturbation factor of $P = 1e - 3$. In the virtual experiment the azimuth and elevation angles are chosen $-81.2°$ and $40.2°$ respectively. The correlation is performed for a misalignment in these angles up to $4°$, which is a generous upper bound of the inaccuracy with which the viewing angle in a real experiment can be determined. The resulting errors in the objective parameter E are listed in Table 6.1. It can be seen that even for large misalignment the algorithm still converges towards the solution. The error in the Young's modulus is naturally not as small as with a perfectly aligned system, however, it is still reasonable.

Table 6.1: Error in parameter E (according to equation 6.20) after correlation with misaligned projection angles. The true angles, [azimuth,elevation]$= [-81.2°, 40.2°]$, are highlighted in the table. Note that the middle dark blue highlighted value is the error without misalignment.

azimuth \elevation	36.2°	39.2°	40.2°	41.2°	44.2°
$-85.2°$	$1.1 \cdot 10^{-4}$	$4.7 \cdot 10^{-2}$	$6.2 \cdot 10^{-2}$	$8.0 \cdot 10^{-2}$	$1.3 \cdot 10^{-1}$
$-82.2°$	$4.5 \cdot 10^{-2}$	$4.4 \cdot 10^{-5}$	$1.6 \cdot 10^{-2}$	$3.3 \cdot 10^{-2}$	$8.5 \cdot 10^{-2}$
$-81.2°$	$5.8 \cdot 10^{-2}$	$1.6 \cdot 10^{-2}$	$3.8 \cdot 10^{-6}$	$1.7 \cdot 10^{-2}$	$6.9 \cdot 10^{-2}$
$-80.2°$	$7.7 \cdot 10^{-2}$	$3.2 \cdot 10^{-2}$	$1.8 \cdot 10^{-2}$	$3.8 \cdot 10^{-5}$	$5.2 \cdot 10^{-2}$
$-77.2°$	$1.3 \cdot 10^{-1}$	$8.3 \cdot 10^{-2}$	$6.8 \cdot 10^{-2}$	$5.1 \cdot 10^{-2}$	$6.1 \cdot 10^{-4}$

Besides accepting the error occurring due to misalignment, it is also possible to incorporate the projection angles as additional unknown parameters in the correlation procedure. To test this, the same virtual experiment is executed, and moreover, per-

spective is included in the projection as well. The difference between the before used orthographic projection and a projection where perspective is used is shown in Figure 6.20a. This introduces another degree of freedom, namely the position of the camera, which is here defined as the distance of the camera to the object along the normal to the projection plane (which is specified by the projection angles). Hence, this virtual experiment has four unknown parameters, i.e., Young's modulus E, azimuth angle θ_{az}, elevation angle θ_{el} and camera distance d_c. In the case of the viewpoint parameters the sensitivity maps, i.e., residual derivatives, are not determined by performing an extra FE simulation with perturbed parameters, but by directly creating new signed distance maps (and from these the residuals and their derivatives) with perturbed projection angles and camera distance. In the virtual experiment four different initial guesses on the azimuth and elevation angles, ranging from a misalignment of 0.2° up to 10° and on the camera distance, ranging from 5 μm to 50 μm (in comparison, the sample itself is 50 μm in length) are assessed. The initial guess on the Young's modulus is the same for each experiment ($10^{-0.2}$ times solution E_p) and the perturbation factor is again $1e-3$. The resulting convergence behavior is presented in Figure 6.20b. It can be seen that even for a large initial misalignment, i.e., 10° error in the projection angles and 50 μm error in the camera position, the correct solution is found within a small amount of iterations and with high accuracy (order 10^{-4}). This leads to the expectation that in application to real experiments, where the camera view can in general be estimated within ∼ 1°, the material parameters can still be determined accurately, especially if the camera viewpoint specification is included as additional unknowns in the correlation procedure.

6.5.3 Other experimental imaging issues

Imaging can induce many other error sources for image correlation algorithms, for instance changes in illumination, lens aberrations and scanning artifacts (when using a scanning electron microscope). Their influence may be smaller or larger, depending on the problem and the specific experimental conditions, and is worth investigating case-specifically. Some issues can be assessed beforehand and corrected for manually. Others can be addressed by adding representative parameters as degrees of freedom in the correlation, similar to the projection angles above, or the digital image correlation framework could be extended with model functions for the distortions to correct for them, such as has been done for electron microscopy artifacts like spatial distortion, drift distortion and scan line shifts [93, 94].

(a) Projections of double bending beam
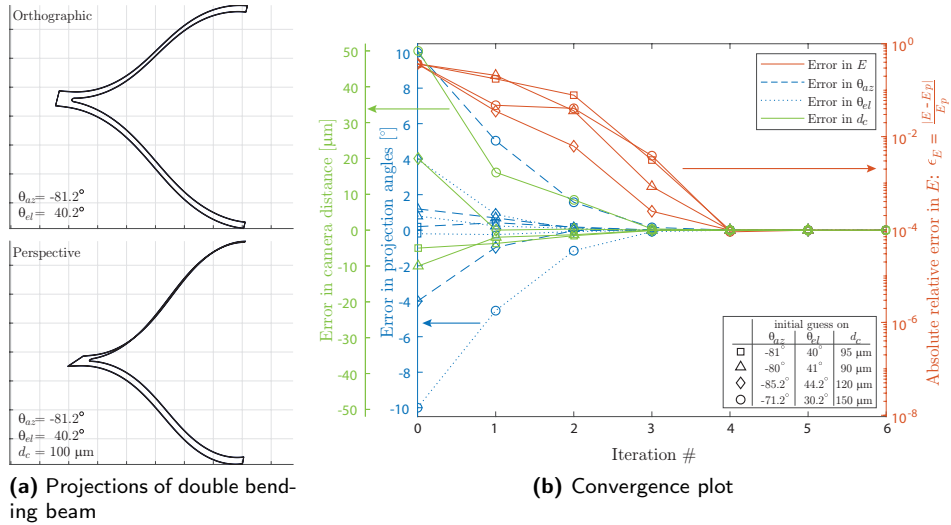
(b) Convergence plot

Figure 6.20: Difference between an orthogonal and perspective projection and convergence plot for the virtual experiment with projection angles as additional unknown parameters. The virtual experiment is repeated for four different initial guesses on the projection angles and camera distance, as listed in the inset table in the right figure. The decrease in error is plotted for all four parameters in the correlation proces, i.e., E, θ_{az}, θ_{el} and d_c. For E the error is calculated by equation 6.20. For the projection angles and camera distance the error is given as the difference in degrees and micrometer respectively between the calculated values and the actual values ($\theta_{az} = -81.2°$, $\theta_{el} = 40.2°$, $d_c = 100\mu$m).

6.6 Conclusions

A novel mechanical identification method, Mechanical Shape Correlation (MSC), has been proposed in this paper. The algorithm is based on Integrated Digital Image Correlation methods, where images taken during an experiment are coupled to a Finite Element model in order to determine correct model parameters. In regular (I)DIC methods a speckle pattern is applied to the sample and correlation of the images is based on the brightness conservation of the pattern. Accordingly, correlation is only possible if the patterned area remains in view and hence large rotations are not permitted. Also, complex and large deformations may lead to severe degradation of the speckle pattern, which inhibits correlation. Furthermore, speckle pattern application can be challenging when dealing with, for instance, specimens of very small or large dimensions. In the MSC method, the images do not consist of a grayscale speckle pattern, but they are projections of the sample, based only on the contour of the structure. The advantage is that complex, three-dimensional deformations form no obstacle for correlation, since the outline of the specimen can be tracked nonetheless. This is beneficial in cases where

such complicated displacement fields occur, but also in cases when it is not possible to apply a speckle pattern. Condition is, however, that the specimen of structure outline changes sufficiently during deformation of the sample.

In this work, the method is applied to virtual experiments on stretchable electronic interconnects, consisting of multiple beams connected to each other. The deformation of the stretchable interconnects is described by two main modes: double bending of the middle beams and torsion of the outer beams. These two deformation modes were analyzed separately and the effect of several algorithmic variables, such as the perturbation factor and the initial guess, was investigated. This was done for an elastic material model with a single unknown parameter, as well as for an elastoplastic power law hardening model with two unknown model parameters, the hardening coefficient A and the hardening exponent m.

In all virtual experiments fast and accurate convergence was obtained within a certain range of initial guesses, which is due to the nature of the signed distance maps, which span the entire image, despite that in the projections the deformations are only reflected in the sample contour instead of the entire sample surface. The perturbation factor, which influences the update in the finite difference approach for calculating the sensitivity of the residual towards the degree(s) of freedom, i.e., the unknown model parameter(s), affects the convergence behavior. A proper perturbation factor for the considered experiments was found to be in the order of 10^{-5} to 10^{-3}. The initial guess regime for which the method converged ranged from two to three times smaller values than the expected solution to two up to four times larger values, depending on how well the deformations can be captured in the signed distance map projections. In the elastoplastic experiment also the dependence of the two parameters A and m via the initial yield strength σ_{y0} played a role. As for any correlation algorithm, physical implications of parameter variations should be taken into account and interdependence of model parameters may lead to poor convergence. Furthermore, improvement of the initial guess robustness is expected if the Gauss-Newton scheme in the algorithm will be replaced by e.g., a modified, constrained minimization approach.

Finally, a step towards real experiments was made. As an ultimate test for the MSC framework, the most rudimentary image segmentation method was explored, i.e. imposing a threshold on the gray level to locate the sample edge, resulting in a pixelized binary image from which the signed distance maps are created. With this image segmentation method, the exact location of the edge is discretely approximated, which reduces convergence. However, convergence was still adequate with a reasonable amount of iterations and with an accuracy of 10^{-4}. Also the influence of misalignment between the camera view in the real experiment and the projection angles used in creating the images from the FE simulation was investigated. It was shown that for angle mismatches up to at least 4° the MSC algorithm still converges towards the solution, however, the accuracy is naturally reduced. Nonetheless, if the projection angles and camera position

(in case a perspective projection is made) are incorporated as additional unknown parameters in the correlation, the algorithm robustly converges towards an accurate ($\sim 10^{-4}$) solution, even for very large misalignments up to at least $10°$ in viewing angle and 50 μm in camera distance. These are promising results for future applications to real experimental images, especially when one of the advanced, (highly) accurate image segmentation methods reported in literature is employed with the MSC method and experimental unknowns, such as projection angles, are added as unknowns in correlation.

Acknowledgements

Chapter 7
Mechanical Shape Correlation: analysis of a real experiment

Abstract

The recently developed Mechanical Shape Correlation method, so far only tested on virtual experiments, has been applied to a real experiment to identify the material parameters of a meso-scale freestanding stretchable electronic interconnect structure. To this end, a stretching experiment was executed on a sample with four beams, triggering the main deformation modes of the structure, while images were captured during the deformation process. The Chan-Vese segmentation algorithm was employed to extract the specimen contour from the experimental images. Caution was taken to adequately match the real experiment with the corresponding model thereof. Special attention was paid to extract the boundary conditions from the experimental images using a global digital image correlation method. First, the MSC method was used to establish the initial configuration of the specimen, which was found to deviate from the ideal perfectly straight configuration, as the clamping pads were displaced and rotated slightly during sample clamping. The parameters describing these deviations, along with those describing the alignment and positioning of the structure within the image frame, were identified successfully. Identification of the plasticity parameters, however, was not feasible for the analyzed experimental test case, which is mainly attributed to the limited amount of plasticity induced in the experiment. The limited sensitivity to these parameters is masked by the larger sensitivity to other dissimilarities between the experimental and numerical images. However, the fruitful analysis of the initial configuration provides confidence that the MSC method is able to work in practice, provided that the experiment is designed such that the sensitivity to the objective parameters is satisfactory, which should be studied thoroughly.

7.1   Introduction

Recently, a novel image-based mechanical characterization method was developed: Mechanical Shape Correlation (MSC) [77]. This method is based on Integrated Digital Image Correlation (IDIC) techniques, where correlation of digital images taken of different loading increments during an experiment is coupled to a Finite Element (FE) simulation, with the goal to identify the parameters of the material model. In contrast to IDIC, where a speckle pattern on the sample is tracked to determine the displacement fields, the correlation in MSC is based on the contour of the specimen. This is an attractive alternative in cases where a speckle pattern cannot be tracked due to, for example, out-of-view rotation of specimen surfaces or if the pattern degrades significantly upon large deformations. It is important, however, that the outline changes sufficiently between increments to be able to track the deformations.

The main application in [77] is a recently developed freestanding stretchable electronic interconnect [132], see Figure 7.1. For designing reliable stretchable electronics it is key to understand the mechanical behavior of the interconnects. Since the micron-size dimensions induce size effects and conditions during manufacturing influence the mechanical properties as well, it is important to evaluate the structures as processed. A key feature of the freestanding interconnect design is that the beams of the structure are free to rotate and align in the stretching direction, thereby enhancing the maximum stretchability tremendously. However, this out-of-view rotation of the beam faces makes it also difficult to analyse the displacements and mechanical properties with (I)DIC methods. The Mechanical Shape Correlation method should be able, however, to track the large contour changes of the interconnects. This has been demonstrated in [77] by means of virtual experiments with these interconnect structures. Several issues expected in real experiments have thereby been addressed, such as the alignment of the images resulting from the numerical simulation and those from the experiment in terms of camera angle and perspective. The aim of the current paper is to assess the MSC method on a real experiment.

Although potential experimental complications have been identified and scrutinized using virtual experiments, there are still some rather specific issues affecting real experiments on the freestanding stretchable electronic interconnects from [132]. The most important one is the presence of "fur-like" features in the available samples that result from the micro-fabrication processing [69], see in Figure 7.1. These features hamper the determination of the true contour of the specimen, thereby complicating the correlation with the numerical contour, in which these features are not present. Furthermore, the micron-sized dimensions of the interconnects imply that images of the experiment need to be captured using a scanning electron microscope (SEM). SEM images reveal a number of artifacts, such as scan line shifts, drift and spatial distortions, that induce error sources affecting image correlation algorithms. Although it is possible to cor-
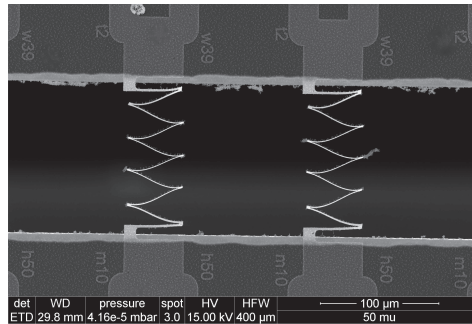
Figure 7.1: Freestanding stretchable electronic interconnect.

rect for them [93, 94], this is not straightforward and would increase the complexity of performing Mechanical Shape Correlation on a real experiment.

Therefore, to assess the MSC method in practice, in this paper a real experiment is performed on the freestanding stretchable electronic interconnect geometry from [132], whereby the original micron-scale structure is scaled up to a 250× larger meso-scale structure (with 12.5 mm long beam members instead of 50 μm long beams). The relative geometry and loading conditions are equivalent and hence, the deformation modes observed at the micron-scale are expected to be the same at the meso-scale. Moreover, for this larger scale the bulk (mechanical) properties of the material are valid, due to the absence of size effects, which makes it easier to validate the material parameters identified with MSC. Therefore, this test case is believed to be relevant for demonstrating the potential of the MSC method.

The paper is organized as follows. First the methodology is explained in Section 7.2: the specimen design and experimental setup are introduced and the MSC algorithm with its main ingredients is briefly described. In Section 7.3 the results of the MSC correlation of the real experiment with the stretchable interconnect geometry are presented. In Section 7.4 conclusions are drawn.

7.2 Methodology

In this Section the methodology adopted for the parameter identification of the stretchable electronic interconnect is presented. First, the sample design is clarified, after which the experimental setup is described. Finally, the Mechanical Shape Correlation algorithm is reviewed, along with the main required input.

7.2.1 Specimen geometry

The up-scaled meso-scale freestanding stretchable interconnect geometry, shown in Figure 7.2, complies to the design introduced in [132], which matches the geometry shown in Figure 7.1, but with four instead of ten beam members. The initially flat structure consists of a rectangular design of multiple freestanding beams that are able to rotate and align with the loading direction upon stretching. The geometry adopted here incorporates four beams, which is the simplest geometry that exhibits all deformation modes upon stretching: torsion of the outer beams and bending of the inner beams.

The size of the up-scaled samples is indicated in Figure 7.2: The beam length and width are 12.5 mm and 0.5 mm. The used material is a 0.075 mm thick Hasberg stainless (spring) steel[1], for which the listed Young's Modulus is 200 GPa and the tensile strength 1400-1600 MPa. Spring steel has been chosen as it is a heavily-used relevant material for beam-like structures and elastic hinges at the macro-scale (in contrast to micron-scale structures which are often made of silicon or aluminum due to available microfabrication processing schemes). However, determination of the plastic parameters of spring steel will be challenging due to its low elongation to failure.
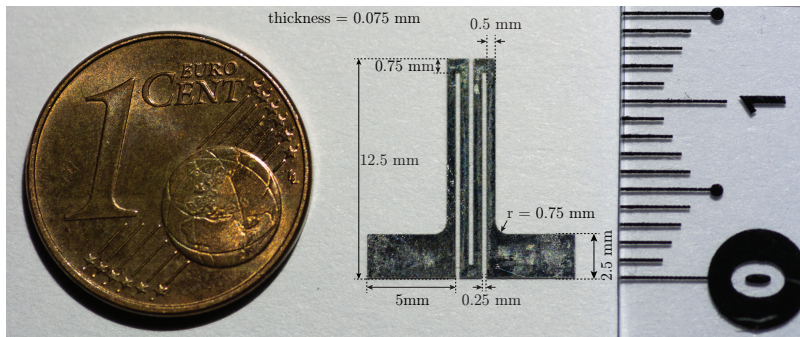
Figure 7.2: Up-scaled freestanding stretchable interconnect sample with dimensions.

7.2.2 Experimental setup

An image of the used setup is shown in Figure 7.3. With the above mentioned dimensions the interconnect samples are well visible to the naked eye, but to capture detailed images during the experiment an optical microscope is used, i.e., the Carl Zeiss Discovery.V20

---

[1]Material number 1.4310:
    https://www.hasberg-schneider.de/en/precision-thickness-gauge-strip-technical-info.html

stereo microscope with a Zeiss PlanApoS 0.63× FWD 81 mm lens. The camera used to capture the images is a Zeiss Axxiocam 506 mono, which is mounted on the microscope on a special camera mount, such that the images are captured straight from above. With this set-up, the alignment between the experimental images and those following from the numerical simulations is more straightforward.
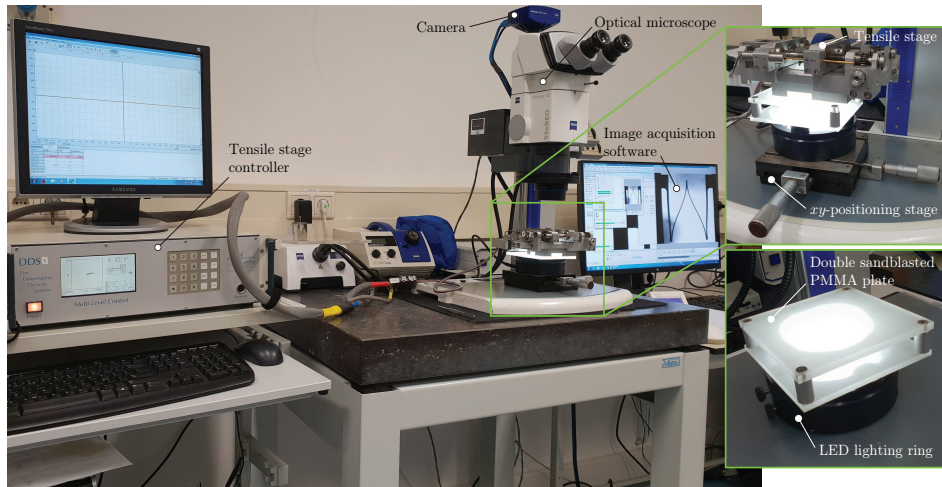
Figure 7.3: Setup used for the experiments. The sample is placed in a micro-tensile stage underneath an optical microscope that is equipped with a camera to capture the images. Underneath the tensile stage a light source is placed with two spaced sandblasted PMMA plates to maximize the contrast between the specimen and the background in the images.

For differentiating the specimen from its background, i.e., to determine the sample contour, a good contrast between test specimen and background is preferred. More importantly, there should be no unexpected reflections of light on the metal surface of the interconnect emitted towards the camera, which would complicate the identification of the sample outline. Therefore, a homogeneous light source (an LED-ring) is placed underneath the sample and a double sandblasted PMMA plate is placed in between to diffuse the light, such that the sample appears black on a homogeneous white background, see Figure 7.4.

For stretching the sample, a micro-tensile stage (Kammrath & Weiss tensile/compression module with a 20N load cell) is used, connected to a controller module that ensures a constant tensile speed of 20 μm/s. In Figure 7.4b an image is shown where the interconnect is stretched by approximately 10 mm. This amount of stretch optimally utilizes the field of view of the used microscopic setup, while still deforming the specimen plastically, as was verified by the lasting deformed shape of the structure when removing is from the tensile stage after the experiment. This is important for identification of the

plastic material properties, which is the objective of the MSC analysis of this experiment.

(a) Undeformed   **(b)** Stretched
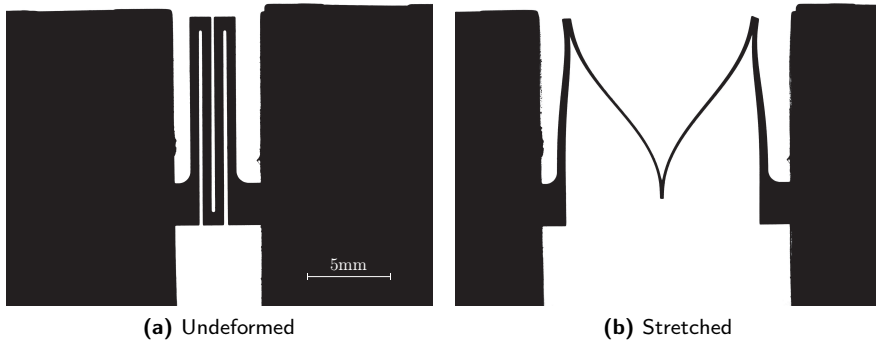
Figure 7.4: Experimental images of the stretchable interconnect sample. (a) The undeformed reference configuration. (b) Stretched by ≈10 mm.

7.2.3   Mechanical Shape Correlation algorithm

The Mechanical Shape Correlation algorithm is an Integrated Digital Image Correlation based method, in which images taken during and experiment are correlated and coupled to a numerical model in order to identify (material) parameters [77]. In contrast to IDIC, the images are not grayscale representations of the speckle pattern on the sample, but they are signed distance maps (SDM) indicating the position of the specimen contour. Each pixel in the image has a value that indicates the shortest distance to this contour. This way, the contour location is reflected in the entire image. Moreover, the images of all time increments are not correlated to the (undeformed) reference image, like in regular (I)DIC, but the experimental signed distance map for each increment is correlated to the signed distance map for the *same* time step resulting from the numerical simulation. The basic idea behind the algorithm is to minimize the difference, i.e., the residual, between each experimental and numerically generated image by iteratively updating the model parameters until an optimal fit between the experiment and simulation is obtained. For more details on the algorithm, the reader is referred to [77].

Signed distance maps

One of the main inputs for the MSC algorithm are the processed images, i.e., the signed distance maps. They need to be determined from the sample contours both from the experimental images and the numerical simulations. Following [77], the Chan-Vese

algorithm is used for segmentation of the experimental images [28, 154], in which the following functional F is minimized:

$$F(C) = \int_{\Omega_i(C)} \left(u_0(\underline{x}) - c_1(C)\right)^2 d\underline{x} + \int_{\Omega_o(C)} \left(u_0(\underline{x}) - c_2(C)\right)^2 d\underline{x} + \mu \cdot L(C) + \nu \cdot A_i(C). \quad (7.1)$$

Here C denotes the evolving curve describing the contour, u_0 represents the intensity values of the (grayscale) image that needs segmentation, with image coordinates $\underline{x} = (x, y)$, and $\Omega_i(C)$ and $\Omega_o(C)$ are the areas of the image parts inside and outside the curve, respectively. Furthermore, c_1 and c_2 (which depend on C) are the average intensities inside and outside the contour respectively. Finally, the curve length $L(C)$ and area inside the curve $A_i(C)$ can be penalized by parameters μ and ν (both ≥ 0), in order to control the smoothness and shape of the segmented contour C.

Following [77], the area inside the contour, i.e. the specimen, is considered white, while the area outside the contour, i.e. the background, is considered black. Therefore, the images taken from the experiment, as shown in Figure 7.4, are inverted. Besides inverting the images, several additional preprocessing steps are taken to improve the correlation with the numerical images. First, the clamps of the tensile stage, i.e. the large black areas on the left and right sides of both images in Figure 7.4 are cropped out, since the clamps themselves are not modelled in the FE simulation.

Furthermore, a Gaussian blurring filter is applied to the images to reduce the impact of image acquisition noise and to obtain a smoother contour. If no blurring filter is applied, the contour follows all small imperfections at the edge of the sample, see Figure 7.5, which are present either because of acquisition noise, or because the processing method resulted in a non-perfectly smooth edge. Either way, it is undesirable that these features are identified as the determined contour, since they are not present in the numerical model. Even if these fine-scale features are part of the real sample (as opposed to noise) it is unfeasible to include all of them in the model geometry.

The contour corresponding to the FE model can be determined directly from the nodal positions and displacements resulting from the simulation, as done for the virtual experiments in [77]. However, to resemble the experimental images as closely as possible, the process of capturing them is mimicked for the numerical images by first creating a binary image at a 10× higher resolution from the simulated contour, which is then down-scaled to the size of the experimental image, thereby smoothing the sharp black-white transitions between background and sample. For this numerically generated image the same process to determine the contour, and signed distance map, is applied as for the experimental images, i.e., the image is blurred with the same Gaussian filter and the Chan-Vese algorithm with the same parameters is employed. These last steps were already introduced in [77] as the first steps towards real experiments.

(a) Original experimental image

(b) Blurred image

(c) Determined contours
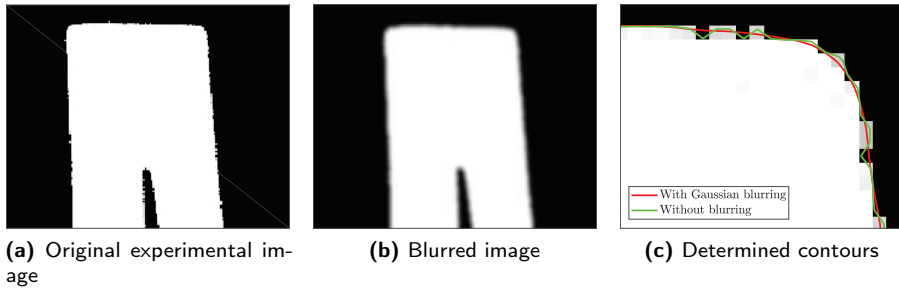
Figure 7.5: The effect of blurring on the contour determined with the Chan-Vese algorithm: (a) zoom of the inverted experimental image; (b) blurred image with a Gaussian blurring filter ($\sigma = 1.5$); (c) contours calculated with the Chan-Vese algorithm (with $\mu = \nu = 0$) for the blurred and original image on top of the original image.

Numerical model

The Finite Element (FE) model is the second important input for the MSC algorithm. The simulation results are compared to the experimental results by directly creating signed distance maps from the simulated contours. Hence, the model should resemble the reality as close as possible. The exact geometry of the experimental samples is implemented, using the geometry and dimensions as used for discharge machining of the specimens, taking into account deviations from this geometry due to processing, such as a slight rounding off of the sharp 90° corners throughout the specimen.

The objective of the MSC analysis is to determine the yielding behavior of the material, and to this end the sample is stretched above the yield point, resulting in plastic deformation. To capture this behavior, an elasto-plastic material model needs to be chosen. The choice for this material model is an important one: it should allow for significant kinematic freedom to be able to simulate the experimentally observed plastic behavior, while it should contain a minimal set of material parameters to provide sufficient sensitivity to all parameters in the MSC algorithm. Here the choice is made for a rate power law model for hardening:

$$\sigma_y = \sigma_{y0} + A\bar{\varepsilon}_p^m, \tag{7.2}$$

with σ_y the yield stress, $\bar{\varepsilon}_p$ the equivalent plastic strain, σ_{y0} the initial yield strength, A the hardening coefficient and m the hardening exponent.

A first MSC step to determine boundary conditions

Applying the exact same boundary conditions in the model as in the experiment is challenging, as demonstrated [119, 123] for the IDIC method. Following suggestions in these papers, here a global DIC step is applied on a region of interest around the clamping pads, where the contrast between the sample and the background is used as a pattern, as opposed to a speckle pattern, which is not present on the examined samples. This is sufficient, since the clamping pads experience rigid body motion only and a negligible strain. Note that although the structure is free to deform three-dimensionally, the clamping pads only displace in-plane and hence DIC is a suitable method to obtain the in-plane rigid body motions. The main displacement is in the x-direction, i.e., the stretching direction, but also the y-displacement and in-plane rotation are calculated for each increment with respect to the reference image. These displacements are translated to displacement boundary conditions on all nodes at the edges of the clamping pads in the FE model.

Furthermore, it is observed in the reference image, Figure 7.4a, that the initial configuration is not perfectly aligned. The beams are slightly rotated with respect to each other due to clamping of the sample in the tensile module. This reference configuration should also be transferred to the simulation. It is not possible to manually determine the rotation and displacement of the pads with respect to a perfect straight alignment with sufficient accuracy. Therefore, a Mechanical Shape Correlation analysis is performed on the reference image only, with the displacements and rotations of the clamping pads as degrees of freedom, see Figure 7.6. The results of this MSC step will be used to 'initialize' the FE model of the clamping pads of the stretching experiment, by adding a prior increment to the simulation in order to position the structure in correspondence with the reference configuration in the real experiment, thereby also incorporating the current stress state due to clamping.

In the distorted clamped reference configuration, the images that are created from the numerical simulation must align with the experimental images in terms of positioning and sizing of the structure within the picture frame. This is determined by the image coordinate vectors in terms of real dimensions. The variables defining these vectors are also added as degrees of freedom in the MSC analysis of the reference image. The three degrees of freedom are the x- and y-component of the (subpixel) location of the origin that is used in the simulation, which is the left bottom corner of the structure (see Figure 7.6), and the pixel size in terms of the real dimensions. Since the boundary conditions for each increment are determined relative to the reference situation, the alignment of the structure on the pixel grid needs to be done only for the first, reference, image, while the same image vectors can be used for the MSC step in later increments. Hence, a two-step approach arises, in which the initial state is correlated in the first step and the actual (plastic) material parameter identification is correlated in the second step.
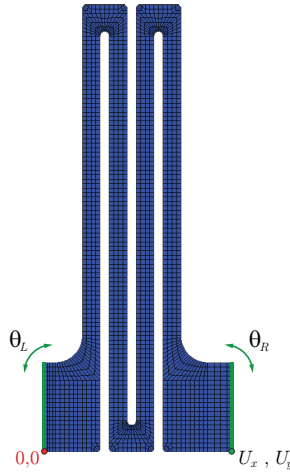
Figure 7.6: Degrees of freedom in the initial MSC analysis to determine the displacements of clamping pads in the initial configuration due to clamping of the sample. The bottom left corner of the left pad is assumed fixed (as the position and size of the structure within the image frame is described with separate degrees of freedom), while the rotation of the left edge around this point θ_L is a DoF. The x- and y-displacement of the right bottom corner of the right pad, U_x and U_y, are DoF's as well, along with the rotation of the right pad edge around this point, θ_R.

7.3   Results

The results of the correlation of the real experiment with the meso-scale freestanding stretchable interconnect structure are presented in this Section. First, the initialization correlation for alignment of the clamped reference configuration is considered, after which the parameter identification of the interconnect material is discussed.

7.3.1   Correlation of the initial configuration

As described in Section 7.2.3, the first correlation concerns the alignment of the initial configuration of the FE simulation with respect to the reference image of the clamped sample. Seven degrees of freedom are thereby determined. Four parameters relate to the actual deformation of the interconnect due to clamping, i.e., the rigid body rotations θ_L and θ_R of the left and right pad respectively and the rigid body displacement of the right pad in both the x- and y-direction, U_x and U_y. The other three parameters are associated with the alignment of the structure on the pixel grid, i.e., the subpixel

location of the FE model's origin, O_x and O_y, and the pixel size pxs in millimeters.

Table 7.1: Degrees of freedom in the correlation of the initial configuration. The initial guess of the parameters is listed, as well as the value resulting from the correlation.

Parameter		Initial guess	Calculated value
Rotation of left pad	θ_L	-0.25°	-0.11°
Rotation of right pad	θ_R	0.25°	0.25°
x-displacement of right pad	U_x	0.0 mm	0.053 mm
y-displacement of right pad	U_y	0.0 mm	0.020 mm
Subpixel x-location of origin	O_x	1081	1072.7
Subpixel y-location of origin	O_y	520	518.9
Pixel size	pxs	$9.25 \cdot 10^{-3}$ mm	$9.297 \cdot 10^{-3}$ mm

The correlation is executed and the resulting parameters are listed in Table 7.1, along with the initial guess of these parameters, which is based on an approximate manual alignment. Since the correlation applies to a real experiment, the actual parameters are unknown and it is not possible to validate the results in terms of the error in the determined parameters. However, a measure for the accuracy of the correlation is the residual, i.e., the difference between the signed distance maps resulting from the experiment and from the numerical simulation. The residual is the minimization objective in the correlation algorithm and hence should decrease upon convergence. The residual images before and after correlation are shown in Figure 7.7, along with the evolution of the mean of the absolute value of the residual during the iterations of the correlation. The residual indeed shows a significant decrease, indicating that the FE simulation is correlating well to the experiment. Furthermore, the calculated value for the pixel size is close to the value specified by the software of the microscope/camera system. Therefore, it is concluded that the results are reliable. Moreover, this is a first successful demonstration of the MSC method to identify experimental parameters, though not yet material parameters.

7.3.2 Parameter identification

The results from the previous correlation are used to implement a pre-step in the FE simulation to adjust the perfectly straight modelled interconnect geometry to the clamped initial state, in which the pads and beams are slightly displaced and rotated with respect to each other. The complete FE simulation, in which the interconnect is stretched by prescribing the previously determined displacements of the clamping pads (using global DIC as described in Section 7.2.3), is then correlated to the experimental images of the stretching experiment in order to identify the parameters in the plasticity
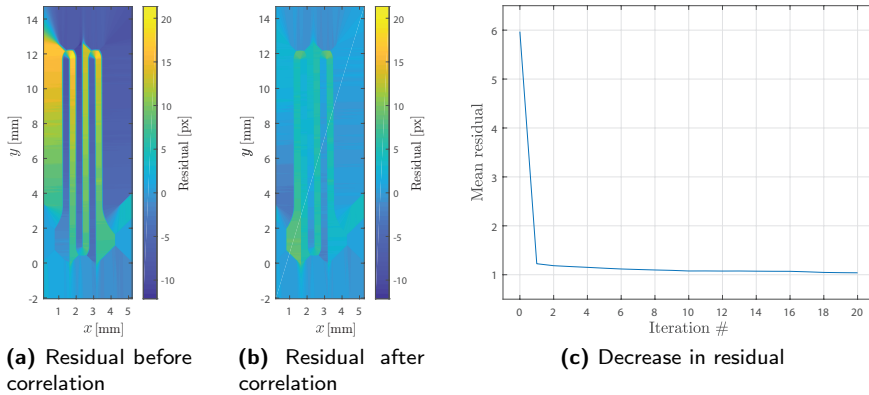
(a) Residual before correlation

(b) Residual after correlation

(c) Decrease in residual

Figure 7.7: Decrease of the residual after the correlation. Left: the residual image before correlation, i.e., where the initial guess on the parameters is used; Center: the residual image after correlation, with the calculated parameters; Right: the decrease of the residual as the mean value of the residual as a function of the iterations during the correlation.

model. During the experiment a total of 50 images were captured, from which only a selection is used, as explained below.

To provide a reasonable initial guess for the material parameters, a uniaxial tensile experiment is executed on a single beam member of the interconnect in order to estimate the parameters in the hardening model of Equation 7.2. The strain is calculated from the elongation of the test specimen, which is determined from the displacements of the beam ends with a simple local DIC method. The stresses are calculated from the forces that are measured directly via the tensile stage, while the evolving cross-sectional area is estimated from the elongation of the sample assuming volume conservation. The parameters of the hardening model, as well as the Young's modulus, have been fitted to the data, see the table in Figure 7.8. Note that even for this simple one-dimensional case it was not possible to obtain an unambiguous solution for (the initial guess of) the model parameters, which is also noticed through the absence of a clear yield point due to the significant amount of hardening. Moreover, the calculated initial yield strength equals the visually estimated set lower bound, which was used because the fitted value unrealistically approached 0 without a lower bound. This dependence between the yield strength and hardening parameters may indicate cross-sensitivity between the plastic parameters, which further challenges the MSC parameter identification. As the fitted values seem to constitute an adequate guess, they are used as an initial guess for the MSC routine. A numerical simulation with the fitted parameters shows that plasticity sets in already early on in the experiment, which suggests that correlation of the plasticity parameters might still be possible with this experiment. To ascertain that the selected images are far enough in the plastic regime, two increments at the end of

the experiment are selected for correlation, namely the images of increment 45 and 50.
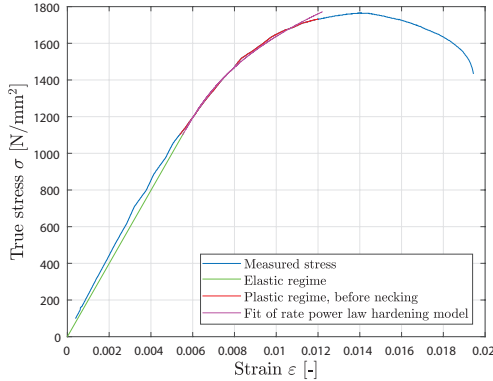
Parameter		Value	
Young's modulus	E	200	[GPa]
Initial yield strength	σ_{y0}	1100	[MPa]
Hardening coefficient	A	5300	[MPa]
Hardening exponent	m	0.36	[-]

Figure 7.8: Stress-strain curve for a uniaxial tensile experiment on a tensile sample made from one of the (12.5 mm-long) interconnect beams. The measured ultimate tensile strength is slightly higher than the specified value (1400-1600 MPa) for the considered material. The three parameters of the hardening model for plasticity, Equation 7.2, have been fitted on the data in order to provide an initial guess for the MSC correlation. The found Young's modulus corresponds to the specified value for the used material. Note, however, that the identified yield strength equals the set lower bound of 1100 MPa.

The MSC material parameter identification is performed for all three parameters (σ_{y0}, A and m) simultaneously with the determined initial guess. As the minimization seems to consistently converge to local minima (not shown), the sensitivity of the correlation towards the three degrees of freedom is investigated by inspecting the correlation matrix, see figure 7.9. The correlation matrix represents the Hessian of the Gauss-Newton scheme that is used in the MSC algorithm and it provides insight in the sensitivity of the objective function to the degrees of freedom, as is suggested in the literature [57, 100, 124]. The sensitivity towards the hardening coefficient, A, is significantly lower than for the other two parameters. Moreover, large cross-sensitivity between the parameters is observed, e.g., the off-diagonal values of M_{21} and M_{31} are higher than the on-diagonal values of M_{22} and M_{33}. Another indication of the limited sensitivity of the objective function in the correlation with respect to the parameters is shown in the sensitivity maps, i.e., the derivatives of the residual, see Figure 7.10. The sensitivity maps are qualitatively equivalent for all three parameters, despite a large perturbation of all parameters (a perturbation factor of 10^{-1} is used to determine the sensitivity maps). This indicates that the residual is affected more by other factors, such as remaining differences between the experiment and simulation, than by a change in the material parameters, which makes correlation of the parameters very difficult.
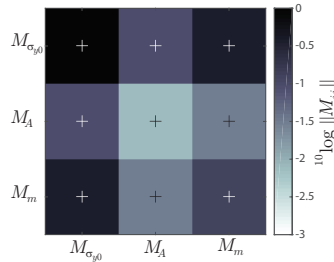
Figure 7.9: Graphical representation of the correlation matrix M for correlation of the three parameters of the hardening model, σ_{y0}, A and m.

The correlation between the experimental and numerical images is strongly affected by the boundary conditions. Despite careful determination of the boundary condition (i.e., the applied displacement) on the clamping pads with a global DIC algorithm, it is possible that discrepancies remain. Therefore, another MSC correlation is executed solely for the initial yield strength, as this is the parameter with the highest sensitivity, while the applied x-displacement of both the left and right pad is also incorporated in the correlation as degrees of freedom, constituting four additional degrees of freedom for the two images. The perturbation on these DoFs is taken 10^{-6} mm, which is approximately 10^{-4} pixel and much smaller than the expected accuracy of the global DIC correlation previously used to determine the boundary conditions a priori. This results in a new correlation matrix, see Figure 7.11, which reveals that the sensitivity towards the boundary conditions is much larger than that of the material parameter (σ_{y0}). The negligible sensitivity of the images with respect to the material parameters makes it impossible to identify the material parameters from this particular experiment.

Improvement of the identification requires increasing the sensitivity of the signed distance residuals towards the material parameters, i.e., to properly trigger a material response in the plastic regime. For this experiment this implies that the specimen should be stretched further, to increase the effect of plasticity in the hinges on the beam shape. Also the number and the selection of increments deserves attention, as the sensitivity may vary for different increments. The small amount of images used was justified here because both increments are relatively far in the plastic regime (judging by the numerical simulation with estimated plasticity parameters and the permanent deformation of the specimen after removing it from the tensile stage posterior to the experiment). Different parts of the structure are in different stress-states (elastic or partially plastic), whereby distinct regions of the signed distance maps cover various parts of the stress-strain-curve. Note that correlation was also attempted for a set of four incremental images, spread further apart across the experiment, for which the same conclusions as above resulted. Also other experiments with the stretchable
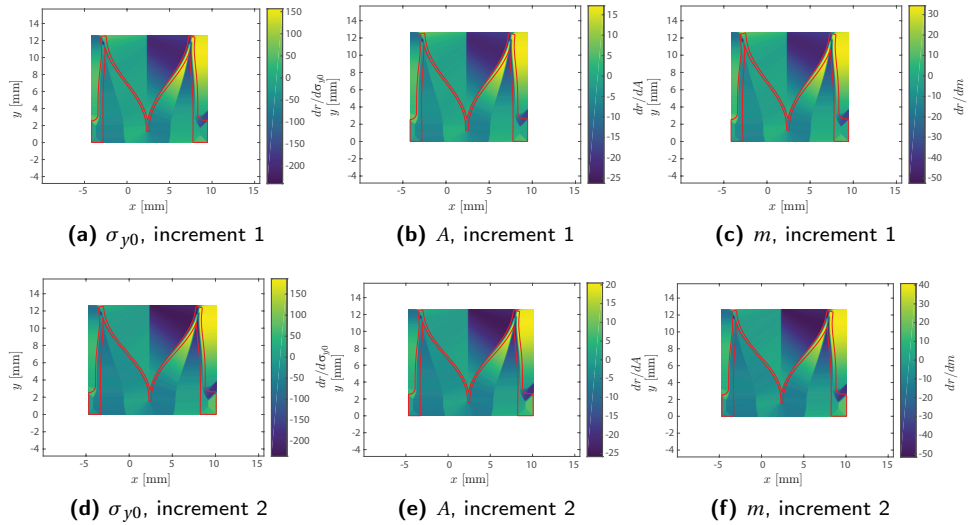
(a) σ_{y0}, increment 1   **(b)** A, increment 1   **(c)** m, increment 1

(d) σ_{y0}, increment 2   **(e)** A, increment 2   **(f)** m, increment 2

Figure 7.10: Sensitivity maps, i.e., residual derivatives with respect to the degrees of freedom, for the three parameters and two increments. The masked region is outlined by the red shape. It is observed that the sensitivity maps are qualitatively equivalent for all three parameters, only the values differ.

interconnect should be considered, as different loading conditions affect the sensitivity of the correlation as well [125].

It was also observed that the geometry in the numerical model is not exactly the same as that of the real specimen. Although rounding of the corners was taken into account, the exact radius was approximate and should be determined more accurately. Furthermore, the beam width appears slightly larger in the real sample than the specified geometry, causing the distance between the beams and the inner radius of the hinges (and hence the signed distance map in these areas) to be inexact in the numerical images. However, the geometry was already inexact in the MSC correlation of the initial configuration, which did converge, indicating that these deviations in geometry are probably not the main issue. Previous research has shown that the exact agreement of boundary conditions is very important [119, 123]. Despite the caution already taken (i.e., the pre-step of using global DIC to extract boundary conditions on the clamping pads, correlation of the initial configuration and incorporating the x-displacement of the pads as degrees of freedom in the correlation), further improvements can be made by incorporating more unknowns on the boundary conditions in the correlation. For instance, the y-displacement and rotations of the pads could be included, as these influence the positioning and displacement of the beams of the structure, thereby affecting the entire signed distance map. However, additional degrees of freedom may
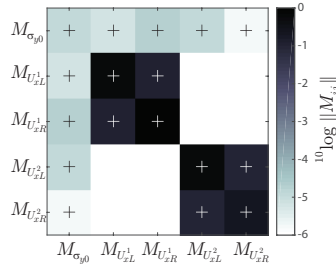
Figure 7.11: Graphical representation of the correlation matrix M for correlation of the initial yield strength σ_{y0} along with boundary conditions on the clamping pads, i.e., the displacement in x-direction U_x, where the subscripts L and R refer to the left and right pad respectively and the superscripts 1 and 2 to the two selected increments. It is observed that the sensitivity towards the boundary conditions is much higher than to the initial yield strength. Moreover, a strong cross-sensitivity exists between the initial yield strength and the boundary conditions.

increase the ill-posedness of the problem and should be carefully considered.

7.4   Conclusions

The previously developed Mechanical Shape Correlation algorithm was applied to a real experiment in order to assess its feasibility in practice. The method was applied to a stretching experiment of a meso-scale stretchable electronic interconnect structure. The procedure to extract signed distance maps from the experimental images and from the numerical simulations was optimized by blurring the images, in order to improve the agreement between them by eliminating edge artifacts. Considerable attention was given to the boundary conditions in the numerical model, as this is known to largely impact correlation for integrated DIC approaches. To this end, a global DIC algorithm was applied to the clamping pad regions to access the in-plane displacements and rotations.

Moreover, the initial configuration of the experiment appeared to be not in agreement with a perfectly straight modeled structure, as clamping the sample in the tensile stage caused small displacement and rotation of the pads. An initialization correlation was executed in order to identify these displacements and rotations, to be used in the subsequent numerical simulation as a pre-step. Also the alignment of the images from the experiment and from the simulation in terms of pixel size and positioning of the structure within the image frame was included in this correlation, leading to a total of seven degrees of freedom. This correlation was successful: the residual decreased and reliable values for all parameters was found. This is the first time the MSC method has

been successfully applied to real experimental data.

It appeared unfeasible, however, to identify material parameters in the hardening plasticity model for the stretching experiment considered here. The sensitivity of the correlation towards the material parameters was found to be too low with respect to the sensitivity towards other discrepancies between the numerical and experimental images. Recommendations for future research on applying MSC to a real experiment encompass increasing the sensitivity towards the material parameters, by ensuring enough plasticity occurs in the sample during the experiment. The used material, i.e., spring steel, was a too challenging case and if another, softer, material is used, this may induce an increased plastic response. Furthermore, it can help to examine the selection of images and analyze other loading modes of the specimen. Additionally, the sensitivity to other artifacts should be diminished as well as possible by, e.g., including more boundary conditions in the correlation and improving the model geometry.

Despite the inability of material parameter identification for this experiment, an adequate correlation was obtained for the parameters describing the initial configuration in this real test case, indicating that it actually is feasible to use the MSC method, provided that a sufficient sensitivity to the objective parameters is reached.

Acknowledgements

Chapter 8
Conclusions and recommendations for future research

For the development of reliable applications of stretchable electronics, it is key to study and predict the mechanical behavior of stretchable interconnects. Numerical modeling is an important tool to this end, but it is essential to incorporate realistic material behavior. For these miniature interconnects the properties are affected by size effects, processing history and loading conditions. Therefore, the necessity arises to directly test and analyse the as-processed interconnects, in contrast to testing standard samples made from the corresponding bulk material. The identification of material properties from these tests calls for advanced analysis methods, as the complex three-dimensional deformations of the interconnect structures complicate the use of existing techniques. Henceforth, the goal of this dissertation was "the development of state-of-the-art image based algorithms for the mechanical characterization of stretchable electronic interconnect structures and the identification of material parameters in representative mechanical models".

In this thesis two classes of techniques were presented: Global Digital Image Correlation (GDIC) methods and Integrated Digital Image Correlation (IDIC) based methods. The first categorie was used for the analysis of horseshoe patterned aluminum interconnects on a polyimide substrate, of which the deformation is characterized by out-of-plane buckling upon interface delamination. The latter set of techniques was applied to the characterization of recently developed nanoscale highly stretchable freestanding aluminum interconnects, also denoted ROPE interconnects, referring to the Rotation and Out-of-Plane Elongation deformation of this design.

In Chapter 2 a DIC method equipped with an adaptive refinement algorithm was introduced. NURBS shape functions were used because of their versatility and their ability to describe many shapes, which is convenient for parametrization of the meandering interconnect geometry. The shape functions discretizing the displacement field are autonomously refined in the regions where needed, based on the image residual, such that an optimized set of shape functions is obtained, which is sufficiently rich to de-

scribe the kinematics. At the same time, the amount of degrees of freedom remains limited in order to promote robustness against correlation to local minima and noise. It was proven by means of virtual and real test cases with strong localizations in the displacement field that the shape function mesh indeed refines autonomously in the areas of localization, without supplying their location to the algorithm a priori. Moreover, the displacement fields were calculated more accurately with this refined mesh than a uniform mesh with the same amount of degrees of freedom.

The deformations of the horseshoe shaped aluminum/polyimide interconnect system are mainly characterized by buckling of the metal interconnect after delamination of the interconnect/substrate interface. The locations of these buckles depend inter alia on the interconnect geometry and are not known a priori. In order to measure these localized deformations, the adaptive isogeometric DIC algorithm was extended to adaptive isogeometric Digital Height Correlation (DHC) in Chapter 3. Height maps of the interconnects, containing three-dimensional information on the surface, captured during a stretching experiment, were successfully correlated in order to obtain the three-dimensional surface displacements. It was shown that the shape function mesh refines autonomously at the buckle locations and remains coarse in other areas, which is beneficial for robustness. This is especially important since it was challenging to obtain reproducable height measurements from the nanoparticle speckle pattern on the specimen.

In Chapter 4 the measured displacement fields of the horseshoe interconnects were used to identify the interface delamination between the aluminum interconnect and the polyimide substrate. It was found that the onset of delamination occurs at approximately 7% global stretch of the specimen. For different specimen geometries different locations and geometries of the buckles were observed and also the global stretch percentage, at which delamination has proceeded enough for buckles to emerge, differs per interconnect geometry. The obtained displacements were qualitatively compared to numerical simulations with a cohesive zone model, in order to identify proper values for the parameters in this model. It was found that it is important to incorporate mode angle dependence of the cohesive zone parameters in the model. This mode angle dependency was attributed to the low surface roughness of the aluminum interconnect, which leads to the absence of fibrils that can align with the load direction. The ratio of the ultimate tractions in shear and normal direction, for which the best correspondence with the experimental data was observed, was found to be $\tau^s_{max}/\tau^n_{max} = 30/6$ MPa, and the critical energy release rate values, $G^n_c = 37$ J/m^2 and $G^s_c = 111$ J/m^2. A predictive simulation with these obtained parameters for a different geometry yielded an adequate agreement with the experimental observations.

For the characterization of the deformations of the freestanding ROPE interconnects an Integrated Digital Height Correlation (IDHC) algorithm was developed in Chapter 5. An experiment was analyzed in which the specimen was loaded out-of-plane, in order to

trigger one of the main deformation modes of the interconnect, i.e., bending of the beam members in an S-shape, while still keeping the surfaces in view to be able to measure height maps of the sample. First, a global isogeometric DIC method was applied to the topographies in order to determine boundary conditions, which are influential for the numerical model that is used in the integrated approach to regularize the displacement field. The IDHC algorithm was used to identify model parameters describing the plastic regime, i.e., the initial yield strength σ_{y0}, the hardening exponent m and hardening coefficient A. In a virtual experiment a successful correlation of all three parameters was achieved, however, the convergence behavior already revealed the underlying complexity of the problem. In the challenging experimental test case, where the micron-sized dimensions and large three-dimensional deformations complicated an accurate topography acquisition and where model errors emerged, a satisfactory simultaneous correlation of all three parameters could not be obtained. However, in uncoupled correlations for the initial yield strength and hardening exponent, convergence, though moderately accurate, was reached and the parameters were established at 225-300 MPa and 0.15-0.2 respectively, which indicates a significant strengthening effect due to miniaturization, compared to the bulk value for aluminum of roughly 70 MPa.

The ROPE interconnect was designed such that upon stretching the beams rotate to align with the stretch direction, providing the high stretchability. However, when performing a stretching experiment on the interconnects, the above mentioned DIC methods cannot be applied, as the surfaces rotate out-of-view. In Chapter 6 a novel method was introduced, Mechanical Shape Correlation (MSC), that correlates two-dimensional projections of the three-dimensional specimen, i.e., signed distance maps in which each pixel is assigned a value representing the distance to the sample contour, whereby the displacement information of the specimen outline is reflected in the entire image. This method is an integrated method as well, where these signed distance maps are generated from an FE model, enabling tracking of three-dimensional displacements via the two-dimensional projection images based on the specimen outline. The method was successfully applied to virtual experiments, where fast convergence and accurate results were demonstrated. Also the influence of inaccuracies in camera alignment in the experimental setting versus the projection angle and the perspective view when generating signed distance maps from the simulation was investigated and it was concluded that for relatively large misalignments adequate converge still is achieved. Moreover, the complications mentioned above can be resolved by including these parameters as unknown degrees of freedom in the correlation.

The MSC method was also applied to a real experiment on a meso-scale freestanding interconnect structure in Chapter 7. First the initial configuration was correlated separately, because the perfectly straight modeled structure did not correspond to the initial configuration of the interconnect in the experiment, since the clamping pads had been slightly displaced and rotated during clamping in the tensile stage. The in-plane displacements and rotations of the pads, as well as the parameters describing the posi-

tioning and sizing of the structure within the image frame, were correlated successfully. This is the first time MSC was successfully applied to real experimental images. The results were used as a pre-step in the correlation of material parameters of the plasticity model in the stretching experiment. However, the sensitivity of the correlation to these parameters was too low to obtain convergence towards a solution.

Recommendations for future research

The presented DIC methods in this thesis constitute in essence an optimization algorithm. Usually for DIC algorithms a Gauss-Newton scheme is used, in which the expensive calculation of second-order derivatives is omitted. This is a significant advantage, especially in integrated DIC calculations, where the FE simulations usually induce the highest computational cost. However, in this method convergence is not guaranteed and it may be slow, especially for initial guesses far from the solution. Hence, if no convergence is achieved, it could be interesting to look at other optimization methods. In Appendix B the gradient-free Nelder-Mead optimization scheme is investigated, for which it is concluded that the robustness is attractive, however, many iterations are required to reach convergence. It is advisable to study the possibility of starting the correlation with a more robust, but slow, optimization scheme and switch to a faster method when approaching the solution.

The experiments that were executed for the analysis of the ROPE interconnects faced many challenges, which affected the correlation of the resulting images. Manufacturing of the test specimens was achieved through a pioneering lithography processing scheme in order to make the very thin interconnects freestanding. This caused warping of the interconnects, which was incorporated in the finite element models under the assumption of a stress-free relaxed state. However, if residual stresses were still present in the samples, this would definitely influence the accuracy of the correlation results. Furthermore, fur-like features on the interconnects were a processing artifact, which influenced mainly the extraction of the sample contour for the MSC methods. Also the frailness of the specimen imposed challenges in sample handling and impacted the amount of usable test specimens, which entailed low reproducibility of the experiments and prevented the possibility of thoroughly exploring different experimental settings, e.g., concerning pattern application. In the cause of the SLIC-project (Stretching the Limits of Integrated Circuit Stretchability), of which this work is part, the processing method has already advanced and it would be interesting to perform novel tests on improved specimens and more rigorously study the effects of different experimental settings on the captured images or topographies and the correlation on them.

Besides the test samples, also the microscopy techniques for imaging the small interconnect dimensions, posed difficulties. Reproducibility of the height maps measured with an optical profilometer was hampered by the present high gradients at the sample

edges and the nanoparticles applied as height pattern. The height maps of the ROPE interconnects are even more troublesome for the DIC algorithms. Due to the small size the resolution in the region of interest is relatively low. The lateral resolution could be increased by using another profilometry system that combines low-noise measurement with multiple surface scans with subpixel shift (e.g., using a piezo stage) and a smart algorithm for combining the scans. For the MSC method, which accepts two-dimensional images, Scanning Electron Microscopy (SEM) can be used to capture high-resolution images of the interconnects. However, it is necessary to correct for artifacts that arise with this method, e.g., scan line shifts and drift distortions. It is possible to combine the MSC algorithm with the in [93, 94] developed correlation framework, which incorporates model functions for these distortions. This will be challenging however.

For the integrated correlation methods, more complex virtual test cases revealed the importance of the proper understanding of the problem one wants to correlate. Although the MSC method converged for an initial guess regime ranging from two to three times smaller values than the true solution to two up to four times higher values, the method is more likely to converge towards an accurate solution if the user is able to supply an educated initial guess, which is a known advice for IDIC methods. Also interdependence, or cross-sensitivity, of model parameters complicates convergence, especially if the initial guess is relatively far from the solution. Therefore, it is recommended to analyze the sensitivity of the correlation towards the parameters of interest and if necessary adjust the experiment (e.g., the loading mode) to achieve better sensitivity, and to provide a proper initial guess by e.g., performing a simple tensile experiment, if possible, to obtain a good estimate on several material parameters.

For Mechanical Shape Correlation, in real test cases the most important factor that negatively affects the correlation was expected to be the inexact agreement between the signed distance maps from the experiment versus those from the numerical simulation. Foremost, the method of extracting the contour information from the experimental images could pose difficulties. Virtual experiments investigating this effect indeed showed reduced convergence and accuracy. Nevertheless, convergence towards the true solution was still obtained. In real experiments, however, were also other inaccuracies play a role, it is important to use more sophisticated methods for contour extraction, such as the in Chapters 6 and 7 used Chan-Vese algorithm. The downside is that computation time increases significantly. It would be interesting to study different methods as well, balancing accuracy with computational costs.

When applying MSC to a real experiment, the importance of sufficient sensitivity towards the objective parameters was revealed. It is recommended that the experiment is designed such that the sensitivity towards these parameters is dominant and the sensitivity to other disagreements between the experiment and simulation is diminished. In order to provide a proof of concept, where the exact material is of lesser importance, it is wise to select a material that experiences significant plastic deformation in order to

ensure sufficient sensitivity to plastic material parameters. However, if a specific material is the objective for identification, other tactics for increasing the sensitivity need to be employed. For instance, different loading modes should be considered to optimize the response to a change in the parameters, boundary conditions can be included as degrees of freedom in the correlation and it should be studied which increments of the experiment are most valuable to correlate on. The conclusions on MSC on the meso-scale experiment stretch the assumption that various experimental issues with the real stretchable electronic interconnects on micron-scale have a detrimental affect on the correlation and that it is not straightforward to circumvent these difficulties. Further study is required to obtain a good identification of material parameters using this method, as is also true for other applications on different scales.

For the identification of material parameters of the ROPE interconnects using IDHC, also the inexact agreement between model and reality appeared highly detrimental. The geometry of the real specimen is rather complex due to deviations from the design through processing, i.e., curving of the beams due to residual stresses and possible defects due to the delicate nature of the micron-sized freestanding structure. Also the measurement technique, which faces complications at the edges of the sample, inhibits accurate measurement of the exact geometry to be transferred to the numerical model. An improved initial geometry could be obtained if a topography measurement is executed on the sample before the etching step where the interconnect is released from the sacrificial layer and hence is still straight. If this topography is correlated to one of the sample after it has been made freestanding, the full-field in-plane and out-of-plane deformations could be determined by the isogeometric global DIC method, which is more accurate than the manual manner at pixel-level in which the in-plane displacements had to be determined in this case.

Furthermore, the adopted simple isotropic material model for plasticity might not be able to describe the true material behavior of the ROPE interconnects sufficiently accurate. At this small scale, the microstructure, which is expected to consist of only few columnar grains, influences the behavior. Therefore, a crystal plasticity material model taking this into account would be a more suitable choice. If this also appears insufficient, variations of this model with increasing complexity can be evaluated, e.g., adding strain gradient or even dislocation density effects [43].

Bibliography

[1] Ahn JH, Je JH. (2012) Stretchable electronics: materials, architectures and integrations. *Journal of Physics D: Applied Physics*; **45(10)**: 103001. DOI: 10.1088/0022-3727/45/10/103001.

[2] Autodesk. *AutoCAD software*; http://www.autodesk.com/products/autocad/overview.

[3] Barker DB, Fourney ME. (1977) Measuring fluid velocities with speckle patterns. *Optics Letters*; **1(4)**: 135-137. DOI: 10.1364/OL.1.000135.

[4] Bay BK, Smith TS, Fyhrie DP, Saad M. (1999) Digital volume correlation: Three-dimensional strain mapping using X-ray tomography. *Experimental Mechanics*; **39(3)**, 217-226. DOI: 10.1007/BF02323555.

[5] Bazhenov SL, Dukhovskii IA, Kovalev PI, Rozhkov AN. (2000) The fracture of SVM aramide fibers upon a high-velocity transverse impact. *Polymer Science*; **43(1)**: 61-71.

[6] Beaubier B, Dufour J-E, Hild F, Roux S, Lavernhe S, Lavernhe-Taillard K. (2014) CAD-based calibration and shape measurement with stereoDIC. *Experimental Mechanics*; **54(3)**: 329-341. DOI: 10.1007/s11340-013-9794-6.

[7] Beeck J van, Neggers J, Schreurs PGJ, Hoefnagels JPM, Geers MGD. (2014) Quantification of three-dimensional surface deformation using global digital image correlation. *Experimental Mechanics*; **54(4)**: 557-570. DOI: 10.1007/s11340-013-9799-1.

[8] Bergers LIJC, Hoefnagels JPM, Delhey NKR, Geers MGD. (2011) Measuring time-dependent deformations in metallic MEMS. *Microelectronics Reliability*; **51(6)**: 1054-1059. DOI: DOI: 10.1016/j.microrel.2011.03.008.

[9] Bergers LIJC, Hoefnagels JPM, Geers MGD. (2014) Characterization of time-dependent anelastic microbeam bending mechanics. *Journal of Physics D: Applied Physics*; **47**, 1 - 14. DOI: 10.1088/0022-3727/47/35/355306.

[10] Bertin M, Du C, Hoefnagels JPM, Hild F. (2016) Crystal plasticity parameter identification with 3D measurements and Integrated Digital Image Correlation. *Acta Materialia*; **116**: 321-331. DOI: 10.1016/j.actamat.2016.06.039.

[11]   Besnard G, Hild F, Roux S. (2006) "Finite-Element" Displacement Fields Analysis from Digital Images: Application to Portevin-Le Châtelier Bands. *Experimental Mechanics*; **46(6)**: 789-803. DOI: 10.1007/s11340-006-9824-8.

[12]   Besnard G, Lagrange J-M, Hild F, Roux S, Voltz C. (2010) Characterization of necking phenomena in high-speed experiments by using a single camera. *EURASIP Journal on Image and Video Processing*; **2010(1)**, 215956.

[13]   Besnard G, Guérard S, Roux S, Hild F. (2011) A spacetime approach in digital image correlation: Movie-DIC. *Optics and Lasers in Engineering*; **49(1)**: 71-81. DOI: 10.1016/j.optlaseng.2010.08.012.

[14]   Björck A. (1996) *Numerical Methods for Least Squares Problems*; Society for Industrial and Applied Mathematics. Retrieved from http://epubs.siam.org/doi/book/10.1137/1.9781611971484. DOI: 10.1137/1.9781611971484.

[15]   Blaysat B, Hoefnagels JPM, Alfano M, Lubineau G, Geers MGD. (2015) Interface debonding characterization by image correlation integrated with double cantilever beam kinematics. *International Journal of Solids and Structures*; **55**: 79–91. DOI: 10.1016/j.ijsolstr.2014.06.012.

[16]   Blayvas I, Bruckstein A, Kimmel R. (2006) Efficient computation of adaptive threshold surfaces for image binarization. *Pattern Recognition*; **39(1)**: 89-101. DOI: 10.1016/j.patcog.2005.08.011.

[17]   Bloch A, François M, Thomas J-C, Flamand O. (2014) Monitoring of Inflatable Structures by Using Virtual Image Correlation. *7th European Workshop on Structural Health Monitoring*; **July 8-11**: 686-693.

[18]   Boor C de. (1972) On calculating with B-Splines. *Journal of Approximation Theory*; **6(1)**: 50-62. DOI: 10.1016/0021-9045(72)90080-9.

[19]   Borden MJ, Scott MA, Evans JA, Hughes TJR. (2010) Isogeometric finite element data structures based on Bézier extraction of NURBS. *ICES Report*; **10(8)**: 1-38.

[20]   Bornert M, Brémand F, Doumalin P, Duprè J-C, Fazzini M, Grédiac M, Hild F, Mistou S, Molimard J, Orteu J-J, Robert L, Surrel Y, Vacher P, Watrisse B. (2009) Assessment of digital image correlation measurement errors: Methodology and results. *Experimental Mechanics*; **49(3)**: 353-370. DOI: 10.1007/s11340-008-9204-7.

[21]   Bowden N, Brittain S, Evans AG, Hutchinson JW, Whitesides GM. (1998) Spontaneous formation of ordered structures in thin films of metals supported on an elastomeric polymer. *Nature*; **393**: 146-149. DOI: 10.1038/30193.

[22]   Boyd JP. *Chebyshev and Fourier Spectral Methods*; DOVER Publications, Inc., 2000; 323. ISBN: 0-07-005521-1.

[23] Brosteaux D, Axisa F, Gonzalez M, Vanfleteren J. (2007) Design and Fabrication of Elastic Interconnections for Stretchable Electronic Circuits. *IEEE Electron Device Letters*; **28(7)**: 552-554. DOI: 10.1109/LED.2007.897887.

[24] Carlbom I, Paciorek J. (1978) Planar Geometric Projections and Viewing Transformations. *Computing Surveys*; **10(4)**: 465-502. DOI:10.1145/356744.356750.

[25] Cattarinuzzi E, Lucchini R, Gastaldi D, Vena P, Lorenzelli L, Hoefnagels JPM. (2015) In-situ Experimental Characterization of Interfacial Toughness of Aluminum Thin Films on Polyimide Substrates. *20th International Conference on Composite Materials: 19-24th July 2015, Copenhagen.*

[26] Cattarinuzzi E, Lucchini R, Gastaldi D, Vena P. (2015) Design of Aluminum/Polyimide Stretchable Interconnects Investigated Through In-Situ Testing. *XVIII AISEM Annual Conference*; DOI: 10.1109/AISEM.2015.7066784.

[27] Cattarinuzzi E. (2016) In-situ mechanical characterization of deformable metal/polymer electrical interconnects. *PhD Thesis*; Politecnico di Milano.

[28] Chan TF, Vese LA. (2001) Active contours without edges. *IEEE Transactions on Image Processing*; **10(2)**: 266-277. DOI: 10.1109/83.902291.

[29] Cheng P, Sutton MA, Schreier HW, McNeill SR. (2002) Full-field speckle pattern image correlation with B-Spline deformation function. *Experimental Mechanics*; **42(3)**: 344-352. DOI: 10.1007/BF02410992.

[30] Chiu SL, Leu J, Ho PS. (1994) Fracture of metal-polymer line structures. I. Semiflexible polyimide. *Journal of Applied Physics*; **76(9)**: 5136. DOI: 10.1063/1.357227.

[31] Chu TC, Ranson WF, Sutton MA. (1985) Applications of digital-image-correlation techniques in experimental mechanics. *Experimental Mechanics*; **25(3)**: 232-244. DOI: 10.1007/BF02325092.

[32] Chung H, Joe Y, Han H. (1999) The effect of curing history on the residual stress behavior of PI thin films. *Journal of Applied Polymer Science*; **74(14)**: 3287-3298.

[33] Collins GP. (2016) Science and Culture: Kirigami and technology cut a fine figure, together. *PNAS*; **113(2)**: 240-241. DOI: 10.1073/pnas.1523311113.

[34] Cottrell JA, Hughes TJR, Bazilevs Y. *Isogeometric Analysis: Toward Integration of CAD and FEA*; Wiley, Chichester. 2009

[35] Cox MG. (1972) The numerical evaluation of B-Splines.*IMA Journal of Applied Mathematics*; **10(2)**: 134-149. DOI: 10.1093/imamat/10.2.134.

[36] Dassault Systèmes Simulia©. *Abaqus 6.13 software*. User manual; http://dsk.ippt.pan.pl/docs/abaqus/v6.13/books/usb/default.htm. (Interactions; Contact Property Models; Mechanical Contact Properties; Surface Based Cohesive Behavior; Damage Evolution; Mixed Mode Definition).

[37] Dong YL, Pan B. (2017) A review of speckle pattern fabrication and assessment for digital image correlation. *Experimental Mechanics*; **57(8)**: 1161-1181. DOI: 10.1007/s11340-017-0283-1.

[38] Drodge DR, Mortimer B, Holland C, Siviour CR. (2012) Ballistic impact to access the high-rate behaviour of individual silk fibres. *Journal of the Mechanics and Physics of Solids*; **60(10)**: 1710-1721. DOI: 10.1016/j.jmps.2012.06.007.

[39] Dufour J-E, Beaubier B, Hild F, Roux S. (2015) CAD-based displacement measurements with Stereo-DIC. *Experimental Mechanics*; **55(9)**: 1657-1668. DOI: 10.1007/s11340-015-0065-6.

[40] Dufour J-E, Hild F, Roux S. (2015) Shape, displacement and mechanical properties from isogeometric multiview stereocorrelation. *Journal of Strain Analysis*; **50(7)**: 470-487. DOI: 10.1177/0309324715592530.

[41] Elguedj T, Réthoré J, Buteri A. (2011) Isogeometric analysis for strain field measurements. *Computer Methods in Applied Mechanics and Engineering*; **200(1-4)**: 40-56. DOI: 10.1016/j.cma.2010.07.012.

[42] Evans AG, Hutchinson JW. (1995) The thermomechanical integrity of thin films and multilayers. *Acta Metallurgica Materialia*; **43(7)**: 2507-2530. DOI: 10.1016/0956-7151(94)00444-M.

[43] Evers LP, Brekelmans WAM, Geers MGD. (2004) Scale dependent crystal plasticity framework with dislocation density and grain boundary effects. *International Journal of Solids and Structures*; **41(18–19)**: 5209-5230. DOI: 10.1016/j.ijsolstr.2004.04.021.

[44] Fenner RT. *Mechanics of solids.* CRC Press LLC, Florida, U.S.A., 1999. ISBN: 0-632-01018-0.

[45] Fleck NA, Muller GM, Ashby F, Hutchinson JW. (1994) Strain gradient plasticity: Theory and experiment. *Acta Metallurgica et Materialia*; **42(2)**: 475-487. DOI: 10.1016/0956-7151(94)90502-9.

[46] François MLM, Semin B, Auradou H. (2010) Identification of the shape of curvilinear beams and fibers. *Applied Mechanics and Materials*; **24-25**: 359-364. DOI: 10.4028/www.scientific.net/AMM.24-25.359.

[47] Gonzalez M, Axisa F, Vanden Bulcke M, Brosteaux D, Vandevelde B, Vanfleteren J. (2008) Design of metal interconnects for stretchable electronic circuits. *Microelectronics Reliability*; **48**: 825-832. DOI: 10.1016/j.microel.2008.03.025.

[48] Gray DS, Tien J, Chen CS. (2004) High-conductivity elastomeric electronics. *Advanced Materials*; **16(5)**: 393-397. DOI: 10.1002/adma.200306107.

[49] Greer JR, De Hosson JThM. (2011) Plasticity in small-sized metallic systems: Intrinsic versus extrinsic size effect. *Progress in Materials Science*; **56(6)**: 654-724. DOI: 10.1016/j.pmatsci.2011.01.005.

[50] Guo Q, Keer LM, Chung YW. (1993) *Thermal Stress and Strain in Microelectronics Packaging*; Publisher: Van Nostrand Reinhold, New-York. **Ch. 10**: Thermal Stress-Induced Open-Circuit Failure in Microelectronics Thin-Film Metallizations, pp 329-359.

[51] Gutbrod SR, Sulkin MS, Rogers JA, Efimov IR. (2014) Patient-Specific Flexible and Stretchable Devices for Cardiac Diagnostics and Therapy. *Progress in Biophysics and Molecular Biology*; **115**: 244-251. DOI: 10.1016/j.pbiomolbio.2014.07.011.

[52] Han K, Ciccotti M, Roux S. (2010) Measuring nanoscale stress intensity factors with an atomic force microscope. *EPL (Europhysics Letters)*; **89(6)**, 66003. DOI: 10.1209/0295-5075/89/66003.

[53] Hankins G, Krajnik K, Galedrige B, Sakha S, Hylton P and Otoupal W. (2014) Improving safety structures on sprint and midget race cars. *SAE technical paper*; **2014-01-0561**; DOI: 10.4271/2014-01-0561.

[54] Hansen TS, West K, Hassanger O, Larsen NB. (2007) Highly stretchable and conductive polymer material made from poly(3,4-ethylenedioxythiophene) and polyurethane elastomers. *Advanced Functional Materials*; **17(16)**: 3069-3073. DOI: 10.1002/adfm.200601243.

[55] Harris KD, Elias AL, Chung H-J. (2016) Flexible electronics under strain: a review of mechanical characterization and durability enhancement strategies. *Journal of Materials Science*; **51(6)**: 2771-2805. DOI: 10.1007/s10853-015-9643-3.

[56] Hild F, Roux S. (2006) Digital image correlation: from displacement measurement to identification of elastic properties - a review. *Strain*; **42**: 69-80. DOI: 10.1111/j.1475-1305.2006.00258.x.

[57] Hild F, Roux S. (2012) Comparison of Local and Global Approaches to Digital Image Correlation. *Experimental Mechanics*; **52(9)**: 1503-1519. DOI: 10.1007/s11340-012-9603-7.

[58] Hoefnagels JPM, Neggers J, Timmermans PHM, Sluis O van der, Geers MGD. (2010) Copper-Rubber interface delamination in stretchable electronics. *Scripta Materialia*; **63(8)**: 875-878. DOI: 10.1016/j.scriptamat.2010.06.041.

[59] Hoefnagels JPM, Maris MPFHL van, Vermeij T. (2019) One-step deposition of nano-to-micron-scalable, high-quality digital image correlation patterns for high-strain in-situ multi-microscopy testing. *Strain*; **e12330**; DOI: 10.1111/str.12330.

[60] Hsu Y-Y, Gonzalez M, Bossuyt F, Axisa F, Vanfleteren J, de Wolf I. (2009) In situ observations on deformation behavior and stretching-induced failure of fine pitch stretchable interconnect. *Journal of Materials Research*; **24(12)**: 3573-3582. DOI: 10.1557/jmr.2009.0447.

[61] Hsu Y-Y, Gonzalez M, Bossuyt F, Axisa F, Vanfleteren J, de Wolf I. (2010) The effect of pitch on deformation behavior and the stretching-induced failure of a polymer-encapsulated stretchable circuit. *Journal of Micromechanics and Microengineering*; **20(7)**: 075036.

[62] Hu W, Niu X, Li L, Yun S, Yu Z, Pei Q. (2012) Intrinsically stretchable transparent electrodes based on silver-nanowire–crosslinked-polyacrylate composites. *Nanotechnology*; **23(34)**: 244002. DOI: 10.1088/0957-4484/23/34/344002.

[63] Huang YY, Terentjev EM. (2010) Tailoring the electrical properties of carbon-nanotube-polymer composites. *Advanced Functional Materials*; **20(23)**: 4062-4068. DOI: 10.1002/adfm.201000861.

[64] Hughes TJR, Cottrell JA, Bazilevs Y. (2005) Isogeometric analysis: CAD, finite elements, NURBS, exact geometry and mesh refinement. *Computer Methods in Applied Mechanics and Engineering*; **200**: 4135-4195. DOI: 10.1016/j.cma.2004.10.008.

[65] Hughes TJR. *The Finite Element Method*; DOVER Publications, Inc., 2000; 20. ISBN: 0-486-41181-8.

[66] Hutchinson JW, Suo Z. (1991) Mixed mode cracking in layered materials. *Advances in Applied Mechanics*; **29**: 63-191. DOI: 10.1016/S0065-2156(08)70164-9.

[67] Jackman RJ, Brittain ST, Adams A, Prentiss MG, Whitesides GM. (1998) Design and fabrication of topologically complex, three-dimensional microstructures. *Science*; **280(5372)**: 2089-2091. DOI: 10.1126/science.280.5372.2089.

[68] Janssen PJM, Hoefnagels JPM, Keijser TH de, Geers MGD. (2008) Processing induced size effects in plastic yielding upon miniaturisation. *Journal of the Mechanics and Physics of Solids*; **56(8)**: 2687-2706. DOI: 10.1016/j.jmps.2008.03.008.

[69] Joshi S, Savov A, Shafqat S, Dekker R. (2018) Investigation of "fur-like" residues post dry etching of polyimide using aluminum hard etch mask. *Materials Science in Semiconductor Processing*; **75**: 130-135. DOI: 10.1016/j.mssp.2017.11.025.

[70] Khang D-Y, Jiang H, Huang Y, Rogers JA. (2006) A stretchable form of single-crystal silicon for high-performance electronics on rubber substrates. *Science*; **311(5758)**: 208-212. DOI: 10.1126/science.1121401.

[71] Kim D-H, Song J, Choi WM, Kim H-S, Kim R-H, Liu Z, Huang YY, Hwang K-C, Zhang Y-W, Rogers JA. (2008) Materials and noncoplanar mesh designs for integrated circuits with linear elastic responses to extreme mechanical deformations. *PNAS*; **105(48)**: 18675-18680. DOI: 10.1073/pnas.0807476105.

[72] Kim DH, Lu N, Ghaffari R, Kim YS, Lee SP, Xu L, Wu J, Kim RH, Song J, Liu Z, Viventi J, Graff B, Elolampi B, Mansour M, Slepian MJ, Hwang S, Moss JD, Won SM, Huang Y, Litt B, Rogers JA. (2011) Materials for multifunctional balloon catheters with capabilities in cardiac electrophysiological mapping and ablation therapy. *Nature Materials*; **10(4)**: 316-232. DOI: 10.1038/nmat2971.

[73] Kim D-H, Lu N, Ma R, Kim Y-S, Kim R-H, Wang S, Wu J, Won SM, Tao H, Islam A, Yu KJ, Kim T-I, Chowdhury R, Ying M, Xu L, Li M, Chung H-J, Keum H, McCormick M, Liu P, Zhang Y-W, Omenetto FG, Huang Y, Coleman T, Rogers JA. (2011) Epidermal Electronics. *Science*; **333**: 838-843. DOI: 10.1126/science.1206157.

[74] Kim J, Lee M, Shim HJ, Ghaffari R, Cho HR, Son D, Jung YH, Soh M, Choi C, Jung S, Chu K, Jeon D, Lee S-T, Kim JH, Choi SH, Hyeon T, Kim D-H. (2014) Stretchable silicon nanoribbon electronics for skin prosthesis. *Nature Communications*; **5**: 5747. DOI: 10.1038/ncomms6747.

[75] Kleinendorst SM, Hoefnagels JPM, Verhoosel CV, Ruybalid AP. (2015) On the use of adaptive refinement in isogeometric digital image correlation. *International Journal for Numerical Methods in Engineering*; **104**: 944-962. DOI: 10.1002/nme.4952.

[76] Kleinendorst SM, Hoefnagels JPM, Fleerakkers RC, Maris MPFHL van, Cattarin-uzzi E, Verhoosel CV, Geers MGD. (2016) Adaptive isogeometric digital height correlation: application to stretchable electronics. *Strain*; **52(4)**: 336-354. DOI: 10.1111/str.12189.

[77] Kleinendorst SM, Hoefnagels JPM, Geers MGD. (2019) Mechanical shape correlation: a novel integrated digital image correlation approach. *Computer Methods in Applied Mechanics and Engineering*; **345**: 983-1006. DOI: 10.1016/j.cma.2018.10.014.

[78] Kleinendorst SM, Hoefnagels JPM, Geers MGD. (2018) Mechanical Shape Correlation: a novel integrated digital image correlation approach. *Advancement of Optical Methods in Experimental Mechanics, Conference Proceedings of the Society for Experimental Mechanics Series*; **3**: 47-54. DOI: 10.1007/978-3-319-63028-1_8.

[79] Kleinendorst SM, Verhaegh BJ, Hoefnagels JPM, Ruybalid AP, Sluis O van der, Geers MGD. (2018) On the boundary conditions and optimization methods in Integrated Digital Image Correlation. *Advancement of Optical Methods in Experimental Mechanics, Conference Proceedings of the Society for Experimental Mechanics Series*; **3**: 55-61. DOI: 10.1007/978-3-319-63028-1_9.

[80] Klinker L, Lee S, Work J, Wright J, Ma Y, Ptaszek L, Webb RC, Liu C, Sheth N, Mansour M, Rogers JA, Huang Y, Chen H, Ghaffari R. (2015) Balloon Catheters with Integrated Stretchable Electronics for Electrical Stimulation, Ablation and Blood Flow Monitoring. *Extreme Mechanics Letters*; **3**: 45-54. DOI: 10.1016/j.eml.2015.02.005.

[81] Koh A, Kang D, Xue Y, Lee S, Pielak RM, Kim J, Hwang T, Min S, Banks A, Bastien P, Manco MC, Wang L, Ammann KR, Jang K-I, Won P, Han S, Ghaffari R, Paik U, Slepian MJ, Balooch G, Huang Y, Rogers JA. (2016) A Soft, Wearable Microfluidic Device for the Capture, Storage, and Colorimetric Sensing of Sweat. *Science Translational Medicine*; **8**: 366ra165.

[82] Kraft O, Gruber PA, Mönig R, Weygand D. (2010) Plasticity in confined dimensions. *Annual Review of Materials Research*; **40**: 293-317. DOI: 10.1146/annurev-matsci-082908-145409.

[83] Kuru G, Verhoosel CV, Zee KG van der, Brummelen EH van. (2014) Goal-adaptive Isogeometric Analysis with hierarchical splines. *Computer Methods in Applied Mechanics and Engineering*; **270(0)**: 270-292. DOI: 10.1016/j.cma.2013.11.026.

[84] Lacour SP, Chan D, Wagner S, Li T, Suo Z. (2006) Mechanisms of reversible stretchability of thin metal films on elastomeric substrates. *Applied Physics Letters*; **88**: 204103. DOI: 10.1063/1.2201874.

[85] Lava P, Cooreman S, Coppieters S, De Strycker M, Debruyne D. (2009) Assessment of measuring errors in DIC using deformation fields generated by plastic FEA. *Optics and Lasers in Engineering*; **47(7)**: 747-753. DOI: 10.1016/j.optlaseng.2009.03.007.

[86] Li T, Suo Z, Lacour SP, Wagner S. (2005) Compliant thin film patterns of stiff materials as platforms for stretchable electronics. *Journal of Materials Research*; **20(12)**: 3274-3277. DOI: 10.1557/jmr.2005.0422.

[87] Li T, Suo Z. (2006) Deformability of thin metal films on elastomer substrates. *International Journal of Solids and Structures*; **43(7-8)**: 2351-2363. DOI: 10.1016/j.ijsolstr.2005.04.034.

[88] Lipomi DJ, Chong H, Vosgueritchian M, Mei J, Bao Z. (2012) Toward mechanically robust and intrinsically stretchable organic solar cells: Evolution of photovoltaic properties with tensile strain. *Solar Energy Materials & Solar Cells*; **107**: 355-365. DOI: 10.1016/j.solmat.2012.07.013.

[89] Lucchini R, Cattarinuzzi E, Maraghechi S, Gastaldi D, Adami A, Lorenzelli L, Vena P. (2016) Delamination phenomena in aluminum/polyimide deformable interconnects: In-situ micro-tensile testing. *Materials and Design*; **89**: 121-128. DOI: 10.1016/j.matdes.2015.09.086.

[90] Lucchini R. (2014) Mechanics of Stretchable Interconnects for Stretchable Electronics Devices. *Ph.D. thesis, Politecnico di Milano.*

[91] Luo PF, Chao YJ, Sutton MA, Peters WH. (1993) Accurate measurement of three-dimensional deformations in deformable and rigid bodies using computer vision. *Experimental Mechanics*; **33(2)**, 123-132. DOI: 10.1007/BF02322488.

[92] Ma Q, Zhang Y. (2016) Mechanics of fractal-inspired horseshoe microstructures for applications in stretchable electronics. *Journal of Applied Mechanics*; **83(11)**: 111008. DOI: 10.1115/1.4034458.

[93] Maraghechi S, Hoefnagels JPM, Peerling RHJ, Geers MGD. (2018) Correction of scan line shift artifacts in scanning electron microscopy: An extended digital image correlation framework. *Ultramicroscopy*; **187**: 144-163. DOI: 10.1016/j.ultramic.2018.01.002.

[94] Maraghechi S, Hoefnagels JPM, Peerling RHJ, Rokoš O, Geers MGD. (2019) Correction of scanning electron microscope imaging artifacts in a novel digital image correlation framework. *Experimental Mechanics*; **59(4)**: 489-516. DOI: 10.1007/s11340-018-00469-w

[95] KULEUVEN. *MatchID software*; http://www.matchid.org.

[96] McCoul D, Hu W, Gao M, Mehta V, Pei Q. (2016) Recent advances in stretchable and transparent electronic materials. *Advanced Electronic Materials*; **2(5)**: 1500407. DOI: 10.1002/aelm.201500407.

[97] Mimoun B, Henneken V, Horst A van der, Dekker R. (2013) Flex-to-Rigid (F2R): A generic platform for the fabrication and assembly of flexible sensors for minimally invasive intstruments. *IEEE Sensors Journal*; **13(10)**: 3873-3882. DOI: 10.1109/JSEN.2013.2252613.

[98] Neggers J. (2013). *Ductile Interfaces in Stretchable Electronics: Multi-Scale Mechanics and Inverse Methods*; Ph.D. thesis. Eindhoven University of Technology: the Netherlands. Page 147.

[99] Neggers J, Hoefnagels JPM, Hild F, Roux S, Geers MGD. (2014) Direct stress-strain measurements from bulged membranes using topography image correlation. *Experimental Mechanics*; **54(5)**: 717-727. DOI: 10.1007/s11340-013-9832-4.

[100] Neggers J, Hoefnagels JPM, Geers MGD, Hild F, Roux S. (2015) Time-resolved integrated digital image correlation. *International Journal for Numerical Methods in Engineering*; **103(3)**: 157-182. DOI: 10.1002/nme.4882.

[101] Neggers J, Hoefnagels JPM, Sluis O van der, Geers MGD. (2015) Multi-scale experimental analysis of rate dependent metal-elastomer interface mechanics. *Journal of the Mechanics and Physics of Solids*; **80**: 26-26. DOI: 10.1016/j.jmps.2015.04.005.

[102] Neggers J, Hoefnagels JPM, Sluis O van der, Sedaghat O, Geers MGD. (2015) Analysis of dissipative mechanisms in metal-elastomer interfaces. *Scripta Materiala*; **149**: 412-424. DOI: 10.1016/j.engfracmech.2015.06.056.

[103] Neggers J, Blaysat B, Hoefnagels JPM, Geers MGD. (2015) On image gradients in digital image correlation. *International Journal for Numerical Methods in Engineering*; **105(4)**: 243-260. DOI: 10.1002/nme.4971

[104] O'Masta MR, Deshpande VS, Wadley HNG. (2014) Mechanisms of projectile penetration in Dyneema$^{\delta}$ encapsulated aluminum structures. *International Journal of Impact Engineering*; **74**: 16-35. DOI: 10.1016/j.ijimpeng.2014.02.002.

[105] Pan B, Qian K, Xie H, Asundi A. (2009) Two-dimensional digital image correlation for in-plane displacement and strain measurement: a review. *Measurement Science and Technology*; **20(6)**: 062001.

[106] Pan B, Qian K, Xie H, Asundi A. (2009) Two-dimensional digital image correlation for in-plane displacement and strain measurement: a review. *Measurement Science and Technology*; **20(6)**: 062001.

[107] Pan B. (2013) Bias error reduction of digital image correlation using Gaussian pre-filtering. *Optics and Lasers in Engineering*; **51**: 1161-1167. DOI: 10.1016/j.optlaseng.2013.04.009.

[108] Peters WH, Ranson WF. (1982) Digital imaging techniques in experimental stress analysis. *Optical Engineering*; **21(3)**: 427-431. DOI: 10.1117/12.7972925.

[109] Quintereo AV, Verplancke R, De Smet H, Vanfleteren J. (2017) Stretchable Electronic Platform for Soft and Smart Contact Lens Applications. *Advanced Materials Technologies*; **2(8)**: 1-10. DOI: 10.1002/admt.201700073.

[110] Réthoré J, Hild F, Roux S. (2007) Shear-band capturing using a multiscale extended digital image correlation technique. *Computer Methods in Applied Mechanics and Engineering*; **196**: 5016-5030. DOI: 10.1016/j.cma.2007.06.019.

[111] Réthoré J, Hild F, Roux S. (2008) Extended digital image correlation with crack shape optimization. *International Journal for Numerical Methods in Engineering*; **73**: 248-272. DOI: 10.1002/nme.2070.

[112] Réthoré J, Besnard G, Vivier G, Hild F, Roux S. (2008) Experimental investigation of localized phenomena using digital image correlation. *Philosphical Magazine*; **88(28-29)**: 3339-3355. DOI: 10.1080/14786430802263111.

[113] Réthoré J, Roux S, Hild F. (2011) An extended and integrated digital image correlation technique applied to the analysis of fractured samples. *European Journal Computational Mechanics*; **18**: 285-306.

[114] Réthoré J, Elguedj T, Simon P, Coret M. (2010) On the use of NURBS functions for displacement derivatives measurement by digital image correlation. *Experimental Mechanics*; **50(7)**: 1099-1116. DOI: 10.1007/s11340-009-9304-z.

[115] Réthoré J. (2010) A fully integrated noise robust strategy for the identification of constitutive laws from digital images. *International Journal for Numerical Methods in Engineering*; **84(6)**:631–660. DOI: 10.1002/nme.2908.

[116] Réthoré J, François M. (2014) Curve and boundaries measurement using B-splines and virtual images. *Optics and Lasers in Engineering*; **52**:145-155. DOI: 10.1016/j.optlaseng.2013.06.018.

[117] Riegel C, Nowinski JL. (1976) An experimental investigation of wave propagation in a rubber string impacted by a projectile. *International Journal of Non-Linear Mechanics*; **11(4)**: 229-237. DOI: 10.1016/0020-7462(76)90002-0.

[118] Rogers JA, Bao Z. (2002) Printed plastic electronics and paperlike displays. *Journal of Polymer Science Part A: Polymer Chemistry*; **40(20)**: 3327-3334. DOI: 10.1002/pola.10405.

[119] Rokoš O, Hoefnagels JPM, Peerlings RHJ, Geers MGD. (2018) On micromechanical parameter identification with integrated DIC and the role of accuracy in kinematic boundary conditions. *International Journal of Solids and Structures*; **146**: 241-259. DOI: 10.1016/j.ijsolstr.2018.04.004.

[120] Rosset S, Niklaus M, Dubois P, Shea HR. (2009) Metal ion implantation for the fabrication of stretchable electrodes on elastomers. *Advanced Functional Materials*; **18**: 1-9. DOI: 10.1002/adfm.200801218.

[121] Roux S, Hild F. (2006) Stress intensity factor measurements from digital image correlation: post-processing and integrated approaches. *International Journal of Fracture*; **140(1-4)**: 141-157. DOI: 10.1007/s10704-006-6631-2.

[122] Ruybalid AP, Hoefnagels JPM, Sluis O van der, Geers MGD. (2016) Comparison of the identification performance of conventional FEM-Updating and Integrated DIC. *International Journal for Numerical Methods in Engineering*; **106(4)**: 298–320. DOI: 10.1002/nme.5127.

[123] Ruybalid AP, Hoefnagels JPM, Sluis O. van der, Geers MGD. (2018) Image-based interface characterization with a restricted microscopic field of view. *International Journal of Solids and Structures*; **132-133**: 218-231. DOI: 10.1016/j.ijsolstr.2017.08.020.

[124] Ruybalid AP, Hoefnagels JPM, Sluis O van der, Maris MPFHL van, Geers MGD. (2019) Mixed-mode cohesive zone parameters from integrated digital image correlation on micrographs only. *International Journal of Solids and Structures*; **156-157**: 179-193. DOI: 10.1016/j.ijsolstr.2018.08.010.

[125] Ruybalid AP. (2019) Identification of multi-layer interface systems : a full-field, micro-mechanical approach. *PhD-thesis*. Chapter 6: Identifying mixed-mode adhesion properties of a flexible OLED.

[126] Savov A, Pakazad SK, Joshi S, Henneken V, Dekker R. (2014) A post processing approach for manufacturing high-density stretchable sensor arrays. *SENSORS, 2014 IEEE Proceedings*: 1703-1705. DOI: 10.1109/ICSENS.2014.6985350.

[127] Schreier HW, Braasch JR, Sutton MA. (2000) Systematic errors in digital image correlation caused by intensity interpolation. *Optical Engineering*; **39(11)**: 2915-1921.

[128] Schreier HW, Sutton MA. (2002) Systematic errors in digital image correlation due to undermatched subset shape functions. *Experimental Mechanics*; **42(3)**: 303-310, DOI: 10.1007/BF02410987.

[129] Scott MA, Borden MJ, Verhoosel CV, Sederberg TW, Hughes TJR. (2011) Isogeometric finite element data structures based on Bézier extraction of T-splines. *International Journal for Numerical Methods in Engineering*. **88(2)**: 126-156. DOI: 10.1002/nme.3167.

[130] Scrivens WA, Luo Y, Sutton MA. (2006) Development of patterns for digital image correlation measurements at reduced length scales. *Experimental Mechanics*; **47(1)**: 63-77. DOI: 10.1007/s11340-006-5869-y.

[131] Sekitani T, Noguchi Y, Hata K, Fukushima T, Aida T, Someya T. (2008) A rubberlike stretchable active matrix using elastic conductors. *Science*; **321(5895)**: 1468-72. DOI: 10.1126/science.1160309.

[132] Shafqat S, Hoefnagels JPM, Savov A, Joshi S, Dekker R, Geers MGD. (2017) Ultra-stretchable interconnects for high-density stretchable electronics. *Micromachines*; **8(9)**: 277. DOI: 10.3390/mi8090277.

[133] Shafqat S, Sluis O van der, Geers MGD, Hoefnagels JPM. (2018) A bulge test based methodology for characterizing ultra-thin buckled membranes. *Thin Solid Films*; **660**: 88-100. DOI: 10.1016/j.tsf.2018.04.005.

[134] Shafqat S, Joshi S, Savov AM, Dekker R, Hoefnagels JPM, Geers MGD. (2020) Multi-axial electro-mechanical testing methodology for highly stretchable freestanding micron-sized structures. *In preparation*

[135] Shi Y, Zhang F, Nan K, Wang X, Wang J, Zhang Y, Zhang Y, Luan H, Hwang K-C, Huang Y, Rogers JA, Zhang Y. (2017) Plasticity-induced origami for assembly of three dimensional metallic structures guided by compressive buckling. *Extreme Mechanics Letters*; **11**: 105-110. DOI: 10.1016/j.eml.2016.11.008.

[136] Silverberg JL, Evans AA, McLeod L, Hayward RC, Hull T, Santangelo CD, Cohen I. (2014) Using origami design principles to fold reprogrammable mechanical metamaterials. *Science*; **345(6197)**: 647-650. DOI: 10.1126/science.1252876.

[137] Sluis O van der, Hsu YY, Timmermans PHM, Gonzalez M, Hoefnagels JPM. (2011) Stretching-induced interconnect delamination in stretchable electronic circuits. *Journal of Physics D: Applied Physics*; **44**: 034008.

[138] Sluis O van der, Hsu Y-Y, Timmermans PHM, Gonzalez M, Hoefnagels JPM. (2011) Stretching induced interconnect delamination in stretchable electronic circuits. *Journal of Physics D: Applied Physics*; **44(3)**: 034008. DOI: 10.1088/0022-3727/44/3/034008.

[139] Sluis O van der, Vermeij T, Neggers J, Vossen B, Maris MPFHL van, Vanfleteren J, Geers MGD, Hoefnagels JPM. (2018) From Fibrils to Toughness: Multi-Scale Mechanics of Fibrillating Interfaces in Stretchable Electronics. *Materials*; **11(2)**: 231. DOI: 10.3390/ma11020231.

[140] Smith TS, Bay BK, Rashid MM. (2002) Digital volume correlation including rotational degrees of freedom during minimization. *Experimental Mechanics*; **42(3)**, 272-278. DOI: 10.1007/BF02410982.

[141] Someya T. (2018) "Continuous Health-Monitoring With Ultraflexible On-Skin Sensors" (talk in the 2018 AAAS Annual Meeting Symposium, Austin, Texas, February 17, 2018). *The University of Tokyo* and *Dai Nippon Printing Co., Ltd.*; `http://www.ntech.t.u-tokyo.ac.jp/en/press/press_for_media/6_AAAS_20180217/index.html`, accessed August 5 2019.

[142] Someya T. (2012) Stretchable Electronics. *John Wiley & Sons*: Weinham, Germany.

[143] Soroka OB, Klymenko SA, Kopeikina MY. (2010) Evaluation of residual stresses in PVD-coatings. Part 2. *Strength of Materials*; **42(4)**: 450-458. DOI: 10.1007/s11223-010-9236-y.

[144] Sterken T, Vanfleteren J, Torfs T, Op de Beek M, Bossuyt F, Van Hoof C. (2011). Ultra-Thin Chip Package (UTCP) and stretchable circuit technologies for wearable ECG system. *IEEE 33th Engineering in Medicine and Biology Society Conference*. DOI: 10.1109/IEMBS.2011.6091734.

[145] Stoppa M, Chiolerio A. (2014) Wearable Electronics and Smart Textiles: A Critical Review. *Sensors*; **14(7)**: 11957-11992. DOI: 10.3390/s140711957.

[146] Su Y, Wang S, Huang Y, Luan H, Dong W, Fan JA, Yang Q, Rogers JA, Huang Y. (2015) Elasticity of fractal inspired interconnects. *Small*; **11(3)**: 367-73. DOI: 10.1002/smll.201401181.

[147] Sun Y, Pang JHL, Wong CK, Su F. (2005) Finite element formulation for a digital image correlation method. *Applied Optics*; **44(34)**: 7357-7363. DOI: 10.1364/AO.44.007357.

[148] Sun Y, Pang JHL. (2007) Study of optimal subset size in digital image correlation of speckle pattern images. *Optics and Lasers in Engineering*; **45(9)**: 967-974. DOI: 10.1016/j.optlaseng.2007.01.012.

[149] Sutton MA, Wolters WJ, Peters WH, Ranson WF, McNeill SR. (1983) Determination of displacements using an improved digital correlation method. *Image and Vision Computing*; **1(3)**: 133:139. DOI: 10.1016/0262-8856(83)90064-1.

[150] Sutton MA, Orteu J-J, Schreier HW. (2009) *Image Correlation for Shape, Motion and Deformation Measurements: Basic Concepts, Theory and Applications*; Springer, New York, U.S.A. ISBN: 978-0-387-78746-6. DOI: 10.1007/978-0-387-78747-3.

[151] Tang Y, Yin J. (2017) Design of cut unit geometry in hierarchical kirigami-based auxetic metamaterials for high stretchability and compressibility. *Extreme Mechanics Letters*; **12**: 77-85. DOI: 10.1016/j.eml.2016.07.005.

[152] Uchic MD, Schade PA, Dimiduk DM. (2009) Plasticity of Micrometer-Scale Single Crystals in Compression. *Annual Review of Materials Research*; **39**: 361-386. DOI: 10.1146/annurev-matsci-082908-145422.

[153] Vanfleteren J, Gonzalez M, Bossuyt F, Hsu Y-Y, Vervust T, De Wolf I, Jablonski M. (2012) Printed circuit board technology inspired stretchable circuits. *Materials Research Society Bulletin*; **37(3)**: 254-260. DOI: 10.1557/mrs.2012.48.

[154] Vese LA, Chan TF. (2002) A multiphase level set framework for image segmentation using the Mumford and Shah model. *International Journal of Computer Vision*; **50(3)**: 271-293. DOI: 10.1023/A:1020874308076.

[155] Vuong A-V, Giannelli C, Jüttler B, Simeon B. (2011) A hierarchical approach to adaptive local refinement in isogeometric analysis. *Computer Methods in Applied Mechanics and Engineering*; **200(49-52)**: 3554-3567. DOI: 10.1016/j.cma.2011.09.004.

[156] Watrisse B, Chrysochoos A, Muracciole J-M, Némoz-Gaillard M. (2001) Analysis of strain localization during tensile tests by digital image correlation. *Experimental Mechanics*; **41(1)**: 29-39. DOI: 10.1007/BF02323101.

[157] Wittevrongel L, Lava P, Lomov SV, Debruyne D. (2015) A self adaptive global digital image correlation algorithm. *Experimental Mechanics*; **55(2)**: 361-378. DOI: 10.1007/s11340-014-9946-3.

[158] Wu W. (2019) Stretchable electronics: functional materials, fabrication strategies and applications. *Science and Technology of Advanced Materials*; **20(1)**: 187-224. DOI: 10.1080/14686996.2018.1549460.

[159] Xu L, Gutbrod SR, Bonifas AP, Su Y, Sulkin MS, Lu N, Chung H-J, Jang K-I, Liu Z, Ying M, Lu C, Webb RC, Kim J-S, Laughner JI, Cheng H, Liu Y, Ameen A, Jeong J-W, Kim G-T, Huang Y, Efimov IR, Rogers JA. (2014). 3D multifunctional integumentary membranes for spatiotemporal cardiac measurements and stimulation across the entire epicardium. *Nature communications*; **5**: 3329. DOI: 10.1038/ncomms4329.

[160] Xu S, Jayaraman A, Rogers JA. (2019) "Skin Sensors Are the Future of Health Care". *Nature*; **571**: 319-321.

[161] Yang Y, Xu K, Vervust T, Vanfleteren J. (2018) Multifunctional and miniaturized flexible sensor patch: Design and application for in situ monitoring of epoxy polymerization. *Sensors and Actuators B: Chemical*; **261**: 144-152. DOI: 10.1016/j.snb.2018.01.141.

[162] Yao S, Zhu Y. (2015) Nanomaterial-enabled stretchable conductors: Strategies, materials and devices. *Advanced Materials*; **27(9)**: 1480-1511. DOI: 10.1002/adma.201404446.

[163] Ye XW, Su YH, Han JP. (2014) Structural health monitoring of civil infrastructure using optical fiber sensing technology: A comprehensive review. *The Scientific World Journal*; **2014**: Article ID 652329, 11 pages. DOI:10.1155/2014/652329.

[164] Ye XW, Dong CZ, Liu T. (2016) A review of machine vision-based structural health monitoring: methodologies and applications. *Journal of Sensors*; **2016**: Article ID 7103039, 10 pages. DOI:10.1155/2016/7103039.

[165] Yoon J, Hong SY, Lim Y, Lee S-J, Zi G, Ha JS. (2014) Design and fabrication of novel stretchable device arrays on a deformable polymer substrate with embedded liquid-metal interconnections. *Advanced Materials*; **26(38)**: 6580-6586. DOI: 10.1002/adma.201402588.

[166] Yu X, Majahan BK, Shou W, Pan H. (2017) Materials, mechanics and patterning techniques for elastomer-based stretchable conductors. *Micromachines*; **8(1)**: 7. DOI: 10.3390/mi8010007.

Appendices

Appendix A
Novel Image Correlation Based Techniques for Mechanical Analysis of MEMS

Abstract

Three techniques have been developed to analyze the mechanical behavior of micromechanical systems, in particular stretchable electronic interconnects. The techniques are all digital image correlation (DIC) based and vary in the type of images used for correlation and the way of regularizing the displacement field, needed because of the ill-posed nature of DIC problems. The first two techniques use Non-Uniform Rational B-Splines (NURBS) which are adaptively refined to autonomously obtain an optimized set of shape functions for the considered problem. The first method applies this to regular grayscale speckle images, while the second technique requires profilometric height images to calculate not only the in-plane deformation, but also the out-of-plane component of the displacement field. The third method is an *integrated* DIC approach and is coupled to a finite element (FE) model of the sample for regularization of the displacement field. It correlates projections of the sample contour rather than a speckle pattern, which makes the method suitable for large, complex and three-dimensional displacements and cases where speckle pattern application is difficult, such as microscale samples. Application of the techniques to i.a. stretchable electronic interconnects yields good results.

Introduction

Stretchable electronics is an active field of research, which enables new applications by integrating flexible and rigid structures, for example biomedical devices which conform to biological tissues such as skin, the heart and the brain [51, 73, 80, 81]. Stretchable electronics contain microscale interconnects that transmit electrical signals and deform mechanically in order to accommodate stretching of the total structure and hence constitute an interesting type of Micro-Electronical Mechanical System (MEMS). Therefore, it is important to characterize the mechanics of the structures. Three techniques based on digital image correlation (DIC) have been developed that can be used to identify the mechanical behavior.

The first technique uses adaptive refinement of a Non-Uniform Rational B-Spline basis for DIC to accurately capture localized phenomena in the displacement field [75]. More important, an optimized set of basis functions is found autonomously, which is useful if it is difficult to select an appropriate set when the kinematics of the specific experiment are unknown beforehand. The algorithm is introduced in Section A and an improvement to the original algorithm is proposed. Furthermore, the method is applied to two samples from the DIC challenge that is formulated by the Society for Experimental Mechanics[1].

The second technique correlates profilometric height images to determine localized features (e.g., buckles) in both the in-plane and out-of-plane displacement fields [76]. This technique has been applied to stretchable electronic interconnects, which buckle locally upon stretching. In Section A this technique is exposed.

The third technique correlates projections of the specimen shape in order to identify model parameters of a coupled finite element model [77]. This method is explained in Section A.

After the three techniques are elaborated, some general conclusions are drawn in Section A.

Adaptive isogeometric digital image correlation

The first method to identify the mechanical behavior of a specimen from a set of images is the adaptive isogeometric digital image correlation method. First the algorithm is explained, after which the method is demonstrated on two samples from the SEM DIC challenge. Both of them show localized behavior, which is a challenge for the adaptive

---

[1] https://sem.org/dic-challenge/,accessed on 2-28-2017.

technique.

Adaptive algorithm

The adaptive isogeometric DIC algorithm is, like any digital image correlation method, based on the optical flow relation, i.e., the brightness conservation relation. This means that it is assumed that the gray value, or brightness, remains the same upon deformation. This implies that if the calculated displacement field is used to back-transform the deformed image g to the reference configuration, the difference between this back-transformed image ($\tilde{g}$) and the reference images (f), also denoted as the residual r, approaches zero for a correctly calculated displacement field. Therefore, the DIC algorithm focusses on minimizing the residual.

This problem is ill-posed, since the number of equations equals the number of pixels, namely the scalar residual value per pixel. However, the number of unknowns equals twice the number of pixels, since the displacement in both x-direction and y-direction is sought. Therefore, it is necessary to regularize the displacement field. This regularization is usually done by approximating the displacement field by a linear combination of shape functions $\underline{\varphi}_i$ and their corresponding coefficients a_i:

$$\underline{U}(\underline{x}) \approx \underline{u}(\underline{x}, \mathbb{a}) = \sum_i \underline{\varphi}_i(\underline{x}) a_i. \tag{A.1}$$

In this work the shape functions used for this discretization are NURBS, or Non-Uniform Rational B-Splines [41, 64]. The advantage of this type of shape functions is that they are very versatile and can describe many shape exactly, which is convenient since they are not only used for regularization of the displacement field, but also for parametrization of the specimen geometry, hence the term *isogeometric* DIC. Furthermore, it was shown by [41] that compared to finite element shape functions less NURBS shape functions, and hence less degrees of freedom, are required to describe the kinematics of the displacement field with the same accuracy, and this enhances the conditioning and the noise robustness of the DIC problem.

The exact choice of the shape functions is very important since it determines whether or not the displacement field can be captured accurately. Therefore, the user of a DIC algorithm needs to have specific knowledge of the experiment he is analyzing, i.e., a good estimate on the kinematics. This information is not always straightforward, and it can be difficult to select an appropriate set of shape functions. Therefore, it was proposed to include adaptive refinement of the basis functions in the algorithm, such that the set of shape functions is autonomously optimized for the considered

problem [75]. A schematic overview of the resulting adaptive isogeometric global digital image correlation algorithm is shown below:

Algorithm 1 Adaptive isogeometric GDIC algorithm calculating the displacement field from a sequence of images taken during an experiment. Note that if the refinement loop is disregarded, a conventional GDIC algorithm remains.

Load all images $(f, g_1, g_2, ..., g_{npic})$

Make initial mesh

for $1:npic$ (increment loop over all images g)
while $\frown$ converged (refinement loop)
Generate (refined) mesh and shape functions $\underline{\varphi}(\underline{x})$

Iterative solving $\mathbb{M} \delta \mathbb{a} = \mathbb{b}$

$$\begin{aligned} &\rightarrow \underline{u}(\underline{x}, \mathbb{a}) &&\text{Used as initial guess for next step} \\ &\rightarrow \tilde{g}(\underline{x}) = g(\underline{x} - \underline{u}) &&\text{Back-deformed image} \\ &\rightarrow r(\underline{x}) = f(\underline{x}) - \tilde{g}(\underline{x}) \end{aligned}$$

Test for convergence using residual $r(\underline{x})$
if $\frown$ converged
Mark shape functions for refinement
end
end
end

The selection of shape functions for refinement is based on a criterion depending on the local residual, i.e., the residual in the area where the considered shape functions has support. The refinement is executed hierarchically, which means that the selected shape functions are replaced by shape functions from a refined basis. This method ensures that refinement is carried out locally, instead of refining entire columns and rows of shape functions at once due the tensor product structure of the shape functions. See [75] for more details on the refinement procedure and algorithm.

It should be specified when the solution has reached a sufficient level of accuracy, i.e., a convergence criterion needs to be set. The convergence criterion is, like the refinement

criterion, based on the residual r. Whether or not convergence is reached depended in the originally proposed algorithm on if either of the following four criteria is met:

1. The residual is small enough: $\|r^i\|_{L^2} < p_1$, where i indicates the refinement step and p_1 is a threshold value.

2. The residual does not decrease significantly anymore:
   $\|r^{i-1}\|_{L^2} - \|r^i\|_{L^2} < p_2 \left(\|r^1\|_{L^2} - \|r^i\|_{L^2}\right)$, where p_2 is a prespecified percentage.

3. No shape functions are marked for refinement. This is the case when there are no shape functions with a significantly high residual in their region of support or when refinement has reached its highest level.

4. The maximum number of iterations or refinement steps is reached.
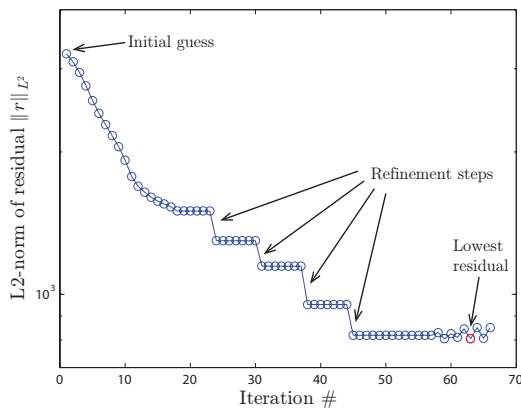

Figure A.1: Typical convergence plot of the adaptive isogeometric DIC method. The norm of the residual is high in the beginning, with the initial, coarse, mesh. In the following iterations the residual decreases. A significant decrease, however, is obtained if the shape functions are refined. The plateaus at each refinement step appear because the result from the previous step is used as an initial guess. Since this is a good initial guess, in contrast to the first initial guess, the residual only decreases slightly in subsequent iterations. In the end the mesh is refined to such extend that correlation becomes slightly more sensitive to instabilities, which can be recognized in the convergence behavior. The algorithm stops if a preset amount of iterations has diverged and the displacement field corresponding to the lowest residual is selected.

However, these criteria can as well induce the method to stop too early, before the most accurate solution possible is obtained. Therefore, a more elegant formulation of convergence is suggested here. All of the above criteria are omitted and the algorithm

continues iterating until the method diverges a preset amount, e.g., 5, of steps. Then the result for the lowest obtained residual is stored as the final displacement field. A typical convergence plot demonstrating this method is shown in Figure A.1. This approach also prevents errors that occur due to sensitivity to noise and local minima in case of a too fine mesh, since if the residual increases because of a redundant refinement step, simply the best result is selected.

DIC challenge sample 3b

Sample 3b of the DIC challenge is a virtual experiment in which a reference image is artificially deformed. The bottom half of the image does not experience any deformation, while for the top half a rigid body shift in positive y-direction is prescribed, in six steps ranging from a shift of 0.05 pixel to 0.5 pixel. The reference image and the final deformed image are shown in Figure A.2. In this figure also the initial mesh and the final refined mesh, after four refinement steps, are shown.
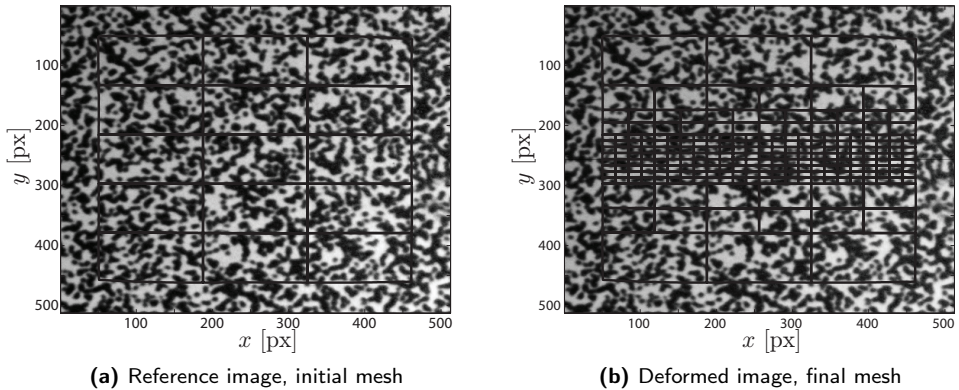

(a) Reference image, initial mesh   **(b)** Deformed image, final mesh

Figure A.2: The initial and refined mesh, after the final refinement step, plotted on top of the reference image and the deformed image of the last increment. In the center of the deformed image a black horizontal line can be observed, which results from the top half of the image moving upwards half a pixel, while the bottom half stays in place.

The applied displacement field basically represents a step functions, i.e., a discontinuous function, which is an extreme case of strain localization. In general, for global digital image correlation the displacement field is assumed to be continuous, unless discontinuities are deliberately introduced in the shape functions [52]. However, in case of the proposed NURBS shape functions no discontinuity is present and it is difficult for these shape functions to accurately describe a step function. Henceforth, it is seen in

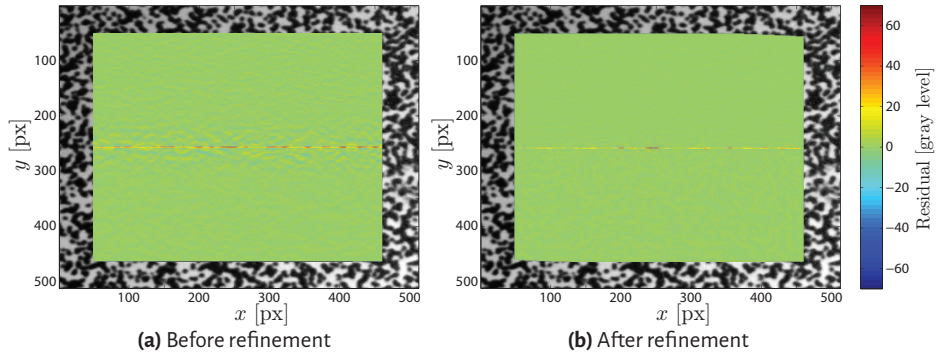Figure A.2 that the shape functions refine in the area around the step.

(a) Before refinement

(b) After refinement

Figure A.3: Residual fields before and after refinement.

The effect of refinement is shown in Figure A.3, where the residual maps are shown before and after refinement. The residual is already low in the area away from the step in the center. This is because the rigid body motion in this area is well described by the coarse initial mesh. However, the step is not well captured and the residual is large in this region. After refinement the area in which the residual is high is significantly smaller, indicating that refinement has improved by refining the mesh.
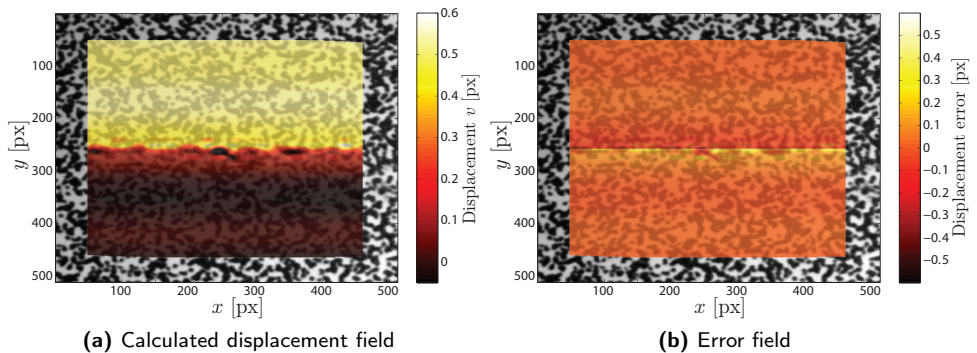

(a) Calculated displacement field

(b) Error field

Figure A.4: Calculated displacement field and error in this displacement field, plotted on top of the reference image.

The resulting displacement field in y-direction calculated by the adaptive DIC algorithm is shown in Figure A.4a. The displacement in x-direction is zero everywhere in the domain and therefore not discussed here. Since this is a virtual experiment and hence the

real displacement field is known, it is possible to calculate the error, i.e., the difference between the calculated and the reference displacement fields. This error field is shown in Figure A.4b. It is observed that the displacement field away from the discontinuity is calculated accurately and the error is low. However, in the region near the step the error is significant. The 'wiggle' pattern is typical for polynomial shape functions and it spreads over the domain of support of the shape functions that are active in the area of the discontinuity. Naturally, a more accurate result would have been obtained if a specific set of shape functions describing the kinematics of this particular problem had been selected. However, the goal of the adaptive DIC algorithm is to obtain an adequate solution autonomously, without the user having to act on the specific kinematics of the problem.
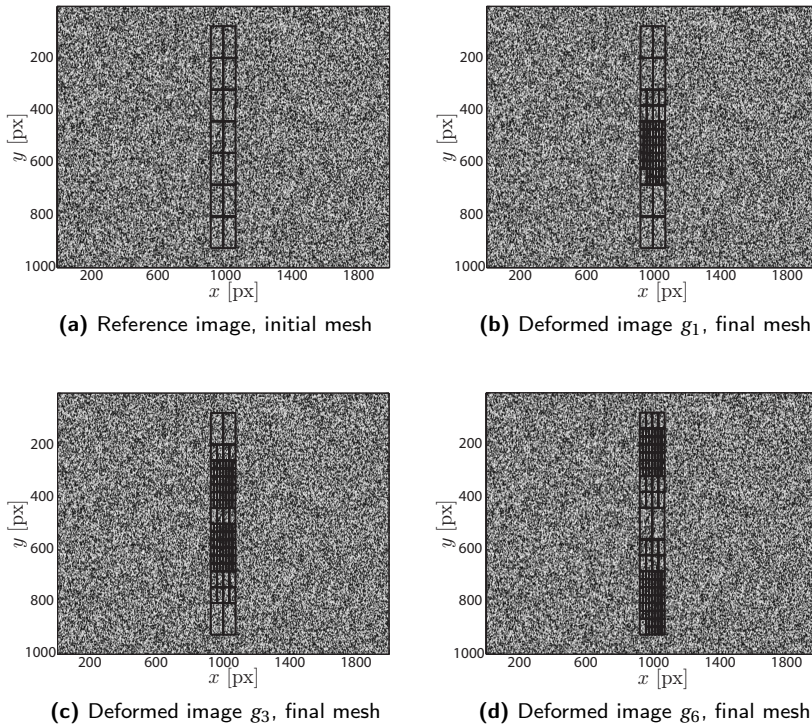

(a) Reference image, initial mesh

(b) Deformed image g_1, final mesh

(c) Deformed image g_3, final mesh

(d) Deformed image g_6, final mesh

Figure A.5: The reference image and a selection of deformed images, for increments 1, 3 and 6. The initial mesh is plotted in figure (a), while the final refined meshes for each increment are depicted on top of their corresponding deformed image.

DIC challenge sample 15

The next sample from the DIC challenge that is analyzed is sample 15. This too is a virtual experiment in which the displacement is virtually prescribed on the reference image. The displacement field in the eight increments represents strain localizations that travel through the specimen alike a wave. The reference image and a selection of the deformed images are shown in Figure A.5. Though difficult to see from the images, the displacement field in the first increment, Figure A.5b, is a strain localization band in y-direction approximately in the center of the domain. In the third and sixth increment, Figures A.5c and A.5d, two strain localization bands are present at different locations. In increment 3 they are closer together, while in increment 6 they are further apart. The displacement field in x-direction is again zero everywhere. To reduce computational cost the region of interest is chosen fairly narrow.
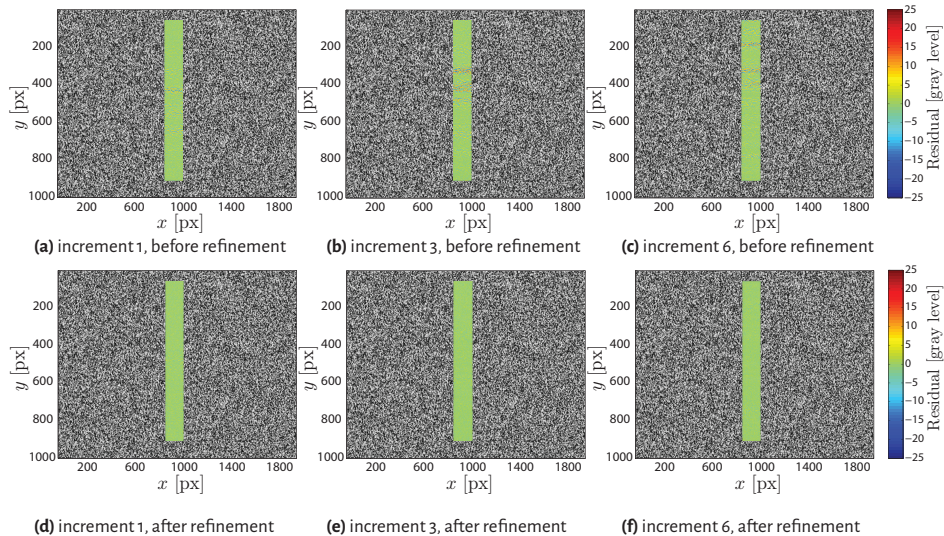

(a) increment 1, before refinement   **(b)** increment 3, before refinement   **(c)** increment 6, before refinement

(d) increment 1, after refinement   **(e)** increment 3, after refinement   **(f)** increment 6, after refinement

Figure A.6: Residual fields before and after refinement.

Since the strain localizations do not evolve at the same location each increment, it it not useful to reuse the refined mesh from the previous increment. Therefore, each increment is started with the initial mesh from Figure A.5a. It can be seen from Figures A.5b-A.5d that the mesh indeed refines in the areas around the strain localizations, indicating that the coarse initial mesh was not suitable to accurately describe the localization.

Again the improvement of the residual is demonstrated in Figure A.6. Before refinement
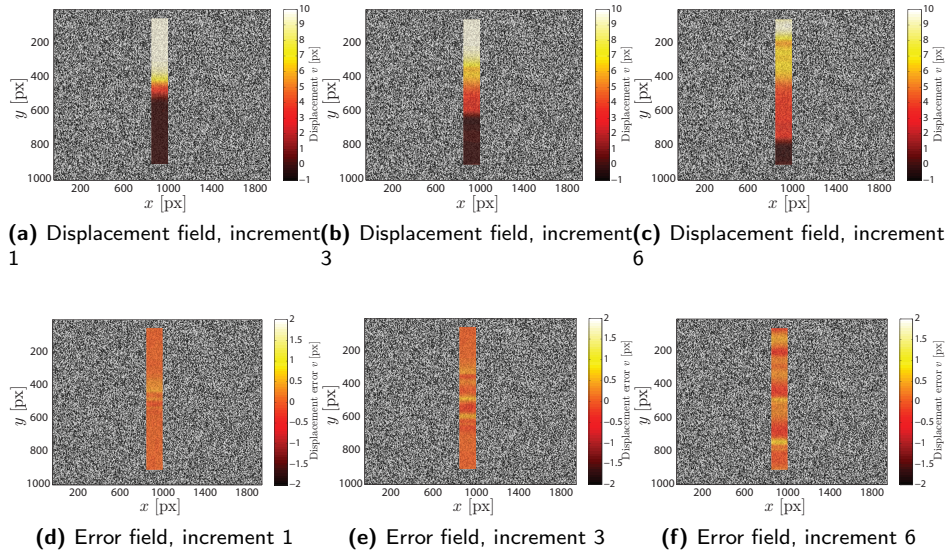
(a) Displacement field, increment 1 **(b)** Displacement field, increment 3 **(c)** Displacement field, increment 6

(d) Error field, increment 1   **(e)** Error field, increment 3   **(f)** Error field, increment 6

Figure A.7: Displacement fields and corresponding error fields plotted on top of the reference image for the considered increments.

the residual field is high in the areas where the strain localization bands are located for all three increments. Using the refined meshes the residual has decreased significantly.

The calculated displacement fields for the considered increments are shown in Figure A.7. Since the reference displacement field is known, also the error fields can be calculated and these are also displayed in Figure A.7. Again the characteristic ripples resulting from the polynomial shape functions are observed in the error fields. The accuracy of the calculated displacement field is approximately 0.5 pixel. Again, if a set of shape functions had been used that is more suitable for such strong strain localizations, the error could have been decreased. However, in many experiments it is not possible to determine an appropriate set beforehand and in such cases an adaptive algorithm that converges to a proper series of basis functions autonomously is advisable.

Adaptive isogeometric digital height correlation

The adaptive isogeometric digital image correlation algorithm has also been extended to be used for height images, i.e., to a digital *height* correlation (DHC) method. This method was applied to meander shaped stretchable electronic interconnects. These

copper wires are glued to a stretchable, e.g., rubber, substrate. Typically after a certain amount of deformation the interconnects start to delaminate from the substrate and they buckle in a certain localized area, see Figure A.8. These buckles often form the onset of failure of the interconnect and hence the device that they are used in. Therefore, it is important to characterize this behavior. Adaptive isogeometric digital height correlation is a useful tool for this purpose.
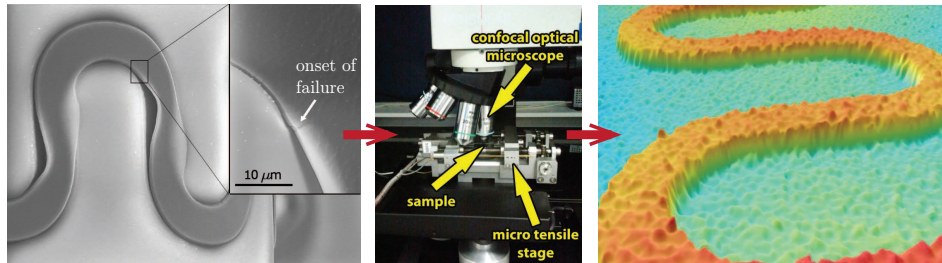

Figure A.8: An interconnect is shown that is partly delaminated from the substrate and buckles locally (reproduced from [76]). Using a confocal optical microscope height images are measured in situ during an experiment with a micro tensile stage. On the right a rendering of a resulting height image is depicted. The rugged surface is a result of a height contrast pattern, needed for DHC, applied to the specimen, similar to a grayscale speckle pattern in 2D DIC.

The algorithm for adaptive isogeometric height correlation is similar to the algorithm described in the previous section. The difference, however, is that not only the in-plane displacements are tracked, but also the out-of-plane deformation can be calculated. This is achieved by correlating profilometric height images of the sample instead of grayscale images. Furthermore, the set of shape functions is used three times: once for each component of the displacement field. An example of a virtual experiment representing the localized buckling behavior is depicted in Figure A.9. The meshes before and after refinement, along with an intermediate stage, are also shown, from which it can be seen that the mesh refinement indeed occurs in the areas where a localization of the displacement field, in this case in the out-of-plane direction, is present. For more details on this method, see [76].

Mechanical Shape Correlation

The third technique is also a digital image correlation technique. It is based on the *integrated* DIC approach, where the regularization of the displacement field is not constructed by a linear combination of shape functions and corresponding coefficients, but
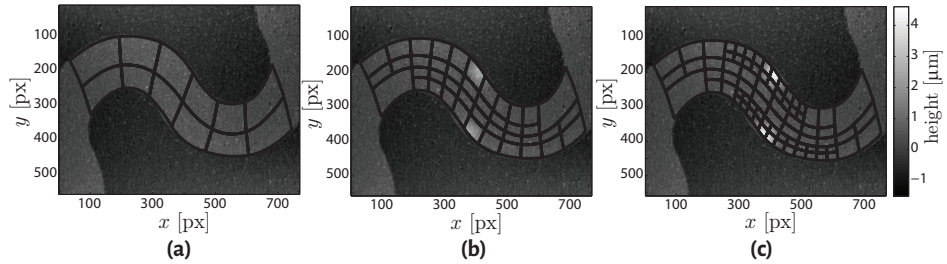
Figure A.9: A virtual experiment concerning the localized buckling of stretchable electronic interconnect. The reference image f (left) is shown along with deformed images g_2 (middle) and g_4 (right), in which the evolution of the buckles is observed. The initial mesh and refined meshes are plotted on top. Reproduced from [76].

a constitutive model is used. This model can be analytical, but more often a numerical finite element (FE) model is defined. The model parameters are the unknowns in the correlation procedure.

However, in Mechanical Shape Correlation instead of grayscale images of the sample containing a speckle pattern, images containing a projection of the sample outline are used. This is useful is situations where the specimen deforms in a complex and three-dimensional manner. In such cases parts of the sample may rotate out of view, other parts that where not visible before may come into view later or the speckle pattern may degrade. Additionally, in case of a sample of microscopical dimensions it can be difficult to apply a speckle pattern. The use of a projection of the sample contour overcomes these problems. Nevertheless, the assumption is that the outline is large with respect to the volume of the structure and that this contour changes significantly upon deformation. Stretchable electronic interconnects are structures that are highly suited to be analyzed with this method. Because of their wirelike structure their contour is large and it changes substantially if the interconnect is stretched.

A schematic illustration of the MSC method is given in Figure A.10. More detail can be found in [77].

Conclusions

Three methods have been developed to analyze mechanical behavior from images taken of a specimen during an experiment. The first method is an adaptive isogeometric digital image correlation algorithm, which uses NURBS shape functions to discretize the
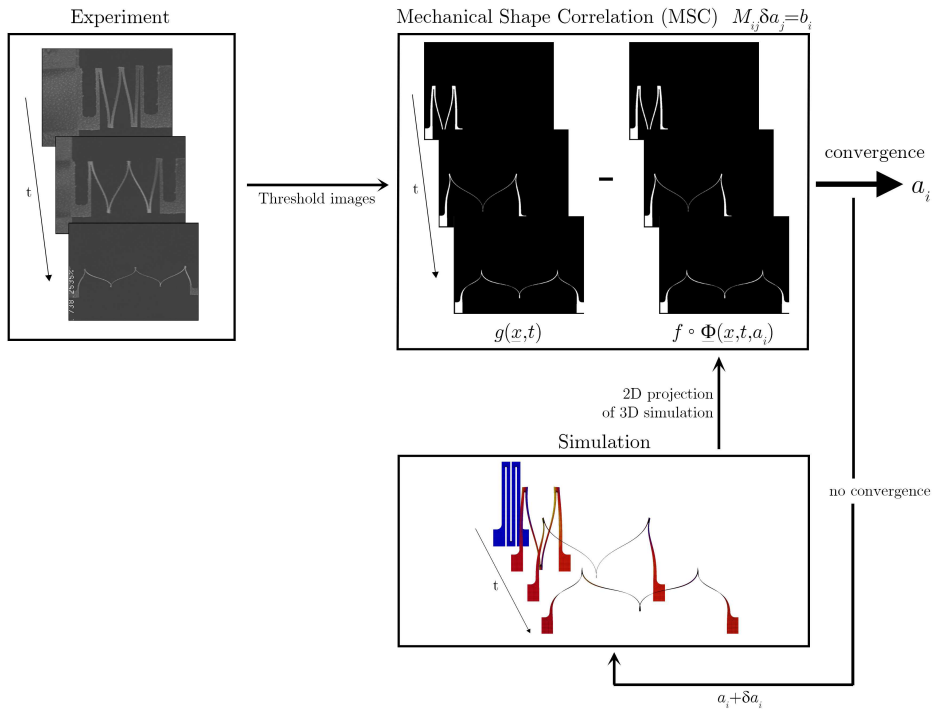
Figure A.10: Schematic representation of the mechanical shape correlation (MSC) method to identify model parameters a_i from an experiment. Simulations supply the images f to which the experiment is compared.

displacement field. The set of shape functions is autonomously optimized by performing adaptive refinement based on the residual image. The technique is demonstrated on two image sets from the SEM DIC challenge, from which it is shown that the results indeed improve upon mesh refinement. More important, this mesh refinement is executed automatically, yielding a more suitable mesh for the considered problem without the need for the user to input specific information about the kinematics of the considered experiment.

The second technique is an extension of the first method, which adds the ability of analyzing the out-of-plane deformation on top of the in-plane displacements. This is enabled by using profilometric height images instead of grayscale images. This method has been demonstrated on stretchable electronic interconnects glued to a rubber substrate. After a certain amount of stretching the interconnects delaminate from the substrate and buckle locally. This three-dimensional deformation can be

measured using the adaptive isogeometric digital height correlation technique, where again autonomously a suitable mesh for the localized behavior is obtained by adaptive refinement of the shape functions.

The last algorithm correlates the contour, or shape, of the sample, and is therefore called Mechanical Shape Correlation. It is a suitable technique for cases where deformation is either or both large, complex and out-of-plane, which makes it difficult to track a speckle pattern. Especially for stretchable electronic interconnects, a special class of MEMS, this technique is applicable, since the deformations are large and parts of the sample rotate out of view.

The techniques have been demonstrated to provide accurate microscale deformation fields in case of stretchable electronics, and are valuable techniques for micromechanical testing in general.

Appendix B
On the boundary conditions and optimization methods in integrated digital image correlation

Abstract

In integrated digital image correlation (IDIC) methods attention must be paid to the influence of using a correct geometric and material model, but also to make the boundary conditions in the FE simulation match the real experiment. Another issue is the robustness and convergence of the IDIC algorithm itself, especially in cases when (FEM) simulations are slow. These two issues have been explored in this proceeding. The basis of the algorithm is the minimization of the residual. Different approaches for this minimization exist, of which a Gauss-Newton method is used most often. In this paper several other methods are presented as well and their performance is compared in terms of number of FE simulations needed, since this is the most time-consuming step in the iterative procedure. Beside method-specific recommendations, the main finding of this work is that, in practical use of IDIC, it is recommended to start using a very robust, but slow, derivative-free optimization method (e.g. Nelder-Mead) to determine the search direction and increasing the initial guess accuracy, while after some iterations, it is recommended to switch to a faster gradient-based method, e.g. (update-limited) Gauss-Newton.

Introduction

Interfacial delamination is a key reliability challenge in composites and micro-electronic systems due to (high-density) integration of dissimilar materials. Predictive finite element models are used to minimize delamination failures during design, but require accurate interface models to capture (irreversible) crack initiation and propagation behavior observed in experiments. A generic inverse parameter identification methodology is needed to identify the interface behavior in their as-received state in the micro-electronics component, while it is subjected to realistic loading conditions, such as thermal loading.

Recently, Integrated Global Digital Image Correlation (IDIC) was introduced, which correlates the image patterns by deforming the images using as few as kinematically-admissible 'eigenmodes' as there are material parameters [100] in the interface model [15], thereby greatly enhancing noise insensitivity and robustness [122]. The main challenge lies in that the interface mechanics only generates very subtle changes in the deformation field of the adjacent material layers, therefore, especially high accuracy and robustness in the simulated deformation field is needed, as well as fast convergence because (FEM) simulations including interface mechanics are notoriously slow.

To obtain high displacement accuracy, besides an accurate geometric and material model, precise boundary conditions have often been overlooked. A study into precise boundary conditions for the case of interface mechanics simulations has recently been conducted, see Ref. [123]. Therefore, boundary conditions is not the topic of this proceeding. High robustness and fast convergence can be equally important, hence, these topics are explored here.

The robustness and convergence is determined by the IDIC algorithm. This algorithm is based on the brightness conservation relation, or optical flow relation, which means that material points retain the same brightness upon deformation of the underlying sample. It is with this principle that the displacement field calculated by using the material model is used to back-transform the deformed image to the reference configuration. If the displacement field is calculated correctly, the reference image and the back-transformed image should overlap perfectly (in the absence of noise and algorithm-induced errors such as interpolation) and hence the difference between these two images, denoted by the residual, will decrease to zero. Therefore, the heart of the IDIC algorithm, as well as for other DIC algorithms, is the minimization of this residual. After all, the residual converges to zero if the FE simulation matches the true, experimental, behavior of the specimen and the back-deformed image calculated with this correct displacement field correlates to the undeformed image.

Different approaches exist to solve this minimization problem. Most commonly used in DIC algorithms is a (modified) Gauss-Newton method. This method is relatively

fast in the proximity of the solution, but gives robustness issues if the initial guess is farther from the solution. Other methods exist which have their own advantages and disadvantages. A key issue in integrated DIC is the computational cost consumed by the number of FE simulations performed. Every iteration in the optimization method requires at least one FE evaluation. Some methods, however, require the derivative of the objective function, i.e., the residual, towards the degrees of freedom, i.e., the model parameters. This derivative is not analytically available and therefore, often a finite difference scheme is used to approximate the derivative. This calculation requires the number of degrees of freedom amount of FE evaluations, thereby increasing calculation cost and CPU time immensely. Therefore, the different optimization methods are compared based on the number of FE simulations needed to converge.

The lay-out of this paper is as follows. First the virtual experiment used to evaluate the performance of the different optimization methods is introduced in Section B. Then, in Section B three different optimization methods are presented and their performance is compared. Finally, conclusions are drawn in Section B.

Virtual test case

The performance of the different optimization methods is analyzed based on a virtual experiment. This virtual experiment concerns a tensile experiment with a dogbone tensile specimen, see Figure B.1, on which a load is prescribed on both edges. In a virtual experiment no real experimental images are used, but a finite element (FE) simulation is executed and the resulting displacement fields are used to artificially deform a reference image, see Figure B.2. These images form the input for the integrated DIC method. The objective is to correlate these images in order to find the model parameters, in this case the Young's modulus E and Poisson ratio v, that were used in the elastic isotropic FE model used to create the images. The parameters used to create the virtual experiment are $E_p = 1.3 \cdot 10^5 \text{Pa}$ and $v_p = 0.28$.

Optimization methods

Three different iterative optimization methods are tested. The first is a Gauss-Newton method that is often implemented in (integrated) digital image correlation approaches. This is a custom coded method. The other two methods are used from the MATLAB optimization toolbox. The first of these methods is a Trust-Region method with a Newton approach. The last optimization method is the Nelder-Mead algorithm. The performance of the IDIC algorithm with the different optimization approaches is evaluated by comparing the number iterations needed to converge within a set accuracy. The
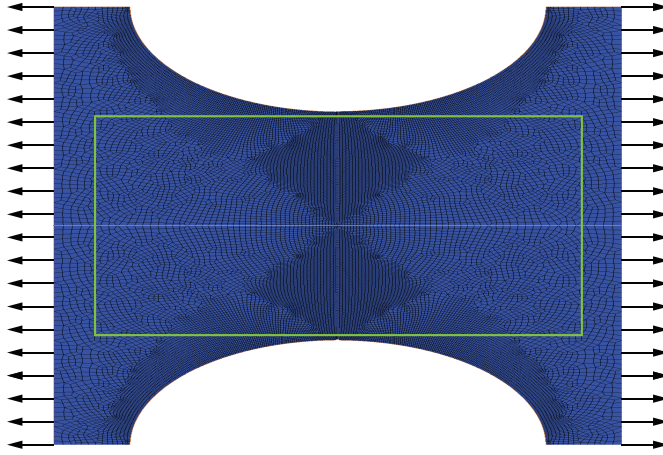
Figure B.1: Finite element simulation for the virtual experiment concerning a dogbone tensile sample. A load is prescribed on the left and right edge. A quarter of the structure is modeled, the red lines indicate symmetry lines. The region of interest is indicated by the green rectangle.

computational cost is mainly determined by the number of FE evaluations executed and. This number per iterations differs for each method and therefore the total number of FE evaluations for convergence is also compared for the considered methods.

The method are tested for different initial guesses on both parameters E and ν. The initial guesses are given relative to the true material property values used to create the virtual experiment, E_p and $|nu_p$, and are chosen on a logarithmic scale. The set of initial guess values for E ranges from a 10 times lower value to a 10 times higher value. For ν the range also start with values 10 times lower than the reference value, but it can not increase to a 10 times higher value, since the Poisson's ratio can not exceed 0.5 physically.

Since the iterations are computationally costly, especially for the methods that require derivative information, a maximum of 20 iterations is set. If a initial guess combination for a certain method crosses this limit, but is in the process of converging to the correct solution, this is indicated by a blue color in the graphs. If the method is diverging, an 'x'-symbol is depicted in addition to the blue color.

Gauss-Newton

The Gauss-Newton method is a modification of Newton's method for finding the objective's minimum. Given the set of m image residuals $r = (r_1, .., r_m)$ and the set of n
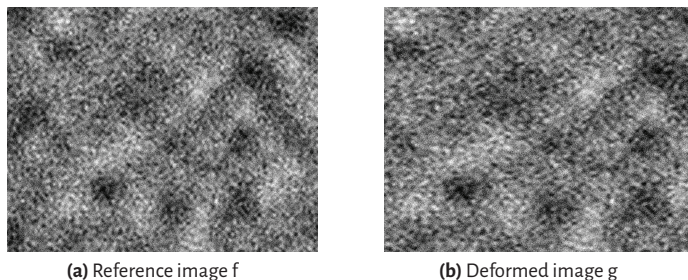
(a) Reference image f   (b) Deformed image g

Figure B.2: Reference image f and artificially deformed image g. The reference image is a generated speckle pattern with both coarse and fine features, which is suitable for digital image correlation analysis.

variables $\lambda = \lambda_1, ..., \lambda_n$) and the initial guess $\lambda^{(0)}$, the method proceeds by the iterations s described in Equation B.1 using Jacobian J_r [14].

$$\lambda^{(s+1)} = \lambda^{(s)} - (J_r^T J_r)^{-1} J_r^T r(\lambda^{(s)}). \tag{B.1}$$

This algorithm is often used in digital images correlation methods. Usually $J_r^T J_r$ is denoted as M, the optical correlation matrix, and $J_r^T r(\lambda^{(s)})$ as b, the right-hand side vector.

To prevent the method from iterating towards non-physical negative values for the model parameters λ, an update limit it introduced. This limit states that the iterative update in λ can not exceed a factor $\alpha < 1$ times the current value of the variable, $\lambda^{(s)}$. Here a factor $\alpha = 0.9$ is used.

The results for a set of initial guesses is shown in Figure B.3. Since this method requires the derivative, each iteration requires $(N_{DOF} + 1)$ number of FE evaluations. The method converges for all initial guesses tried, however, for low values of the Young's modulus converges becomes slow. The method is concluded to be relatively robust, but slow if far from the solution.

Trust-Region

For the Trust-Region method the MATLAB optimization toolbox is used. The used Optimization Toolbox algorithm is $\mathtt{trust-region-reflective}$ in the $\mathtt{fmincon}$ solver. Trust-Region algorithms makes use of trust regions; a defined subdomain N in
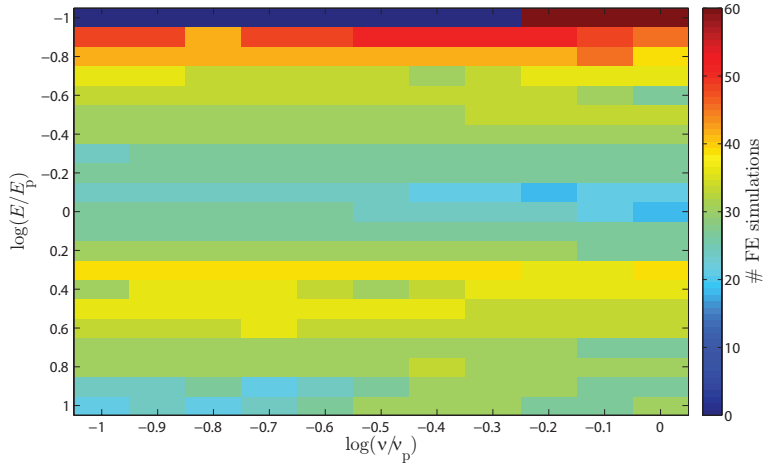
Figure B.3: Number of iterations needed before convergence within a set accuracy limit is reached for the Gauss-Newton method for a range of initial guesses. On the x-axis the initial guess in Poisson ratio v, relative to the reference value v_p, is plotted. On the y-axis the initial guess in Young's modulus E, with respect to the reference value E_p.

which the objective function f is approximated with a simpler function q which reflects the behavior of the true objective function. A trial step s is computed by minimizing over this trust region. When the sum of squares is lower for the trial $x + s$, the current point is updated. Otherwise, the current point remains and the trust region N is shrunk. The approximated function q is often the Taylor approximation of $f(x)$. Similar to Gauss-Newton, the Trust-Region algorithm requires an objective gradient and the Hessian Matrix of the posed function, which tends to be slower but more robust to local minima. Using a Trust Region further increases robustness.

Figure B.4 shows the amount of iterations required to reach the convergence criterium, with 3 (i.e. $N_{DOF} + 1$) FE simulations per iteration due to the calculation of the gradient and Hessian. The Trust-Region method shows less robustness for low initial guesses, but convergence performance is higher than the custom Gauss-Newton method.

Nelder-Mead

The Nelder-Mead algorithm is a derivative-free method, i.e. no Hessian matrix or gradient is required. The Nelder-Mead method is simplex-based. A simplex S in $\mathbb{R}^n$ is defined as the convex hull of $n + 1$ vertices $x_0, ..., x_n \in \mathbb{R}^n$. One iteration of the Nelder-Mead method consists of the following three steps:
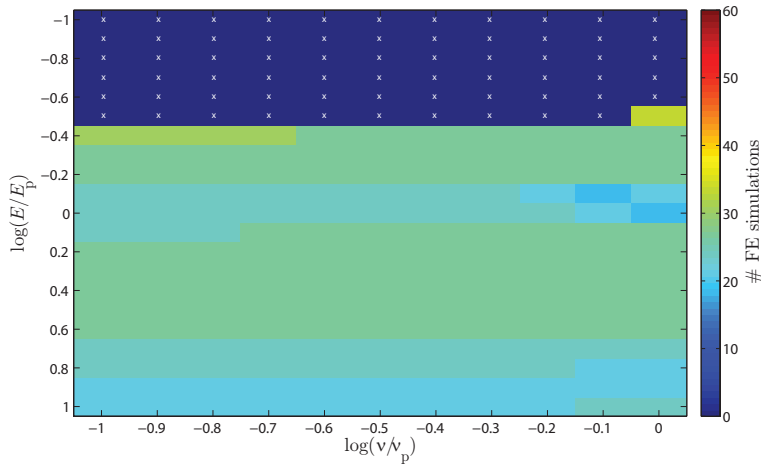
Figure B.4: Number of iterations needed before convergence within a set accuracy limit is reached for the Trust-Region method for a range of initial guesses. On the x-axis the initial guess in Poisson ratio ν, relative to the reference value ν_p, is plotted. On the y-axis the initial guess in Young's modulus E, with respect to the reference value E_p.

1. **Ordering**: Determine the indices h, s, l of the worst, second worst and the best vertex, respectively, in the current working simplex S.

2. **Centroid**: Calculate the centroid c of the best side; this is the one opposite the worst vertex x_h.

3. **Transformation**: Compute the new working simplex from the current one.

The transformation of the simplex is controlled by four parameters; α for reflection, β for contraction, γ for expansion and δ for shrinkage. Figure B.5 shows resp. (1) reflection, expansion, contraction and (2) shrinking operations. Based on the function values of vertices $x_0, ..., x_n$, an appropriate transformation step is chosen. It depends on this choice how many FE evaluations are required per iteration.

The following results are for the MATLAB Optimization Toolbox using the Nelder-Mead algorithm. The Nelder-Mead algorithm shows significant convergence towards a minimum for all given initial guesses, which proves robustness, but takes many FE simulations to accurately converge. This is also visible in Figure 4.7. For all cases in Figure 4.4, the algorithm was converging.
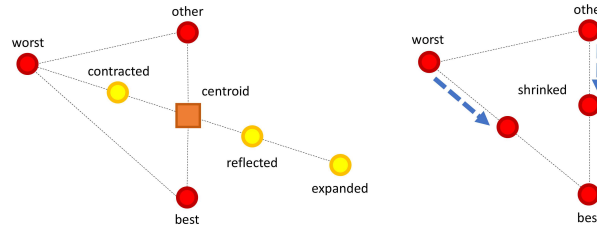
Figure B.5: Operations in the Nelder-Mead algorithm.

Comparison of the methods

To compare the methods more visually, a convergence plot for each method is shown for one specific initial guess combination: $\log(v/v_p) = -0.1$ and $\log(E/E_p) = -0.3$. Nelder-Mead takes significantly more simulations to converge and cannot rely on a derivative for the search direction, but takes multiple iterations to determine the direction. Gauss-Newton is the fastest method, followed by Trust-Region.

Conclusions

In integrated digital image correlation methods attention must be paid to the influence of using a correct geometric and material model, but also to make the boundary conditions in the FE simulation match the real experiment. Another issue is the robustness and convergence of the IDIC algorithm itself, which has been explored in this proceeding. The basis of the algorithm is the minimization of the residual. Different approaches for this minimization exist, of which a Gauss-Newton method is used most often. In this paper several other methods are presented as well and their performance is compared in terms of number of FE simulations needed, since this is the most time-consuming step in the iterative procedure.

The results presented show varying performance and robustness for different methods. Derivative free methods, like Nelder-Mead, tend to require a great amount of iterations, but it should be noted that this may not be bad for performance, because perturbation of input parameters λ is not required and hence less FE evaluations, the most computationally expensive step, are executed per iteration. The custom Gauss-Newton with update limit is a robust and performance-wise a decent solution, though using the MATLAB Optimization Toolbox should be considered because of code reliability and future-proofing, since toolboxes are commercially maintained by Mathworks. Further-
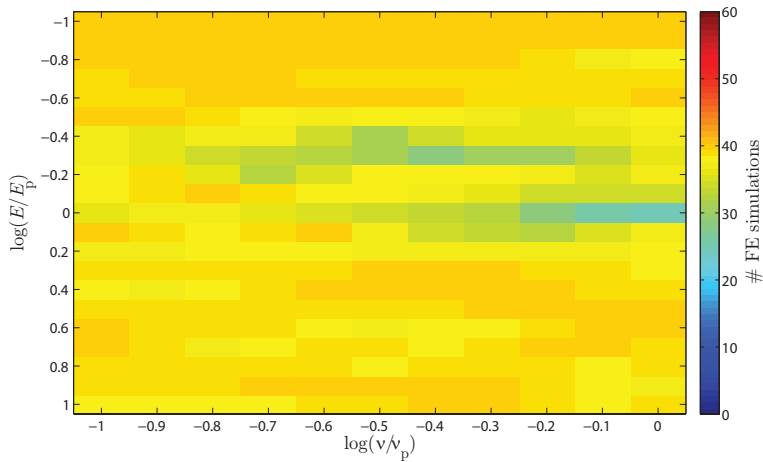
Figure B.6: Number of iterations needed before convergence within a set accuracy limit is reached for the Nelder-Mead method for a range of initial guesses. On the x-axis the initial guess in Poisson ratio v, relative to the reference value v_p, is plotted. On the y-axis the initial guess in Young's modulus E, with respect to the reference value E_p.

more, implementation of the Toolbox functions enables for using other optimization methods in the future, as new methods are introduced by Mathworks.

Another recommendation is extend the use of an update limit in the custom Gauss-Newton implementation, such that constraints based on physical boundaries are enforced, reducing the solution domain, thereby enhancing the robustness.

In practical use of the IDIC program, when choosing the initial guess is difficult, it can be useful to use a very robust, but slow, derivative-free method (e.g. Nelder-Mead) to determine the search direction and increasing the initial guess accuracy. After some iterations, getting nearer the solution, one can switch to a faster gradient-based method, e.g. Gauss-Newton. Using the implementation of MATLAB Optimization Toolbox, switching optimization methods runtime is possible. The analysis is done using a varying Young's Modulus and Poisson ratio, but IDIC can be used to determine many other constitutive parameters. The different optimization methods may differ in performance and robustness when other mechanical properties are to be identified.
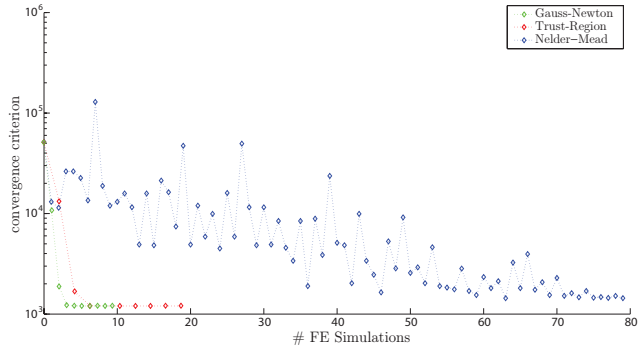
Figure B.7: Convergence plot for all three tested methods.

Appendix C
Mechanical Shape Correlation: a novel integrated digital image correlation approach

Abstract

Mechanical Shape Correlation (MSC) is a novel integrated digital image correlation technique, used to determine the optimal set of constitutive parameters to describe the experimentally observed mechanical behavior of a test specimen, based on digital images taken during the experiment. In contrast to regular digital image correlation techniques, where grayscale speckle patterns are correlated, the images used in MSC are projections of the sample contour. This enables the analysis of experiments for which this was previously not possible, because of restrictions due to the speckle pattern. For example, analysis becomes impossible if parts of the specimen move or rotate out of view as a result of complex and three-dimensional deformations and if the speckle pattern degrades due to large deformations. When correlating on the sample outline, these problems are overcome. However, it is necessary that the outline is large with respect to the structure volume and that its shape changes significantly upon deformation, to ensure sufficient sensitivity of the images to the model parameters. Virtual experiments concerning stretchable electronic interconnects, which because of their slender wire-like structure satisfy the conditions for MSC, are executed and yield accurate results in the objective model parameters. This is a promising result for the use of the MSC

method for tests with stretchable electronics and other (micromechanical) experiments in general.

Introduction

Mechanical Shape Correlation (MSC) is a novel technique, based on integrated digital image correlation (I-DIC) [100, 122], where a finite element (FE) model is coupled to the image correlation procedure. In such a method the constitutive parameters of the FE model are the unknowns in the correlation procedure, with the objective to obtain a good set of model parameters that describe the experimentally observed behavior of the test specimen correctly. In contrast to images of a speckle pattern applied to the test specimen, as usually used in DIC, in MSC the images used for correlation are projections of the deforming sample shape. This is beneficial in cases where complex three-dimensional deformations occur, such that parts of the specimen rotate out-of-view and other parts rotate into view, or if pattern application is difficult, such as on microscale samples. Usually in DIC approaches correlation is limited to in-plane deformations, or in case of Quasi-3D DIC (also referred to as Digital Height Correlation, DHC) [9, 52, 76, 99] or stereo-DIC [91, 150] it is also possible to track the out-of-plane deformation of the surface. However, this surface is required to stay in view and not to move or rotate out of view. By correlating the outline of the specimen this restriction is relaxed and full three-dimensional movement of the sample is allowed. However, for the MSC method the assumption is that the boundary area is large with respect to the volume of the structure and that it changes shape significantly upon deformation, such that deformations are reflected in the specimen edge.

A schematic depiction of the method can be seen in Figure C.1. During an experiment pictures are taken of the specimen. These images are processed in order to obtain a projection. Also a numerical simulation is executed and similar projections are made. The projections from the experiment and the simulation are compared. If they do not correlate, the model parameters, which are the unknown in the correlation procedure, are updated and a new simulation is performed. This iterative operation is repeated until convergence is reached and the correct set of model parameters to portray the experimental behavior of the structure is achieved.

The method is demonstrated by means of virtual experiments, dedicated to stretchable electronic interconnects. These interconnects are wire-like structures and hence their outline is large with respect to the volume of the structure. In this case the interconnects are not glued to a stretchable substrate, but they are free-standing and hence free to deform three-dimensionally, making it difficult to analyze their mechanical behavior with existing techniques. Therefore, these structures make an interesting test case for the MSC technique. The deformation of the interconnects can globally be split in two
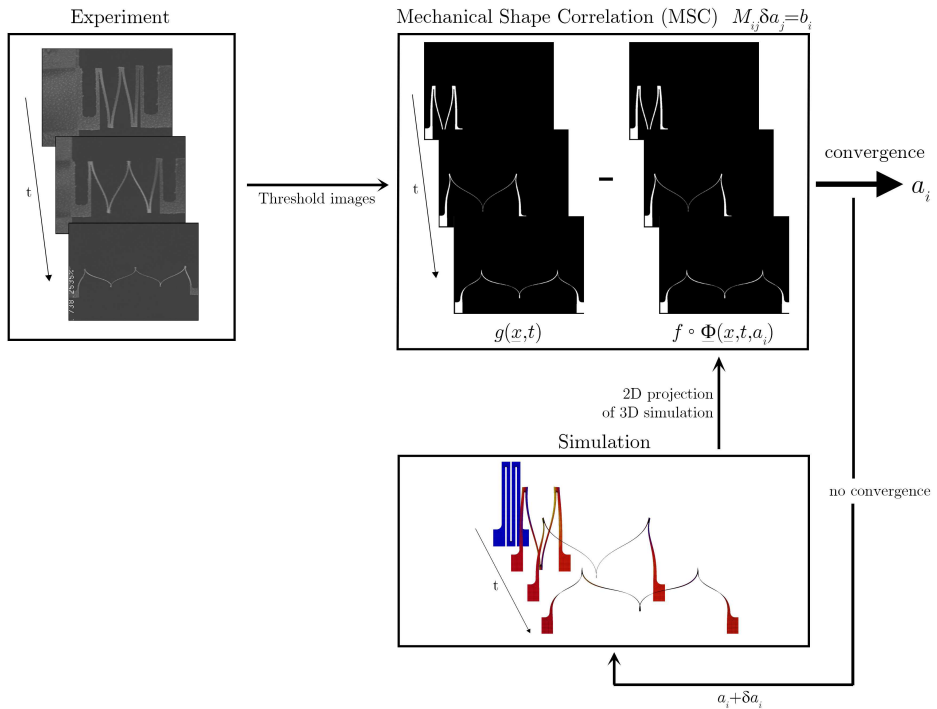
Figure C.1: Schematic representation of the mechanical shape correlation (MSC) method to identify model parameters a_i from an experiment. Simulations supply the images f to which the experiment is compared.

main modes: torsion of beams and double (S-shaped) bending of beams. These two modes are treated separately in the virtual experiments in this work.

The outline of the paper is as follows. In SectionC the MSC algorithm is introduced and compared to the integrated digital image correlation algorithm, highlighting the differences. Next the image type used for Mechanical Shape Correlation, i.e., the specimen projections, are explained and the important steps in the formation of these images are stepped through. In Section C two virtual experiment concerning the main deformation modes in the stretchable electronic interconnect structures are presented. In the last section conclusions are drawn.

Algorithm

The algorithm for Mechanical Shape Correlation is based on Integrated Digital Image Correlation (I-DIC) methods, see e.g. [100]. In I-DIC grayscale images of the sample, containing a speckle pattern, before and after deformation are compared, based on the optical flow relation, which means that material points are assumed to have the same gray value before and after deformation. A Finite Element (FE) simulation is performed which represents the experiment, in which some model parameters of interest are the unknowns in the correlation procedure. The resulting displacement field from this simulation is used to back-deform the deformed images, such that if the displacement field is calculated correctly the back-deformed image matches the undeformed, reference, image. The difference between these images is denoted as the *residual*, which naturally approaches zero if a good correlation is obtained. If this is not the case, the unknown model parameters are updated and the procedure is repeated.

The difference in MSC is that the the displacement field resulting from the FE simulation is not used to create back-deformed images, but projections, i.e., images, are generated from the model itself at different time increments. This image type is introduced in the next section. These FE images are correlated to similar projections that are made from the experimental images at the same time steps. Again, the residual is defined as the difference between these images. Similar to I-DIC the model parameters are updated iteratively to obtain a good correlation between the experiment and the simulation, as shown in Figure C.1.

Images

In conventional digital image correlation methods contrast in the images is usually provided by some sort of speckle pattern, either naturally present due to the specimen texture or artificially applied with, e.g., spray paint. In the Mechanical Shape Correlation technique the images consist of a projection of the specimen outline. The most elementary projection one could think of is the binary projection, where the background is assigned a contrasting color with respect to the structure itself, e.g., black and white, see Figure C.2a. However, since large parts of the image are monochromatic, the residual will only be non-zero in a relatively small area even if correlation is not achieved. This results in a low overall residual and the method will converge too soon. Therefore, the projection chosen for MSC is the signed distance map, i.e., the value for each pixel represents the closest distance to the sample contour, see Figure C.2b. With these images the whole field is affected if the unknown parameters in the FE simulation do not characterize the experimentally observed kinematics correctly. Therefore, the residual field is more likely to direct the algorithm to the correct solution.
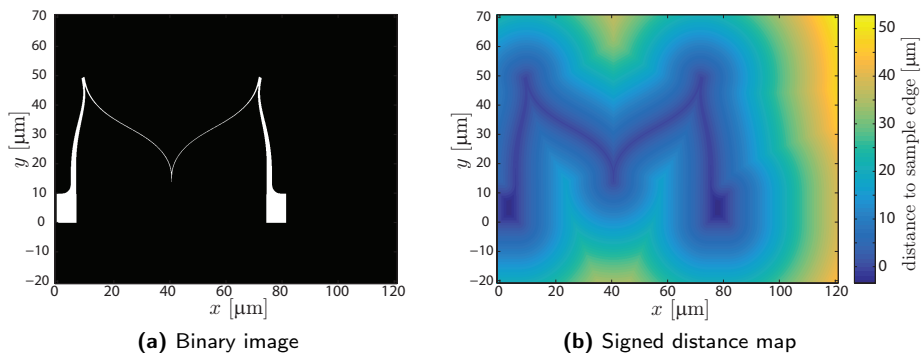
(a) Binary image

(b) Signed distance map

Figure C.2: Projection images used for the Mechanical Shape Correlation method. Two options are shown: on the left a binary projection in which the background is black and the structure itself is white. On the right a signed distance map is shown, where the colors indicate for each pixel the closest distance to the edge of the structure.

Projection of Finite Element simulation

A common type of elements used in FE simulation is shell elements. It deserves some attention as to how to create the projection images from these simulations. Since shell elements are infinitely thin, a projection perpendicular to the structure will not incorporate the real thickness of the sample. Therefore, this thickness should be artificially included in creating the signed distance maps. The first step is to determine the perimeter of the model, see Figure C.3. This is done by starting at an arbitrary point on the contour, however, it is easiest is to start at a corner. A node in the corner appears in only one elements, hence it is easy to search for such a node. Next all other nodes in this one element are scanned. The characteristic of the nodes located on the model perimeter is that they are shared by only two or three elements (or only one for the corners), while nodes in the center of the structure are shared by four elements. The node in the current element that satisfies this characteristic is the next in line on the contour. Furthermore, it is part of the next element in line, which is then scanned for the next node on the perimeter. This process is repeated until the starting node is attained again. Note that the assumptions made for this method only hold for rectangular elements, for other types the procedure should be adjusted accordingly. Also note that only the corner nodes of the elements are taken into consideration; the nodes at the edge centers, which are present for quadratic elements, are ignored. The next step is to construct the sample edge location more accurately, by defining more points (denser than the number of pixels on this distance). Interpolation using the FE shape functions (e.g., linear or quadratic, depending on the element type) is used to determine the positioning of these
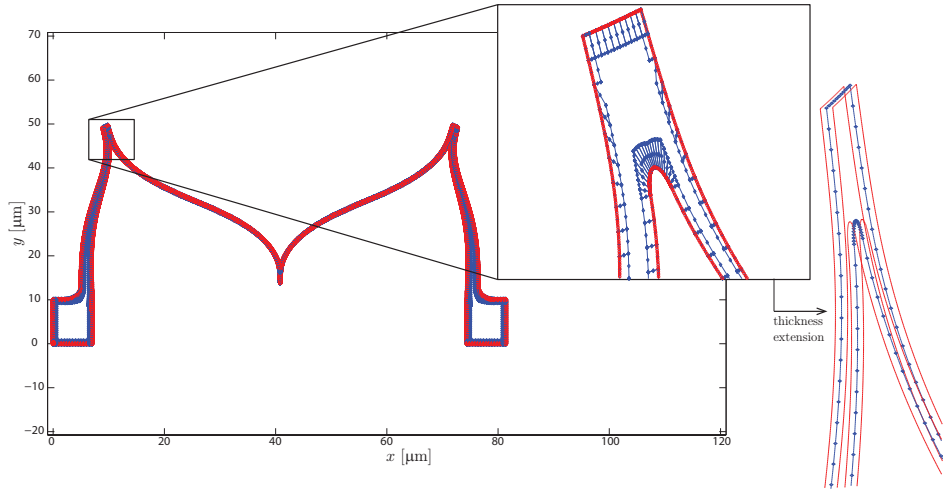
points.

Figure C.3: Determination of the sample contour from an FE simulation. In the case of shell elements, all element corner nodes located on the perimeter of the structure have in common that they are only shared by two or three elements, while nodes located in the center share four elements. Based on this characteristic it is possible to follow the contour of the structure, by starting at some point at the perimeter and repeatedly searching for the next node that satisfies this feature. After the perimeter is determined, the thickness of the specimen is artificially incorporated.

Now that the sample contour is accurately defined, the thickness can be incorporated. The rotation information of all nodes, resulting from the FE simulation, is taken into account to determine the locations of the virtual bottom and top contour, see the right part of Figure C.3. Now when a projection is made using these edges, and also the side edges connecting the top and bottom contours, the thickness of the sample is incorporated.

Masking

As can be seen from the extended structure in Figure C.3 many lines are crossing inside the structure, while we are only interested in the total outline since that is the only information that can be obtained from real experimental images. Because the determined edges consist of many points, which can be very close together for sharp edges, it is difficult to determine the convex hull of the shape to locate the outer contour and eliminate the internal curves. Therefore the signed distance map for the pixels

located inside the sample geometry can not be accurately determined. Furthermore, even if the signed distance map could be determined accurately, a small deviation in the calculation of the displacement field results in a relatively large effect in the signed distance map and hence the residual inside the structure, since the distances inside the structure are very small. This can lead to numerical instability and poor convergence. An elegant solution is to mask the structure itself and correlate only on the area outside the structure. The impact of masking on the method's performance is tested by means of a virtual experiment in the next section.

Virtual experiments

Two virtual experiments are executed to test the performance of the MSC method. The first experiment concerns one of the main deformation modes of the considered stretchable electronic interconnects: double bending of beams. In this experiment the effect of masking versus no masking is examined. The second virtual experiment concerns the other main deformation mode: torsion of beams.

Double bending of beams

The effect of masking is tested by means of a virtual experiment concerning a double bending beam, see Figure C.4. In this virtual experiment no real experiment is executed with this structure, but an FE simulation is performed and the projections made from this are used as the 'experimental' images. The model is an elastic model, with only one unknown model parameter: the Young's modulus E. The value used for the virtual experiment is 69GPa, or $6.9 \cdot 10^{-2} \text{N}/\mu\text{m}^2$, since the structure is modeled in micron. This value is the solution which is attempted to be determined using the Mechanical Shape Correlation method. The same model used to create the virtual experiment is also plugged in the MSC algorithm, however a variety of initial guesses for E are given. Also the perturbation factor P is varied. This factor is a parameter in the MSC algorithm, which originates from the derivative of the objective function being needed to minimize the residual. Since it is not possible to do so analytically, the derivative is approximated using a finite difference scheme. The step size for this calculation is taken relative to the value of the considered parameter, i.e., the perturbation factor P is introduced. The quantity of this factor affects the convergence behavior of the method and therefore different values for P are investigated in this research.

Since the real value for the Young's modulus is known, it is possible to determine the error in this parameter. This error is plot against the number of iterations for the situation when masking is applied versus no masking, and for different values of the initial guess and perturbation factor P. The resulting convergence graphs are shown in
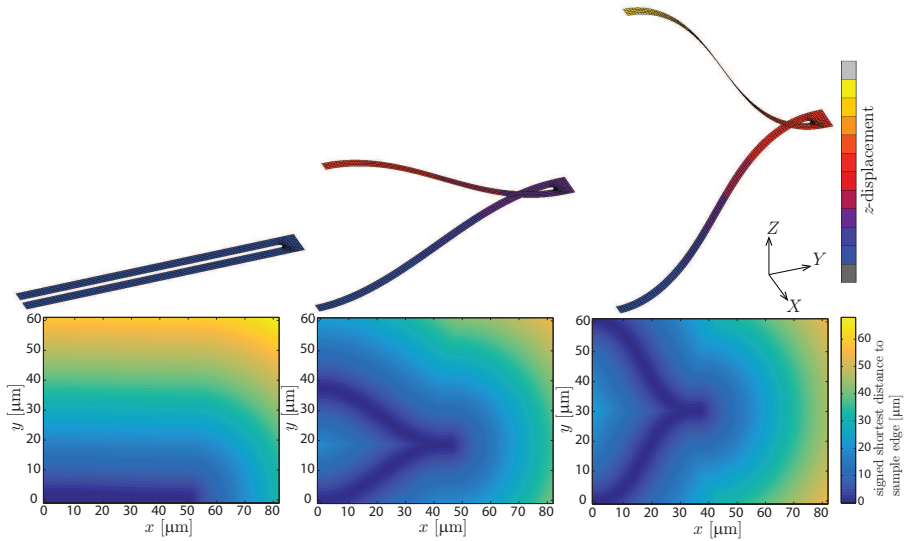
Figure C.4: Virtual experiment with a simple double bending beam. One end of the beam structure is constrained, while the other end is lifted with a prescribed force. The FE model is elastic with a Young's modulus of 69GPa. Not that the xy-coordinates in the signed distance maps correspond to the yz-coordinates in the FE simulation.

Figure C.5. It can be seen that for all settings the convergence behavior is improved in case the structure itself is masked. Especially for a small perturbation factor the effect is large. This is because a small perturbation increases the effect of numerical instability due to very small deviations.
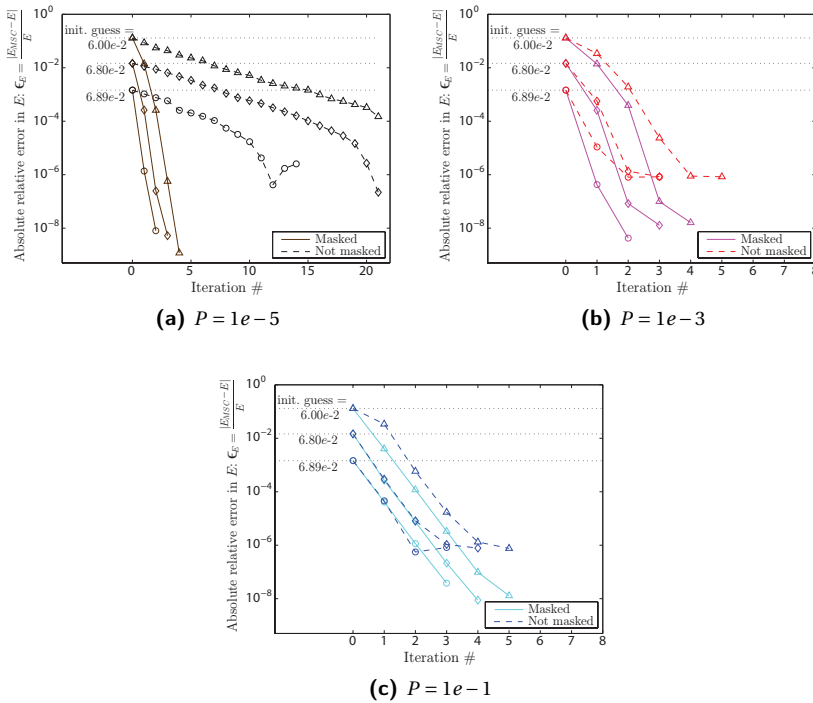
(a) $P = 1e - 5$

(b) $P = 1e - 3$

(c) $P = 1e - 1$

Figure C.5: Comparison of the convergence behavior of the MSC method for images where the structure itself is masked and images for which the structure is not masked, i.e., where the entire image is used. The comparison is executed for different values of the perturbation factor P and for different initial guesses.

Torsion of beams

The second virtual experiment is executed for a beam in torsion, which is beside the bending of beams also a deformation mode in stretchable electronic interconnect. A beam of $50\mu m \times 10\mu m$ is modeled and a prescribed moment is applied on one end, while the other end is clamped. The model is again elastic with one parameter, the Young's modulus E, which determines how much the beam rotates upon the prescribed moment. Signed distance projections are made at various increments and these are used as the 'experimental' input images, see Figure C.6.
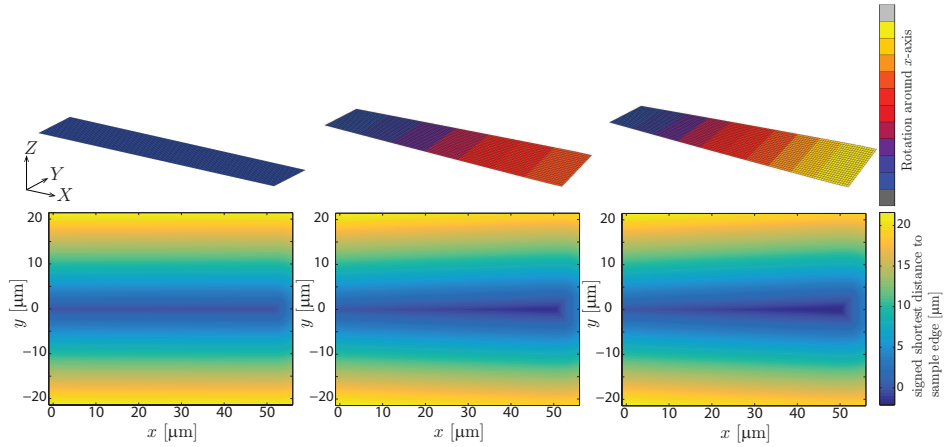
Figure C.6: Signed distance maps for a selection of increments of the virtual experiment concerning a torsion beam. Note that the y-coordinate in the signed distance maps coincides with the z-coordinate in the FE simulation.

The algorithm is run again for different initial guesses and various values of the perturbation factor P. The convergence behavior based on the error is plot in Figure C.7. It can be seen that convergence with a good accuracy is reached in a reasonable amount of iterations for all tried variations in initial guess and P. This gives a good perspective to use the method with other test cases.
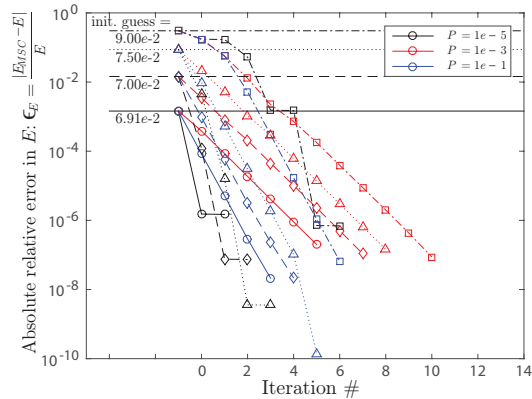

Figure C.7: Convergence plot of the MSC algorithm for the torsion beam experiment, for different values of the perturbation factor P and different initial guess values.

Conclusions

A novel method called Mechanical Shape Correlation has been developed. It is an integrated digital image correlation based method, which uses a finite element model for regularization of the displacement field. The goal of such a method is to obtain an adequate set of constitutive model parameters, such that the FE model describes the real, experimentally observed, behavior of the sample correctly. The novelty lies in the use of projections of the sample contour as input images for the algorithm, rather than grayscale speckle patterns. This approach makes it possible to apply the technique to experiments for which existing techniques are difficult to use, because of complex three-dimensional deformations that makes parts of the specimen move out of view or because of complications with pattern application.

The MSC algorithm was explained along with some important changes with respect to the IDIC algorithm. The most important change is the type of images used and attention was paid as to how to create these projections from FE simulations and the important steps taken herein. Also masking of the structure itself in the created projections plays an important role. Two virtual experiments were executed to examine the method's performance. The first virtual test case includes analysis of the difference in results in case the structure is masked in the images or not masked. It was concluded that the convergence behavior improves if masking is applied for all considered parameter variations, including the initial guess and perturbation factor P, but that the effect is strongest for small perturbation factors. In both virtual experiments a good accuracy in the objective model parameter, the Young's modulus E, was obtained in a reasonably low amount of iterations. These results are promising for the method's performance in other test cases.

Publications

Journal publications

Kleinendorst SM, Hoefnagels JPM, Verhoosel CV, Ruybalid AP. (2015) On the use of adaptive refinement in isogeometric digital image correlation. *International Journal for Numerical Methods in Engineering*; **104**: 944-962.

Kleinendorst SM, Hoefnagels JPM, Fleerakkers RC, Maris MPFHL van, Cattarinuzzi E, Verhoosel CV, Geers MGD. (2016) Adaptive isogeometric digital height correlation: application to stretchable electronics. *Strain*; **52(4)**: 336-354.

Kleinendorst SM, Hoefnagels JPM, Geers MGD. (2019) Mechanical shape correlation: a novel integrated digital image correlation approach. *Computer Methods in Applied Mechanics and Engineering*; **345**: 983-1006.

Kleinendorst SM*, Fleerakkers R*, Cattarinuzzi E, Vena P, Gastaldi D, Maris MPFHL van, Hoefnagels JPM. (2020) Experimental-Numerical Characterization of Metal-Polymer Interface Delamination in Stretchable Electronics Interconnects. *Submitted for publication*

Kleinendorst SM, Geers MGD, Hoefnagels JPM. (2020) Parameter identification of freestanding stretchable electronic interconnects using Integrated Digital Height Correlation. *In preparation*

Other publications (conference proceedings)

Kleinendorst SM, Hoefnagels JPM, Geers MGD. (2018) Mechanical Shape Correlation: a novel integrated digital image correlation approach. *Advancement of Optical Methods in Experimental Mechanics, Conference Proceedings of the Society for Experimental Mechanics Series*; **3**: 47-54.

Kleinendorst SM, Verhaegh BJ, Hoefnagels JPM, Ruybalid AP, Sluis O van der, Geers MGD. (2018) On the boundary conditions and optimization methods in Integrated Digital Image Correlation. *Advancement of Optical Methods in Experimental Mechanics, Conference Proceedings of the Society for Experimental Mechanics Series*; **3**: 55-61.

---

*S.M. Kleinendorst and R. Fleerakkers are joined first author

Kleinendorst SM, Borger RRM, Hoefnagels JPM, Geers MGD. (2018) Novel image correlation based techniques for mechanical analysis of MEMS. *Micro and nanomechanics, Conference Proceedings of the Society for Experimental Mechanics Series*; **5**: 19-28.

Hoefnagels JPM, Kleinendorst SM, Ruybalid AP, Verhoosel CV, Geers MGD. (2017) Self-adaptive isogeometric global digital image correlation and digital height correlation. *Advancement of Optical Methods in Experimental Mechanics, Conference Proceedings of the 2016 Annual Conference on Experimental and Applied Mechanics*; **3**: 165-172.

Acknowledgements

Completing a PhD is not an easy task, which I experienced in the past couple of years. Therefore, I'm grateful for the support I received from the people around me, whom I'd like to thank here.

First of all, Johan, thank you for the great cooperation that we've had for the past years. I really enjoyed working together with you. I like how you were never out of ideas to help me continue whenever I was stuck and how I could always walk in and you would make some time for me. Thank you for your patience and understanding when things weren't going smoothly. Your positivity meant a lot to me and really helped me to continue. Furthermore, I'm grateful for your fast input and replies (sometimes in the middle of the night, haha) to my thousand-and-one questions towards finishing the final chapters of my thesis, even though sometimes I was very last minute. It has been a pleasure not only work-related, but also to go on conference trips and 'lab-onions' with you. I couldn't wish for a better supervisor (and now first promotor!) and I'm glad you gave me the opportunity to pursue this PhD under your guidance.

Marc, I would like to thank you for the guidance you offered during our monthly meetings and outside them. I like your calm and structured approach of explaining things and how you sometimes made me look at a problem from a different perspective to help me solve it. Also thank you for being understanding and keeping trust in me when I started losing that myself. You are a kind person and I enjoyed working with you both on a professional and personal level.

To the other staff members of the Mechanics of Materials group and other groups within the Mechanical Engineering department, thank you for always being open to questions and making time for discussions. Especially, Olaf, thank you for our, at some point almost weekly, Friday 8:00am meetings in which you shared your valuable knowledge on FE modeling. And Marc, thank you for your support in the Multi-Scale lab whenever I wanted to perform some experiment with my limited experience, being a numerical person, or sent a student at you. Joris, thank you for both work-related support and our wonderful musical collaboration "The Newtonians", I enjoyed rehearsing and performing with you at the MaTe-party and the EM-symposium very much.

As a PhD generally means working alone most of the time, it's nice to have colleagues working besides you. It's great to have been part of such a nice office, to share coffee (or, in my case, tea) breaks with, go on the occasional office outing, share successes with (paper acceptance pies!), but also to have someone to complain to if things don't go according to plan. In particular, Rody, my desk-neighbour, thank you for helping me out numerous times with all of my computer issues, whether I specifically asked for it or was merely letting out my frustrations. Thank you 4.13 office guys, those who have been there almost the entire time together with me: Jim, Luv, Maqsood,

Mirka, Siavash and Stefan, and those who were there at various points in time: Emanuela, Job, Majid, Mary, Mohsen, Nik, Nilgoon, Steyn, Sven, Tito and Vahid. Special thanks goes out to Salman, my project partner: you are a very kind person and it was nice to collaborate with you. A warm thank you also to colleagues from other offices, with whom I have nice memories on MoM-outings and fun nights at the EM symposium. In particular: Andre, thank you for your help and discussions on various DIC related topics, and Ondrej, for your collaboration on the image segmentation part.

I also enjoyed the educational side of a PhD. Hans, I liked being part of the 'Structure and Properties of Materials' course for several years. Furthermore I'd like to thank the students that I supervised for their Bachelor's or Master's projects or contributed otherwise to my project: Bart, Dion, Don, Janko, Remco, Rob, Robin and Thijs.

To all my friends from studying, high school or whom I met otherwise: thank you for the good times we have together, regularly asking me how I'm doing and being there for me. Jos, Lennart and Michel, it's been fun to share breaks in the Simonkamer and solve the daily 'In het midden'-puzzle together. And in particular: Caroline, we've shared the same road at the university for eleven years. We've shared many fun things, but you were also always there for me when I needed it, thank you for that!

Mom and dad, thank you for your unconditional love and support. You've always supported my choices and encouraged me to make the best out of myself. You are always there to help me, both practically and emotionally and I'm happy to have you as my parents. Stephan, Thomas, Simone, Christel, Demi and Kevin, it's always nice to be around you and I'm thankful for the good brotherly and sisterly bond that we have. To Gert, Ine, Inge, Jan and Noud: it's nice to have such a warm in-law family, thank you for welcoming me in your family.

Last, but not least, to my dearest Ruud. You're my rock and I consider myself very lucky to have you. I think I wouldn't have been able to make it without your support, in every sense. You always know exactly what to do or say to make me feel better in difficult times. You make me feel loved and always show me that you're proud of me. I'm happy to call you my husband. I'm delighted to share my life with you and look forward to our bright future with the family that we already started with our sweetest son Brent!

Gerwen, October 2019
Sandra

Curriculum Vitae

Sandra van de Looij - Kleinendorst was born on October 26th 1988 in Dordrecht, the Netherlands. After finishing secondary education (VWO) at Udens College in Uden in 2007, she enrolled in the Bachelor program of Mechanical Engineering at Eindhoven University of Technology. She continued her education in the Master program of Mechanical Engineering at the same university. As part of the curriculum, she completed an internship in the Mechanical Engineering & Materials department in the research group of prof. Matthew R. Begley at University of California Santa Barbara (UCSB) in the United States of America. In 2014 she graduated *cum laude* within the Mechanics of Materials group of prof. Marc Geers, with her thesis entitled "On the use of adapative refinement in isogeometric digital image correlation". In the same year, she started her PhD.-research entitled "Image Based Mechanical Characterization Methods For Stretchable Electronic Interconnects" within the project "Stretching the limits of IC stretchability (SLIC)" within the same group, under the supervision of dr. Johan Hoefnagels and prof. Marc Geers, of which the results are presented in this dissertation. As part of the program she obtained the Engineering Mechanics graduate school certificate.